Measurement of Creep Deformation in Weldments

Thesis

The Open University

Faculty of Mathematics, Computing & Technology

Department of Design, Development, Environment and Materials

MEASURMENT OF CREEP DEFORMATION IN WELDMENTS

by

Yuki Sakanashi

March 2013

A THESIS SUMMITTED TO THE DEPARTMENT OF DESIGN, DEVELOPMENT, ENVIRONMENT AND MATERIALS OF THE OPEN UNIVERSITY FOR THE DEGREE OF DOCTOR OF PHILOSOPHY

DATE of SUBMISSION: 28 MARCH 2013

DATE of AWARD: 23 JULY 2013

ProQuest LLC.
789 East Eisenhower Parkway
P.O. Box 1346
Ann Arbor, MI 48106 – 1346

Preface

This thesis is submitted for the degree of Doctor of Philosophy of The Open University, UK. This work described in this thesis was carried out in the Department of Materials Engineering, Faculty of Mathematics, Computing and Technology, between April 2009 and March 2012.

It is original work of the author except where reference is made to the work of others. None of this work has been submitted for a degree or other qualification at this or any other university. Some of the results of this work have been published in conference proceedings as followings:

1. Y. Sakanashi, S.Gungor and P.J.Bouchard. Measurement of creep deformation in stainless steel welded joint. Society of Experimental Mechanics (SEM) Annual Conference Proceeding 2011.
2. Y. Sakanashi, S.Gungor and P.J.Bouchard. Creep deformation measurement of 316H stainless steel multi-pass welded joints using digital image correlation. 4th International Conference on the Integrity of High Temperature Welds/Creep Conference Proceeding 2012.

Yuki Sakanashi

March 2013

Acknowledgement

First of all, I would like to thank to the Open University for giving me the chance to return to University to study for a PhD research degree. I am also thankful to EDF Energy, former British Energy Generation Limited, for funding support during this period.

Special thanks to my supervisor, John Bouchard for his continuous support. I could not have reached this stage without his guidance. I really do appreciate his help and kindness.

Special thanks to my supervisor, Dr.Salih Gungor for your continuous help. I am grateful for all your support.

I am thankful to Mike Spindler and Dave Dean who are working in EDF Energy for their advice, help and support.

I am also grateful to Stan Hiller for his contributions to my project and Peter Ledgard for his continuous assistance.

Thanks to all my colleagues during this period, Dr. Murat Acar, Dr. Ashwin Rao, Yeli Traore, Sanjoo Paddea, Dr. Sue Storer, Dr. Bama Perumal, Dr. Genoveva Burca, David Githinji, Abdul Khadar Syed, Shanmukha Moturu, Jose Rodolpho Leo, Jeferson Araujo de Oliveira, Stefano Coratella, Gerardo Carvajal, Ellies Muyupa and other students, members of staffs.

I also would like to say special thanks to Courtney Courtnage for continuous support since I joined the OU.

At the end of my studies, Universe sent two wise men to help my PhD, Imran Bhamji and Alex Forsey, thanks for supporting my project and thesis correction. I could not have finished my PhD without your help.

Finally, I'd like to state my great thanks to my dearest daughter Becky and son Joe, for being so patient and forgiving for the last 4 years. Special thanks to my friend Steve Phillips, Yoshie Buckly and Kae Silva for looking after my children and special thanks to my parents, Kazuko and Hiroshi, in Japan for your understanding and cooperation.

Yuki Sakanashi

March, 2013

Table of Contents

Measurement of Creep Deformation in Weldments

Abstract

This PhD project has developed a new high temperature strain measurement system using Digital Image Correlation (DIC) in order to investigate spatially varying and time dependent deformation during high temperature creep tests of engineering materials. Several challenges associated with measuring creep deformation at elevated temperature have been overcome including the choice of specimen design, specimen oxidation, furnace temperature uniformity, image distortion caused by thermal currents and sufficient illumination. It is demonstrated that the system created can produce reliable measurement data over a period of several months with a spatial resolution of 0.6 mm for temperatures up to 650 °C, but in principle higher resolution and temperatures should be achievable.

The research aim of this project, funded by EDF Energy (formerly British Energy), was to attempt to measure spatially varying creep deformation properties across thick and thin section weldments that operate at high temperatures in UK advanced gas cooled reactor power plant (AGR). The new measurement system is applied to examine the creep behaviour of a thick section multi-pass welded joint made from Type 316H austenitic stainless steel which was supplied by EDF Energy. Specifically the local creep deformation properties across the weldment in the parent material, heat affected zone (HAZ) and multi-pass weld layers are investigated in medium term creep tests (>2300 hours). This

is achieved by cutting samples from three different locations of the thick section joint, that is from top, middle and bottom positions, and subjecting them to tensile and creep testing at a temperature of 545°C. Spatially resolved stress-strain (tensile) and strain-time (creep) results were obtained transversely across the whole section of the multi-pass weldment and across the thickness direction. The DIC in-situ measurements also provided strain information in the transverse to loading direction from which the reduction of area of the specimen and true stress and strain distribution were calculated. The weld metal showed faster creep rates than HAZ and parent materials and this is attributed to the observed introduction of substantial plastic strain in the parent material on initial loading. Locally the creep strain distribution in the weld metal appears to correlate with individual weld passes. The full-field measurement results allowed the development of creep deformation leading to ultimate rupture to be observed.

The high temperature tensile and creep results presented in this thesis demonstrate the capability of the new DIC based system created for full field measurements of displacement and strain at high temperature during creep tests enduring several thousand hours. The system opens a new horizon for studying deformation and rupture behaviour of complex structures at elevated temperature.

Chapter 1

Introduction

1.1 Background

In response to an expected long-term increase in demand for electricity, the UK government have announced plans for a new generation of nuclear power plants and confirmed a list of sites it deems suitable for their construction by 2025 [1]. Nuclear power is an energy source option with near zero carbon emissions. Figure 1.1 shows the IAEA's estimate of total greenhouse gas (GHG) emission from complete electricity generation chains. As you can see nuclear electricity generates much smaller GHG emissions compared to fossil fuels and others [2]. The global warming phenomenon caused by rising atmospheric carbon dioxide concentrations and climate change is one of the most important issues facing the world today [3]. Effective means to solve these problems which have been considered are using alternative energy sources which do not emit CO_2 to generate electricity. However, in order to generate a large amount of alternative electricity effectively, nuclear power generation seems to be one of the best ways to solve this problem with current technology. It is able to supply an amount of continuous and reliable electricity without emitting carbon dioxide.

Nevertheless, nuclear power can be extremely dangerous as we know from the 11th March 2011 Japanese earthquake and tsunami that rocked TEPCO Fukushima Daiichi nuclear power plant, leaving radioactivity leaking from the

plant [4],[5]. Although natural disasters destroyed whole towns at an instant moment, radioactivity stays there for a long time. Radiation affects both humans and nature. Many people are not able to return their home town because its radioactive level is still high even after 2 years.

Moreover recently, two Belgium nuclear reactors, DOEL 3 and Tihange 2 were taken out of operation because unexpected flaws were detected by ultrasound sensors examination [6]. During the inspection performed at DOEL 3 in June 2012, numerous flaw indications in the base metal of the reactor vessel were detected in particular in the bottommost ring. A total of 7,776 flaw indications in the core lower shell and 931 flaw indications in the core upper shell were found. Similar flaws were revealed in September 2012 in the reactor pressure vessel of another nuclear power plant Tihange 2. A total of 1,931 flaw indications in the upper core shell and 80 flaw indications in the lower core shell were detected.

Safety is the top priority in operating nuclear power stations. Plant lifetime safety is managed partly through monitoring and assessing any structural damage or degradation phenomena arising such as found at DOEL 3 and Tihange 2. Plant safety cases have to be prepared to ensure safety is maintained at all times during any mode of normal or fault operation.

The Advanced Gas-Cooled Reactor (AGR) is a second generation reactor and was developed from Magnox reactor technology in the UK to improve thermal efficiency. Figure 1.2 shows an illustration of an AGR.

The AGR uses graphite as the neutron moderator and carbon dioxide as coolant. The fuel is uranium oxide pellets, enriched to 2.5%, in stainless steel tubes. The carbon dioxide circulates through the core, reaching 650°C and then past steam generator tubes outside it, but still inside the concrete and steel pressure vessel. Control rods penetrate the moderator and a secondary shutdown system involves injecting nitrogen to the coolant [7]. There are several different types of nuclear reactors operating in the UK. A total of AGRs currently operate at 6 sites in the UK.

The heat generated by the nuclear reaction is used to raise high-pressure steam, which then drives steam turbines coupled to electrical generators, to generate electricity. The coolant circulates through the core at a pressure of about 40 bar and reaches a temperature of around 650°C, and then passes through the boiler (steam generator) assemblies outside of the core but still within the steel lined, reinforced concrete pressure vessel. The temperature of the coolant outlet reduces to about 400°C before it re-enters the core [8].

The circulation of the coolant and the steam requires a long network of corrosion resistant pipes joined together. The high-pressure and high temperature operating conditions means that the structural materials used in AGRs requires very good properties. AISI 316 type austenitic stainless steel is used for many systems on an AGR reactor, because it has good creep strength at high temperatures. Coolant and steam systems comprise a network of pressure vessels and piping components that are constructed by welding then together. But weld zones inherently have non uniform metallurgy and material deformation

properties and therefore tend to be most prone to degradation at high temperature owing to creep deformation and damage mechanisms.

In creep life assessment of structures, various evaluation methods [9] have been developed to predict accumulated creep strain, damage in structures and rupture life. In order to apply such methods, it is necessary to measure the material creep deformation and rupture properties at high temperature. The location of creep damage often starts in and around welded materials and this is probably associated with local zones having inferior creep properties that will vary across welded joints [10]. In a typical creep test, the creep strain is measured using uniform material specimens which are cut from individual zones of weldments (parent, HAZ and weld) and the global strain is averaged along the gauge length using extensometers.

In order to measure graded creep properties across a weldment, where strain localization may occur, either micro-specimens have to be extracted and tested [11], [12] or, ideally, a means developed to measure the full field deformation response of the welded joint. Several measurement techniques have been considered for full field creep deformation characterisation. Electron speckle pattern interferometry (ESPI) [13] and moiré interferometry [14] are commonly used at room temperature to measure full-field displacement. However, these techniques require the refractive index of the medium (e.g. air) to be constant and therefore their accuracy is adversely affected by the influence of temperature variations between the test object and the image recording equipment [15].

In recent years, efficient tools for full-field deformation measurement have been developed. The fast evolving capabilities of digital image acquisition and software for image analysis have provided opportunities for developing reliable strain measurement system allowing full-field visualization of structures [16]. The Digital Image Correlation (DIC) technique can be used under various circumstances, including monitoring the inception of localized phenomena such as necking and crack initiation during mechanical testing of materials [17]. A full-field strain measurement system has the potential to provide us with detailed information about the creep strain spatial distribution and local creep deformation development as a function of time. The general objective of this thesis is to show how the DIC technique can be applied to create a reliable high temperature creep deformation measurement system. The specific research aim of this project is to attempt to measure spatially varying creep deformation properties across thick and thin section weldments that operate at high temperatures (up to 650 °C) in UK advanced gas cooled reactor power plant.

1.2 Project Aim

The premise of this thesis is that DIC can be implemented to measure creep deformation in stainless steel weldments. However, high temperature tests are very demanding for conventional strain measurement techniques. The problems in measurement of creep strain at elevated temperature using optical methods include choice of specimen design, specimen surface oxidation, optical access, furnace temperature uniformity, image distortion caused by thermal currents

(heat haze) and sufficient illumination. These critical issues have to be improved to make DIC a viable technique to use on a stable measurement system. Solutions for each issue are identified, implemented and assessed to substantiate the stability, reliability and accuracy of full field strain measurement at high temperature in a newly developed system. A multi-pass welded joint is tested to prove the viability of the new high temperature measurement system and to advance the state of knowledge relating to creep deformation and damage development in thick stainless steel weldments.

1.3 Structure of Thesis

This thesis presents both the development of a high temperature DIC system for measuring creep deformation and shows how has been applied to investigate spatial and time resolved deformations during creep tests at elevated temperature. Chapter 2 is a literature review in two parts covering creep behaviour of stainless steel and digital image correlation. The first part introduces the basic characteristics and mechanisms of creep in austenitic stainless steel and multi-pass welded joints. Then, the basic background of DIC and the conventional optical techniques for creep strain measurement are reviewed and assessed. Chapter 3 illustrates how DIC has been applied to measure spatially varying stress-strain properties in a cross weld tensile test at room temperature. Development of the high temperature DIC system is presented in Chapter 4 including work carried out to solve major problems. This chapter also discusses how the reliability, stability and accuracy of the system have been optimised.

Application of the new system to study tensile and creep deformation of a multi-pass weldment is presented in Chapter 5. Extensive results for the multi-pass weldment are reported demonstrating the capability of the new measurement system and revealing the complex creep properties of the joint. Finally, Chapter 6 presents overall conclusions and suggested future work.

1.4 References

[1] "Nuclear Research and Development Capabilities, Select committee on science and Technology 3rd report of session," House of Lords, 2011.

[2] "Climate change and nuclear power 2012,"*Internetional Atomic Energy Agency (IAEA) Publication November* 2012.

[3] H. Rogner, "Nuclear power and climate change," *Department of Nuclear Energy, Internetional Atomic Energy Agency (IAEA) Vienna, Austria*, vol. II, no. 2, pp. 1–11, 2002.

[4] IAEA, "IAEA International Fact Finding Expert Mission of the Nuclear Accident Following the Great East Japan Earthquake and Tsunami," *Preliminary Summary*, 2011.

[5] "The Fukushima Nuclear Accident Independent Investigation Commission," *The National Diet of Japan.*2012.

[6] I. Tweer, "Flawed Reactor Pressure Vessels in Belgian Nuclear Plants Doel-3 and Tihange-2," *FANC Provisional evaluation report*, 2013.

[7] T. Mckeen, "Advanced gas cooled reactors," *Nuclear energy material and reactors* vol. II.

[8] P. D. Wilson, "The Nuclear Fuel Cycle," *OUP*, 1996.

[9] "R5 Issue 3 Assessment procedure for the high temperature response of structures. EDF Energy Ltd, May 2012." .

[10] Hongo Hiromichi, Yamazaki Masayoshi, Watanabe Takashi, Tabuch Masaaki, Tanabe Tatsuhiko, and Monma Yoshio, "Evaluation for creep properties of 316FR weld metal with miniture weld metal and full-thickness welded joint specimens," *The society of Material Science, Japan*, vol. 53, no. 5, pp. 566–571, 2004.

[11] A.Garzillo, C. Guardamagna, L. Moscotti, and A. Ranzani, "A technique for the residual life assessment of high temperature components based on creep rupture testing on welded miniature specimens," *International Journal of Pressure Vessels and Piping*, vol. 66, pp. 223–232, 1996.

[12] "Recommendations for creep testing of PE (ex-service) materials." vol. 3, Part III, 2005.

[13] J. N. Petzing and J. R. Tyrer, "Recent development and applications in electronic speckle patten interferometry," *The Journal of Strain Analysis for Engineering Design*, vol. 33, no. 2, pp. 153–169, Jan. 1998.

[14] J.M.Burch and C.Forno, "High resolution moire photography," *Optical Engineering*, vol. D, no. 4, 1982.

[15] J.S.Lyons, J.Liu, and M.A.Sutton, "High-temperature deformation measurement using digital-image correlation," *Experimental Mechanics*, pp. 64–70, 1996.

[16] Murat Acar, "Effects of plastic strain history on the properties of stainless steel boiler tube welds," PhD thesis,The Open University, UK, 2011.

[17] J. Rupil, S. Roux, F. Hild, L. Vincent, C. E. A. Saclay, and N. S. Lcm, "Fatigue microcrack detection with digital image correlation," *The Journal of Strain Analysis for Engineering Design*, vol. 46, no. 6, pp. 492–509, 2011.

[18] "Copyright British Energy Group plc," 2006.(http://www.british-energy.com/documents/How_an_AGR_power_station_works.pdf) Access date :March 2013.

1.5 Figures

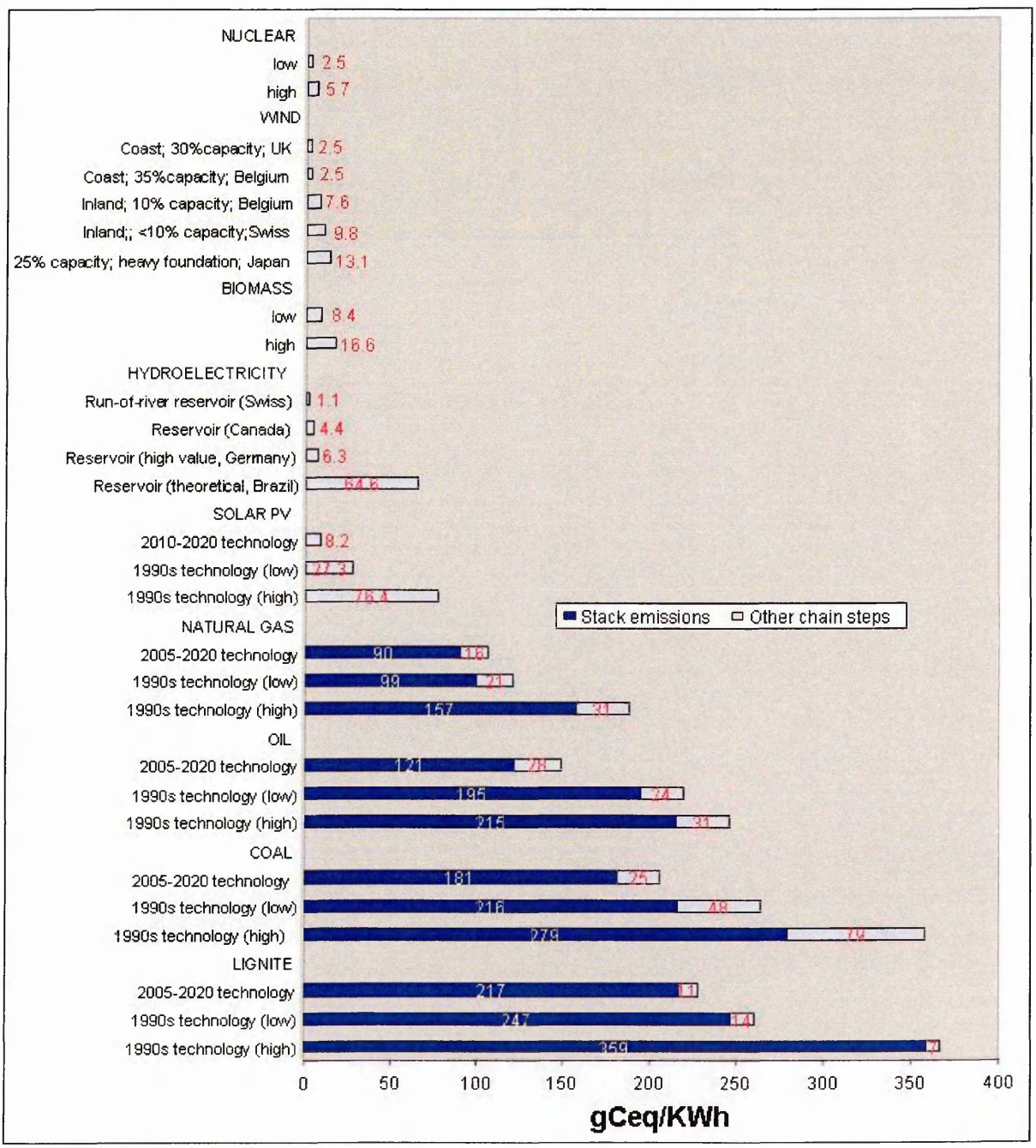

Figure 1.1Full energy chain GHG (Greehouse Gas) emissions (in grams of carbon equivalent per kWh) for different electricity generating options. Range are from 1990s technology to advanced technology (2005-2020) [2]

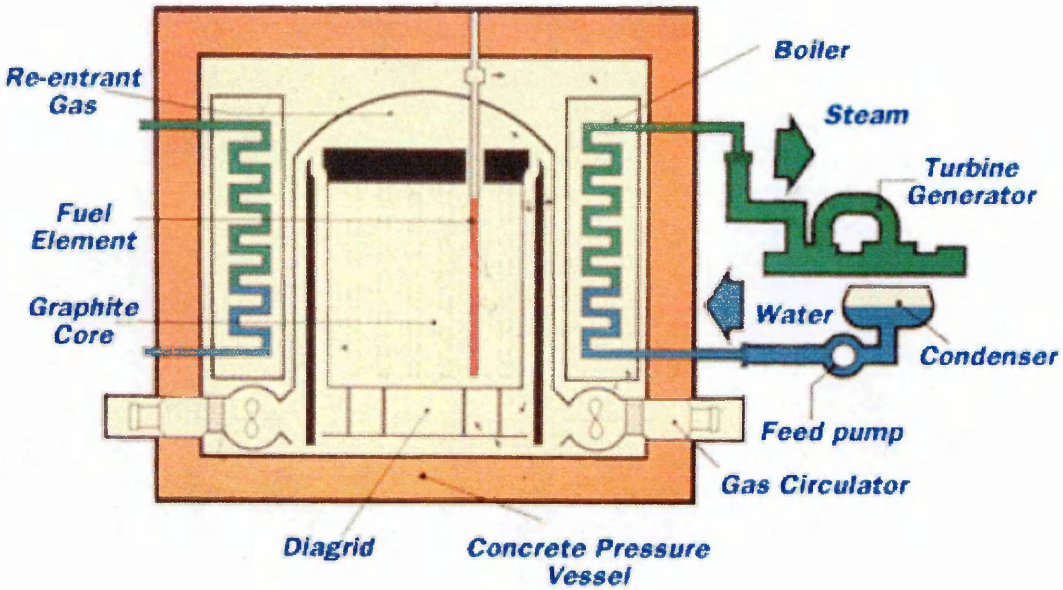

Figure 1.2 Advanced gas-cooled reactor (AGR) [18]

Chapter 2

Literature Review

This thesis is concerned with the application of digital image correlation (DIC) to measure spatially varying deformation in stainless steel weldments under external load at low temperature and, uniquely, time-dependent-location-specific deformation behaviour at elevated temperature. The first part of the present Chapter (section 2.1) describes the deformation behaviour of austenitic stainless steels at low temperature and high temperature creep mechanisms leading to rupture. This is followed by a review of the more complex behaviour of multi-pass weldments. Section 2.2 surveys various methods for measuring strain at high temperature including point to point measurements and full field techniques. The final part of the Chapter (section 2.3) introduces the DIC method for determining displacement fields reviewing various elements of analysis procedures and factors affecting accuracy.

2.1 Creep Behaviour of Austenitic Stainless Steel

2.1.1 Austenitic Stainless Steel

Steel is the alloy of iron principally. The primary alloying element is carbon, which content in the steel is between 0.002% and 2.1% by weight. Stainless steel is an important class of engineering material widely used in various industries and

aggressive environments. Stainless steel has various grades as classified by its microstructure, namely martensitic, austenitic, and duplex (austenite plus ferrite) [1]. Austenitic type of stainless steel has added Cr and Ni and a face-centred cubic lattice crystal structure. It also contains higher carbon which produces precipitation hardening [2]. Austenitic stainless steel has good high temperature properties and excellent corrosion and radiation resistance. As its high-temperature strength is greater than that of ferritic stainless steel, it is frequently used as a structural material within the high temperature systems of industrial plant. In particular, austenitic stainless steel is used as a structural material in nuclear power plant that operates at high temperature where components can also be exposed to a corrosive environment and high density neutrons.

Type 316 austenitic stainless steel has been enhanced by adding molybdenum which gives better corrosion resistant properties of this material. In addition, it has excellent forming and welding characteristics. However, the material is vulnerable to sensitisation through grain boundary carbide precipitation [2] under certain thermal cycle conditions, for example in the heat affected zone (HAZ) of weldments, and this reduces its corrosion resistance. Type 316L is a low carbon version of 316 stainless steel which is less susceptible to sensitization and therefore is extensively used in welded components. Type 316H is a higher carbon version of 316 which generally has application at elevated temperature [3].

2.1.2 Material Behaviour under Load and Temperature

The mechanical stress-strain properties of stainless steel change with temperature of the material. Figure 2.1 shows the variation of the yield strength of stainless steel at elevated temperatures. The tensile strength starts to reduce significantly above 800 K as the temperature increases. [2]

Figure 2.2 describes the material deformation behaviour, that is stress-strain curves, at room temperature (a) and high temperature (b). There are two different material behaviours under room temperature or at intermediate temperature depending on stress levels. When a small tensile load is applied, the material extends elastically and returns to its original shape on unloading. However, with larger applied load, the material deforms elastically and then plastically. This shifting point is called yielding, after which the material does not return to its original dimension, but deforms permanently [4]. The plastic deformation is not time dependent under room temperature and intermediate temperature (Figure 2.2 (a)). However, the material behaves differently at elevated temperature. The yield stress drops off at high temperature as shown in Figure 2.1.

If the applied stress is higher than the yield stress on loading, instantaneous strain occurs and the material deforms plastically. As stainless steel strain hardens due to the build up of dislocations during plastic deformation, increasing load has to be applied to increase deformation. On the other hand, if the applied stress is less than the yield stress, only elastic deformation occurs. However, at high temperature, material softens due to recovery. Recovery is a phenomenon where the material gradually softens and the creep deformation carries on with time. At

a microstructural level, a leading dislocation climbs out of its slip plane and it may meet the other side of dislocation after climbing some distance which leads to glide in a new slip plane climbing out of the array. Consequently, the climbing process continues like this and represents the recovery. Therefore, plastic deformation carries on with increasing time even below the yield stress (Figure 2.2 (b)).

Under constant load, deformation stops when the force and deformation resistance are balanced at low temperature, but strain increases depending on time with several different mechanisms at high temperature [2].

2.1.3 Creep Curve

Creep describes the time dependent deformation of material under applied stress [4]. Creep deformation behaviour of a material can be characterised by a uniaxial creep test where the extension (and thereby strain) is recorded under constant load at high temperature. This strain-time plot is referred to as a creep curve. The gradient of the curve at any point defines the creep strain rate, especially creep rate in the secondary is called the minimum creep rate or the steady-state creep rate. Fig. 2.3 is a schematic diagram showing a typical creep curve for a metal. Note the instantaneous strain which develops upon initial loading which is elastic or potentially elastic-plastic if the applied load exceeds the elevated yield strength of the material.

A classical creep curve can be divided into three different regions, that is primary, secondary and tertiary. In primary creep (or transition creep), the

material strain hardens to support the applied load and the gradient of the creep curve decreases because the recovery mechanism starts. In secondary creep, (or steady-state creep) the creep rate often becomes almost constant, which means that strain and time can be approximated by a linear relationship. This is the region where materials spend most of their creep life. The reason for the creep rate becoming constant is that strain hardening and recovery processes compete against each other in an evenly matched way in this region. Thus the gradient, or secondary creep rate that is either the minimum creep rate or the steady-state creep rate $\dot{\varepsilon}$ is an important result arising from a creep test that is commonly used in creep deformation constitutive laws for material life prediction. Another important result characterising secondary creep behaviour is the minimum creep strain rate, particularly where steady state conditions do not prevail. In tertiary creep, recovery dominates and the creep rate starts to accelerate leading to fracture which is referred to as creep-rupture. Rupture is caused by accumulation of microstructural creep damage such as grain boundary cracking and cavity generation [4]. Furthermore, in a uniaxial creep test necking occurs somewhere in the deformed region under tensile load leading to a stress concentration and an exponential increase in the strain rate. The creep rupture life and ductility, defined by the extension or local reduction of area, are important properties used for materials selection and design.

During the creep process, hardening dominates in the primary region and recovery takes priority in the tertiary region. In Fig. 2.3, the constant stress (dashed line) is based on engineering strain and the constant load line is based on

true stress. The lines diverge because the material has large reduction area in the end.

2.1.4 Creep Deformation Maps

At high temperature, strain increases over time at constant stress which causes creep deformation. There are various types of deformation mechanism that can operate depending on the temperature, stress, type of material, grain size, etc. This time dependent accumulated strain attributes to the vacancy flow present in diffusion creep. This diffusion becomes significant at temperatures above 30-40% of the absolute melting temperature (depending on the material). Diffusion that occurs during high temperature deformation is related to the increase of mobility of atoms with temperature. The activation thermal energy distributes among the atoms of material which allows dislocations to move fast their position due to the presence of vacancies within the crystal lattice [3]. Dislocation movement (glide and climb) also contributes to accumulation of plastic deformation at high stress. There are various mechanisms affecting creep deformation which can be determined by temperature and stress values. As various deformation mechanisms occur at high temperature, it is convenient to characterize which creep deformation mechanisms are dominant in one map. Frost and Ashby [5] collected data from many sources and developed the concept of a deformation map. Figure 2.4 is called a deformation mechanism map or Ashby map.

The map is constructed by plotting the logarithmic normalized shear stress against the normalized homologous temperature, T/T_m, where T is the absolute

temperature of interest and T_m is the absolute melting point temperature. Creep deformation is mainly affected by diffusion and dislocation glide and climb. Each predominant mechanism can be identified with the ranges of stress and temperature from this map. In particular, (1) at high stress, deformation occurs through dislocation glide on the crystal plane (dislocation creep) that is without diffusion, (2) at intermediate stress at high temperature, deformation occurs by dislocation climb and lattice diffusion (Nabarro-Herring creep), (3) at low stress, creep occurs by deformation along grain boundary through diffusion of vacancies and atoms (Coble creep). If you know the stress and temperature, the creep behavior can be identified from this creep mechanism map. This map is for a specific material of given grain size. Figure 2.5 is a deformation mechanism map of the 316 stainless steel with a grain size of 50 micron. In 316 stainless steel material with a grain size of 50 microns, the lattice diffusion creep (Nabarro-Herring) region is not observed but grain boundary diffusion (Coble creep) is observed at low stress and dislocation creep (power law creep) occurs at high stress [2].

2.1.5 Diffusion Creep

There are two different types of diffusion creep mechanisms, Nabarro-Herring creep and Coble creep. Nabarro-Herring creep is a form of diffusion creep where atoms diffuse through the lattice. Figure 2.6 (a) shows schematically how the counter flow of atoms occurs due to vacancies generated at boundaries under tension stress. Although Nabarro-Herring creep is considered within crystal lattice diffusion, diffusion creep occurs not only within the grain but also along the grain

boundary. Figure 2.6 (b) shows the diffusion process of vacancy transfer along grain boundaries, and is generally called Coble creep. Nabarro-Herring creep is dominant at higher temperature and Coble creep is dominant at around $0.4T_m$ when creep tests are carried at low stress levels.

Diffusion creep appears at low stress and work hardening does not occur (no motion of dislocation such as dislocation creep), thus the deformation speed is constant because it is not related to strain rate [3].

2.1.6 Dislocation Creep

Diffusion creep theories explain creep behavior at low stress. On the other hand, dislocation creep dominates at high stress. The dislocation motion can be explained by glide or climb. Figure 2.7 shows the principles of dislocation movement.

The deformed material contains a number of dislocation sources. Dislocations glide across their glide planes and are held up at obstacles, forming a piled-up array. The immobile dislocations cause dislocation tangles. This process constitutes the hardening part. At low temperature, when material yields dislocations move and generate strain hardening, but under constant load conditions the deformation usually stops. However, during creep, diffusion helps dislocations climb due to recovery.

Although the recovery effect can be ignored at low temperature, strain hardening and recovery processes compete during creep at high temperature. When in balance, a steady creep rate, $\dot{\varepsilon}$, arises which in many materials is found to

be proportional to the applied stress, σ, through a power law, $\dot{\varepsilon} = A\sigma^n$, where the stress exponent 'n' is considerably larger than unity (three or more) for dislocation creep [2].

2.1.7 Creep Stress and Temperature Dependence

The creep deformation and rupture life of materials depends upon the applied stress and operating temperature. Classical creep tests are carried out at constant load and constant temperature to characterise properties of materials. Ideally long term behavior under low applied loads is required, however it is difficult to carry out creep tests lasting 10^5hour or more. Thus there is a need to predict and evaluate the long term behavior of material from short term creep tests.

Material under load at high temperature spends most of its life in the secondary creep region. Therefore, the secondary creep strain rate is an important property that can be used in the design and assessment of structures operating at high temperature. At any specified stress and temperature, the secondary creep rate can be calculated from appropriate constitutive equations relating stress, temperature and strain rate for a given type of creep process, such as the following power law relationship: [3]

$$\dot{\varepsilon} = A\sigma^n \qquad [2\text{-}1]$$

where A and n are stress-independent constants and creep is a thermally activated process, its temperature sensitivity being determined by an Arrhenius-type expression with an activation energy Q.

$$\dot{\varepsilon} = A_0 \sigma^n \exp\left(\frac{-Q}{RT}\right)$$

where A_0 and n are constants and R is the universal gas constant.

Values for n and Q depend on the material and vary with stress, temperature and the type of creep mechanism. The constant n from equation [2-1] is the stress exponent and varies according to the mechanism. By calculating this stress exponent from experimental data, we can find out which mechanism is working under the material conditions (temperature and stress) being considered. For example, under low stress conditions a diffusion creep mechanism may dominate where the value of n=1, and at high stress where dislocation creep is dominant the range of n may vary from 3 to 8 in metal (depending on the material) [3].

Sakamoto et al [6] classified the creep deformation behavior of 316 and 304 stainless steels and 2.25Cr-1Mo ferritic steel into four types and clarified the temperature and the stress dependency of each creep deformation characteristic. They proposed that the relationship between creep rate and time can explain creep deformation behavior more clearly than creep strain and time. Figure 2.8 shows four different types of creep deformation behaviors of 2.25Cr-1Mo ferritic steel with different temperatures and stresses. Type A shows a typical creep curve which has primary, secondary and tertiary regions. Type B has two steady-state regions. Type C has a long transition region and no steady-state region. Type D

shows tertiary behaviour over most of its creep curve. The creep behaviour depends on the temperature and stress condition. These materials here which have short rupture time tend to have Type A behaviour. Type C and Type D curves occur with low stress at any temperature range. Figure 2.9 shows the relationship between creep stress and type of creep deformation for 304 and 316 stainless steels and 2.25Cr-1Mo ferritic steel. As you can see these four different types of creep deformation can be sorted out with stress and temperature. Figure 2.10 shows the relationship between creep rate and life fraction at 550 °C which belongs to Type B creep deformation in 316 stainless. The dashed line indicates time t = 400 hours. Inflection in the curves does not depend on stress but appears at certain time. This inflection point (t_i) is the time transition between primary and secondary and is closely related to microstructure transformation. Figure 2.11 show the times of inflection for Type B, t_i superposed on a time-temperature-precipitate (TTP) diagram for 316 steel. The curves in the graph indicate the starting time of precipitation. At lower temperatures of 550 °C and 600 °C, the inflection time t_i corresponds to the precipitation starting time of $M_{23}C_6$ carbides and in the case of 650 °C, the inflection time t_i almost corresponds to those of Laves phase. Consequently, in the case of temperatures below 600 °C, the transition time from primary to secondary of Type B creep deformation corresponds to the development of $M_{23}C_6$ carbides and over 600 °C corresponds to development of Laves phase.

2.1.8 Creep Fracture Map

When metallic materials are loaded at high temperature, creep deformation occurs and eventually the material ruptures. There are three main types of fracture behaviour observed at high temperature; intergranular fracture, transgranular fracture and high temperature rupture [2], [7], [8]. Figure 2.12 shows the different types of fractures [2]. Figure 2.13 is a creep fracture map for Type 316 stainless steel [9] in which the logarithmic normalized shear stress is plotted against normalized homologous temperature T/T_m. This map indicates areas defined by stress and temperature ranges where different fracture mechanisms are dominant. Transgranular creep fracture is observed at high stress and intergranular creep fracture is observed at low stress. Transgranular creep fracture has two different types of creep fractures that transitions from control by lattice diffusion at high temperature (HT) to diffusion along dislocation cores at low temperature (LT). Intergranular fracture also has two different types of fracture characterised by triple point cracking and cavitation failure due to cavity nucleation and consolidation at grain boundaries. Intergranular cavitation is controlled by either diffusion or power-law growth [9].

Transgranular creep fracture occurs in a high magnitude stress field. Figure 2.14 shows the principle of this mechanism. The micro mechanism of this fracture involves nucleation of cavities at inclusions. During the creep process, cavities nucleate due to stress concentration at inclusions. Under deformation the cavities grow inside crystal grains until local internal necking leads to cavities connecting and transgranular fracture. On the other hand, intergranular creep fracture occurs

in a low magnitude stress field. Figure 2.15 (a) shows the mechanism of triple point cracking which also called the wedge type cracking [2] and appears at relatively high stress levels in this field. Under tension stress, dislocation glide occurs then gaps appear between the crystal grains. The stress concentration occurs at these triple points and then gaps grow by wedging action associated with grain boundary sliding. The second type of intergranular fracture develops with cavity nucleation at grain boundaries, cavity growth owing to vacancy diffusion followed by interconnection of cavities creating grain boundary micro-cracks that lead to failure [2]. Figure 2.15 (b) illustrates the mechanism of grain boundary cavity failure. This type of intergranular failure occurs at low stress and relatively higher temperature creep conditions [3].

Yagi et al [10] have observed the influence of stress and temperature on the fracture mechanisms associated with the creep crack growth behaviour of 316 stainless steel using round bar specimens and compact tension (CT) specimens. They identified three kinds of creep fracture mechanisms in their creep tests: cavity-type intergranular crack, wedge-type intergranular and transgranular growth which were dependent on the testing temperatures and stresses. The relationships between stress and time to rupture are shown in Figure 2.16. Figure 2.17 shows their microscopical fracture features associated with creep crack growth under each different type of stress and temperature conditions.

An intergranular (C-type) creep fracture mechanism was found with many cracks and cavities formed ahead of the crack tip for cases of low stresses and high temperature (for example as would be experienced in operating plant). In these

cases intergranular fracture occurred due to growth of cavities formed at the interface between the matrix and $M_{23}C_6$ or sigma phase precipitated on grain boundaries. For high stresses and lower temperatures intergranular fracture due to wedge-type cracking (W-type) was observed. Whereas transgranular fracture (T-type) was observed for high stress and high temperature, where between the condition for W-type and C-type mechanism.

2.1.9 Austenitic Weld Metal

Welding is a complex process producing a complex state of material that varies across a joint. When multiple weld passes are deposited this produces considerable variations in microstructure, from the starting weld pass to the end pass, because of the complex thermal history that occurs during the welding process [11]. Each weld bead is deposited in the molten state with additional heat input from the welding torch and this rapidly heats up surrounding base material, following which the structure conducts away the heat and the region cools down. Prior weld beads are also reheated by following beads and cool down again, so that the process is repeated. Therefore, both the local parent material and weld metal experiences a sequence of repetitive thermal cycles during the welding process. Consequently, the microstructure and degree of work hardening of weld metal can vary depending on the location of the weld beads. Likewise parent metal close to the weld is exposed to strain-hardening/softening processes associated with multiple welding cycles.

Weld metal microstructures depend on the type of solidification mode, precipitates formed (e.g. carbides) and dislocation organization. There are four solidification and solid state transformation possibilities for austenitic stainless steel weld metals [1]. Table 2.1 shows the types of solidification and its reactions and resultant microstructures. Figure 2.18 is related to the Fe-Cr-Ni phase diagram, where Ni_{eq} and Cr_{eq} are Nickel and Chromium equivalent volume fractions. Here, A and AF regions of the diagram illustrate solidification modes associated with primary austenite solidification, where austenite (γ) is the first phase to form, whereas in the FA and F regions (with higher Cr_{eq}/Ni_{eq} ratio) solidification develops with delta ferrite (δ) as the primary phase [1]. Austenitic welds (A mode) can fail in short times and at low strains, however, when large amounts of delta ferrite (e.g. more than 10%) are present, it transforms to sigma phase more rapidly than austenite. The sigma phase is a particularly hard, brittle constituent [12]. Therefore, typical 316 weld filler metals contain a composition that promotes 3 to 8% of delta ferrite in the weld zone as this is required to improve weld ductility for practical use in industry. However, the ferrite content can vary considerably within multi-pass weldments because of the repeated welding cycles.

Okane et al reported [13] that the creep rupture strength of welded joints was affected by metallurgical change. Type 316 weldment cracks, leading to a creep rupture, propagated in the region that had fine carbides scattered in the austenite matrix adjacent to delta ferrite. The delta ferrite in the weld metal was distributed along the columnar grain structure in the austenite matrix and micro-

cracking took place along the growth direction of its columnar structure. They found many precipitates clearly at the region where the crack occurs. As austenitic stainless steel weld metal consists of generally a mixture of two phases of ferrite and austenite, the interfaces between the phases can be considered to be metallurgical notches introducing a stress concentration at the interface when the weld metal loaded. Cr-carbide is precipitated and accumulated during long time exposure to high temperature at the interface between the delta ferrite and the austenite phase where the notch exists. This promoted cracking at the austenite matrix adjacent to the ferrite grain distributed along the growth direction of the columnar structure in the weld metal. In their study, this Cr-carbide was almost all M_3C_2 and $M_{23}C_6$.

2.1.10 Multi-pass Welded Joints

In the evaluation of the structural integrity of power plants, it is necessary to consider the welded joints as these are often the weak points in the structure. Mechanical properties vary significantly in and around the welded joint relative to the parent metal. Thus, creep rupture mainly occurs around welded joints because of this non homogeneity. There are three distinct regions in a welded joint, in terms of the microstructure and mechanical properties and material: the weld material, the heat affected zone (HAZ) and the parent metal. In a multi-pass weld, the first pass and last pass have dissimilar mechanical properties due to differences in the number of thermo-mechanical cycles that are experienced.

In the process of multi-pass welding, each bead of weld metal is deposited at high temperature (above melting point) and quickly cools down as heat is conducted away by the surrounding structure. Prior deposited weld beads are reheated due to later beads and again cool down. Zaizen et al [14] measured the heat cycle of submerged arc welding for 308 weld metal and observed the microstructure variation in multi-pass weld metal due to the welding thermal history. Figure 2.19 shows the effect of heat cycles in a multi-pass weld [14]. The temperatures were measured at the position of the first pass bead and recorded for the following subsequently deposited six beads. As additional beads are added the peak temperature becomes lower and the cooling rate becomes slower, as the distance of the added bead from the first bead increases. They found the dislocation density increased as the number of multi-pass heat cycles increased and this promoted generation of precipitation. As prior beads cooled more slowly due to deposition of following beads, precipitation increased and resulted in harder material than later deposited beads. According to their results, the first and second welding heat cycles do not increase the first pass weld metal hardness but the hardness can increase from HV 150 to HV 190 between the third to the sixth welding heat cycle. Therefore, the cooling rate is often the most critical factor in welding applications. The cooling rate is reduced as the welding heat input is increased or the plate thickness is reduced [14]. The melting of base metal and the subsequent mixing with filler metal changes the final weld metal deposits. Figure 2.20 shows the amount of re-crystallized weld metal in multi-run welding with different size of electrodes. The cross-sectional area indicates the weld metal

ductility which increases with larger size of electrodes (Figure 2.21) whereas smaller electrodes show greater dilution. High heat input and greater dilution promotes precipitation hardening [15] which produces higher strength but lower toughness.

A narrow gap Type 316 stainless steel thick plate welded joint was investigated by Hongo et al [16], [17], [18], [19] using specimen samples taken from various locations of multi layer welded joints (Figure 2.22). A Moiré interferometry technique was applied to measure the local creep strain distribution using a large full thickness flat specimen (Figure 2.23). The creep behavior of a multi-pass weld layer is very complicated. The creep strain of the top and bottom layers of the multi-pass weld metal was found to be considerably larger than that of the middle of position. Austenitic type of stainless steel has a large thermal expansion coefficient and small thermal conductivity [18] and the order of the multi-pass welding process affects the creep properties of each pass. In the welded joint examined, the creep strength of weld metal and HAZ adjacent to the weld zone were generally high due to welding thermal history. The fracture started propagating in the surface layer of the weld metal region due to lower creep strength. The strain distribution and dislocation configuration were related to the hardness variation (Figure 2.24). Figure 2.25 shows the void distribution observed for the near-surface region, and the mid-thickness position from a large full thickness specimen for which the gauge width included the whole plate section (t_r =18,457 hours). The voids start generating around the surface before those in the centre of the weld. Figure 2.26 also shows the fracture surfaces where

the near-surface region had a dendrite structure and was associated with a brittle fracture surface, and the mid-thickness position had many dimples which was associated with ductile fracture. In this large full thickness specimen, the increased number of voids near the surface connected together and grew leading to stress concentration and crack propagation along the columnar grain interfaces. Due to this crack growth from the surface, stresses increased in the mid-thickness position, resulting in fracture [18]. Miniature specimens taken from different positions, top, middle and bottom of this thick section weldment were also tested. Figure 2.27 shows the void distribution from the miniature specimen taken from near surface at t_r =985 hours and t_r =15,765 hours. From this result, there was no void formation at t_r =985 hours and although a few voids were observed at t_r =15,765 hours, the numbers were significantly smaller compared to a large full thickness specimen near surface region. This comparison indicated that the voids started appearing and growing under the multi-axial stress state associated with the large full thickness specimen long before the uni-axial stress (miniature specimen) [18]. Fujimoto et al [20] also reported that voids started appearing and growing under tri-axial stress concentration conditions much earlier than under the uniaxial stress conditions [21].

Theoretical analysis using an accurate model is another way of estimating the creep life. Nakacho et al [22], [23], [24] developed simple numerical models using the finite element method for creep deformation simulation of thick section multi-pass welded joints. In their finite element simulation, the thick section welded joint was divided into several regions which consisted of one dimensional

elastic-plastic-creep elements. However, as a complex residual stress distribution exists in the multi-pass weld as an initial stress, it is essential to consider the influence of the multi-axial stress state. The multi-axial stress state, σ_x in the thickness direction can be considered as the second largest factor next to σ_y in the loading direction. Residual stress was applied to each element as an initial stress state thus representing the multi-axial residual stress state and its effect on creep behavior more accurately than an uni-axial stress state model [22]. The creep properties were represented by a Garofalo creep constitutive equation with stress dependence as:

$$\varepsilon^c = \varepsilon_p(1-\exp(-\gamma\cdot\tau)) + \dot{\varepsilon}_s\cdot\tau \qquad [2\text{-}2]$$

where ε^c : *Creep strain*

ε_p : *Maximum primary strain* $= C_1\cdot\sigma + C_2$

$\gamma = C_3\cdot\exp(C_4\cdot\sigma)$

$\dot{\varepsilon}_s$: *Secondary creep rate* $= C_3\cdot\sigma^n$

$C_1, C_2, C_3, C_4, C_5, n$: *Constants*

τ : *Time*

σ : *Stress*

This equation is a function of stress σ. In this model, the stress changes with accumulation of creep deformation as a function of time. However, it is difficult to determine true stress which can not be obtained from the creep rate under a nominal stress creep test because a constant load acts on the specimen in the

tensile direction, and thus as the specimen extends, the cross section area is reduced and true stress is increased.

Hongo et al [18] investigated not only a thick section of 316 stainless steel but also 304 stainless steel and 2.25Cr-1Mo ferritic steel. Kinugawa et al [25] executed a finite element (FE) analysis using the above creep constitutive model and applied it to the multi pass welded joint 304 stainless steel creep test. The full field strain distribution was compared with the Moiré interferometry strain measurements. Figure 2.28 shows the specimen sample locations. The FE calculation required local properties. High temperature tensile and creep properties of parent, weld (top, middle and bottom) were obtained by samples taken from local regions, however it was difficult to obtained HAZ data. Thus HAZ properties were measured using a cross weld specimen (WJS in Figure 2.28), and calculated from the reduction of HAZ section area several times using interrupted tensile and creep tests. The true stress arises under constant load, so they assumed each creep rate depended on the true stress value averaging across the primary and secondary regions. The simulation was executed for the large full thickness specimen with the mesh and its division shown in Figure 2.29. The comparison of FE computation with measurement for contours of apparent strain in loading direction are shown in Figure 2.30. The computation results obtained gave slightly higher strains than measured by Moire interferometry and indicated steeper gradients around weld boundaries. The differences were considered to be associated with the computation assumption of plane stress and the fact that the HAZ properties were not uniform across the weldment thickness.

A more detailed knowledge of the strain variation between the regions in a welded joint under creep conditions is required for a more complete analysis and determination of creep behavior. For this reason, directly measured full field strain under creep conditions is of great interest to engineers who are responsible for the structural integrity of power plants.

2.1.11 Creep Constitutive Equations

In the design of pressure vessels for elevated temperature operation, it is necessary that there is no significant deformation by creep and therefore prediction of its accumulation throughout projected service life is essential [26], [27]. For welded joints in pressure vessels, many practical ways of assessing life have been considered, but nothing definitive has resulted. In order to predict the creep life of material, it is necessary to relate accumulation of creep strain to the expected operating stress and temperature conditions. Creep constitutive equations for different materials and conditions have been suggested by many researchers. Generally creep strain can be express by stress σ, time t and temperature, T [28].

$$\varepsilon^c = f(\sigma, t, T) \qquad [2\text{-}3]$$

This equation can be divided as follows,

$$\varepsilon^c = f_1(\sigma) \cdot f_2(t) \cdot f_3(T) \qquad [2\text{-}4]$$

Equation [2-4] can be expressed by a stress dependent $f(\sigma)$ relationship. Well known stress dependant equations are

Norton $\qquad f_1 = B\sigma^n \qquad [2\text{-}5]$

Prandtl $f_1 = R\sinh(\alpha\sigma)$ [2-6]

Dorn $f1 = D\exp(\beta\sigma)$ [2-7]

Garofalo $f_1 = A[\sinh(\gamma\sigma)]^n$ [2-8]

All characters except σ are material constants. Norton's law is the most famous because it can be applied for a wide range of materials and the formula is relatively simple. Dorn's equation is expressed very well when used for a higher stress range. Prandtl and Garofalo can be used for a wide range of stress values. Especially Garofalo is considered to have attributes of both Norton and Dorn covering both high stress and low stress ranges and providing an accurate expression of creep strain rate [28].

On the other hand, time dependent equations can be expressed by the $f(t)$ relationship.

Secondary creep $f_2(t) = t$ [2-9]

Bailey $f_2(t) = bt^m$ [2-10]

Bailey's equation is used for many different materials and conditions but cannot describe well very long term secondary creep states. In this case, the secondary creep simple equation can be used instead.

The main cause of rapid creep strain accummulation in the tertiary state (of a uniaxial creep test) is related to a reduction of cross section of area due to specimen elongation. However, under constant stress, creep strain increase is often observed in the last stage of a creep test, because material degradation occurs due to diffusion, voids generate and grow mainly in the crystal grains and boundaries during the creep process. This is known as creep damage. Failure

which occurs owing to creep damage with little creep deformation is usually referred to as a creep-brittle rupture.

Creep deformation constitutive equations usually represent primary creep and secondary creep behaviour, but not tertiary creep. However, the field of damage mechanics is becoming more popular, in which can be expressed the whole creep phenomena including creep rupture. Takahashi evaluated the creep-fatigue life of 316 stainless steel using a ductility exhaustion method [29], [30], [31], [32]. The ductility exhaustion method is one of creep damage prediction, mainly developed in UK [26]. This method has delivered very good accuracy in life prediction for creep-fatigue which can provide a reliable estimation of creep damage [33]. Yongui et al [34] applied a continuum damage mechanics (CDM) model to a thick multi-pass welded joint of stainless steel. The void distribution was measured by a laser microscope several times during the creep tests and the quantity of creep damage was calculated from its images. A finite element analysis was performed using CDM constitutive damage equation and the damage distribution and evolution were simulated successfully [34].

Creep deformation proceeds through a thermal activation process and material deforms under different mechanisms as described earlier. However, each mechanism follows an Arrhenius law relationship which depends on a temperature expression with an activation energy Q [3]

$$f_{3(T)} = A \exp\left(\frac{-Q}{RT}\right) \qquad [2\text{-}11]$$

where A_0 is constant and R is the universal gas constant

In order to express equation [2-5] as the simplest formula using above equations [2-5], [2-10] and [2-11],

$$\varepsilon^c = C \exp\left(\frac{-Q}{RT}\right) \cdot t^m \cdot \sigma^n \qquad [2\text{-}12]$$

C : Constant

for isothermal condition, the equation becomes

$$\varepsilon^c = C \cdot t^m \cdot \sigma^n \qquad [2\text{-}13]$$

Generally this equation [2-13] is widely used in creep analysis.

In structural integrity assessment, choosing the right creep constitutive model for the actual component is important. For UK Advanced Gas Cooled Reactor (AGR) components, various constitutive models are provided in the R66 AGR Material Data Handbook from EDF Energy [35]. This handbook advocates use of the RCC-MR law [36] for the creep deformation and lifing assessment of welded austenitic stainless steel components operating at high temperature. The RCC-MR constitutive law provides a good representation of mean primary and secondary creep deformation behavior for Type 316H stainless steel [36]. The formula is described by a primary expression up to time, t^{fp} (the time change from primary to secondary), thereafter by a secondary expression which includes the primary creep strain. These expressions, only valid up to 1% creep strain, are defined as follows:

Primary creep $t < t^{fp}$ $\varepsilon_p = C_1 t^{C_2} \sigma^{n_1}$

Secondary creep $t < t^{fp}$ $\varepsilon_s = \varepsilon_{pfp} + C.\sigma^n (t - t_{fp})$

where ε_p and ε_s are creep strain in %, t is the time in hours, σ is the stress in MPa and C, C_1, C_2, n and n_1 are material constants, which are a function of temperature, as shown in Table 2.2. Under conditions of constant stress, the time at the end of primary creep, t^{fp} is determined as follows:

Time at the end of primary $t_{fp} = C_3 \sigma^{n_3}$ Strain at the end of primary: ε_{pfp}

Where $C_3 = \left[\frac{C}{C_1 C_2}\right]^{\left(\frac{1}{C_2-1}\right)}$ and $n_3 = \frac{(n-n_1)}{C_2-1}$

Application of this RCC-MR constitutive law will be described in Chapter 4.3.2.

2.2 Strain Measurement Techniques

Life assessment of safety critical structures requires the knowledge of stress and strain history at critical locations. Measuring and understanding the deformation and stress behaviour of structure is therefore a necessity. Consequently, demand for reliable deformation measurement techniques is paramount. Traditionally, strain gauges have been widely used for this purpose. However, although strain gauges are relatively easy to implement and give highly accurate strain measurements, they only provide measurements at a point at a time, so their use is limited to locations where there strain gradients are low. For example, the assessment of stress concentrations and welded joints require the knowledge of strain variation in the region. Full field techniques based on optical interference, such as moiré and speckle interferometries are more suitable for this purpose. These optical techniques offer very high sensitivity to deformation with

the added advantage of being non-contact. However, they require vibration isolation and their accuracy is adversely affected by the temperature variations in their optical paths. An alternative full field optical technique called Digital Image Correlation (DIC) has recently become more popular than those based on laser interferometry because of its ease of use and insensitivity to vibrations. The DIC technique is a computational method, based on comparing light intensity patterns on a pixel level between two different digital images captured before and after deformation.

DIC was developed in the early 1980s at the University of South Carolina where Sutton *et al* [37] produced numerical algorithms for image correlation and carried out preliminary experiments with digital images. It became the DIC foundation as known today as 2D DIC [38]

In the past two decades, the DIC technique has been improved dramatically. Problems affecting the measurement accuracy, such as rigid body motion, lens distortion, deforming subsets, etc., have been solved or greatly reduced [39], [40], [41], [42], [43]. The technique has been applied to investigate many problems in various industries, with different size scales: from small scale micro-region measurement [44], to the thermal strain measurement on electronic packaging [45] and large scale bridge deflection [46]. Applications of DIC are not restricted to images obtained by optical imaging, but it can also be applied to those images acquired using scanning electron microscopy (SEM), for in-situ tensile test for local strain measurement [47] and X-ray tomography for deformation analysis of periodontal tissue in the medical industry [48].

2.2.1 Strain Measurement at High Temperature

Many safety critical structures and components in power plants operate at elevated temperature environments where the property and the behaviour of materials are different than those at ambient temperatures. The design and structural integrity assessment of these components and structures require the knowledge of the behaviour of these components at the operating temperatures. Accurate and reliable measurement of the mechanical properties at elevated temperatures is a challenge as the sensitive and delicate measurement instruments must be able to operate in harsh environments. Conventionally, high temperature strain gauges and extensometers (or LVDT transducers) are commonly used for high temperature tensile and creep tests. However, these methods can only provide displacement/strain values between two points, so their use is somewhat limited when the component or structure under investigation contains strain gradients, as observed due to changes in material properties, such as in weldments, and geometry, such as notches, holes and cracks. In such circumstances, it is desirable to capture full field deformation for a better understanding of structural behaviour and determination of spatially varying deformation properties. In this section both point and full-field displacement measurement techniques applicable to elevated temperatures will be described.

2.2.2 Point Measurement Techniques

2.2.2.1 High Temperature Resistive Strain Gauge

Strain is defined as the change in length by an amount of deformation when a body force is applied as shown in Figure 2.31, where L is the initial length and ΔL is the change in length. The strain gauge is the most common method used to measure strain at present and its principle is based on the fact that the strain varies in proportion to the amount of electrical resistance [49]. The most widely used strain gauge is the bonded metallic strain gauge as shown in Figure 2.32. The metallic strain gauge consists of a very fine wire or foil which is arranged on a grid pattern. The grid pattern maximizes the amount of metallic wire or foil subject to strain in the parallel direction. The grid is bonded to the thin back plate, called a 'carrier', this carrier is mounted to the sample directly. The strain of the specimen is transmitted to the strain gauge and the change in the electrical resistance of the wire/foil due to the change in its length is linearly related to the strain in the material. The relationship between the resistivity and strain is $\varepsilon = \frac{\Delta R / R_G}{GF}$, here ε is strain, ΔR is the change in resistance caused by strain, R_G is the resistance of the undeformed gauge, and GF is the gauge factor. As the change in resistivity of strain gauge is such a small value, a wheatstone bridge is used for transforming to voltage. The output voltage v from bridge is $v = \frac{BV \cdot GF \cdot \varepsilon}{4}$ where BV is the bridge excitation voltage [50]. To make use of the strain gauge at elevated temperature, the thermal characteristics of the leads, the adhesive bond and strain gauge itself must be considered.

A weldable high temperature strain gauge that can be used between 300°C to 1000°C has been developed by Hitec Product, inc [50]. They provide the strain gauge as already assembled with shim and a high temperature cable that can withstand the heat and has been used to test for thousands of hours in a hostile environment [50].

2.2.2.2 High Temperature Capacitive Strain Gauge

Capacitive strain sensors can measure strain at elevated temperature and have long term stability. The sensors measure the actual distance between two plate areas which is related to the capacitance resistance of the device. The measurement signal is converted to strain by reference to the gauge length. These capacitive sensors can be used for multi-layered structures [51].

2.2.2.3 LVDT Transducer

The Linear Variable Differential Transformer (LVDT) is a type of electrical transformer used for measuring linear displacement. Figure 2.33 shows the design of a typical LVDT displacement transducer. It consists of a shaft within a hollow pipe which contains a coil, and the output voltage varies with the shaft position. There are three solenoid coils in the pipe and a current is driven through the centre coil, which is called the primary (A in Figure 2.33), and the outer coils, called the secondary (B in Figure 2.33), are connected in reverse series which cause a voltage induction in each secondary coil, which is proportional to its mutual inductance with the primary. The LVDT transducer is attached to a frame that is fixed at the top and the bottom of the test specimen; the strain is measured

between these two points. LVDT transducers can measure large deformations in a repeatable way even at high temperatures, but they are not suitable in dynamic loading because of their large weight.

2.2.3 Full-field Measurement Techniques

2.2.3.1 Laser Speckle Interferometry

When a rough surface is irradiated with a coherent light beam, such as produced by a laser, each point of the rough surface reflects the light in a different direction, creating a 'speckle pattern' on the image plane. This speckle pattern is unique for a surface; if the surface deforms, the speckle pattern will change its form. The speckle interferometry exploits this feature and captures the change in the speckle pattern, which is related to the surface deformation. The change in speckle patterns can be determined by taking the difference between them. This can simply be obtained by optically interfering the speckle patterns obtained from the initial and the deformed surface states. ESPI (Electronic Speckle Pattern Interferometry) [52] uses a CCD camera for taking the difference between the initial speckle image and the deformed speckle image. Speckle interferometry is a non-contact optical method and as it can be observed in real time, the whole process of a tensile test can be measured including plastic deformation until specimen rupture. There are not many examples where it has been applied to high temperature creep measurements, apart from measurement of surface deformation in a short term (30 min) creep test [53]. ESPI is a powerful full-field optical technique for the analysis of the strain field at the surface of

inhomogeneous material under load. However, this sensitive electric measurement system is not suitable for long term high temperature creep tests.

2.2.3.2 Moiré Interferometry

Moiré is the generic term for full field measurement techniques, which utilise the interference effect between some form of specimen grating and reference grating to magnify the surface deformations and create a contour map which is related to surface displacement – a moiré fringe pattern or interferogram [54]. The moiré pattern is a full field representation of the relative displacement between the gratings. This property of moiré makes it an excellent tool for observing and quantifying the gradients in localized deformation. In practice, a grating is attached on the surface of the test piece. The grating deforms together with the test piece and when an undeformed (reference) grating superimposed onto it, a moiré pattern depicting the nature and the magnitude of the deformation field is obtained. Each moiré fringe represents a line of constant displacement in the direction perpendicular to the direction of the reference grating. The moiré effect described above is termed mechanical moiré because the fringes are formed from the mechanical crossing of the two gratings. The mechanical moiré effect is limited by the frequency (inverse of pitch) of the grating employed. Optical moiré, commonly known as moiré interferometry, provides higher sensitivity by employing the principles of light interference and diffraction. Figure 2.34 shows a basic moiré interferometer with a specimen grating exposed to a two-beam interference system. The diffraction effect split the incoming light beams into multiple preferred rays on the grating. When the grating is undeformed, the -1

and +1 diffraction order from the beams emerge perpendicular to the grating without any interference. When the specimen is deformed, the -1 and +1 orders will exit the specimen grating warped and interfere with each other. The result is a moiré fringe pattern of the in-plane displacements.

Several researchers have studied deformation at high temperature using moiré interferometry [55],[56],[57],[58],[59]. A difficult requirement of high temperature moiré work is to apply a specimen grating which has to remain highly visible through a test at high temperature. A few different types of grating can be applied at high temperature (e.g. deposited metal-film grating, etching grating, refractory grating). For example, Cloud et al [55] have developed high resolution grating photography using refractory grating. The surface strain was measured using a sample fringe pattern after 1020 hours at 600 °C. Huimin et al [57] and Hyde et al [59] also achieved around 1000 hours creep strain measurement at elevated temperature. However, strain was derived from two images, initial and after deformation, and therefore did not provide continuous evolution data. Similarly, Hongo et al [60] developed a system based on a moiré interferometry technique to measure the creep strain distribution in a multi-pass welded joint. Although their results show the strain distribution across the weld, HAZ and parent for a long term creep test, they reported that the method requires tedious specimen preparation since a durable diffraction grating needs to be produced on the specimen surface and frequent interruptions were necessary during the creep test for the test piece to be taken out of the furnace to perform the measurements and this was not ideal for reliable results. Thus the technique was

not suitable for continuous "in-situ" time-dependent measurement of creep strains.

2.2.3.3 Digital Image Correlation

The digital image correlation (DIC) technique, which provides full field measurement of surface deformations, has been successfully employed by many researchers to map the strain variation spanning cross-weld specimens during room temperature tensile tests [61], [62], [63], [64], [65]. The working principle of DIC is based on sophisticated computational algorithms that track the grey value patterns in digital images of the test surfaces, taken before and after a loading event that produces surface deformations. The principles of DIC method will be discussed in detail in the next section, Here, an introduction is made for the use of DIC at elevated temperatures.

Lyons et al [66] were the first to demonstrate the capability of DIC to measure strains at high temperatures. They measured free thermal expansion and strains due to tensile loads on Inconel 718 superalloy specimens at temperatures up to 650°C [67]. They used LSI boron nitride and aluminium oxide-based ceramic coating on the specimen surface to create the speckle pattern for DIC image matching and to prevent oxidation at high temperature. They also used a small fan near the furnace window to stop heat current causing thermal variation on displacement data. The results indicated accurate strain measurement of thermal expansion and during a tensile test. Using the same system, Liu et al [68] studied the strain field on a single edge notched specimen at 650°C and 704°C. The test duration was 146 hours and the results were verified with FEM.

Maharaj, al [69][70][71]have developed an optical creep strain monitoring system for life assessment in power generation plants in UK. This monitoring system combined DIC and ARCMAC, Auto-Reference Creep Management and Control, optical strain gauge system. The system used a pair of optical gauges for point-to-point monitoring of changes in strain across steam pipe weld. The strain gauge consists of two Inconel gauge plates with fixed silicon nitride spheres, DIC was used to determine the separation of the centres of the circular points between the gauge plates. They evaluated on site strain variation in their experiment. However, this technique is unable to provide full-field creep deformation measurement, since only the strain between point-to-point marker is determined.

2.3 Principle of Digital Image Correlation

Digital Image Correlation (DIC) is simply a pattern matching technique that compares digitised images of a test surface taken during different stages of deformation. The images, which contain naturally occurring or artificially created random and unique patterns, are divided into smaller regions (subsets). The pattern in each subset of an image is matched to the same pattern at a different stage of the deformation by software (for example, LaVision [72], Dantec [73]). Figure 2.35 shows the principle of speckle pattern tracking using the DIC technique. The speckle pattern is the feature of surface which can be black dots, white dots, such as a random pattern. The natural structure surface can be used for speckle pattern but applying paint enhances the pattern contrast. It depicts how a subset (the red square in the figure) tracks the speckle pattern in each image through the deformation stages. The centre position of the subset after

deformation is determined using correlation functions by the software. The displacement vectors in two dimensions can then be computed with the distances of the centre positions of each to produce a displacement vector field. Subsequently the strain components can be calculated using this displacement vector field of the test area.

Each image is taken with a camera and corresponds to a different load step continuously over time. The photograph imaged on each pixel element is converted to an analogue electrical signal. However, for computer analysis this needs to be converted into a digital electric signal in binary representation (AD conversion). RGB (Red, Green, Blue) 24 bit images can be created and converted to an eight-bit grey scale, the values of each pixel range from 0 to 256 with the lowest number corresponding to black and the highest values white. Each pixel has a discrete intensity value that corresponds to the light reflection of the surface pattern of the specimen. DIC can then determine the translational positions of the centre of the subset by examining the pixel intensity arrays in subsets on two corresponding images.

The displacement of any subset after deformation is determined by searching for a similar luminance value distribution of each subset in the images after deformation. The method uses a correlation function, whose value depends on the closeness of the light intensity distribution in each subset. Two types of correlation functions are usually used in DIC. These are:

$$C = |F(x, y) - G(x^*, y^*)| \qquad [2\text{-}14]$$

$$C = \frac{\sum[F(x,y) * G(x^*, y^*)]}{[\sum(F(x,y)^2) * \sum(G(x^*, y^*)^2]^{1/2}} \qquad [2\text{-}15]$$

The first type of correlation function, given in Equation [2-14], calculates the absolute value of the differences between image intensities before and after deformation. Here $F(x, y)$ is the light intensity grey scale value at the coordinate (x, y) for the initial image and $G(x^*,y^*)$ is the grey scale value at the coordinate (x^*,y^*) of the deformed image. The aim is to find out the position that minimizes the coefficient C. On the other hand, the typical correlation function is given in Equation [2-15] which expresses the similarity between two images. Here, $F(x, y)$ and $G(x^*,y^*)$ are deviations (difference from average values), $\sum F(x,y)^2$ and $\sum G(x^*, y^*)^2$ are dispersions. Taking a square root (standard deviation) gives a correlation coefficient normalized with a range of -1 to 1. In this function, the maximized value of the coefficient C is the highest correlation. In the LaVision Davis software [72], there is a selection between these equations.

2.3.1 Determination of Displacement Field

First the pattern of the image must be defined. This is achieved by dividing the image into small subsets. Figure 2.36 illustrates a schematic figure showing subsets before and after deformation for DIC analysis. The initial image of the un-deformed subset is fixed, then each subset of the deformed image is sequentially shifted one pixel, and maximization of equation [2-15] determines the best position of the deformed image. Here, (x, y) and (x*, y*) are positions of un-deformed and deformed images respectively, these coordinate points are related

by the deformation that occurred between two images. The centre position of the deformed image is defined by the relationship between (x, y) and (x*, y*).

$$x^* = x + u + \frac{du}{dx}\Delta x + \frac{du}{dy}\Delta y$$
$$y^* = y + v + \frac{dv}{dx}\Delta y + \frac{dv}{dy}\Delta y \qquad [2\text{-}16]$$

Here u and v are the displacement for the subset centres in the x and y directions respectively. The distances from the centre of the subset to the point (x, y) are denoted by Δx and Δy. Therefore, an initial square subset can be deformed into a parallelogram shape subset as shown in Figure 2.36. If the point P moves to P′ and Q moves to Q′, the displacements can be expressed by equation 2-16. The subset translation accuracy is related to the approximation used and this depends on which order of displacement gradient is used. In this figure, the approximation employed is a first order Taylor expansion assuming the strain is constant which is a zero-order shape function, that is a pure translation. However, it is possible to consider a higher order displacement gradient for more complex deformation.

The correlation coefficient is a function of displacements (u, v) and displacement gradients, $\frac{du}{dx}, \frac{du}{dy}, \frac{dv}{dx}, \frac{dv}{dy}$. The image correlation is performed by determining values for u, v $\frac{du}{dx}, \frac{du}{dy}, \frac{dv}{dy}$, and $\frac{dv}{dy}$ which maximizes the correlation coefficient (C). An iterative approach is used to maximise the correlation coefficient by using a non-linear optimization technique. Frequently, the Newton-Raphson method is solved in this implementation of the process in order to determine the six variables to maximise the correlation coefficient C. This iteration

method gives a correction for the initial guess of these six parameters and converges to the result. As a typical procedure for this image pattern matching, the displacement gradient is set to zero at first to determine the first guess displacement approximately, then the displacement gradient with sub-pixel interpolation intensity values is used to determine the six variables [74], [75].

2.3.2 Sub-pixel Interpolation

The correlation peak position detected by pattern matching is used to determine the pixel unit movements. However, the corresponding point positions between pixels generally exist in both images. Therefore, sub-pixel unit exploration is required in order to find out the correspondence points. As there are no grey intensity values between digitized pixels, in order to detect sub-pixel positions, an approximation to grey scale values in pixels is necessary. There are several interpolation methods for pixel intensity values to fit the image surface [75], [76]. Figure 2.37 shows graphically a typical array of the digitized values before interpolation based on 8×8 subset size. Bi-linear interpolation approximates the grey intensity values at a position (x^*,y^*) between the pixels linearly. Figure 2.38 shows the four neighbouring pixels, where $G(i, j)$, $G(i+1,j)$, $G(i, j+1)$,$G(i+1, j+1)$ are the intensity values for the centre of each pixel; i and j are real numbers representing pixel coordinates.

The interpolation position between the pixels (i, j), $(i+1,j)$, $(i, j+1)$ and $(i+1, j+1)$, is defined by

$$G(x^*, y^*) = a_{00} + a_{10}(x') + a_{01}(y') + a_{11}(x')(y')$$

where

a_{00}=grey level of pixel (i,j)

a_{10}=grey level of pixel $(i+1,j)$ - a_{00}

a_{01}=grey level of pixel $(i,j+1)$ - a_{00}

a_{11}=grey level of pixel $(i+1, j+1)$ - $a_{00} - a_{10} - a_{01}$

x' and y' are the distances from (x,y) to (x^*,y^*) which means $x' = x^*-i$ and $y' = y^*-j$ respectively. a_{00}, a_{10}, a_{01} and a_{11} are coefficients of the bi-linear function which can be determined by the intensities of these four neighbouring pixels. Figure 2.39 shows the grey-scale intensity surface using bi-linear interpolation.

2.3.3 DIC using Fourier Transform

The calculations performed during DIC analysis are quite demanding in terms of computer time. Fourier transform, which is commonly used for image processing, can be effectively employed to speed up the computations during DIC. An image consists of various types of information such as shape, contour, colour, shade and so on. As mentioned before, all these data are converted to digital electric signals (binary system, e.g. 2 bits to 14 bits) in terms of grey scale intensities at the pixel level. Any complex digital signal (function) can be expressed as integrated functions of neatly combined sine and cosine curves using Fourier transforms (Figure 2.40) [77].

The concept can be expressed with the following equation.

$$f(\theta) = a_1 \cos\theta + a_2 \cos 2\theta + a_3 \cos 3\theta + ...$$
$$+ b_1 \sin\theta + b_2 \sin 2\theta + b_3 \sin 3\theta + ...$$
$$+ C$$

which can also be expressed as:

$$= C + \sum_{n=1}^{\infty} (a_n \cos n\theta + b_n \sin n\theta)$$

where C is constant, $a_{1,2,3,.....n}$ and $b_{1,2,3,.....n}$ are coefficients

This is known as a Fourier series.

The Fourier transform is the expansion of Fourier series substituting Euler's equation ($e^{i\theta} = \cos\theta + i\sin\theta$) which can be applied to any function.

$$F(f) = \int_{-\infty}^{\infty} f(t) \cdot e^{-i\theta} dt$$

As one function can be transformed to the other, the function can be reversed to the previous function, known as the inverse Fourier transform.

$$f(t) = \int_{-\infty}^{\infty} F(f) \cdot e^{-i\theta} df$$

This function can be expressed by using an imaginary number i and separated into real part and imaginary part using the Euler's equation ($e^{i\theta} = \cos\theta + i\sin\theta$) [77].

$$F(f) = \int_{-\infty}^{\infty} f(t) \cdot \cos\theta + i\sin\theta dt$$

In this function, the real part expresses the phase of the function and the imaginary part expresses the amplitude of the curve. Here, the amplitude is the magnitude of the frequency related to image intensity (i.e. brightness), and the phase contains information on image shape, contour and change of shade [78]. If

the inverse Fourier transform is applied only on the imaginary part of the function, it is possible to extract only the intensity information, which can be used in DIC for the pattern matching. On the other hand, the real part can be used to extract the phase information which conveys just the contour of the image. This method is called Phase Only Correlation (POC) which is often used in medical imaging [79].

2.3.4 Image Reconstruction

Sub-pixel interpolation is often used after the first iteration (i.e. first cyclic correlation) in which all variables (C, dx and dy) are estimated to establish the displacement position with integer pixel resolution. Then, the coefficient C and displacements are determined by reconstructed images which are applied by intensity interpolation. The sub pixel intensity interpolation also affects the correlation and measurement accuracy [76], [80] and bi-linear interpolation is the default setting in the LaVision DIC software program. However, the use of the interpolation function eliminates image noise and provides sub-pixel accuracy, but it often causes the loss of original information such as image features. In order to avoid over smoothing, the Whittaker reconstruction algorithm [81] is selected for high accuracy mode in this analysis. This reconstruction is a non-linear interpolation, which takes sampling points (i.e pixel information) and produces a low frequency wave. As sub-pixel interpolation is applied after the first iteration which is determined at integer pixel accuracy between the initial and second images, the displacement of sub-pixel is less than one pixel. Thus, this sampling

reconstruction type is suitable for sub-pixel accuracy. Furthermore it removes noise and avoids any excessive smoothing of image so that it should be able to restore the original image without loss of information [72].

2.3.5 Correlation Peak Fitting

In order to estimate the amount of movement accurately, a Gaussian weight function is applied for correlation peak fitting with sub pixel interpolation. The correlation function is applied to two images with integer pixel accuracy at first iteration as an initial estimation, then, the sub-pixel interpolation is applied for higher accuracy using bi-linear interpolation or Whittaker reconstruction algorithm (in DaVis [72]). After images are reconstructed, these intensity functions can be fitted to a Gaussian interpolation function (Figure 2.41). Fitting the quadratic curve of a Gaussian bell shape to the data selected at several points (3 points in DaVis [72]) around correlation peaks, the displacement can be determined with sub-pixel accuracy. After both images are fitted to Gaussian shape intensity functions, the correlation function is applied in order to find out the correlation strength between two functions. The correlation peak is found by executing a convolution, which calculates overlap area when two functions are superposed. The correlation peak position is found when this overlap area is maximized, which determines final destination with sub-pixel accuracy.

2.3.6 Factors Affecting DIC Accuracy

The measurement accuracy of DIC can be affected by many factors, such as environment, manual parameter setting issues during image acquisition and implementation of complex computational algorithms. Environment and parameter settings such as illumination, camera lens distortion, analysis subsets size and speckle pattern affect the image contrast. The image contrast is important because it changes intensity function shape and sufficient contrast makes the correlation process work well, on the other hand, lack of contrast can be a limiting factor. The accuracy is also affected by the computation algorithm, such as the sub-pixel intensity interpolation, subset shape function [76], [80], [82], [83] and correlation peak optimisation as mentioned in the previous section. Among these issues, subset size and speckle size are dominant [84], [42], [40]. In general, in order to achieve a reliable pattern match in DIC, a large subset is chosen since it contains a relatively larger area of intensity pattern by which two correlating subsets can be identified. Table 2.3 shows how the accuracy of the displacement vectors depends on the size of the subset (interrogation window) in LaVision software [72]. In general a larger subset size causes smaller errors.

But a larger subset leads to a larger error for steep gradients in the displacement or strain field. On the other hand, a small subset can be approximated by a subset shape function more accurately in cross-correlation computation. The ideal subset size must also consider the speckle pattern. The speckle size and numbers have a significant influence on the accuracy of the measured displacement. Although a large number of speckles in one subset

provide more information, which contributes to high-quality pattern matching, a large number of small speckles can cause intensity pattern noise on the displacement determination using the correlation function. Thus, the appropriate size and number of speckles in one subset need to be determined based on the displacement gradient. In order to achieve best accuracy for DIC, it is important to consider the combination of speckle pattern and subset size.

In order to attain reliable measurement, each subset has to contain sufficient unique and individual features. Pang et al [40] proposed subset size selection to calculate the displacements using three different texture test image pairs, as illustrated in Figure 2.42. Figure 2.43 shows the standard deviation (σ) error of the *u*-displacement and the *v*-displacement for the three test image pairs with subset sizes ranging from 17×17 pixels to 71×71 pixels. The standard deviation error of measurement displacement is defined as:

$$\sigma = \sqrt{\frac{1}{N-1}\sum_{i=1}^{N} d_i^2}$$

Here d_i is the displacement component of point *i*. Thus the standard deviation error reflects the deviation of measured displacements from their mean value.

The results show that the standard deviation error increases as the subset size decreases and also observed that the error calculated from image pairs (c) are much larger than the image pairs (a) and (b) due to image contrast, which contains clear speckle patterns. A larger subset improves the accuracy because of the large number of intensity pixels in the correlation procedure. However, the measurement accuracy is related to combination of subset size and translation

displacement. Figure 2.43 shows results for a distance between neighbouring points of 10-pixel displacement.

Generally, a small displacement with a larger subset can start detecting incorrect positions, thus a small subset is desirable in the case of small displacement. Furthermore, using a zero or lower order of sub-pixel interpolation does not translate small displacement vectors such as shear or rotation due to low interpolation resolution, so choosing a large subset size can lead to erroneous results due to interpolation errors.

Lecompte et al [42] assessed speckle pattern quality and compared three different speckle patterns prepared by the same distribution with different camera zoom (Figure 2.44). According to their results, the larger the subset used, the more accurate measured displacements were. In the case of small subset, a more precise result is attributed to the smaller speckle size. However, the larger speckle size gives better results when a large subset is used. Their results showed that a correct balance of speckle size and subset size is essential to gain sufficient accuracy of the DIC measured displacement.

2.3.7 Summary

Digital image correlation is performed by pattern matching using a correlation function. The correlation coefficient gives the strength of similarity of two images, and a computational iteration calculation is used for determination of the displacement field. In image processing, Fourier transforms are used for cross-correlation. The image intensity array can be transformed to Gaussian shape

Fourier functions in order to deal with computational algorithm processing. Sub-pixel interpolation and image reconstruction are applied in order to improve accuracy of pattern matching. However, these transformation processes change the original information and errors from image processing (software error) can arise.

The accuracy of the DIC technique is related to speckle pattern and subset size. For an homogeneous displacement field, a large subset with large speckle pattern (can be considered high contrast) provides best accuracy for pattern matching. However, in the case of small translational displacement, large subsets start causing errors. A small subset is preferable for small translation, with a small speckle pattern. This is also suitable for a heterogeneous displacement field with steep gradients. Image interpolation and reconstruction is performed at the subset level, and this contributes higher accuracy.

2.4 References

[1] J. C. Lippold and D. J. Kotecki, *Welding metallurgy and weldability of stainless steels*. Wiley-Interscience, 2005.

[2] Kouich.Maruyama, *High Temperature Strength Material Science*. Uchida Rokabubo Co.,Ltd., 1997.

[3] R.W.Evans and B.Wilshire, *Introduction to Creep*. The Institute of Materials, 1993.

[4] W.D.Callister., *Material Science and Engineering, An Introduction*. John Wiley & sons.Inc, 2000.

[5] M.F.Ashby and D.R.H.Jones, Engineering Material 1,2nd ed., 2002.

[6] M. Sakamoto, K. Yagi, H. Morishita, K. Kubo, Y. Monma, and C. Tanaka, "Classification of creep deformation behaviour of 2.25Cr-1Mo steel, 304 and 316 stainless steel," *The society of Material Science, Japan*, vol. 39, no. 441, pp. 86–92, 1989.

[7] G.Sasikala, K.Bhanu, and S. Rao, "Creep deformation and fracture behaviour of type 316 and 316L stainless steel and their weld metal.," *Metallurgical and Materials Transactions A*, vol. 31A, 1999.

[8] D. H. Kumar, T. Shaktivelu, M. Nanda Gopal, K. S. Chandravathi, K. Laha, S. K. Albert, H. Kumar, B. Shanmugarajan, and a. SomiReddy, "Creep Failures in Laser Welded 316L(N) Stainless Steel Joints," *Journal of Materials Science Research*, vol. 2, no. 1, pp. 124–134, Dec. 2012.

[9] G.Langdon and D. A. Miller, "Creep Fracture Maps for 316 Stainless Steel," *Metallurgical Transaction A*, vol. 10A, pp. 1635–1641, 1979.

[10] K. Yagi, M. Tabushi, and K. Kubo, "The influence of fracture mechanisms on the creep crack growth behavior of 316 stainless steel," *Engineering Fracture Mechanics*, vol. 57, no. 5, pp. 463–473, 1997.

[11] Yukio.Takahashi, S. Date, and T. Nakazawa, "Effect of grain size on high temperature strength of fast reactor spec.SUS316," *The society of Material Science, Japan*, vol. 46, no. 11, pp. 1274–1279, 1997.

[12] R. G. Thomas, "The effect of δ-ferrite on the creep rupture properties of austenite weld metals," *Welding Research Supplement 82-s*, 1978.

[13] I. Okane and O. Koj, "Creep rupture properties of weld joints of type AISI 304 and 316 austenitic stainless steels," *Japan Welding Society*, vol. 5, pp. 121–126, 1972.

[14] T. Zaizen, S. Aoki, K. Suzuki, and S. Bando, "Effect of the welding heat cycles on the hardness and microstructures of 308 type stainless steel weld metal," *Japan Welding Society*, vol. 1, no. 37–45, 1983.

[15] Abe.Pollack and C.C.Chen, "Influence of welding on steel weldment properties." Microalloying International, Inc, pp. 416–428.

[16] Hongo.Hiromichi, "Creep rupture behaviour of butt welded joint of 304 stainless steel thick plate using small and large specimens," *Japan Society of Material Science*, pp. 509–515, 1990.

[17] Hiromichi.Hongo, "Creep deformation behaviour of weld metal and heat affected zone on 316 steel thick plate welded joint," *Japan Society of Material Science*, vol. 48, no. 2, pp. 116–121, 1999.

[18] Hongo.Hiromichi, Yamazaki.Masayoshi, Watanabe.Takashi, Tabuch.Masaaki, Tanabe.Tatsuhiko, and Monma.Yoshio, "Evaluation for creep properties of 316FR weld metal with miniature weld metal and full-thickness welded joint specimens," *The Siciety of Material Science, Japan*, vol. 53, no. 5, pp. 566–571, 2004.

[19] Hiromichi.Hongo, H. Masuda, and Y. Monma, "Effect of local fluctuation of the high temperature strength properties in weld metal on creep deformation behavor of multilayer welded joint," *Journal of the Society of Materials Science, Japan*, vol. 54, no. 2, pp. 155–161, 2005.

[20] M. Fujimoto, M. Sakane, S. Date, and H. Yoshida, "Multiaxial creep rupture and damage evaluation for 2.25Cr-1Mo forged steel," *The Society of Material Science, Japan*, vol. 54, no. 2, pp. 149–154, 2005.

[21] J.R.Rice, "On the ductile enlargement of voils in triaxial stress fileds." *J.Mech, Phys, Solids*, vol. 17, pp. 201–217, 1969.

[22] K. .Nakacho, Y. Ueda, J. Kinugawa, and M. Yamazaki, "Development of a simple model for creep analysis of thick welded joint (Report1)," *Japan welding society*, vol. 12, no. 2, pp. 249–254, 1994.

[23] K. Nakacho, Yukio.Ueda, Junichi.Kinugawa, and Masayosh.Yamazaki, "A simple model for analysis of creep behaviour of thick welded joints," *Japan Welding Society*, vol. 50, 1992.

[24] K. Nakacho, Y. Ueda, J. Kinugawa, and M. Yamazaki, "Creep characteristics in thick welded joints and their improvement (report1)," *Trans.JWRI*, vol. 26, no. 1, pp. 141–145, 1997.

[25] Junichi.Kinugawa, Muramatsu.Yoshiki, Monma.Yoshio, Y. Masayoshi, Hongo.Hiromichi, and Watanabe.Takashi, "Computation of creep deformation of welded joint of 304 stainless steel by using finite element method," *Japan welding Ssociety*, vol. 7, no. 1, pp. 117–124, 1989.

[26] "R5 Issue3 Assessment procedure for the high temperature response of structure. EDF Energy Ltd, May 2012." Gloucester. UK.

[27] "R6 Revision 4 Assessment of the Integrity of Structure containing Defects. EDF Energy Ltd," October 2011,Gloucester. UK..

[28] H. Ishikawa, *Nonlinear Mechanics of Solid.* Yokendo,Ltd, 2000.

[29] Y. Takahashi, "Evaluation of creep-fatigue life prediction methods for low-carbon nitrogen-added 316 stainless steel," *Journal of Engineering Materials and Technology-Transactions of the ASME*, vol. 120, no. 2, pp. 119–125, 1998.

[30] Y. Takahashi, "Further evaluation of creep-fatigue life prediction methods for low-carbon nitrogen-added 316 stainless steel," *Journal of Pressure Vessel Technology-Transactions of the ASME*, vol. 121, no. 2, pp. 142–148, 1999.

[31] Y. Takahashi, Y. Nakayama, H. Koto, K. Taguchi, Y. Fukudo, S. Sato, and P. E. P. Pep, "Creep-fatigue life estimation for austenitic stainless steel weldments," *International Conference on Integrity of High-Temperature Welds*, pp. 221–230.

[32] Y. Takahashi, "Evaluation of creep-fatigue life prediction methods for low-carbon/nitrogen-added SUS316," *Japan Society of Material Science*, vol. 47, no. 5, pp. 527–533, 1998.

[33] Z. Fan, D. J. Smith, X. Chen, and M. W. Spindler, "Creep-fatigue lives prediction and sensitivity study of 316H at 550 ◦ C," vol. 24, no. 2, pp. 132–140, 2011.

[34] Y. Li, Y. Monma, H. Hongo, and M. Tabuchi, "Evaluation of creep damage in a welded joint of modified 9Cr–1Mo steel," *Journal of Nuclear Materials*, vol. 405, no. 1, pp. 44–49, Oct. 2010.

[35] "AGR Material Data Handbook R66, British Energy Generation Ltd," .

[36] "RCC-MR, Section 1,Sub-section Z, Technical Appendix A3, AFCFN, Paris 1985." .

[37] M.Sutton, W.Wolters, W.Peters, W.Ranson, and S.McNrill, "Determination of displacements using an improved digital correlation method," *Image and Vision Computing*, 1983.

[38] M.A.Sutton, J.J.Orteu, and H.W.Schreier, *Image Correlation for Shape, Motion and Deformation Measurements.* Springer, 2009.

[39] B. Pan, L. Yu, D. Wu, and L. Tang, "Systematic errors in two-dimensional digital image correlation due to lens distortion," *Optics and Lasers in Engineering*, vol. 51, no. 2, pp. 140–147, Feb. 2013.

[40] S. Yaofeng and J. H. L. Pang, "Study of optimal subset size in digital image correlation of speckle pattern images," *Optics and Lasers in Engineering*, vol. 45, no. 9, pp. 967–974, Sep. 2007.

[41] M. A. Sutton, J. H. Yan, V. Tiwari, H. W. Schreier, and J. J. Orteu, "The effect of out-of-plane motion on 2D and 3D digital image correlation measurements," *Optics and Lasers in Engineering*, vol. 46, no. 10, pp. 746–757, Oct. 2008.

[42] D.Lecompte, A.Smits, S.Bossuyt, J.Vantomme, D. V. Hemelrijck, and A.M.Habraken, "Quality assessment of speckle patterns for digital image correlation," *Optics and Lasers in Engineering*, vol. 44, no. 11, pp. 1132–1145, Nov. 2006.

[43] S. Yoneyama, A. Kitagawa, K. Kitamura, and H. Kikuta, "In-Plane Displacement Measurement Using Digital Image Correlation with Lens Distortion Correction," *JSME International Journal Series A*, vol. 49, no. 3, pp. 458–467, 2006.

[44] J. Chen and et al, "Two-step digital image correlation for micro-region measurement," *Optics and Lasers in Enginnering*, vol. 43, 2005.

[45] N.Shishido, "Thermal strain measurement on electronic packages using digital image correlation method," *The Society of Material Science, Japan*, 2008.

[46] S. Yoneyama, "Bridge deflection measurement using digital image correlation," *The Japan Society of Mechanical Engineers*, 2006.

[47] F. Lagattu, F. Bridier, P. Villechaise, and J. Brillaud, "In-plane strain measurements on a microscopic scale by coupling digital image correlation and an in situ SEM technique," *Materials Characterization*, vol. 56, no. 1, pp. 10–18, Jan. 2006.

[48] M.Kohara, "Dynamic examination of multi-bracket appliance by digital image correlation technique," *J Meikaii Dent Med*, vol. 37, no. 1, pp. 50–55, 2008.

[49] "BSSM Code of Practice for the installation of electrical resistance strain gauges CPI:1992." .

[50] "Hitec Products, Inc. 100 Park Street, Unit 12 Ayer, MA 01432." .

[51] S.Shibli and G. Merckling, *Creep & Fracture in High Temperature Components: Design & Life Assessment Issues*. Proceedings, ECCC Creep Conference September 12-14, 2005, London, U.K., 2005.

[52] J. N. Petzing and J. R. Tyrer, "Recent development and applicatins in electronic speckle pattren interferonmetry," *The Journal of Strain Analysis for Engineering Design*, vol. 33, no. 2, pp. 153–169, Jan. 1998.

[53] B. Brussels, A. H. Cardon, and P. Em, "Electronic Speckle Pattern Interfer rometry for observation of damege initiation and development in composites," *sem.org-SEM-X-Int-Cong-s066p04*, pp. 5–7.

[54] D. Post, B. Han, and P. Ifju, *High Sensitivity Moiré: Experimental Analysis for Mechanics and Materials*. Verlag,New York: Springer, 1994.

[55] G.Cloud, R.Radke, and J.Peiffer, "Moiré Gratings for High Temperatures and Long Times," *Experimental Mechanics*, pp. 19–21, 1979.

[56] J.M.Burch and C.Forno, "High resolution moire photography," *Optical Engineering*, vol. D, no. 4, 1982.

[57] Xie.Huimin, Peter.Dietz, Dai.Fulong, and Axes.Schmidt, "A study on the creep deformation of high temperature pipeline using the Moiré method," I*nternational Journal of Pressure Vessels and Piping*, vol. 71, pp. 219–223, 1997.

[58] Bruce.Kang, Xingbo.Liu, Cezar.Cisloiu, and Keh-minn.Chang, "High temperature moire ´ interferometry investigation of creep crack growth of inconel 783 - environment and b-phase effects," *Material Science and Engineering*, vol. 347, pp. 205–213, 2003.

[59] T.H.Hyde, H.Xie, and W.Sun, "High Temperature Gratings for the Moire and Moire Interferometry Methods and their Application t o Deformation Measurement Review," *Strain*, vol. 37, no. 2, pp. 205–213, 2001.

[60] H. Hongo, H. Masuda, and Y. Monma, "Development of simple strain distribution measurement system by interferometry using CCD image elements," *The Iron and Steel Institute of Japan*, vol. 79, no. 4, pp. 75–79, 1992.

[61] B. L. Boyce, P. L. Reu, and C. V Robino, "The Constitutive Behavior of Laser Welds in 304L Stainless Steel Determined by Digital Image Correlation," vol. 37, no. August, 2006.

[62] M.O.Acar., S. Gungor., S. Ganguly., P.J.Bouchard, and M. E. Fitzpatrick, "Variation of Mechanical Properties in a Multi-pass Weld Measured Using Digital Image Correlation," *Proceeding of the SEM Annual Conference*, 2009.

[63] F. Reynolds, A Duvall, "Digital Image Correlation for Determination of Weld and Base Metal Constitutive Behavior," *Welding Research Supplement*, pp. 355–360, 1999.

[64] M.O.Acar, S.Gungor, M. E. Fitzpatrick., and P. J. Bouchard, "Numerical Study of Strength Mismatch in Cross-Weld Tensile Testing," *International Congress Advance in Welding Science and Technology for Construction, Energy and Transportation Systems (AWST_2011)*, 2011.

[65] Murat Acar, "Effects of plastic strain history on the properties of stainless steel boiler tube welds," PhD thesis,The Open University, UK, 2011.

[66] J.S.Lyons, J.Liu, and M.A.Sutton, "High-temperature deformation measurement using digital-image correlation," *Experimental Mechanics*, pp. 64–70, 1996.

[67] Jed.Lyons, Michael.Sutton, and Anthony.Reynolds, "Experimental Characterization of Crack Tip Deformation Fields in Alloy 718 at High Temperatures," *Journal of Engineering Material and Technology*, vol. 120, no. January, 1998.

[68] Jin.Liu, M.Sutton, Jed.Lyons, and Xiaomin.Deng, "Experimental investigation of near crack tip creep deformation in alloy 800 at 650°C," *International Journal of Fracture*, 1998.

[69] Chris.Maharaj, "A Review of Method to Estimate Creep Damage in Low-Alloy Steel Power Station Steam Pipes," *Strain*, 2009.

[70] A. Morris, C. Maharaj, A. Puri, and J. Dear, "Recent developments in method to study creep strain variations," *ASME Pressure Vessels and Piping Dvision Conference*, no. PVP2008–61119, 2008.

[71] A. Morris, C. Maharaj, I. Almer, A. Puri, and J. Dear, "Developments in combined arcmac and strain measurement systems for creep measurement," *ASME Pressure Vessels and Piping Dvision Conference*, no. PV2008–61118, 2008.

[72] "DaVis StrainMaster Software, Manual, LaVision GmbH." .

[73] "DANTEC DYNAMICS A/S, Laser Optical Measurement System and Sensors, Tonsbakken 16-18 Skovlunde, Denmark." .

[74] P. Bing, X. Hui-min, X. Bo-qin, and D. Fu-long, "Performance of sub-pixel registration algorithms in digital image correlation," *Measurement Science and Technology*, vol. 17, no. 6, pp. 1615–1621, Jun. 2006.

[75] H.A.Bruck, M.A.Sutton, and W.H.Peters, "Digital Image Correlation Using Newton-Raphson Method of Partial Differential Correction," *Experimental Mechanics*, vol. 29, p. 261, 1989.

[76] H.W.Schreier and M.A.Sutton, "Systematic errors in digital image correlation caused by intensity interpolation," *Optical Engineering*, vol. 39, p. 2915, 2000.

[77] A. Takeuchi, *Fourier transform.* Blueback.inc, 2009.

[78] H. Kiya, *Digital Image Processing*. CQ Press, 1996.

[79] M. Hagiwara, "Detection of Subpixel Displacement for I age Using Phase-Only Correlation," *The Institute of Electronics*, 2009.

[80] Y.Q.Wang, "Image matching error assessment in digital image correlation," *SEM Annual Conference*, 2009.

[81] E. Whittaker, "Expansions of the Interpolation-Theory," *Proc. Roy. Soc., Edinburgh*, vol. 35, p. 181, 1915.

[82] M.Sutton and H.W.Schreier, "Systematic error in digital image correlation due to undermached subset shape function," *Exp. Mech*, 2002.

[83] P. Zhou, "Subpixel displacement and deformation gradient measurement using digital image/speckle correaltion," *Optical Engineering*, vol. 40, p. 1613, 2001.

[84] M. Ueda, "Study on accuracy evaluation of deformation and strain distribution measurement using digital image correlation," *The Japan Society of Mechanical Engineering*, vol. 76, p. 119, 2009.

[85] "www.correlatedsolutions.com (access date:Nov 2011)." .

[86] W. Z. Pan B, "Study on subset size selection in digital image correlation for speckle patterns," *Optics Express*, vol. 16, p. 7037, 2008.

2.5 Tables and Figures

Solidification Type	Reaction	Microstructure
A	$L \rightarrow L + A \rightarrow A$	Fully austenitic, well-defined solidification structure
AF	$L \rightarrow L + A \rightarrow L + A + (A + F)_{eut} \rightarrow A + F_{eut}$	Ferrite at cell and dendrite boundaries
FA	$L \rightarrow L + F \rightarrow L + F + (F + A)_{per/eut} \rightarrow F + A$	Skeletal and/or lathy ferrite resulting from ferrite-to-austenite transformation
F	$L \rightarrow L + F \rightarrow F \rightarrow F + A$	Acicular ferrite or ferrite matrix with grain boundary austenite and Widmanstätten side plates

Table 2.1 Solidification types, reactions and resultant microstructures (L:Liquid, A:Austenitic, F:Ferritic) [1]

T	C1	C2	n1	C3	n3	C	n	tfp
540	2.46E-12	0.4129	4.1578	1.98E+21	-7.4584	3.19E-27	8.54	6.63E+02
545	2.70E-12	0.41709	4.1688	2.97E+20	-7.2025	1.31E-26	8.37	4.28E+02
550	2.96E-12	0.42131	4.18	4.49E+19	-6.9467	5.29E-26	8.2	2.78E+02
555	2.70E-12	0.42943	4.2208	3.75E+19	-6.9741	7.86E-26	8.2	1.99E+02
560	2.45E-12	0.43777	4.2626	3.19E+19	-7.0031	1.16E-25	8.2	1.43E+02
640	2.02E-12	0.59767	4.689	6.89E+20	-8.6461	5.00E-23	8.17	6.05E+01
645	2.23E-12	0.60956	4.6956	1.56E+21	-8.8828	7.22E-23	8.16	4.10E+01
650	2.45E-12	0.6218	4.7024	3.93E+21	-9.1423	1.04E-22	8.16	2.78E+01
655	2.16E-12	0.63678	4.7548	1.18E+21	-8.959	3.06E-22	8.01	2.11E+01
660	1.89E-12	0.65234	4.8091	3.51E+20	-8.7744	8.89E-22	7.86	1.60E+01

Table 2.2 RCC-MR creep deformation law material constant for AISI Type 316H austenite stainless steel [36]

Size of the interrogation window	Accuracy of the calculated vectors
128×128	down to 0.01 - 0.03 pixel
64×64	down to 0.02 - 0.05 pixel
32×32	down to 0.05 - 0.2 pixel
16×16	larger than 0.1 - 0.3 pixel

Table 2.3 Relation between the accuracy of the displacement vector and the subset size [72]

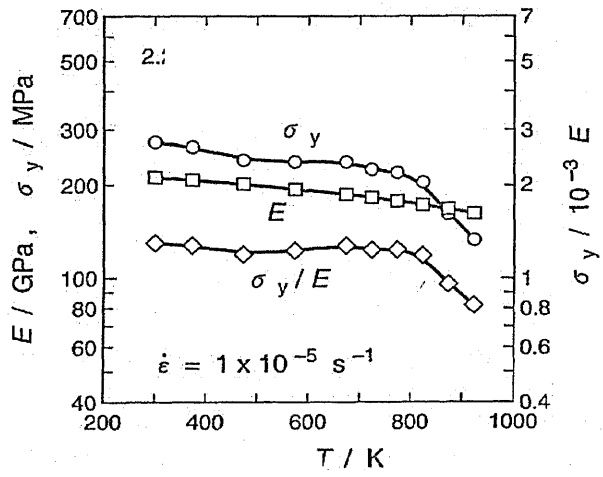

Figure 2.1 Variation of the yield strength of stainless steel at elevated temperature [2]

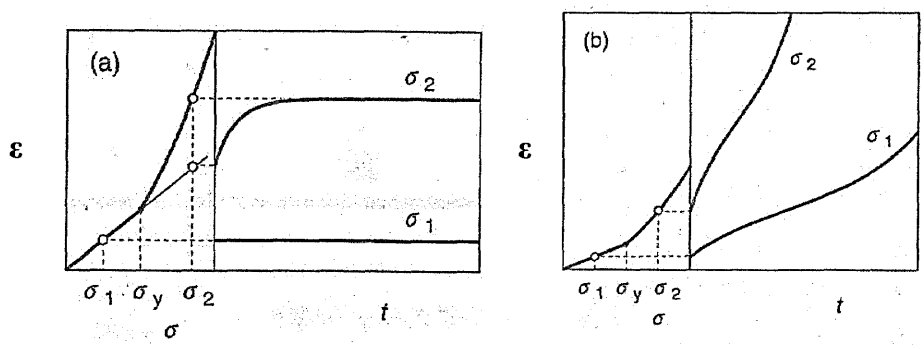

Figure 2.2 Stress-strain curves at room temperature and high temperature [2]

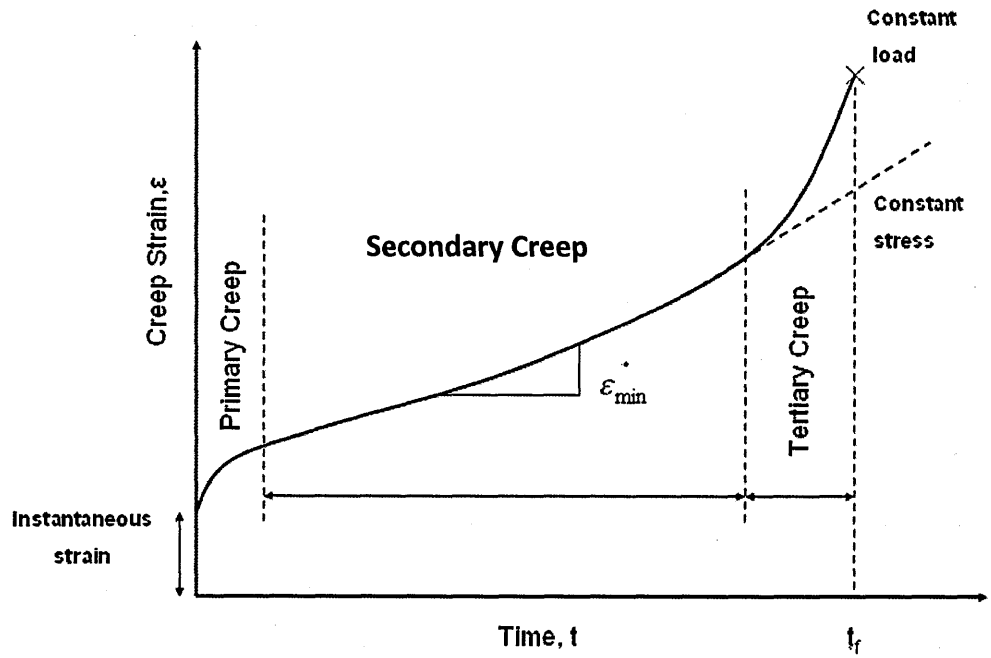

Figure 2.3 Schematic creep curve

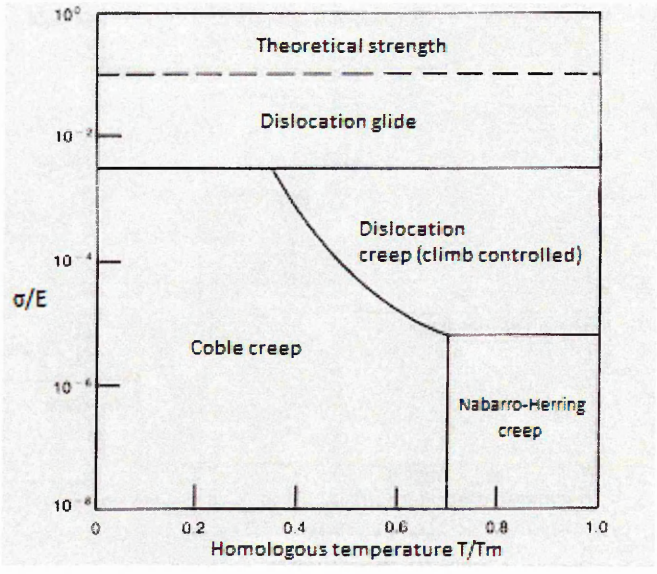

Figure 2.4 Creep mechanism map (Ashby map) [3]

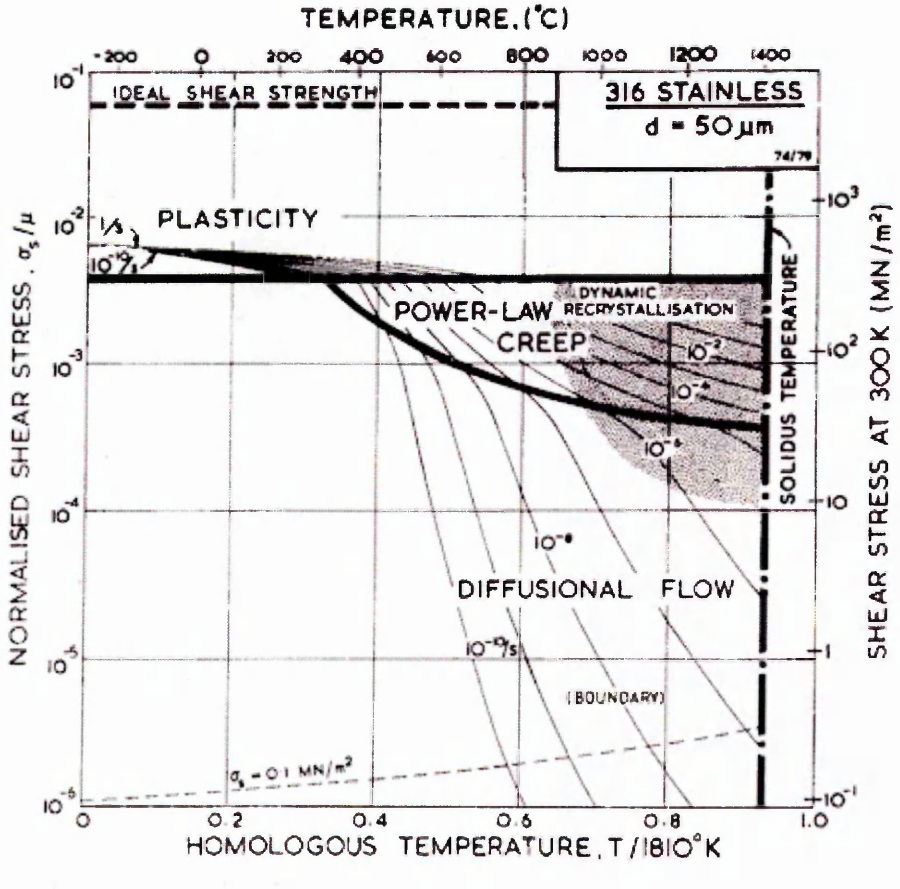

Figure 2.5 Creep mechanism map of 316 stainless steel with a grain size of 50 micron [5]

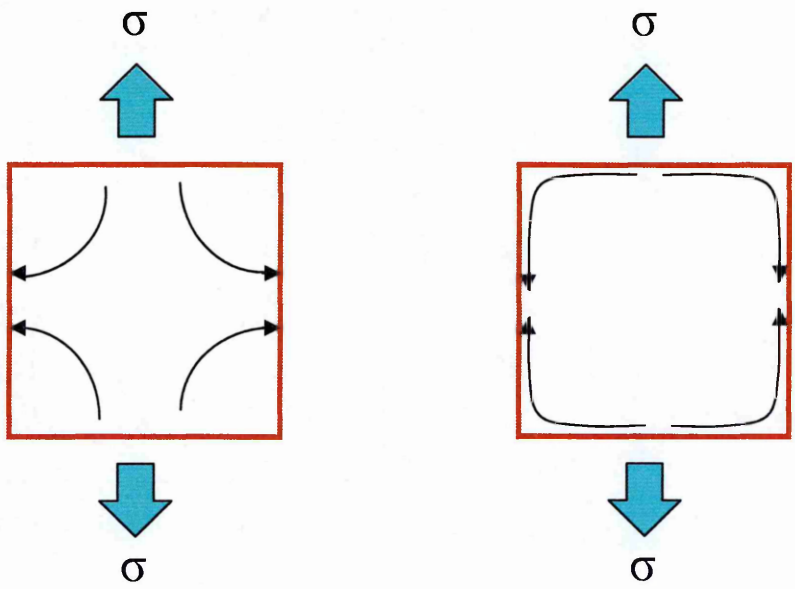

(a) Nabarro-Herring creep (b) Coble creep

Figure 2.6 Schematic diagrams showing flow of vacancy in diffusion creep

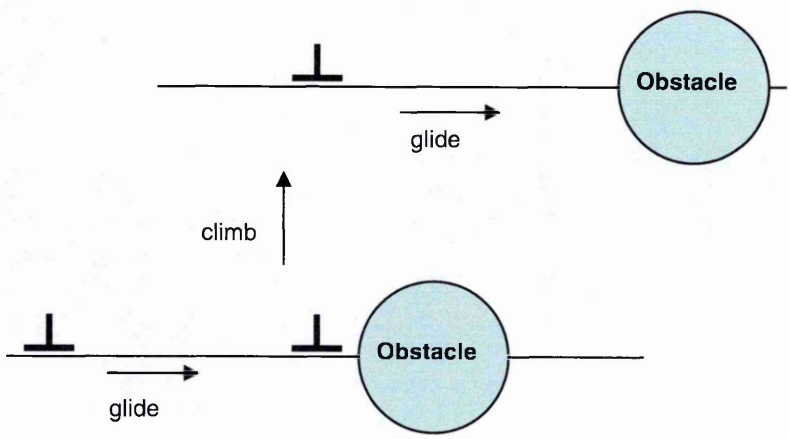

Figure 2.7 Dislocation Creep

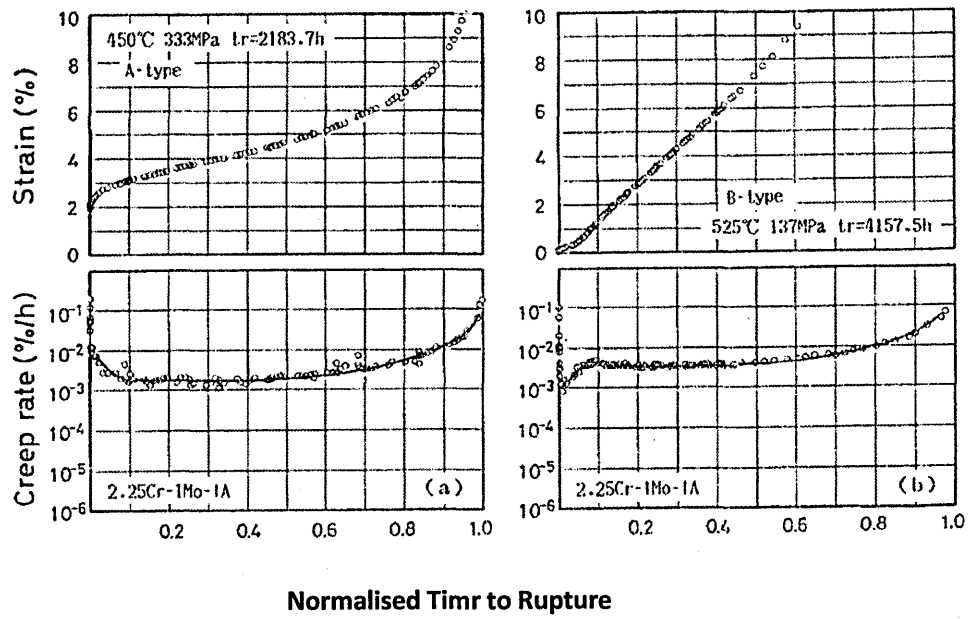

(a) Type A (b) Type B

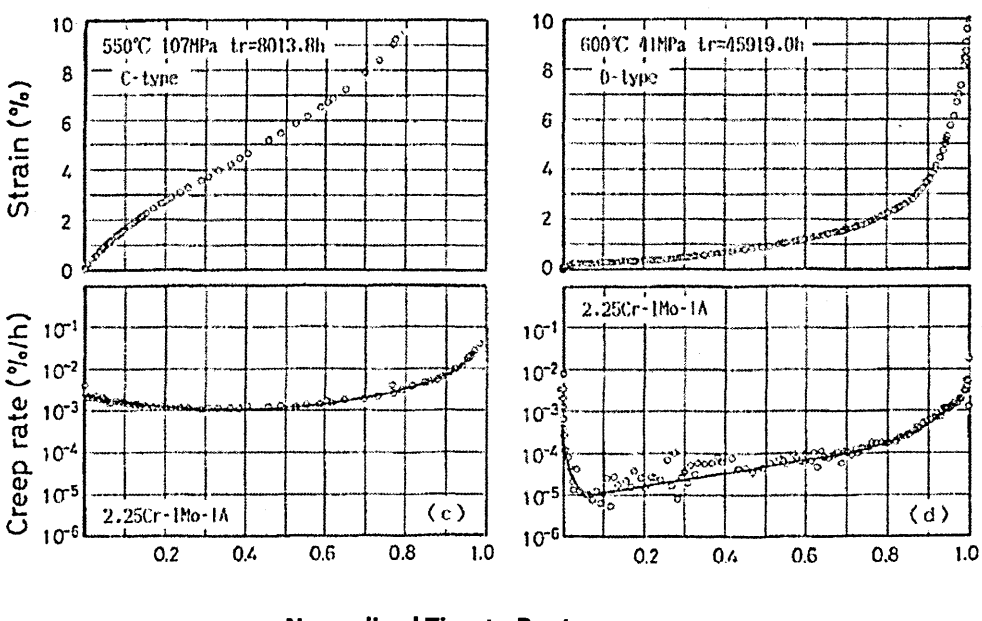

(c) Type C (d) Type D

Figure 2.8 Creep deformation behavior of 2.25Cr-1Mo ferritic steel [6]

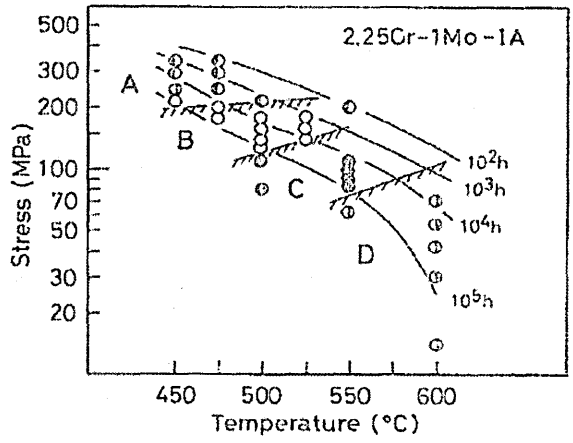

(a) 2.25Cr-1Mo-1A steel

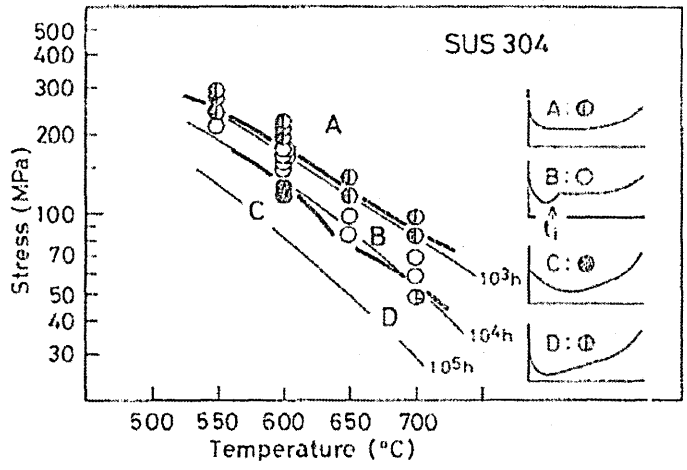

(b) 304 steel

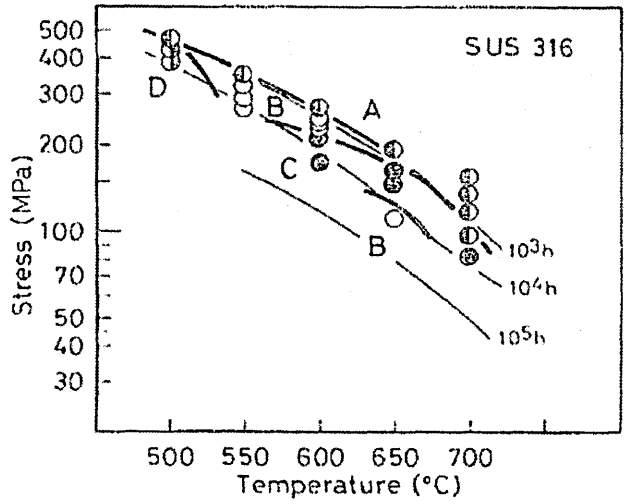

(c) 316 steel

Figure 2.9 Relationship between creep stress and type of creep deformation [6]

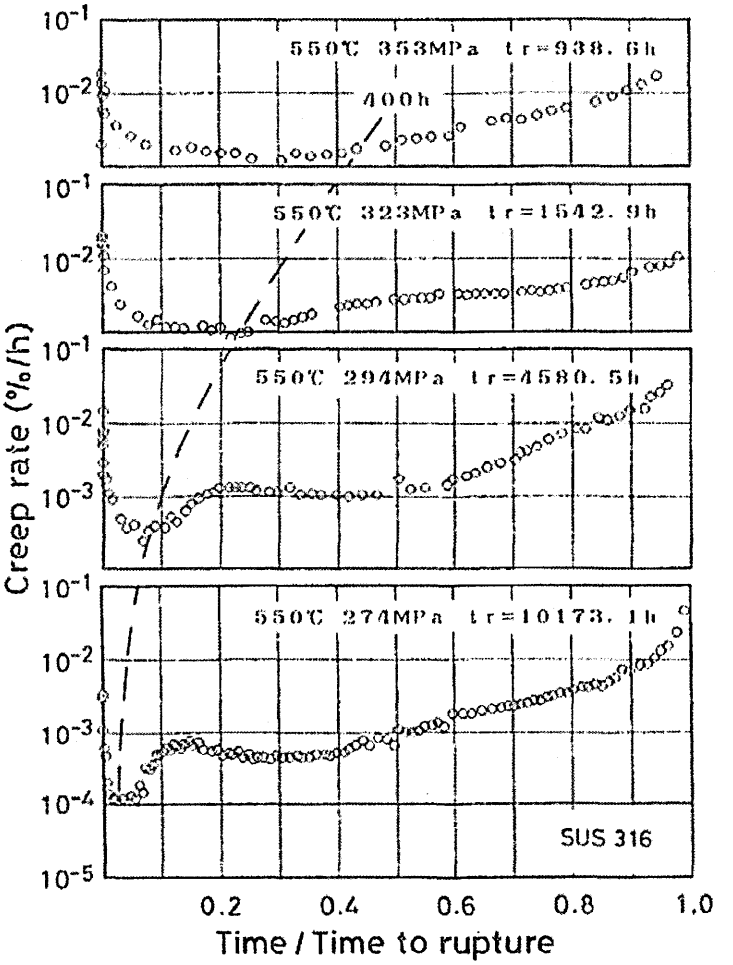

Figure 2.10 Relationship between creep rate and life fraction t/t_r at 550 °C in Type 316 stainless steel (dashed line shows inflection point) [6]

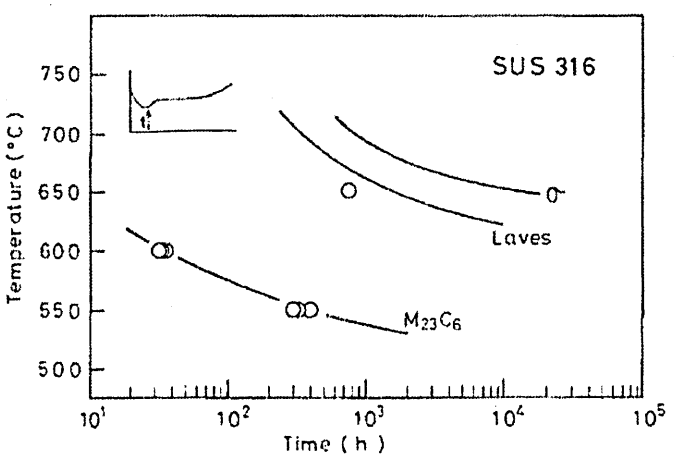

Figure 2.11 Times of inflection for Type B, t_i, superimposed on time-temperature-precipitate diagram for 316 steel [6]

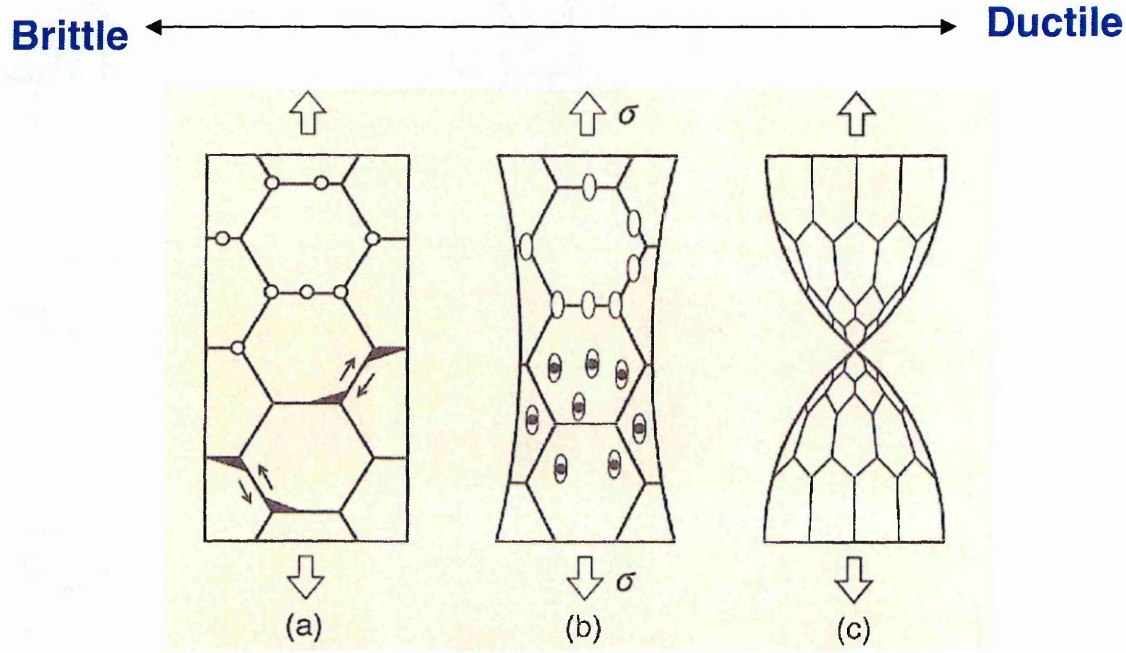

Figure 2.12 Creep fracture mechanisms. (a) Intergranular creep fracture due to cavity growth with wedge crack. (b) Transgranular creep fracture due to cavity growth within grains. (c) High temperature rupture [2]

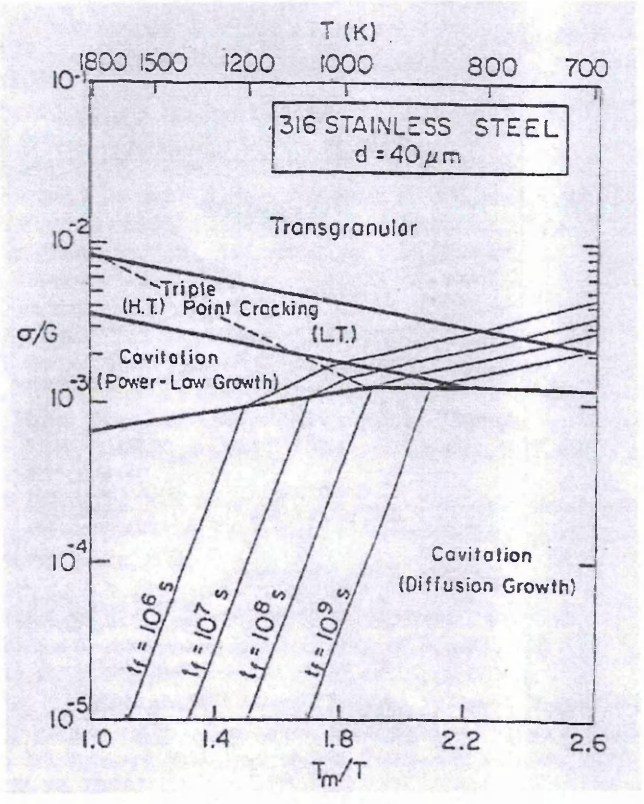

Figure 2.13 Creep fracture mechanism map of Type 316 stainless steel with a grain size of 40 micron [9]

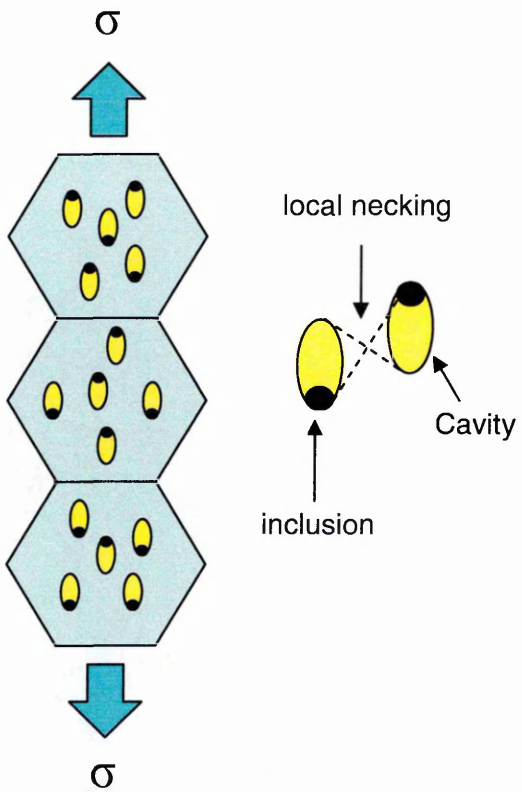

Figure 2.14 Transgranular creep fracture

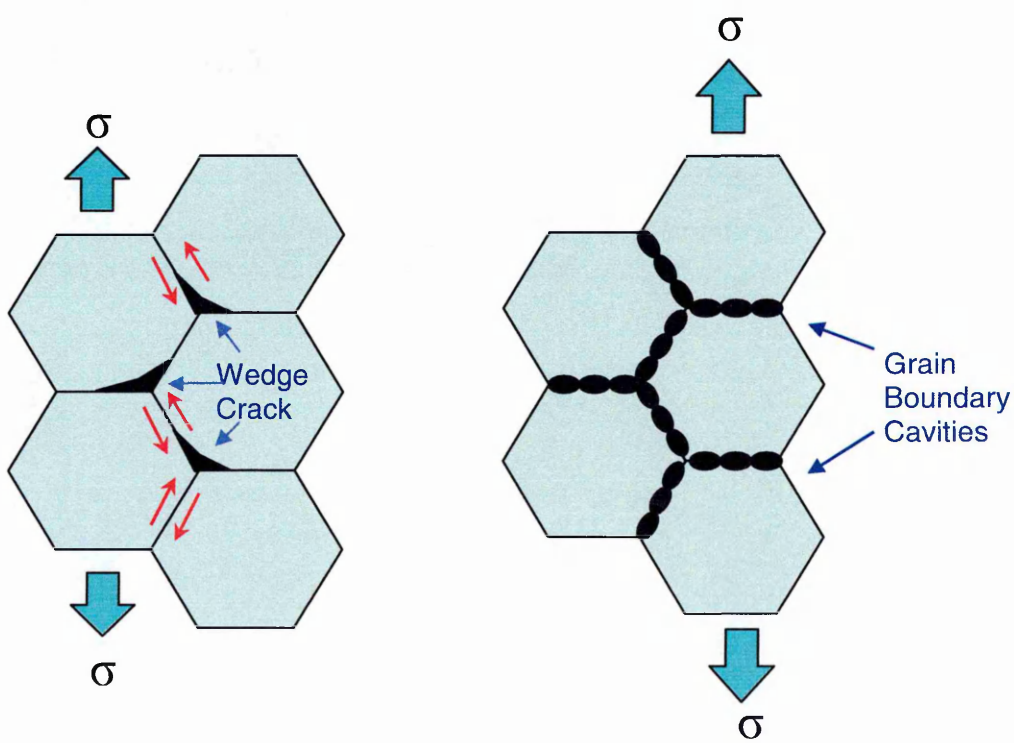

(a) Triple points initiated creep fracture **(b) Cavity based creep fracture**

Figure 2.15 Types of intergranular creep fracture

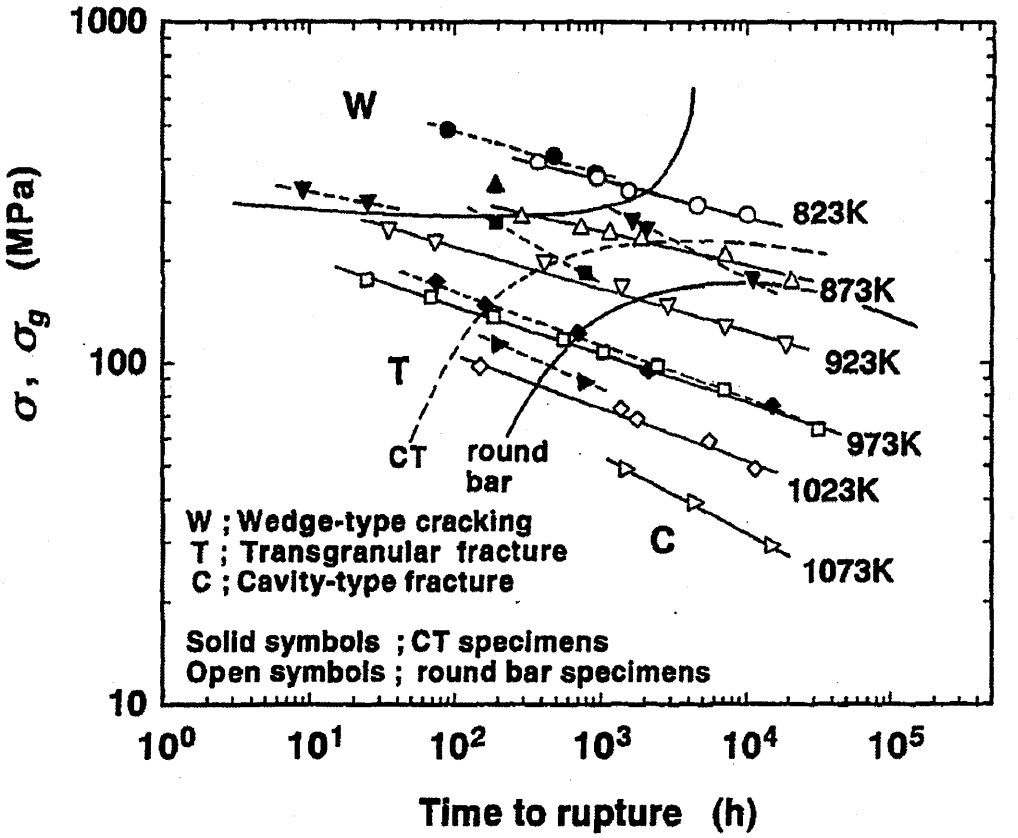

Figure 2.16 Relationship between stress vs time to rupture, and creep fracture mechanism of round bar specimen and CT specimen [10]

(a) W-type, 873K 50μm

(a) 'W-Type' intergranular fracture due to wedge type cracking at high stress and low temperature (873 K)

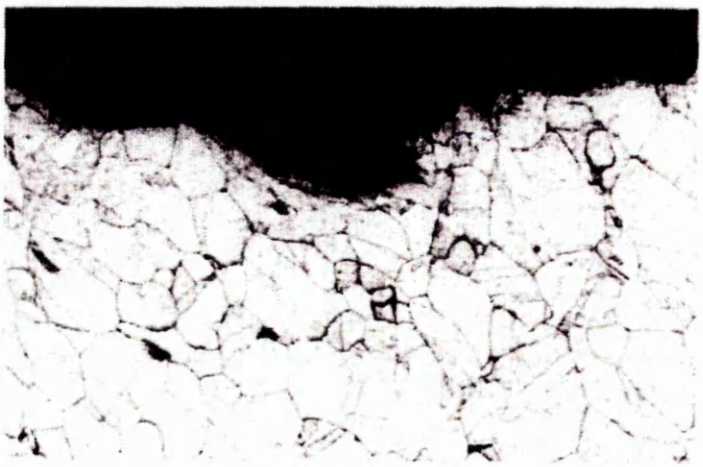

(b) T-type, 923K 50μm

(b) 'T –Type' transgranular fracture at low stress and high temperature (923 K).

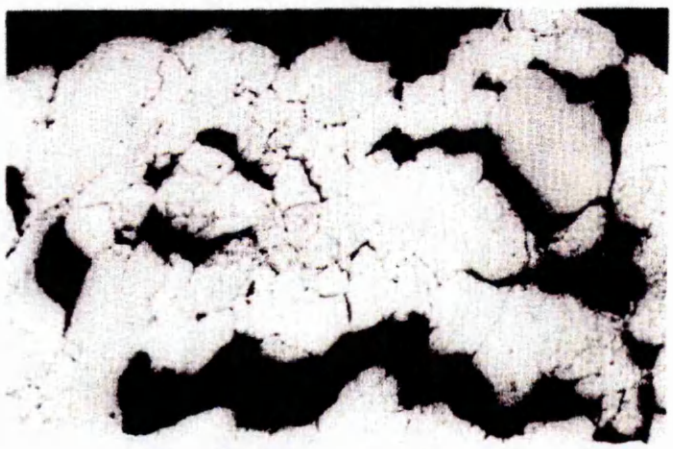

(c) C-type, 973K 50μm

(c) 'C-Type' intergranular fracture due to growth of cavities at low stress and high temperature (923 K)

Figure 2.17 Microscopical fracture features associated with creep crack growth of stainless steel under different stress and temperature conditions [10]

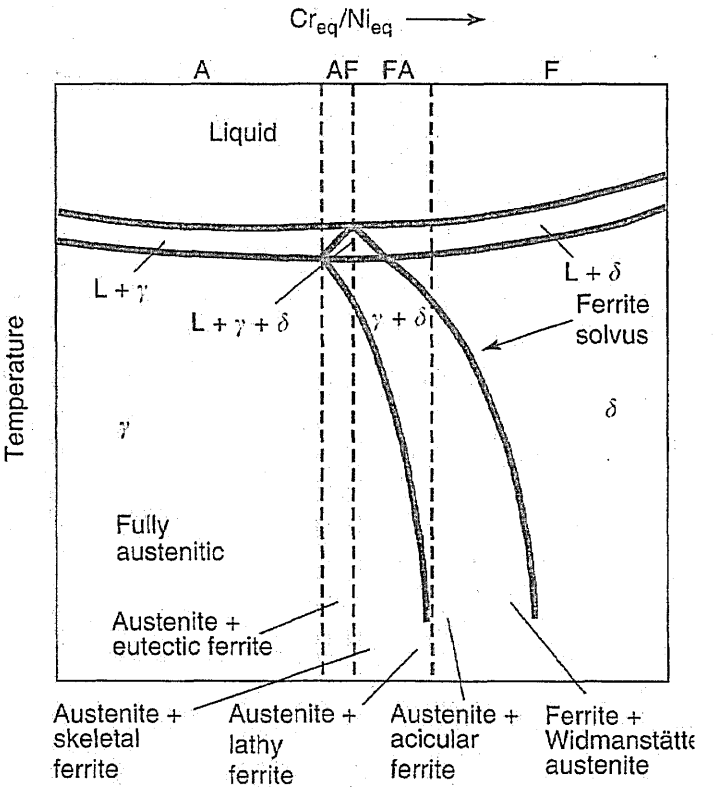

Figure 2.18 Solidification phase diagram for stainless steel showing the effect of composition in terms of Cr and Ni equivalents [1]

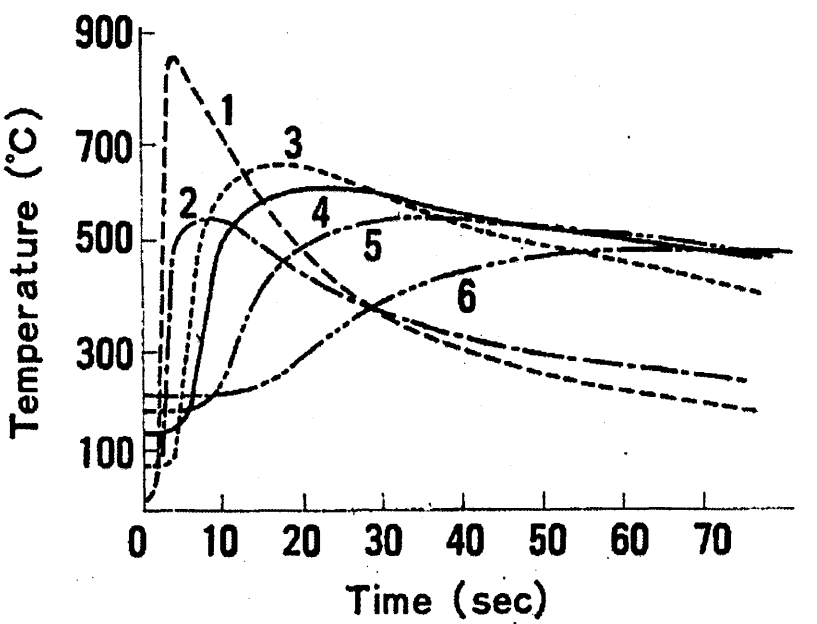

Figure 2.19 Transient temperature history as a function of distance from the weld (1 = close to weld, 6 = distant from weld) [14]

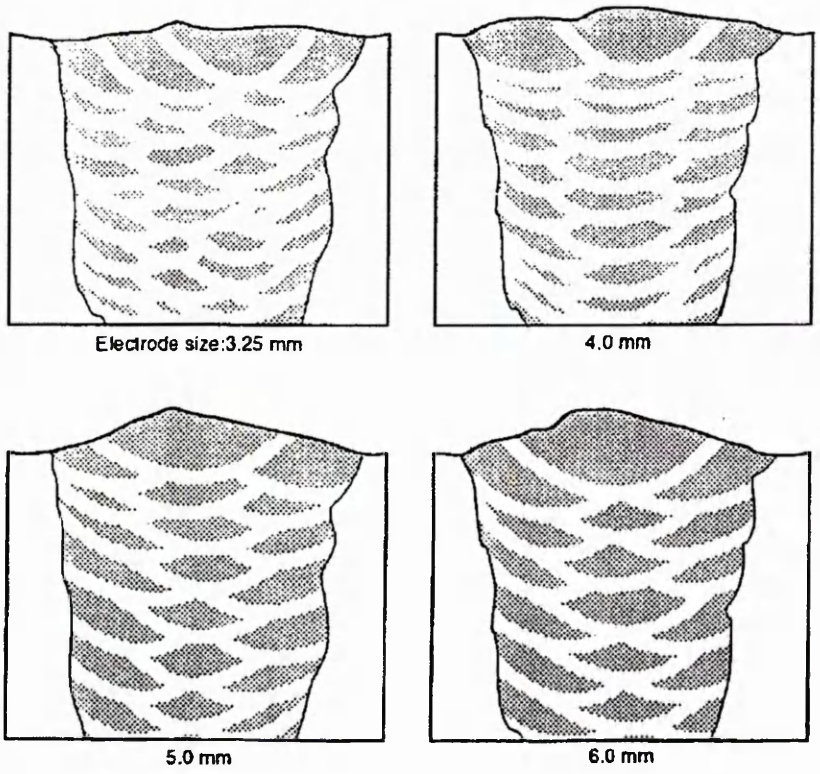

Figure 2.20 Recrystallized weld metal in multi-run welding with different size electrodes : White area represent r crystallized weld metal [15]

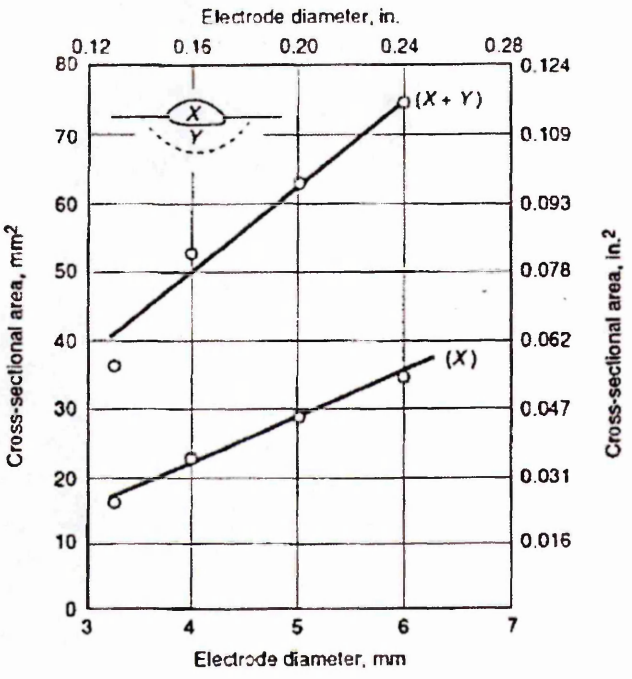

Figure 2.21 Cross-sectional area changes with different size of electrode [15]

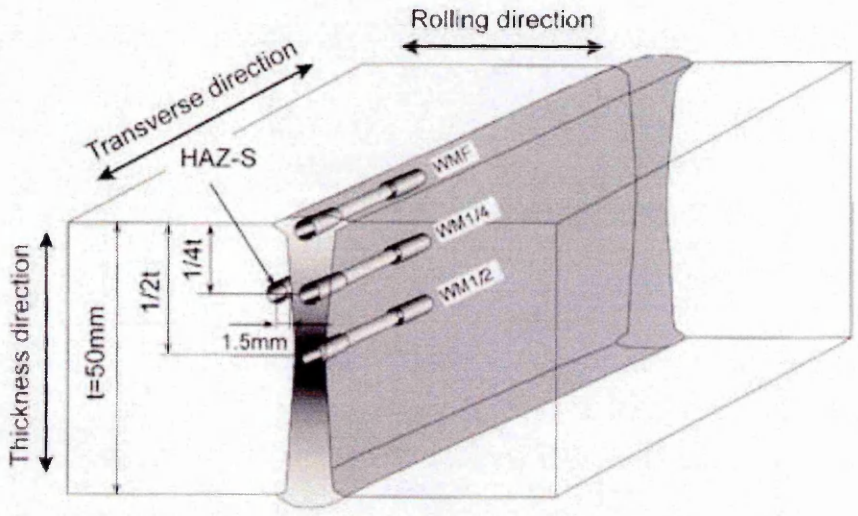

Figure 2.22 Location of sampling for miniature specimen in the welded joint [18]

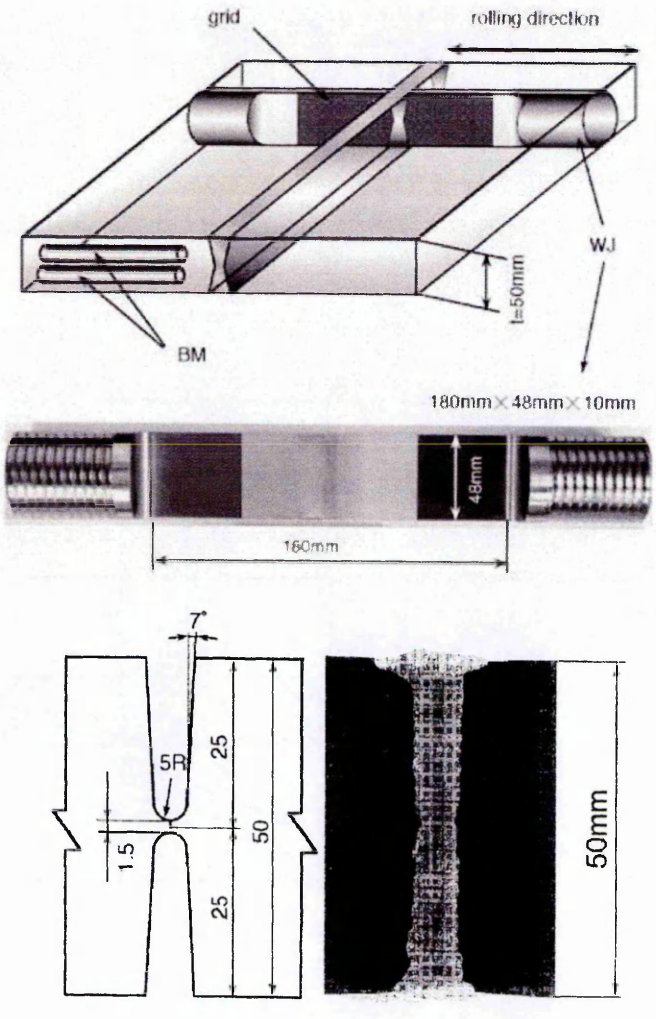

Figure 2.23 Sampling location of thickness welded joint specimen and double U grooves geometries and its microstructure [18]

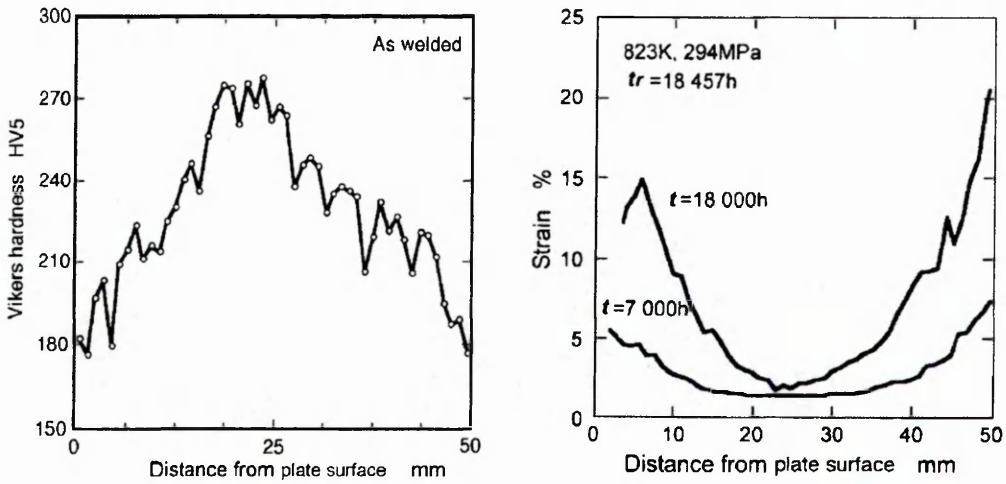

Figure 2.24 Hardness variation and strain distribution across the thickness (50mm)[18]

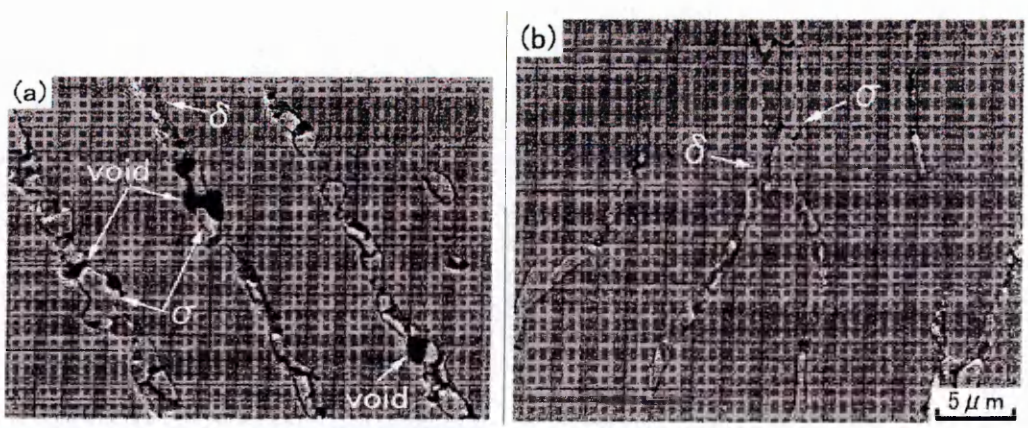

Figure 2.25 Scanning electron micrographs showing the void distribution in the ruptured welded joint specimen (t_r=18,457h): (a) near surface region (b) mid-thickness position [18]

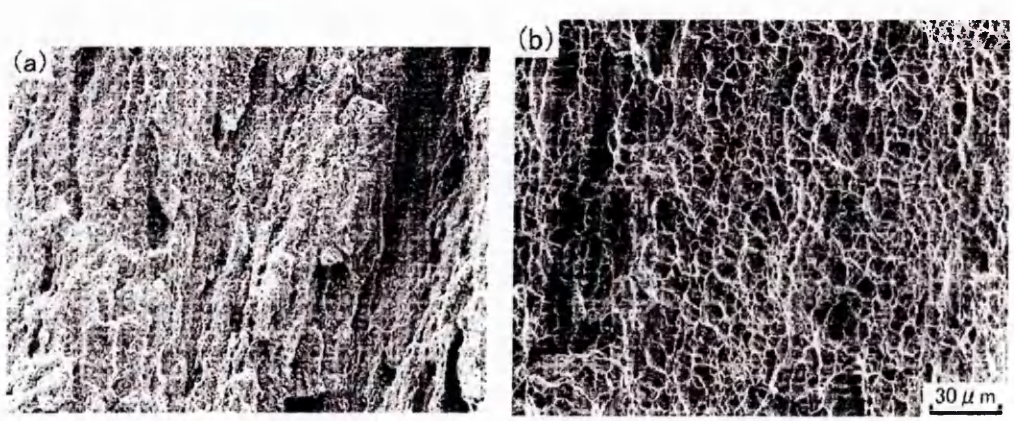

Figure 2.26 Scanning electron micrograph showing fracture surface of the welded joint specimen (t_r=18,457h): (a) near surface region (b) mid-thickness position [18]

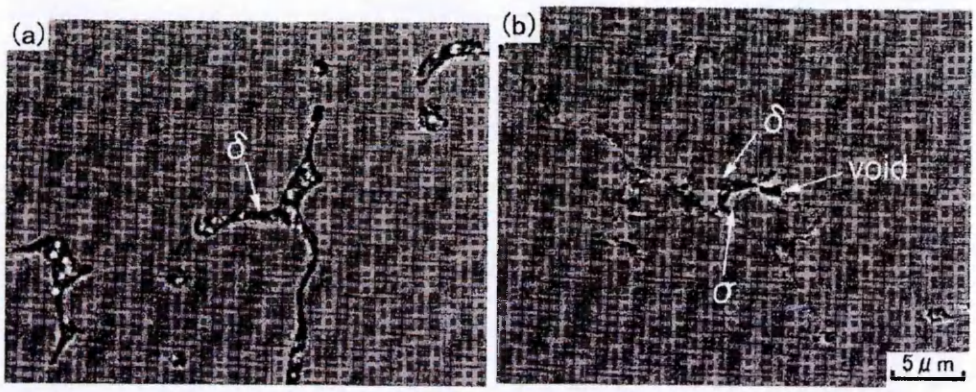

Figure 2.27 Scanning electron micrographs showing the void distribution in the miniature specimen taken from the near surface region: (a) 294 MPa, t_r=985 h, (b) 235 MPa, t_r=15,765 h [18]

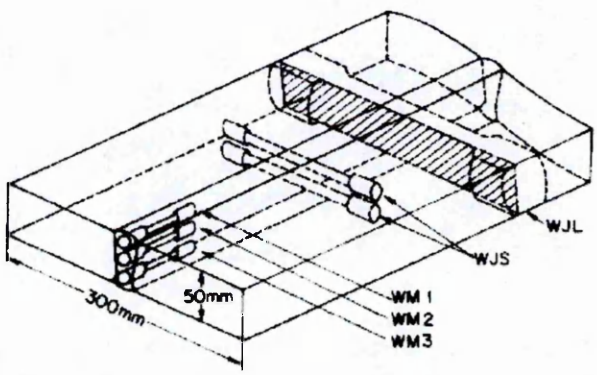

Figure 2.28 Sampling of test specimens from welded joint [25]

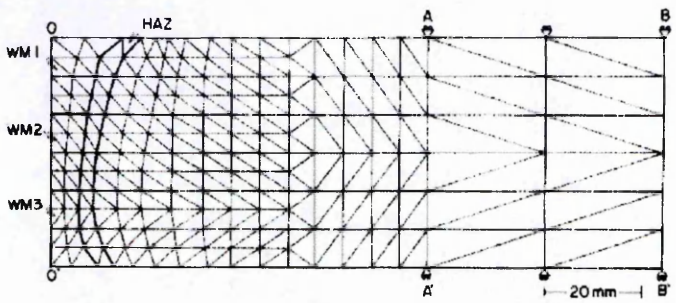

Figure 2.29 Mesh divisions for the specimen [25]

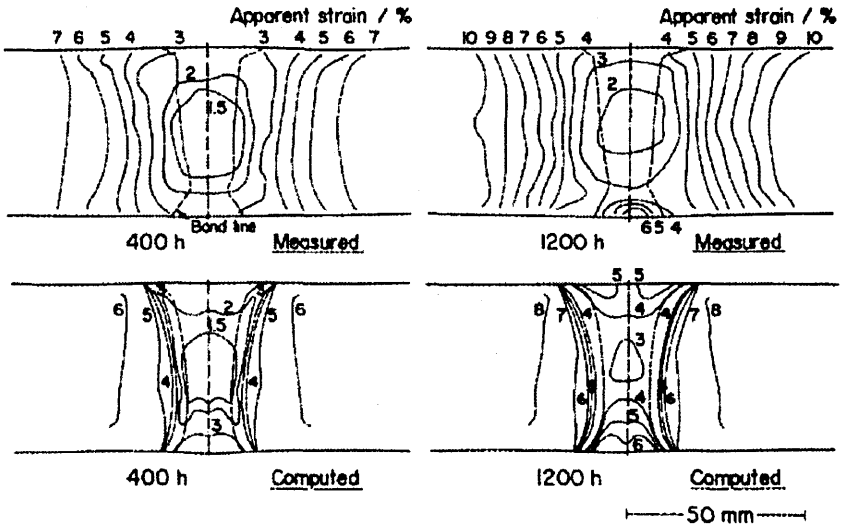

Figure 2.30 Comparison of computations with measurements for contours of apparent strain in loading direction [25]

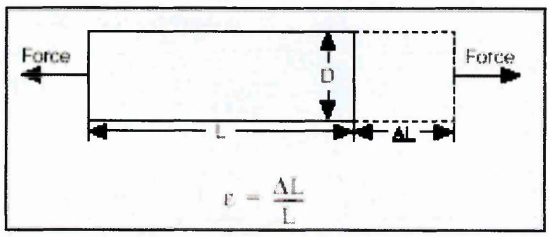

Figure 2.31 Strain change in length by amount of deformation

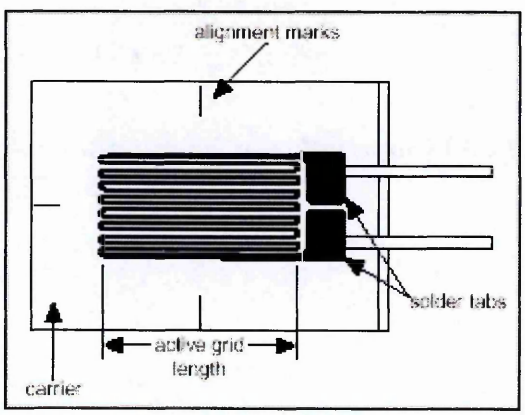

Figure 2.32 Metallic bonded strain gauge

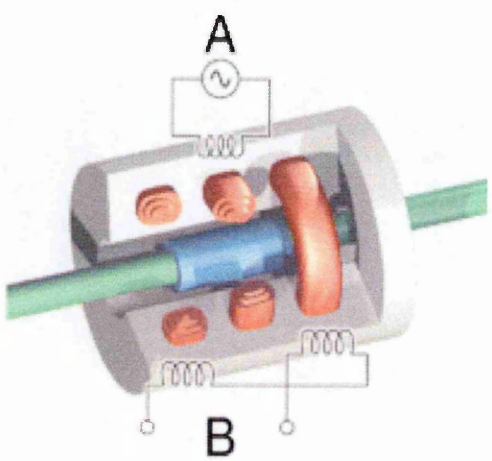

Figure 2.33 Design of LVDT displacement transducer

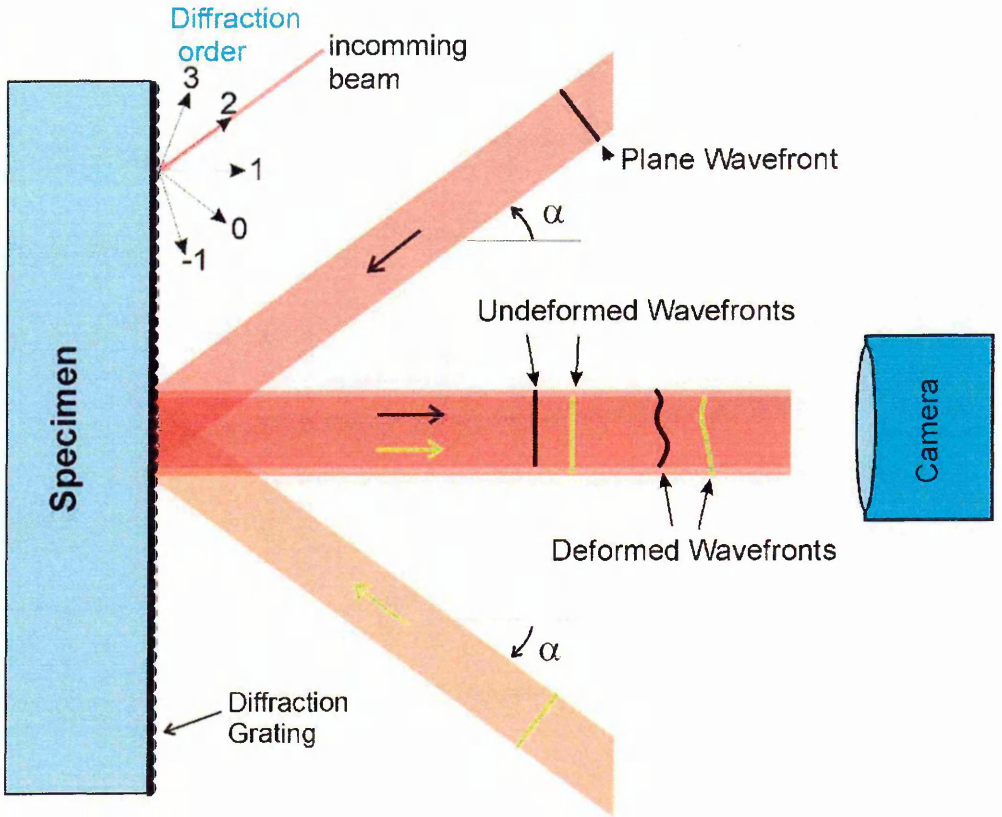

Figure 2.34 Moiré interferometer with a specimen grating exposed to a two-beam interference system

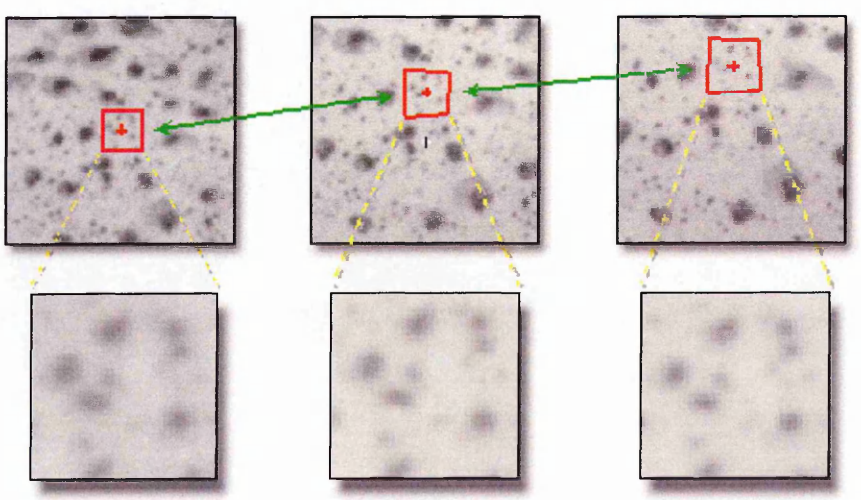

Figure 2.35 Pattern tracking using Digital Image Correlation [85]

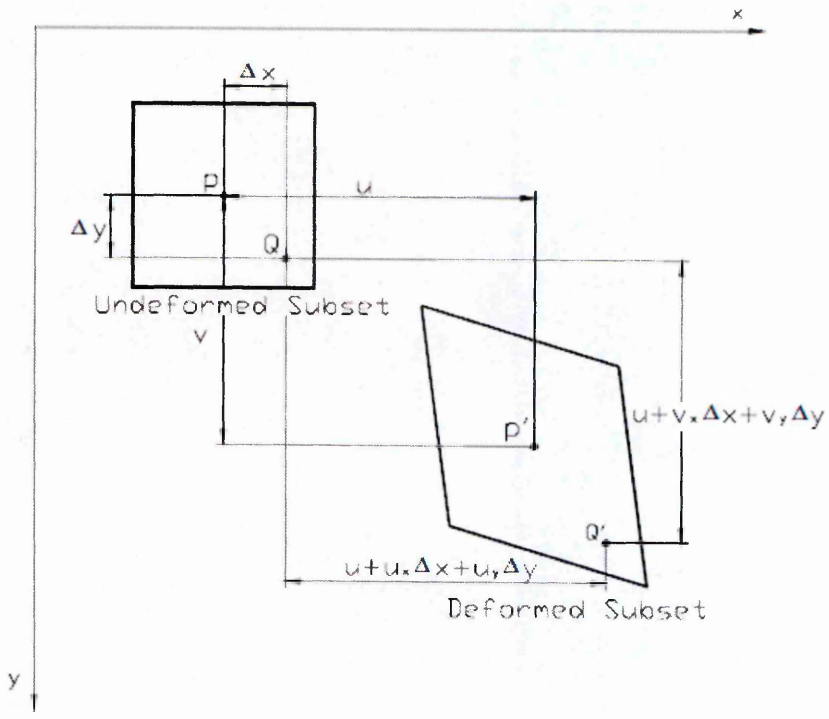

Figure 2.36 Schematic figure of deformed subsets in DIC [74]

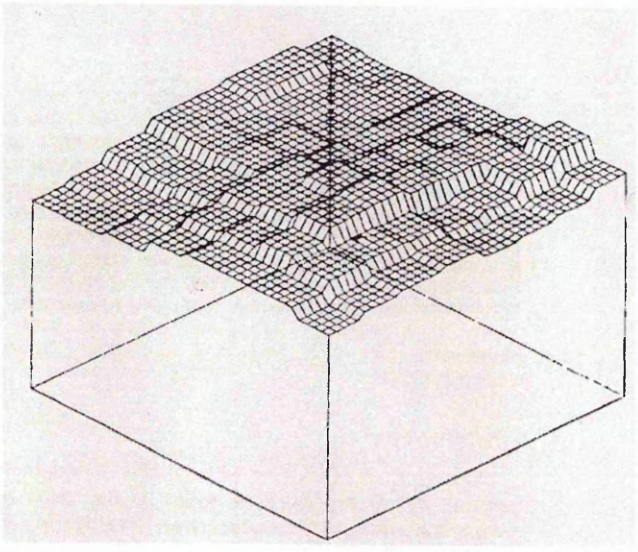

Figure 2.37 Grey-scale intensity surface before interpolation [75]

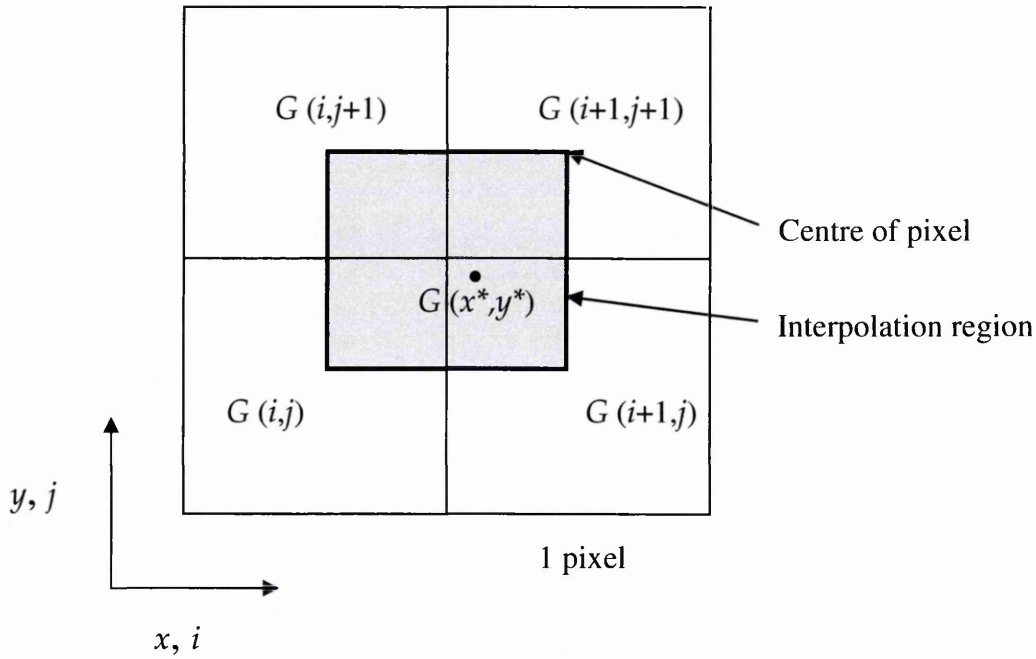

Figure 2.38 Four neighbouring pixels

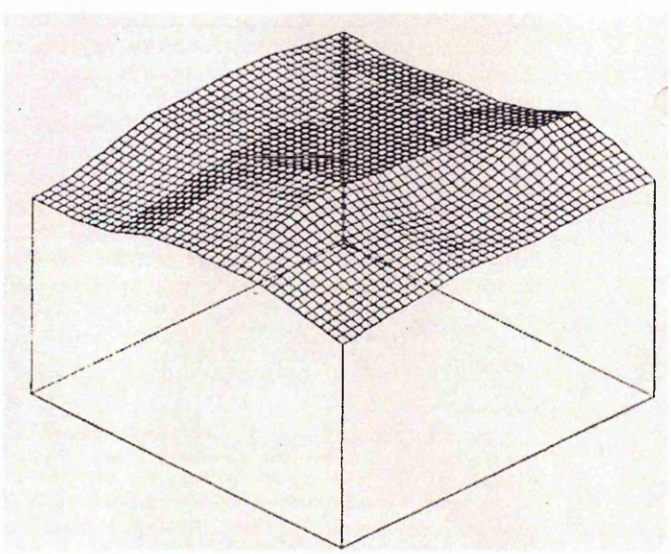

Figure 2.39 Grey-scale intensity surface using bi-linear interpolation [75]

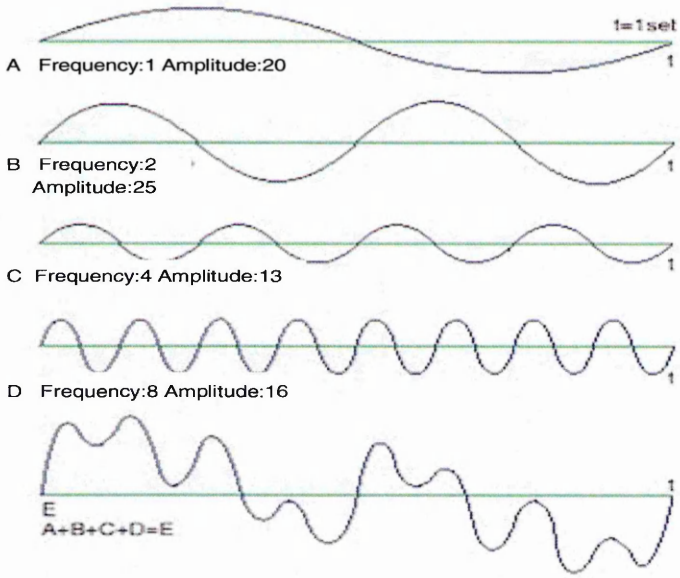

Figure 2.40 Signal E can be expressed by sum of signal A to D

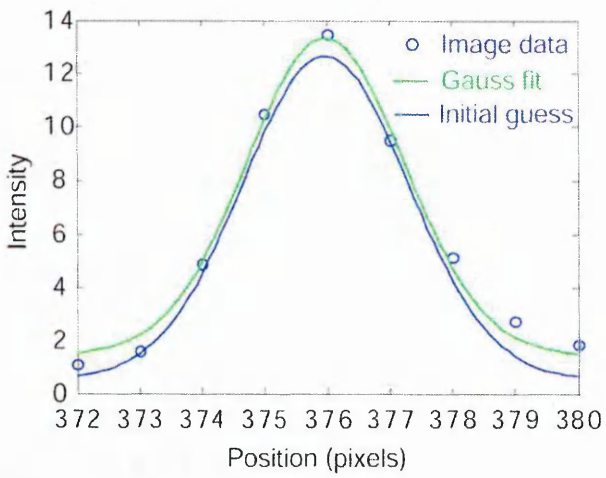

Figure 2.41 Intensity peak profile by Gaussian fit

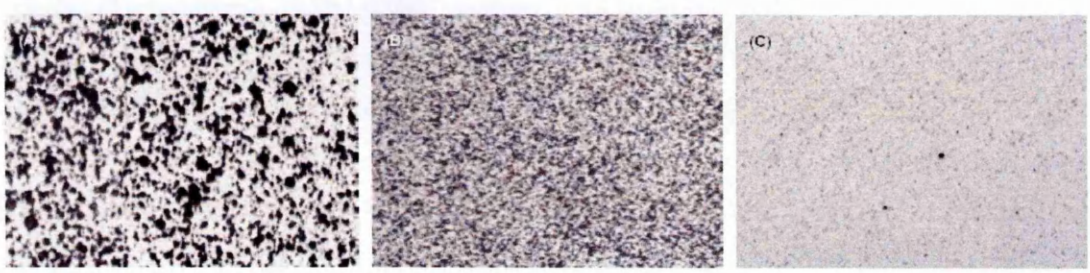

(a) (b) (c)

Figure 2.42 Three different texture reference images [86]

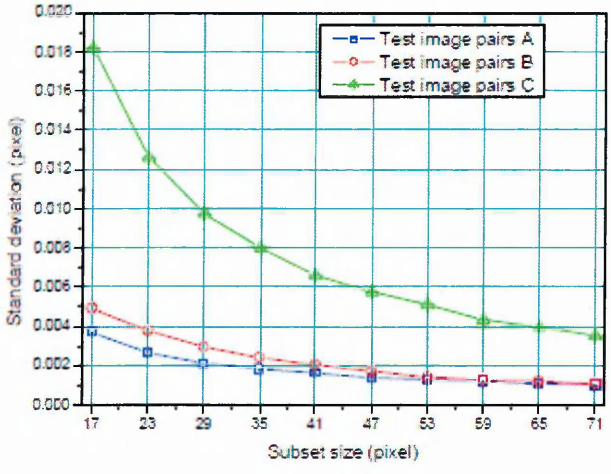

Figure 2.43 Standard deviation of the three sets of image pair vs the subset size [86]

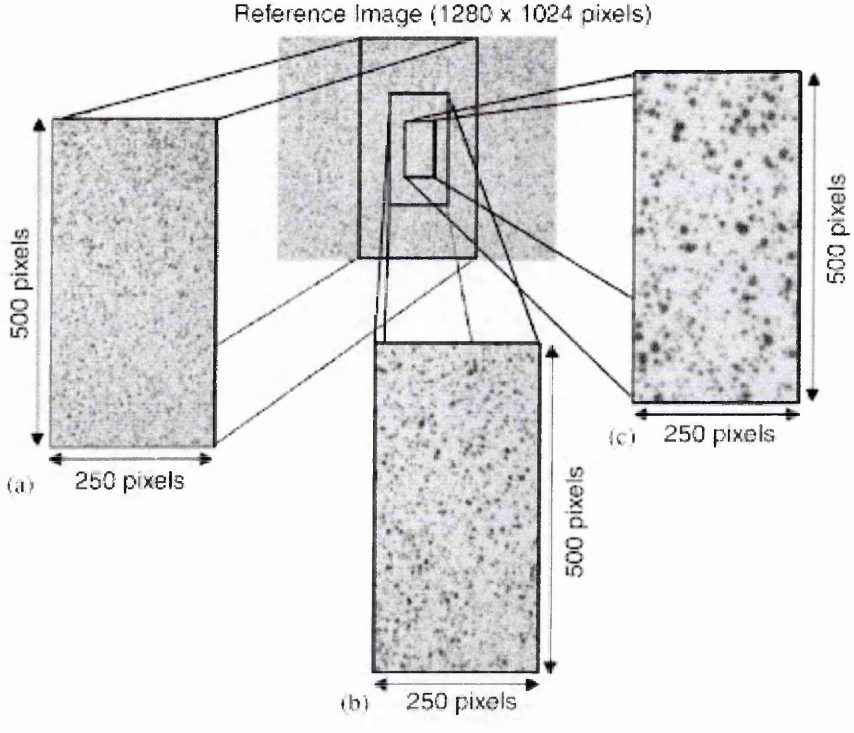

Figure 2.44 Sprayed speckle pattern with three different zooms yielding the three new reference speckle patterns [42]

Chapter 3

Application of DIC to Measure Cross-weld Tensile Deformation

3.1 Introduction

The theory of DIC, factors affecting its accuracy and recent research relating to its application to measure the deformation of surfaces has been reviewed in Chapter 2. Before addressing the challenges of developing a DIC based system to measure creep deformation at high temperature (see Chapter 4), and applying it to investigate the behaviour of a complex multi-pass weldment (Chapter 5), the present Chapter demonstrates application of the DIC technique to tensile tests at room temperature. In particular spatially resolved surface deformation, and thereby position dependent stress-strain properties, across a weldment are measured in tensile tests performed on extracted cross-weld samples. The measured properties from this kind of test can be used to observe and help understand how welding thermal cycles have affected the deformation properties of surrounding parent material and previously deposited weld metal [1],[2],[3],[4],[5],[6],[7].

The opportunity to apply DIC to investigate the deformation and stress-strain properties across a simple benchmark weldment was provided by the NeT TG4 project. NeT is the European Network on Neutron Techniques

Standardization for Structural Integrity, which was established in 2002 to develop experimental and numerical techniques and standards for the reliable characterisation of residual stresses in structural welds. The network operates by creating a dedicated Task Group (TG) for each problem being tackled. Task Group 4 (TG4) was formed to develop and manage round robin studies examining an austenitic stainless steel 3-pass slot weld test specimen [8]. An important objective of the TG4 project was to characterise the role of cyclic hardening in the evolution of residual stress in multi-pass stainless steel welds, as this information can be used to help optimise and validate material constitutive models used weld residual stress computation mechanics [6]. Application of the DIC technique to cross-weld samples extracted from the test weldment offered the potential to map the stress-strain properties in the weld metal, heat affected zone (HAZ) and parent material of a TG4 round robin test specimen.

3.2 Test Specimens

A weldment for testing (component ID100001) was supplied to the Open University by the NeT TG4 project. The base plate material was made from AISI type 316L (N) austenitic stainless steel with the chemical composition given in Table 3.1. The dimensions of the base plate were 194 mm long, 150 mm wide and 18 mm thick as shown in Figure 3.1. Prior to welding, a slot 80 mm long and 6 mm deep with a bottom radius of 4 mm and side-wall angles of 20° was machined by milling, giving a ~10 mm width on the top surface (Figure 3.2) [9]. The plate was solution heat treated, after machining the slot, in order to relieve any residual

stresses introduced by fabrication. The procedure was (1) heat at 5°C/minute to 1050°C, (2) hold at 1050°C±10°C for 45 minutes and (3) furnace cool to 300°C. The test weld was made by depositing 3 weld passes in the slot, using an automated Tungsten Insert Gas (TIG) welding process. The detail of welding parameters are summarized in Table 2 [9].

Figure 3.1 also shows the x-y-z coordinate system of the plate material. The origin is located in the centre of the top surface. The value of x corresponds to the transverse distance, in millimetres, from the weld centre-line (i.e. perpendicular to the weld line). y = 0 corresponds to the top surface of the plate and is defined positive in the plate thickness direction. The welding direction (longitudinal) corresponds to the +z direction with the centre of the weld being at z = 0, thus the slot on the surface starts z = -40 and ends z = 40 in this coordinate system.

Five samples for DIC tensile testing were cut from the supplied TG4 weldment, by Electric Discharge Machining (EDM). The specimen design dimensions are given in Figure 3.3, the gauge length is 70 mm, the width at the gauge section is 6 mm and the nominal thickness is 2 mm. This design was determined by referring with the ASTM E8/E 8M -08 Standard Test Method for Tension Testing of Metallic Material [10]. In previous work, this design was chosen and checked through finite-element analysis [7], which indicated this specimen design is adequate for this test work.

The specimens were cut centred at z = ±10 mm positions in the plate, shown in Figure 3.4. The position of z=0mm was used for a deep hole drilling residual stress measurement. Two set of 5 specimens were cut avoiding this centre location

from 10mm each, set A and B are shown in this Figure. Set A was used for this experiment. The top three specimens coincided approximately with weld passes 1, 2 and 3. Each specimen was oriented with the 6 mm dimension parallel to the top surface. A photograph of the machined tensile specimens is shown in Figure 3.5 with details of their locations relative to the top surface. The actual thickness and width of each specimen are recorded in Table 3.3.

3.3 Experimental Procedure

An Instron screw-driven tensile testing machine was used for these tests with a calibrated 30 kN capacity load cell. Specimens were held via universal joints with wedge grips. The specimen alignment was confirmed that its straightness of setting by the vertical laser beam. An extensometer was clipped on the rear of a specimen, centred to span the length (25mm) of extensometer. The cross head speed of the tensile test machine was set to 0.2 mm/min (nominal strain rate of 0.008/min) giving an estimated test time of 5 hours (based on an assumed fracture elongation of 50%). All tests were run until the specimens ruptured.

The major advantage of the DIC measurement method is its ability to quantify the local deformation in a non-uniform material from which spatially resolved stress-strain properties can be determined (see Chapter 2.3). A single tensile test can provide several hundred uniaxial stress-strain curves along the gauge length and thereby can quantify the local variation in tensile properties across a weldment. Displacements during a tensile test are calculated from a set of

digital images of the gauge length surface taken at regular intervals during deformation. Computational algorithms are used to track the local deformations from grey value patterns in the sequence of digital images of the test surface. The image gray scale value corresponds to the intensity of light reflected by the surface of the specimen.

DIC measurements require an appropriate digital camera and computer analysis software. In this experiment, the commercial imaging correlation software, Davis [11] and a digital SLR camera (Nikon D300), with a sensor size of 4,288 x 2,848 pixels (12.3 Megapixels) and a 200 mm macro lens were used. A high contrast speckle pattern is essential to facilitate pattern recognition and production of accurate results. A DC fibre-optic light source was used to illuminate the specimen surface which was prepared by EDM, this system produced sufficient contrast for the DIC measurements.

In this experiment, the camera was focused on approximately one half of the gauge length including the weld section in order to better resolve the deformation in the weld region and HAZ, see Figure 3.6. Using a field of view length of 50 mm, the camera and lens were set up to give a pixel size of 9 ~ 12 μm and corresponding speckle size in the order of 30 ~ 40 μm which is sufficient to obtain accurate results (see Chapter 2.3).

3.4 DIC Analysis Procedure

Details of the DIC analysis method used in the present work will be discussed in Chapter 4.6, so only a brief overview of the procedure is provided

here. Images were taken every 10 seconds in the elastic region and then at a reduced frequency of every 40 seconds until the specimen ruptured. Nikon's software, Camera Control Pro [12], was set to take each raw image with time intervals controlled by Time- Lapse Photography during the tensile test. The images were recorded in 48 bit RGB format and converted to 8 bit gray scale using Corel-Draw software [13]. The converted images were imported into the DIC analysis software, DaVis [11].

Imported images were corrected for rigid body rotations and translations using functionality in the DaVis DIC software. The centre of the extracted gauge area of the first image was taken as a reference to correlate and correct all images. The specimen gauge area was cropped from the camera image to calculate the full field of the displacement map and then the strain distribution. The extracted work space was divided into small subsets and a cross-correlation algorithm was applied to each window. Once the peak position was computed by the correlation function, the displacement vector was determined from the distance between each subset centre point. Appropriate parameter settings were selected, multi-pass, decreasing window size started 128 x 128 pixels with 50%, 2 iterations overlap then 64 x64 pixel with 6 iterations for this experiment. The detail of DIC analysis parameters will be explained in Chapter 4.6. According to the pixel size (9 ~ 12 μm), one subset size obtains approximately 0.6mm each. 8 subsets were obtained across the specimen width (note: both sides edged subsets were eliminated), and averaged. Due to the camera's focus, approximately 65 subsets were obtained along the gauge length, thus 65 stress-strain curves can be created by one test.

The displacement results calculated by the DIC software were exported into the general purpose analysis software Matlab [14]. A script programme [15] was used to determine strains by differentiating seven point displacement data (the detail will be explained in Chapter 4.6). Stress-strain curves for each subset were averaged across the width of the gauge length and the gradient of the linear elastic region of the curve identified. A linear straight line was fitted to the data points in the elastic region and the elastic range defined by user input in minimum and maximum stress values of this straight line within elastic region. This linear line was offset to 0.2% and 1% strain, which enabled the 0.2% and 1% proof stress properties to be determined from intersection points of the offset elastic lines with the DIC measured stress-strain curves.

3.5 Test Results

Photographs of the ruptured specimens are shown in Figure 3.7. Specimen 1, which includes the last pass weld metal near the top surface, failed in the weld metal with only 25% elongation. The other specimens ruptured in the parent material at higher elongations. The measured tensile properties (0.2% and 1% proof stress data and elongation) for positions x = 0, 4, 8 and 12 mm from all the tests are summarised in Table 3.4. The top surface of each specimen (y = 0, 2, 4, 6, 8 mm) was measured using DIC. It is reasonable to assume that the deformation measured at this surface is representative of the average through thickness properties of the specimen (i.e. at y = 1, 3, 5, 7 and 9 mm).

Figure 3.8 shows an evolution of DIC images, strain vectors and contours maps at elastic region, plastic region and final from last images, results is from top position test, specimen ID 1.

Figure 3.9 shows a map of the measured yield stress (0.2% proof stress) across the weldment. This map was created by combining results from specimens 1 to 4 and half the gauge length of specimen 5. The tolerance along the x- axis direction in creating this plot was ±1 mm. Figures 3.10 to 3.14 plots the spatial variation in measured 0.2% and 1% proof stress properties across the weldment. Figure 3.10 shows how the yield strength peaks at two locations around the fusion boundary. The effect is less pronounced at y = 3 mm (Figure 3.11) and y = 5 mm (Figure 3.12). The highest yield properties are evident near the root of the weld at y = 5 mm (Figure 3.12) and 7 mm (Figure 3.13). Figures 3.15 and 3.16 compare the 0.2% and 1% proof stress results from the 5 specimens with each other and illustrate how the properties in the weldment vary with depth from the top surface of the specimen. The maximum yield strength stress in the whole region is located in the region of the first weld pass. Work hardening increases the strength of the austenitic stainless steel. From a metallurgical point of view, welding can modify the microstructure of the base metal when work hardening occurs, which increases the kinetic of precipitation of carbides in austenitic stainless steel. Hence, welding causes a variation of the mechanical properties [7]. Smith et al [6]carried out the finite element simulation of this three-pass groove-weld and single-pass specimen optimizing a mixed hardening constitutive model. Their isotropic-kinematic mixed model was capable of correctly modelling the cyclic response of

the multi-pass weld metal, showing that the initial stress-strain properties of deposited weld metal have high yield strength which cyclically hardens in multi-pass weld metal. Our results supported this evidence which also suggests that deposited weld beads have cyclically hardened previously deposited weld metal. Furthermore, the location around the fusion boundary, adjacent heat affected zone (see Figures 3.10 to 3.16) indicates higher proof stress. The base metal near the fusion boundary may be strain hardened as a result of the thermo-mechanical cycles and restraints during welding.

Figures 3.17 and 3.18 show weld centre-line (x = 0 mm) stress-strain curves for material at depths y = 1, 3, 5 and 7 mm. The y = 1, 3 and 5 mm results come from specimens 1, 2, 3 containing the third, second and first weld beads respectively and represent the average properties through the thickness of each specimen. The local stress-strain curve was chosen to include a subset region with the required points (e.g. x = 0, y = 1 mm). Figure 3.19 compares the stress-strain curves at various depths on the weld centre-line with each other directly. The highest local 0.2% yield stress of about 370 MPa was found at y = 5 mm and 7 mm, which corresponds to the root of the weld. In contrast the lowest 0.2% yield stress of 273MPa was found near the surface at y = 1 mm. These results again show that the yield stress increases with depth and suggests that successive weld passes have cyclically hardening previously deposited weld metal.

Figures 3.20 and 3.21 illustrate how the stress-strain curves vary near the surface (y = 1 mm), with increasing distance, x, from the weld centre-line. The 0.2% proof stress is lowest (273MPa) at the weld centre-line and increases to 327

MPa at x = 8 mm in the HAZ, that is an increase of about 50 MPa. This location is near the fusion boundary in the weld (x = 6 mm) where the specimen eventually ruptured. These measurements imply that the welding cycles have introduced work hardening of the surrounding parent material, as previously observed by Acar [7] in thin section Type 316H stainless steel tube welds using multiple measurement techniques. Spatial varying stress-strain data for weldments are valuable information which can be used to help optimise and validate material constitutive models used in weld residual stress computation mechanics [6].

3.6 Conclusions

1. A digital image correlation method has been successfully applied to measure "in-situ" the spatial variation in deformation across a 3-pass Type 316 stainless steel weldment during a tensile test at room temperature. A series of stress-strain curves, each based on a gauge area of 0.6 mm by 50 mm, were determined from the recorded deformation history showing the variation in yield properties along the length of the specimen in parent material, the HAZ and weld metal.
2. Measurements were carried out on 5 test specimens, three of which sampled first, second and third pass weld metal. The yield stress (0.2%) of first pass, second pass and third pass were 370 MPa, 329 MPa and 273 MPa at the weld centre line respectively. The first pass weld metal, at the bottom of the groove,

had a significantly higher yield stress, probably owing to accumulated work hardening associated with the deposition of subsequent weld passes.

3. The yield stress was observed to increase with increasing transverse distance from the weld centre-line peaking in the HAZ adjacent to the fusion boundary implying that the welding cycles had introduced work hardening of the surrounding parent material.
4. Measurements of location dependent stress-strain properties allows the consequences of cyclic hardening associated with multi-pass welding to be observed and mapped. This information can be used to help optimise and validate material constitutive models used in weld residual stress computation mechanics.

3.7 References

[1] M.Hofmann and R.C.Wimpory, "NET TG1: Residual stress analysis on a single bead on a steel plate using neutron diffraction at the new engineering instrument 'STRESS-SPEC'," *International Journal of Pressure Vessle and piping*, vol. 86, pp. 122–125, 2009.

[2] P.J.Bouchard, "The NeT bead-on-plate benchmark for weld residual stress simulation," *International Journal of Pressure Vessels and Piping*, vol. 86, pp. 31–42, 2009.

[3] M.Turski and L.Edwards, "Residual stress measurement of a 316L staunless steel bead-on-plate specimen utilising the contour method," *International Journal of Pressure Vessels and Piping*, vol. 86, pp. 126–131, 2009.

[4] X.Shan, C.M.Davies, T.Wangsdan, N.P.O'Dowd, and K.M.Nikbin, "Thermo-mechanical modelling of a single-bead-on weld using the finite element method," *International Journal of Pressure Vessels and Piping*, vol. 86, pp. 110–121, 2009.

[5] M.C.Smith and A.C.Smith, "NeT bead-on-plate round robin: Comparison of residual stress predictions and measurements," *International Journal ofPpressure Vessels and Piping*, vol. 86, pp. 79–95, 2009.

[6] M.C.Smith, P.J.Bouchard, M.Turski, L.Edwards, and R.J.Dennis, "Accurate prediction of residual stress in stainless steel welds," *Computational Materials Science*, vol. 54, pp. 312–328, Mar. 2012.

[7] Murat.Acar, "Effects of plastic strain history on the properties of stainless steel boiler tube welds," PhD thesis,The Open University, UK, 2011.

[8] R.V.Martins, C.Ohms, and K.Decroos., "Full 3D spatially resolved mapping of residual strain in 316L ausyenitic stainless stell weld specimen," *Material Science and Engineering*, vol. A527, pp. 4779–4787, 2010.

[9] J. A. Francis, M. Smith, and A. C. Smith, "Protocol for the Manufacture of a Three-Pass Slot Weld Specimen in Austenitic Stainless Steel:NeT-TG4:Procedure for Specimen Manufacture."

[10] "ASME E8/E 8M-08 Standard Test Method for Tensile Testing of Metallic Materials." 2008.

[11] "Strain Master, LaVision GmbH, Anna-Vandenhoek-Ring 19 Gottingen Germany."

[12] "Nikon Camera Control Pro 2, Nikon 2011 Nikon Corporation." .

[13] "Corel PHOTO-PAINT X4, (c) 2008 Corel Corporation." .

[14] "MATLAB The Mathwork Inc3 Apple Hill Drive Natick, Massachusetts 01760 USA." 2012.

[15] M.O.Acar., S. Gungor., S. Ganguly., P.J.Bouchard, and M. E. Fitzpatrick, "Variation of Mechanical Properties in a Multi-pass Weld Measured Using Digital Image Correlation," *Proceeding of the SEM Annual Conference*, 2009.

[16] I.G. Arcelor, "AISI 316L (N) plate No. 17579 Heat S1864, . Materials Test Certificate, 28 August 2006." .

3.8 Tables and Figures

Element	C	Cr	Mn	Mo	Ni	P	Si	S
wt. %	0.027	17.5	1.7	2.47	12.5	0.024	0.37	0.0002
Element	Ti	Ta	Nb	Cu	B	Co	N	Fe
wt. %	0.005	0.003	0.005	0.1	0.0005	0.04	0.072	Balance

Table 3.1 Chemical composition of Net TG4 parent AISI 316L(N) plate [16]

Parameter	Plate Material	Welding Process	Filler Wire	Arc Voltage	Welding Current	Travel Speed	Interpass Temp
Nominal specification or Values	AISI type316	TIG	AISI type316	9-11	130-170A	100 mm/min	< 80°C

Table 3.2 Summary of welding procedure [9]

Specimen ID	Specimen width (mm)	Specimen thickness (mm)
1	6.26	1.95
2	6.25	1.95
3	6.26	1.97
4	6.25	1.96
5	6.25	1.96

Table 3.3 Measured width and thicknesses of Set A DIC tensile specimens

ID	Position (mm)	x = 0mm		x = 4mm		x = 8mm		x = 12mm		Elongation %
		$\sigma_{0.2\%}$	$\sigma_{1\%}$	$\sigma_{0.2\%}$	$\sigma_{1\%}$	$\sigma_{0.2\%}$	$\sigma_{1\%}$	$\sigma_{0.2\%}$	$\sigma_{1\%}$	
1	y = 1	273	319	287	328	327	365	290	325	25
2	y = 3	329	366	339	379	298	337	264	296	48
3	y = 5	370	405	350	391	284	322	252	290	47
4	y = 7	369	405	306	353	263	298	244	273	48
5	y = 9	327	368	283	320	249	282	232	261	49

Table 3.4 Summary of measured 0.2% and 1% proof stress results in MPa

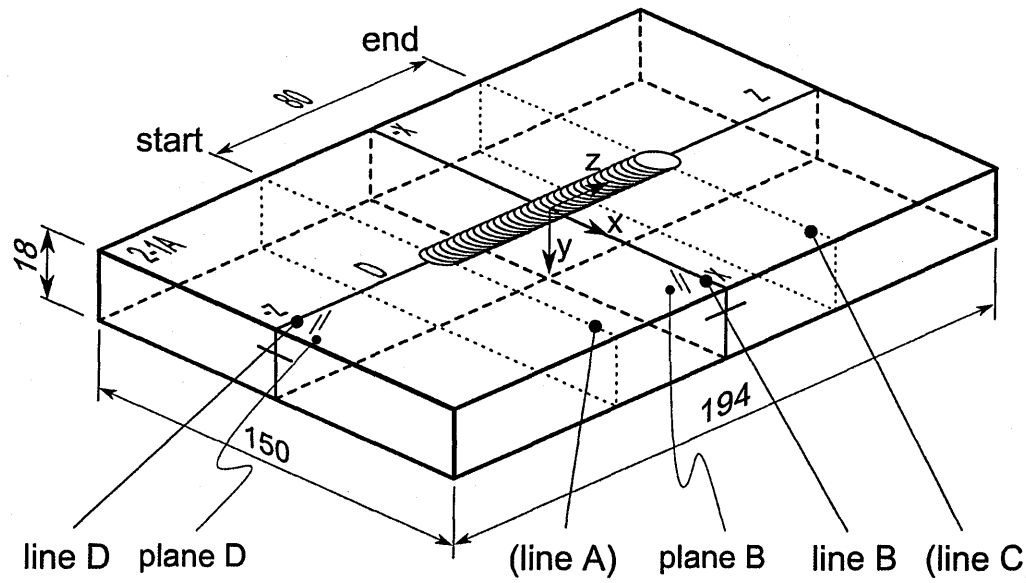

Figure 3.1 View of TG4 3-pass slot weld test specimen showing dimensions and position of weld, from [9]

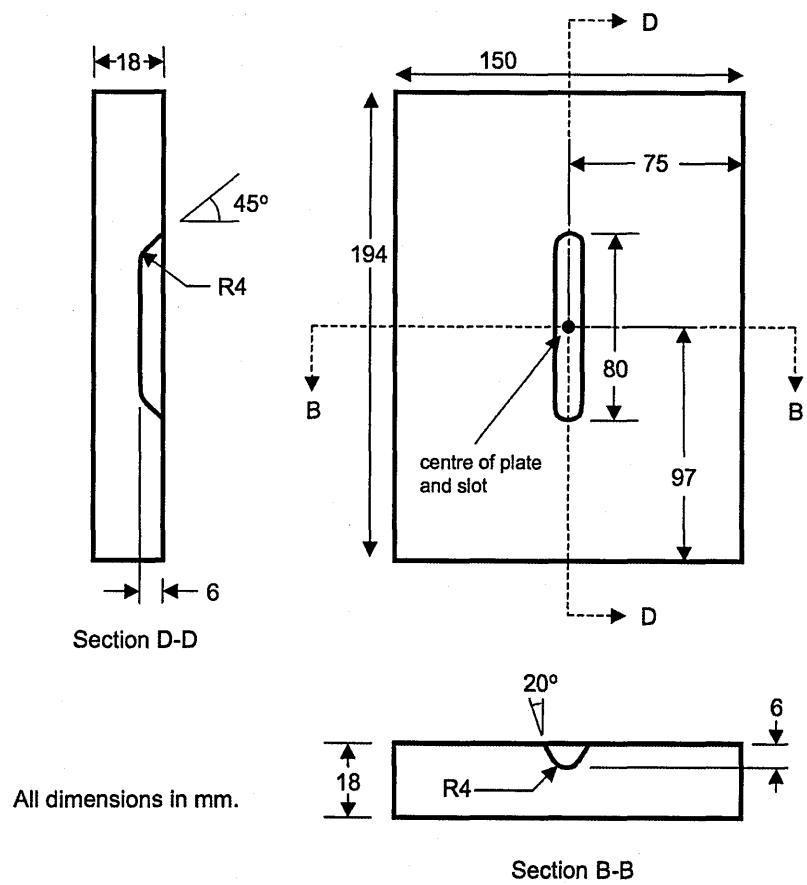

Figure 3.2 TG4 specimen dimensions and slot configuration, from [9]

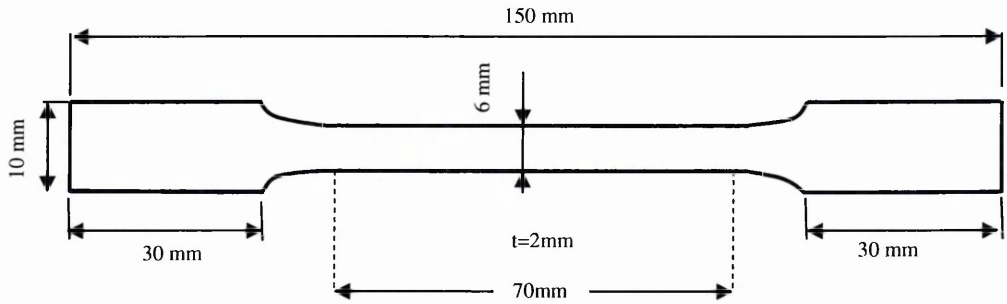

Figure 3.3 Specimen design for DIC tensile tests

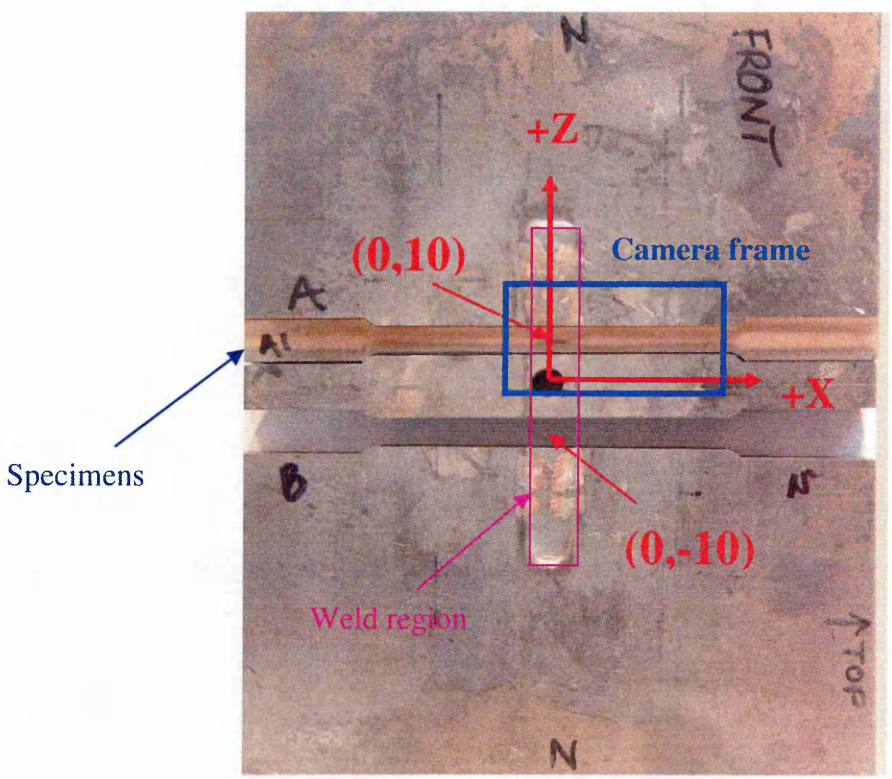

Figure 3.4 Photograph showing locations from where Set A and Set B tensile specimens were extracted

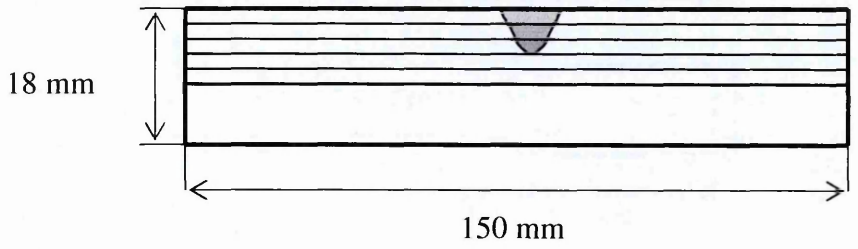

Specimen ID	Measurement surface	Average location	Description
1	y =0 mm	y=1 mm	Includes last pass weld pass (top layer)
2	y=2 mm	y=3 mm	Includes second pass weld pass (middle layer)
3	y=4 mm	y=5 mm	Includes first pass slot weld pass (bottom layer)
4	y=6 mm	y=7 mm	Heat affected zone (HAZ)
5	y=8 mm	y=9 mm	Parent material

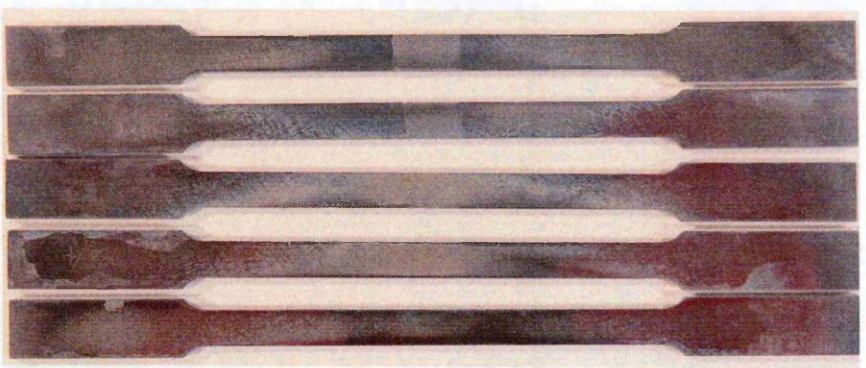

Figure 3.5 Through-thickness extraction locations of tensile specimens (top), table describing specimens and photograph showing plan view of machined test specimens (bottom)

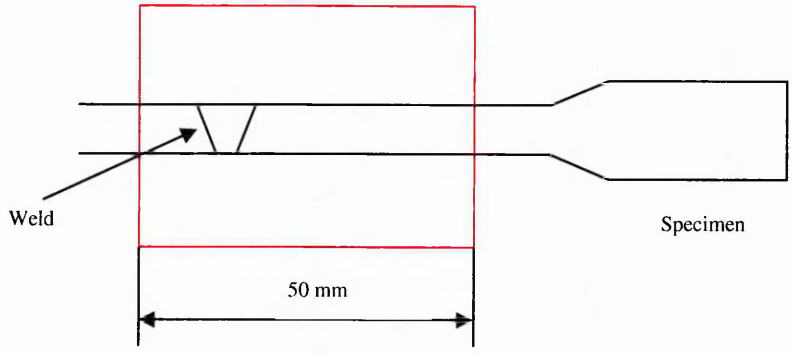

Figure 3.6 Sketch showing DIC measurement window

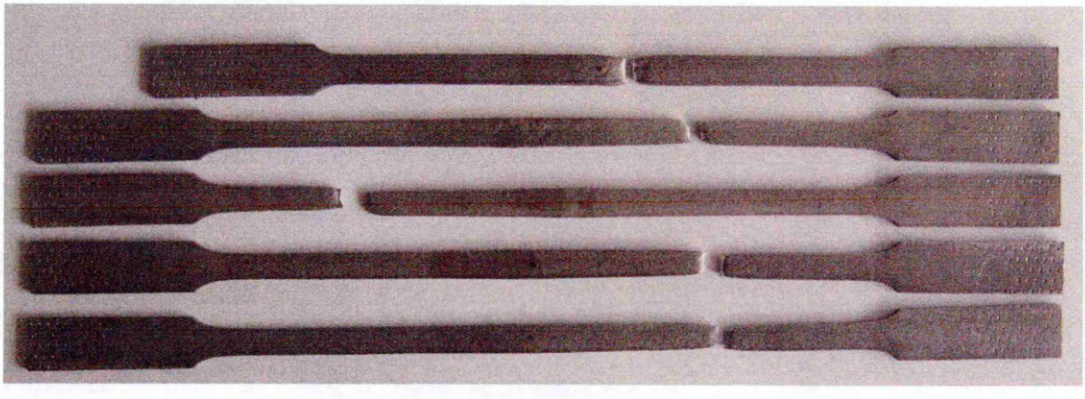

Figure 3.7 Photograph showing locations and approximate elongation of ruptured DIC tensile test specimens

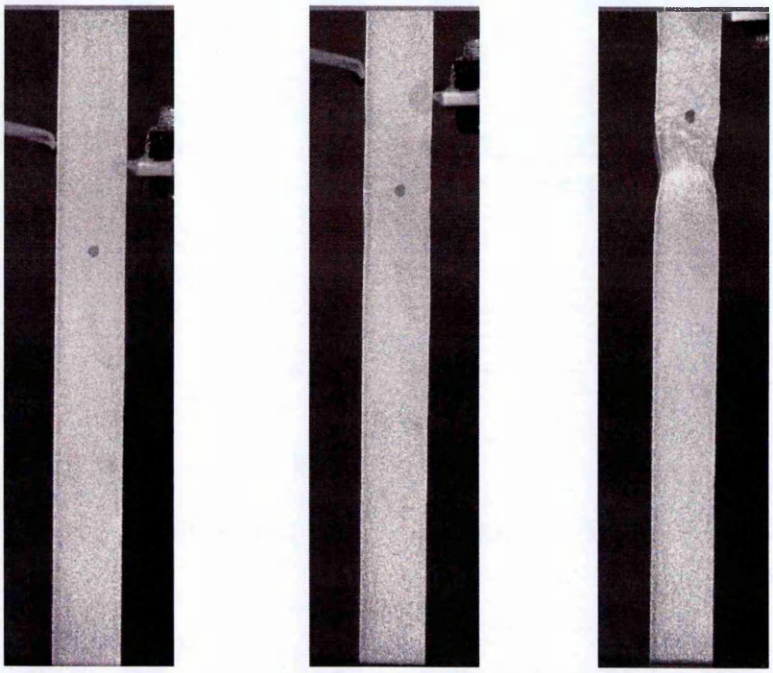

(a) Elastic region (b) Plastic region (c) Last

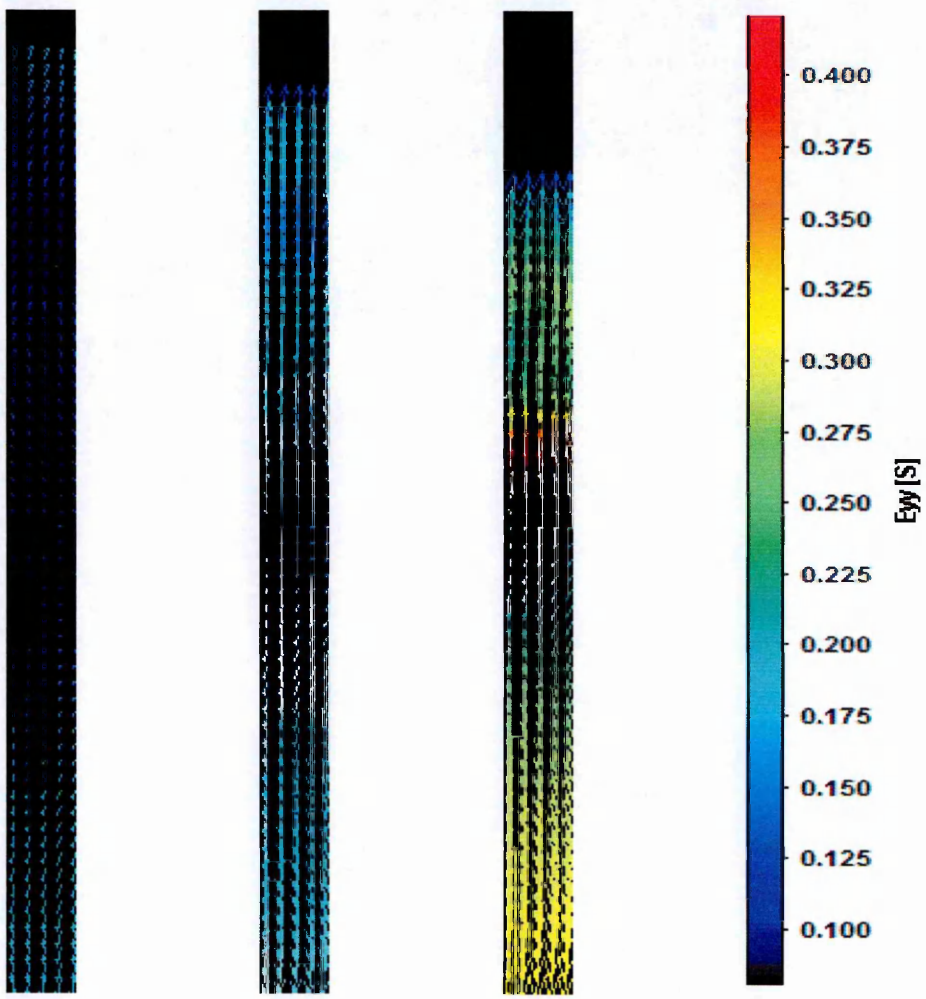

(a) Elastic region (b) Plastic region (c) Last

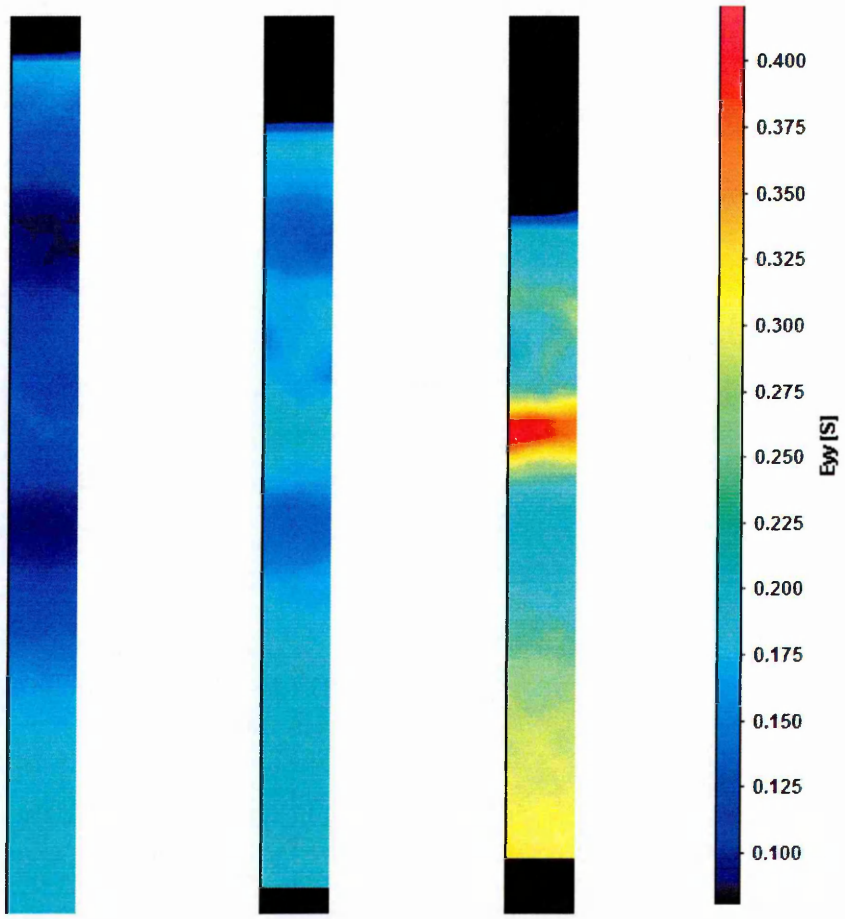

(a) Elastic region (b) Plastic region (c) Last

Figure 3.8 Example of DIC test images, strain vectors and contour maps at different stages from top position test (specimen 1)

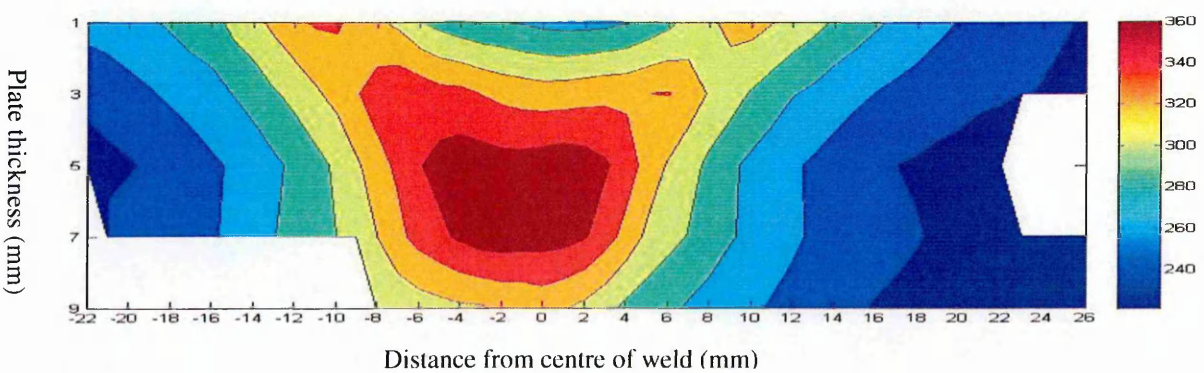

Figure 3.9 Map of the measured yield stress (0.2%) across the weldment, Distance from centre of weld (x-axis) vs plate thickness (y-axis) (the tolerance in the x-axis positioning is about ±1 mm).

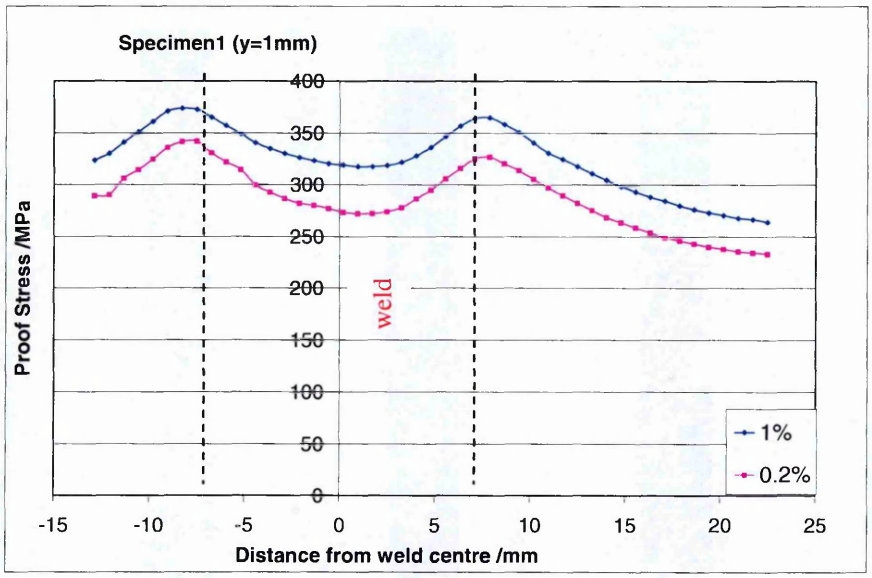

Figure 3.10 Variation in measured 0.2% and 1% proof stress along the top surface gauge length of specimen 1 (properties averaged across the specimen at y = 1 mm)

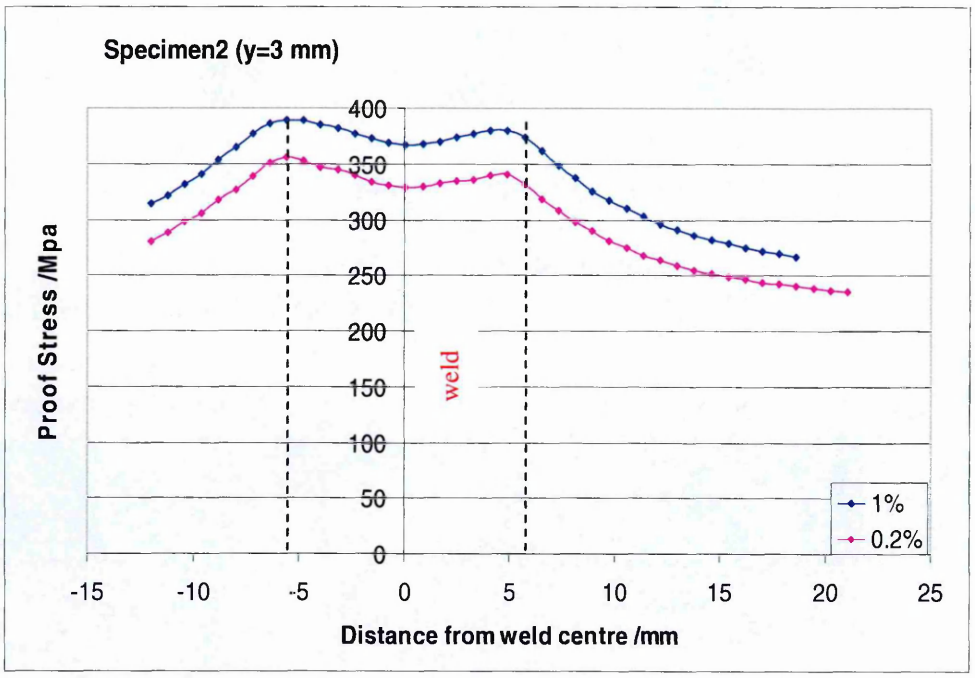

Figure 3.11 Variation in measured 0.2% and 1% proof stress along the top surface gauge length of specimen 2 (properties averaged across the specimen at y = 3 mm)

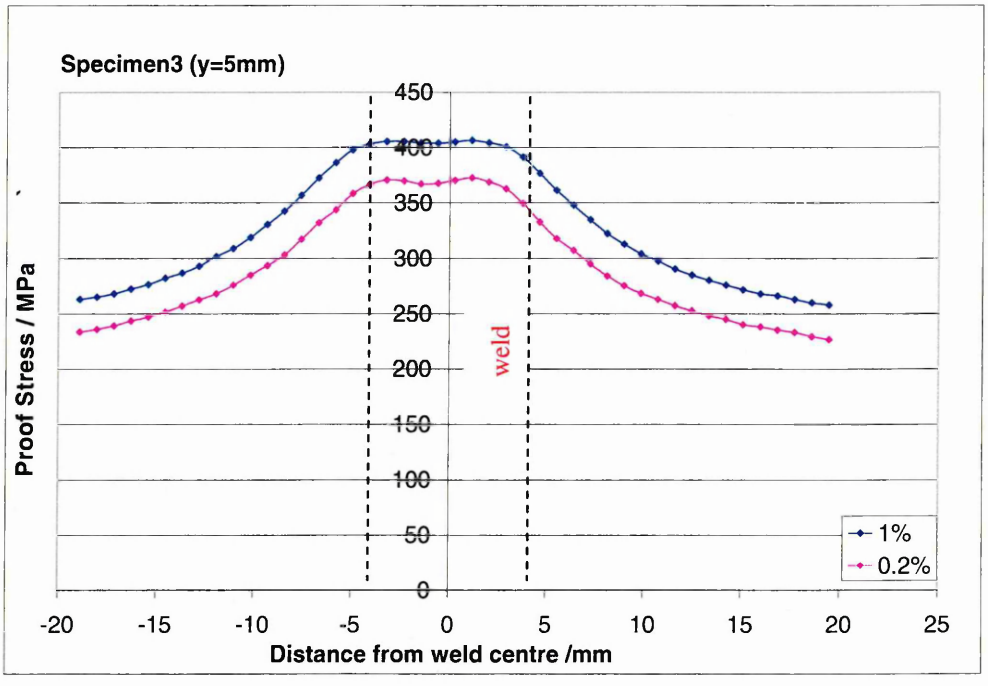

Figure 3.12 Variation in measured 0.2% and 1% proof stress along the top surface gauge length of specimen 3 (properties averaged across the specimen at y = 5 mm)

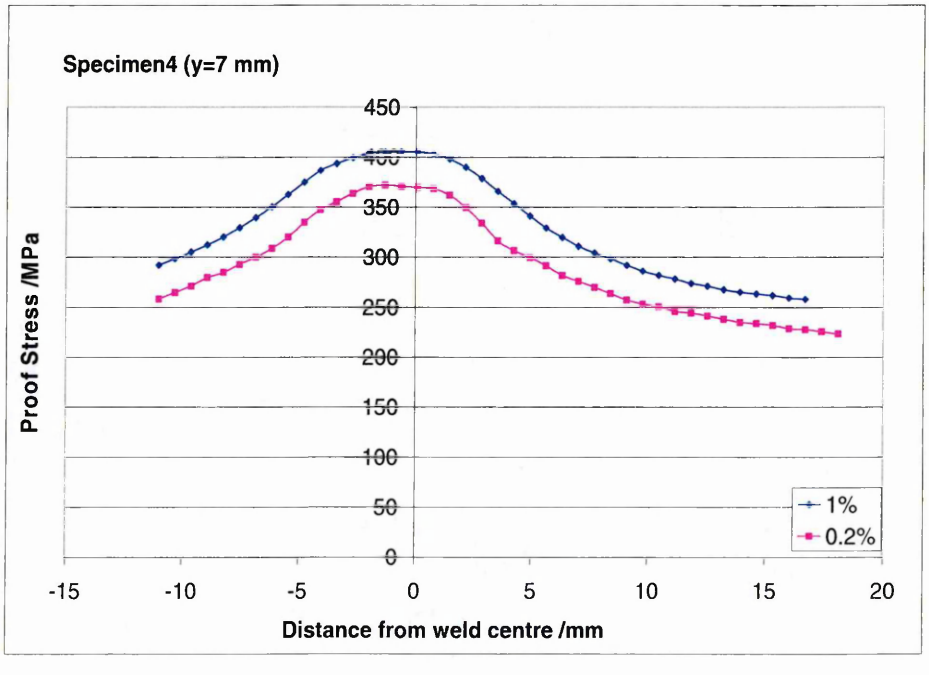

Figure 3.13 Variation in measured 0.2% and 1% proof stress along the top surface gauge length of specimen 4 (properties averaged across the specimen at y = 7 mm)

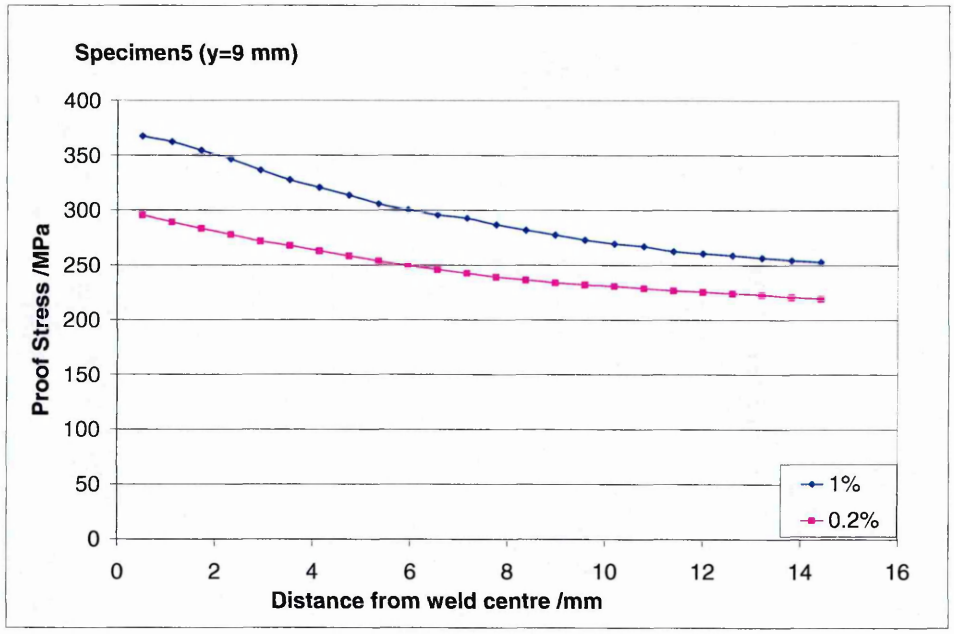

Figure 3.14 Variation in measured 0.2% and 1% proof stress along the top surface gauge length of specimen 5 (properties averaged across the specimen at y = 9 mm)

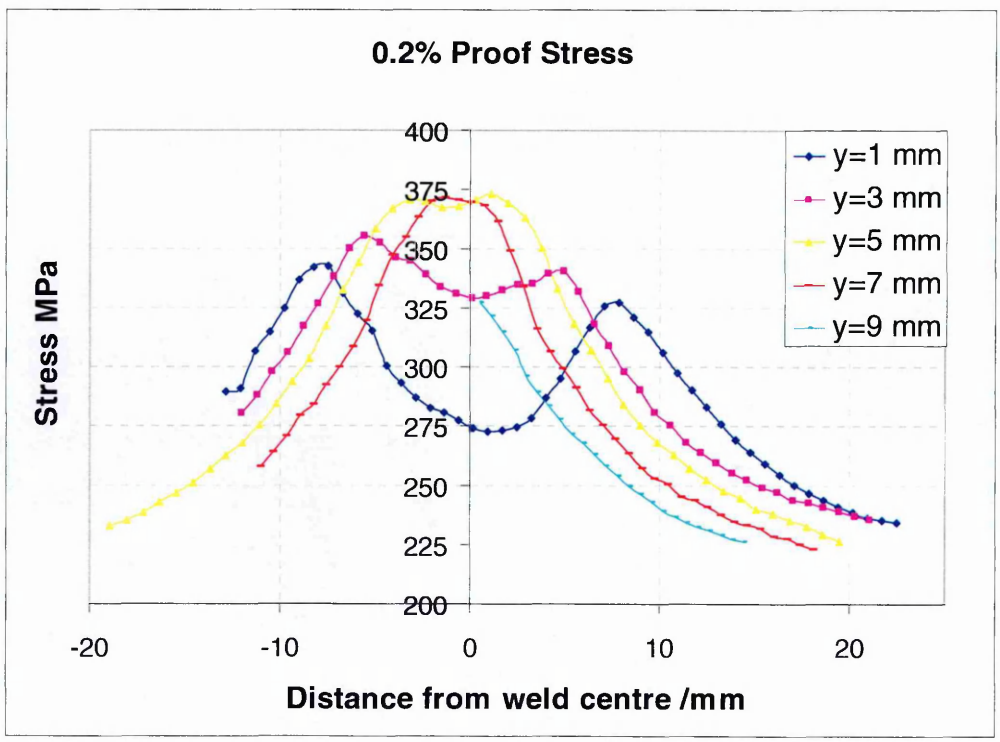

Figure 3.15 Comparison of measured 0.2% proof stress across the top surface gauge length of specimens 1 to 5 (average properties at y = 1, 3, 5, 7, 9 mm)

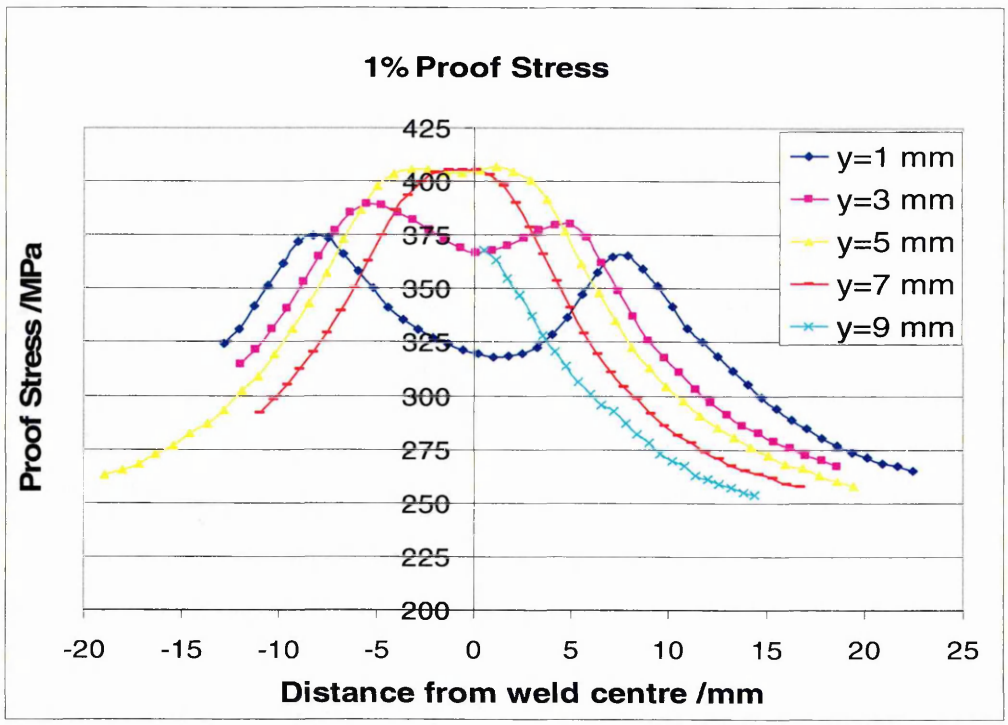

Figure 3.16 Comparison of measured 1 % proof stress across the top surface gauge length of specimens 1 to 5 (average properties at y = 1, 3, 5, 7, 9 mm)

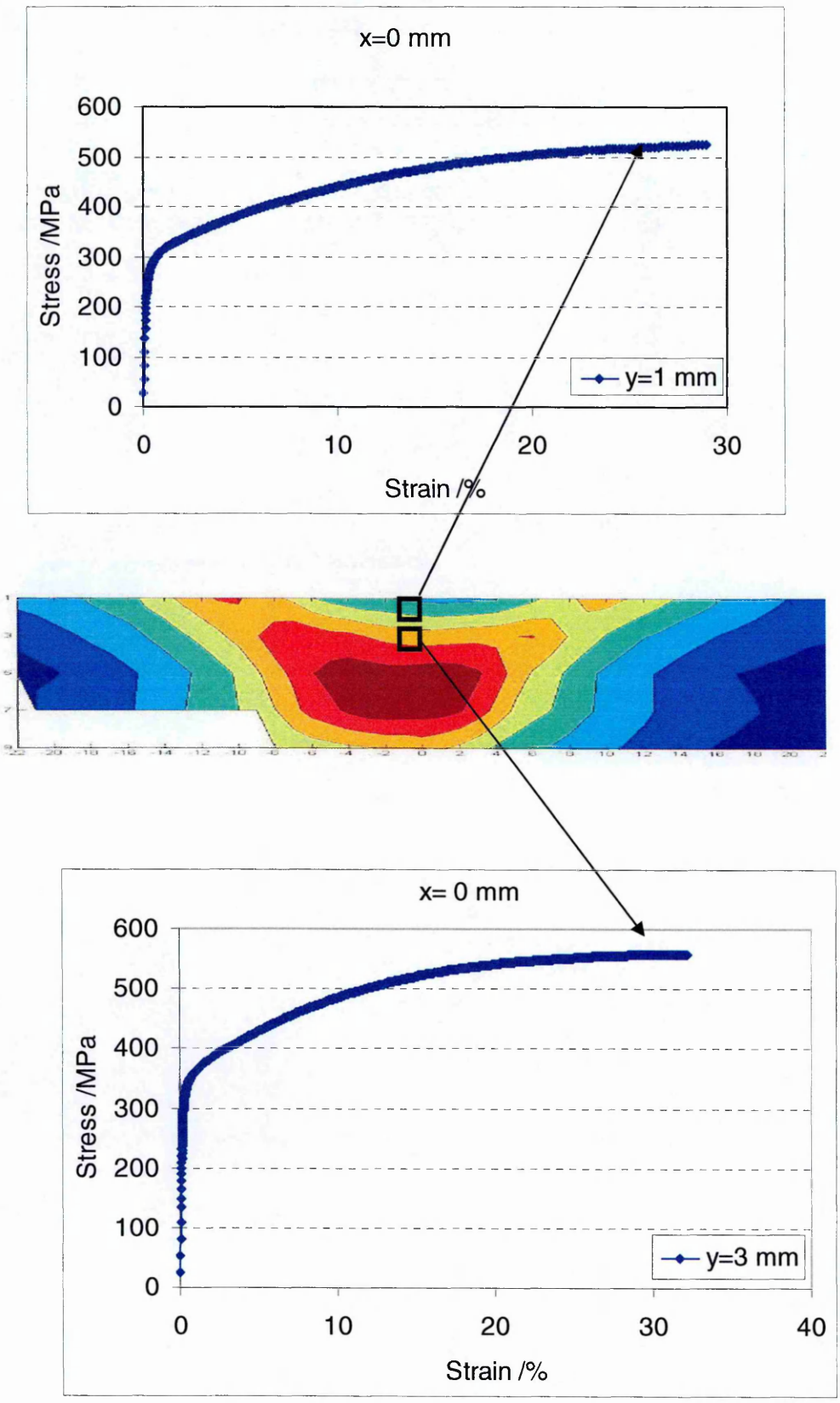

Figure 3.17 Comparison of weld centre-line (x = 0 mm) stress-strain curves at average locations y = 1 mm (top) and y = 3 mm (bottom).

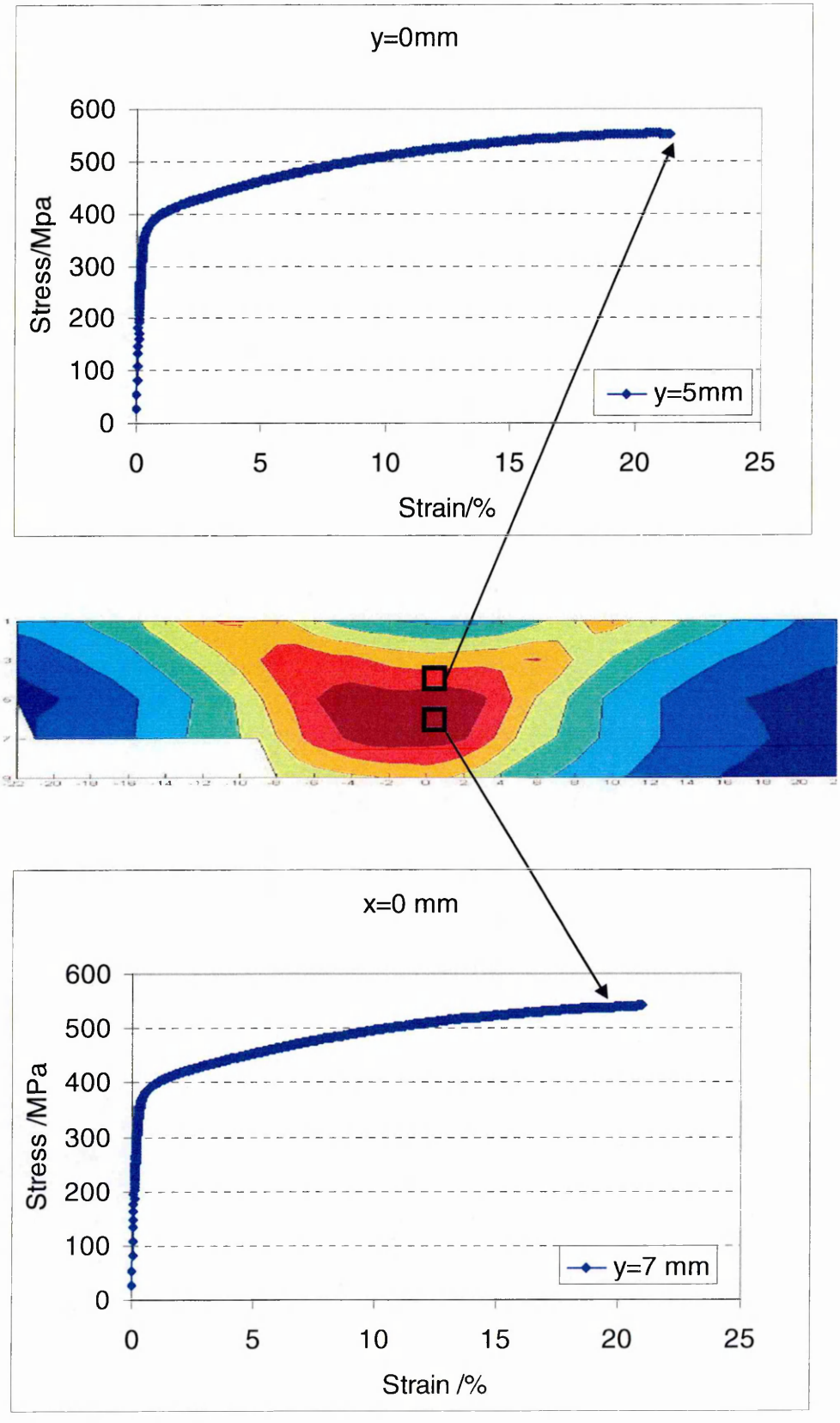

Figure 3.18 Comparison of weld centre-line (x = 0 mm) stress-strain curves at average locations y = 5mm (top) and y = 7mm (bottom)

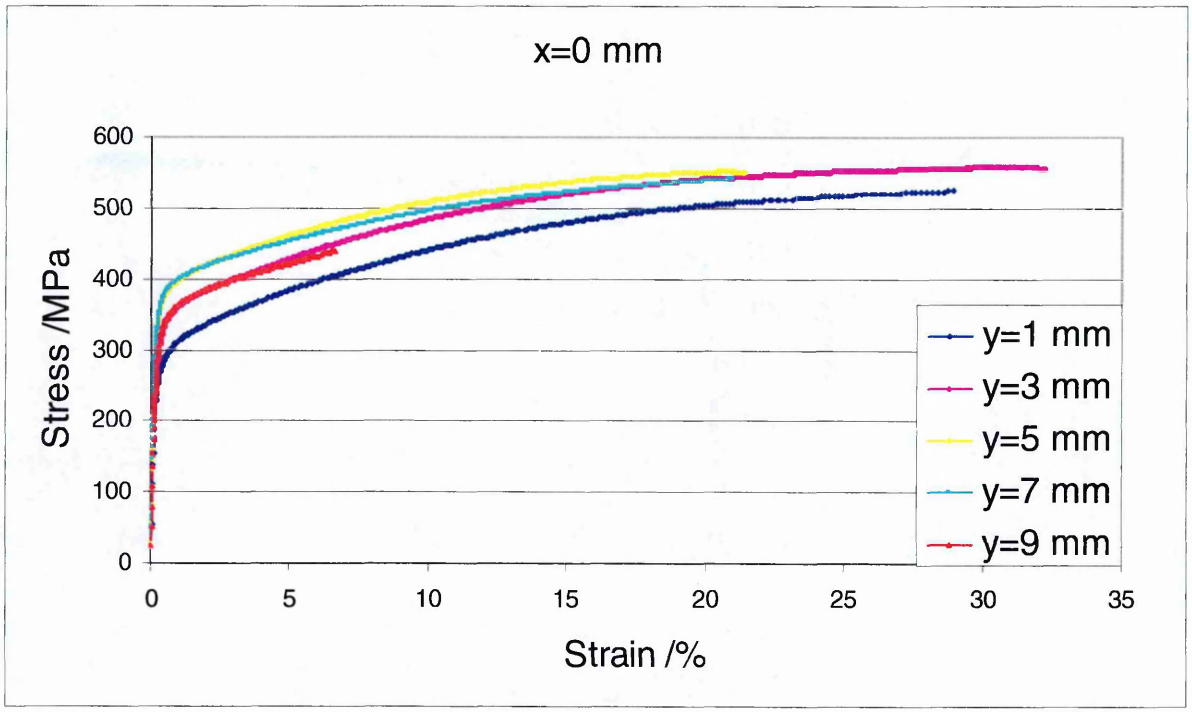

Figure 3.19 Comparison of measured stress-strain curves at the weld centre (x = 0 mm) corresponding to average depths y = 1, 3, 5 7, 9 mm

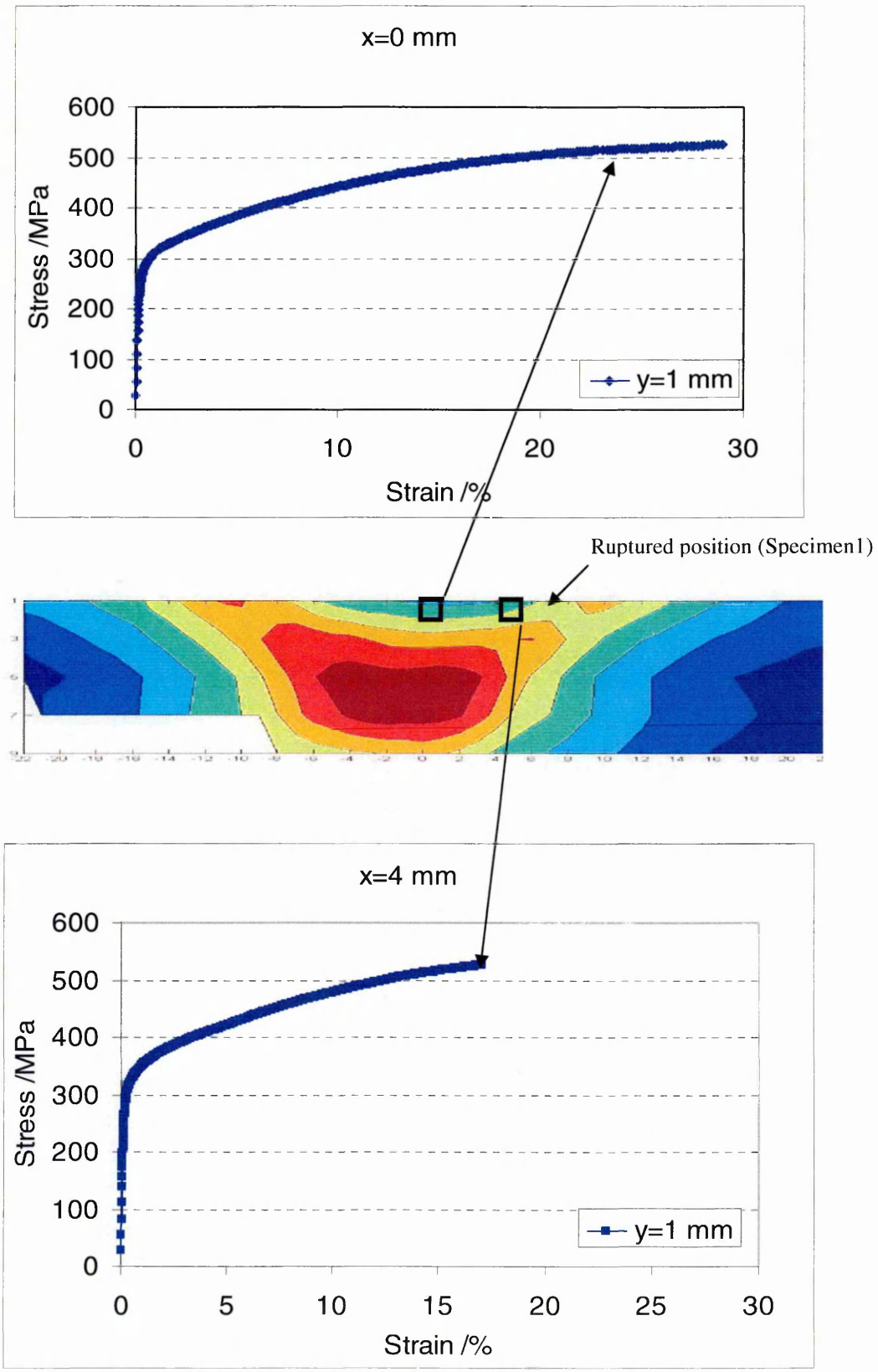

Figure 3.20 Comparison of near surface (y = 1mm) stress-strain curves at x = 0 mm (top) and x = 4 mm (bottom)

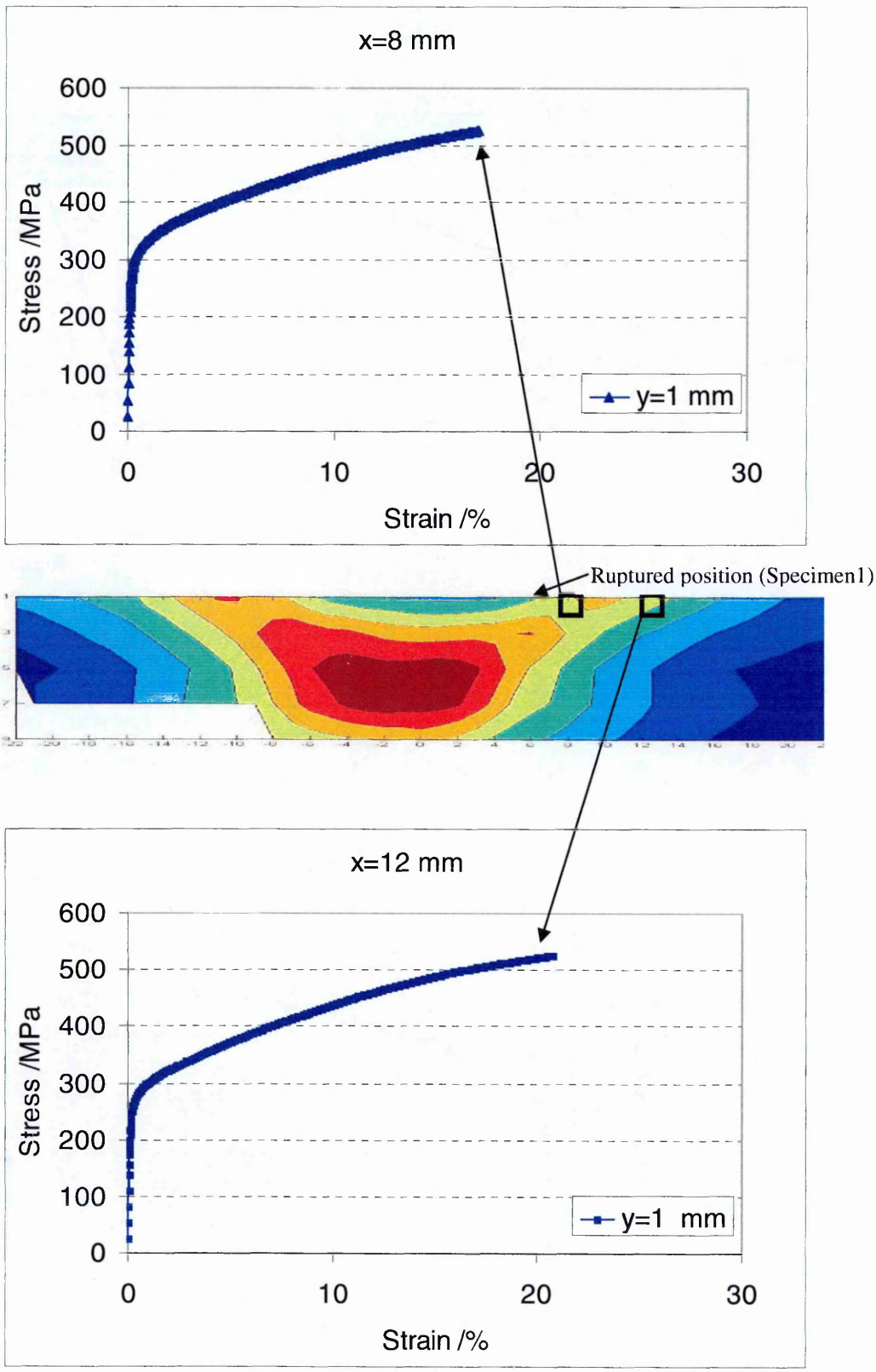

Figure 3.21 Comparison of near surface (y = 1 mm) stress-strain curves at x = 8 mm (top) and x = 12 mm (bottom).

Chapter 4

Development of a High Temperature DIC System

A high temperature strain measurement system using DIC has been developed in this study. The use of DIC at high temperature is not straightforward mainly due to the difficulty with the acquisition of stable and consistent images. In this chapter, the details of a system that was developed for the measurement of full field deformation of cross-weld specimens are presented. The factors affecting the measurement accuracy are described and the techniques developed to obtain reliable measurements are discussed.

4.1 Factors Affecting High Temperature DIC Measurement

In the application of DIC at elevated temperatures, three main issues need to be overcome to obtain stable images with suitable contrast. These are: (1) the degradation of specimen surface due to oxidation, (2) constant illumination of the sample surface, and (3) image distortion caused by thermal currents between the specimen surface and the camera lens. These are discussed below.

4.1.1 Surface Oxidation

The accuracy of the measurements by the DIC technique relies on the constancy of the image contrast and speckle patterns, as discussed in Chapter 2.3. However, a creep test is carried out at elevated temperature for a long period and the appearance of the specimen surface is likely to change due to oxidation. This oxidation is the critical issue for creep strain measurement at high temperature using DIC. Although many experiments have been demonstrated at high temperature using optical systems in previous works [1][2][3][4][5], there has been no report of strain measurements at high temperature for a long-term creep test.

The oxidation changes the surface texture of the sample and so does the speckle pattern in the image. The image intensity, brightness and contrast reduce over time at elevated temperatures and the appearance of the speckle pattern changes. In order to apply DIC and achieve accurate results, sufficient numbers of speckles in a subset are required to track the displacement of the surface. A good quality initial image is essential and the image quality has to be sustained until the end of a long-term creep test. For this purpose, it is necessary to create a stable speckle pattern by applying paint. VHT Flame coating [6] was chosen for this experiment. VHT is a silicon ceramic based paint that has been tested as stable up to 1093°C [9]. Preparing a surface with VHT requires a curing cycle for 30 min each at 121°C (250°F), 204°C (400°F) and 315°C (600°F). Figure 4.1 shows a comparison of the specimen surface at 650°C after 1 day and after 7 days. After 1 day in the furnace the sample surface has more contrast than after 7 days as the speckle pattern is fading.

Figure 4.2 shows the image of painted specimen surface after the paint durability test. The sample was put in the oven at 600°C degrees for 5 months. Although oxidation occurred, majority of the coating still stayed on the surface and the image contains good contrast, which has sufficient detail for DIC pattern matching. Besides, the degradation was slow, which meant that the DIC correlation was possible between subsequent images, although the correlation with the first image was not. So, applying the coating on the specimen surface prevents surface oxidation sufficiently and allows a long-term creep test to be performed.

4.1.1.1 Accuracy Test of Surface Coating at Room Temperature

When a test is conducted using a speckle pattern produced using paint, it is important to take into account the effect of measurement accuracy. Using paint to produce a speckle pattern can also provide a surface coating that prevents oxidation on the specimen at elevated temperatures. The image of an unprepared EDM cut surface can be used for DIC experiments at room temperature, creating a speckle pattern under white-light illumination. The speckle size and regularity on the surface affects the accuracy of the DIC computation. The speckle pattern (size and number of each subset) and contrast are important to consider. As described previously, image subsets with a smaller speckle size and larger number of speckles in one subset give us more information to correlate. The number of speckles in a subset can be increased by increasing the subset size; thus a larger subset size can improve the displacement measurement accuracy. The accuracy data from Table 2.3 in chapter 2.3 is quoted by the company that provides the

software, however the texture of the image is not considered in this accuracy data, and thus there are some cases in which we may not be able to obtain this accuracy depending on the image quality.

The accuracy of image displacement is strongly related to the contrast in the intensity pattern in the image. By applying a painted speckle pattern, the contrast of the speckle pattern in the image can be improved. However, producing a small enough speckle size for many standard test sample sizes can be difficult and so the speckle size in each subset will often be larger, reducing the speckle number in each subset leading to a decreased measurement accuracy.

In this section, the accuracy of the painted image is assessed to clarify the coating effect through comparison with a natural EDM cut surface image (i.e. non-painted surface).

4.1.1.1.1. Image Histogram

The distribution of image intensity can be shown in a histogram. An image histogram plots the number of pixels for each intensity value and this graph gives useful information to judge effects of the image contrast and exposure. The image intensity value in the horizontal axis is plotted against the number of pixels present in the vertical axis. The intensity range is 0 to 255 in 8 bit gray scale, where 0 is black (dark image) and 255 is white (bright image). Figure 4.3 is an example of an image histogram. Figure 4.4 shows examples of under and over exposure image histograms. The under exposure histogram has a high pixel count towards 0 (many pure black pixels, the image is dark), the over exposure histogram has high count towards 255 (many pure white pixels, the image is light). Figure 4.5 shows

examples of over and under contrast histograms. The over contrast histogram has a wide intensity range, with high count values at 0 and 255. The under contrast histogram has zero values at both ends of the intensity range which means that the full range of grey scale is not utilized. The ideal histogram has zero pixel numbers at 0 and 255 intensity levels, the peak is not shifted to one side and the histogram curve is smooth from 0 to the left side to 255 to the right side.

Figure 4.6 shows histograms of images used in this investigation, (a) is the as-cut EDM surface and (b) is the painted surface. The non-painted image has a high count in the bright area and the intensity range is small which means that this image has low contrast. The painted image has a wider intensity range, the difference between maximum and minimum value is larger, and therefore this shows much higher contrast than the non-painted image.

4.1.1.1.2 Test Method

Two different surface preparations were tested to determine their effect on the DIC results. The surfaces were prepared using a painted speckle pattern for one and an EDM surface (non-painted) image for the other. A test was simulated by shifting the images 1 pixel movement to measure the pattern matching accuracy. The painted image was sprayed with white and black paint and a random pattern was created on the sample surface. Both images were imported to Corel Draw image software [7] and shifted using the offset function in the horizontal direction. The 1 pixel displacements were applied and images saved as translated images. The before and after translated images were imported to LaVision DIC software [8] and displacement vectors calculated. The image for DIC

analysis was extracted from a window size of 400 × 400 pixel in the centre of specimen as shown in Figure 4.7. Figure 4.8 shows both extracted images, that is from the EDM surface (without paint) and the painted surface. A 128 × 128 pixel subset size was used for this analysis and a multi-pass decreasing window size was applied. The details of parameter setting for the software will be explained in Chapter 4.6. Nine displacement vectors were calculated in this extracted image, the example is shown in Figure 4.9. The calculated displacement vectors are compared to the exact value '1' and translated in Corel draw [7] to calculate errors.

4.1.1.1.3 Results and Discussion

Table 4.1 shows the calculated displacement values and error for each subset centre when the image is shifted by 1 pixel. The vector numbers are shown on Figure 4.9. The result of the painted image shows closer values to the exact value of 1. The averaged error of the non-painted image and painted image were 7.96e-4 and 1.93e-4 respectively.

The painted image data shows smaller errors than the non-painted image owing to the image intensity pattern. The error of the movement is also associated with pixel intensity noise. Wang et al [9] reported that the measurement bias can be reduced by increasing spatial gradients in the intensity pattern, which is achievable by increasing contrast in the image. From the image histogram discussed before, the painted image contains much higher contrast than the non-painted image. Thus for these intensity patterns the improved image contrast has reduced the error in the displacement measurement.

4.1.1.1.5 Conclusion

The effect on image correlation of a painted speckle surface versus an untreated wire EDM surface has been evaluated. The painted surface image shows superior results (smaller errors) compared with the image of a non-painted (wire EDM) surface. The better image contrast contributes to higher precision in the small displacement computation. Applying paint on a sample surface also facilitates DIC measurements at high temperature by inhibiting oxidation.

4.1.2 Illumination System

One of the most important issues for performing DIC is to have sufficient light to obtain a good quality image. The illumination affects the quality of the speckle pattern; if the speckle pattern is not clear and consistent over time, this will lead to errors in the DIC analysis process. If the surface of specimen becomes specular (usually by flaking of the paint, revealing the substrate beneath) and directly reflects the light, the speckle pattern changes during the test and can no longer be assumed to be fixed to the surface of the sample. This is because the reflection will change with position relative to the illumination.

The illumination is probably the most important issue for obtaining reliable image acquisition at high temperature in a DIC test. The specimen is set inside the furnace, which has a small window (40mm×20mm) with a long tunnel (150mm) and the images are taken though this window (Figure 4.10). However, it is difficult to expose the whole of the gauge length with a conventional illumination system because the light has to reach the specimen surface through such a long tunnel.

Stability of the light source is important for a high temperature DIC system. For long-term creep tests, the light has to stay on all the time, more than three months in this case study. In the initial experiments the halogen light bulb in a fibre optic illumination unit occasionally failed during the tests, which caused loss of data. In order to solve this problem, a fibre-optic flash light system was developed for this study. A light-pulse is triggered at the same time as the camera's shutter and provides with much stronger intensity illumination on the specimen surface. Figure 4.11 shows the comparison of the continuous fibre-optic light source and the flash light source, with same shutter speed and aperture. The flash light system provides the better speckle pattern; the range of intensity values is wider from the image histogram, indicating higher contrast, and more opportunity to carry on longer tests.

Although it is not observed at the test temperatures used in this study, black body radiation may cause imaging problems at elevated temperatures up to 1100°C. When the heated sample starts to emit radiation of a wavelength that the camera is sensitive to the brightness of the captured images increases and the speckle contrast decreases. Two different approaches have been developed for this black-body radiation problem. Grant et al [1] accomplished this by suppressing black-body radiation through the use of filters and blue illumination. Thermal expansion and Young's modulus were measured and the capability of their method provided accurate DIC measurements up to 1100°C. Pan et al [5] used a high pass optical filter and an infrared heating device to enable DIC to be

performed. The full-field thermal deformation and coefficient of thermal expansion of the sample were determined using this system.

4.1.3 Thermal Current Image Distortion

4.1.3.1 The Assessment of the Thermal Current Effect

When using DIC to measure strain at high temperature, thermal convection currents between the camera and furnace can cause image distortion, which results in errors in the measurements. Different temperatures of air have different densities, which changes the refractive index of the air and so bends the light.

Lyons et al [2] conducted a series of experiments to assess the image distortion caused by thermal currents and minimized the local air convection using a fan, which homogenized the air temperature.

In order to find the extent of image distortion in the present DIC system, a simple experiment was carried out. A specimen was placed inside a furnace with no load and held at a range of constant temperatures, 100°C, 200°C, 300°C, 400°C, 500°C, 600°C and 650°C. At each temperature images were taken at 2 second intervals, 28 images were saved and analyzed using DIC imaging software [10] to calculate the displacements. Figure 4.12 is the variation of pixel displacement with time at different temperatures caused by thermal air currents.

As the temperature rises, the thermal currents increase until 600°C. The displacement error reaches its highest at 600°C, however it decreases again at 650°C. The reason is that thermal stability inside furnace relies on a balance of convection and radiation. Generally, the convection dominates inside the furnace at temperatures under 600°C and the radiation dominates over 600°C, which

suppresses thermal convection [11]. The data for using a window to cover the outside of the tunnel in the furnace clearly shows the effect of reducing the thermal currents as shown in red line in 4.12.

Figure 4.13 shows creep curves from two tests that were identical except for temperature variation along the gauge length. One has a temperature of 550°C with no temperature variation between top and bottom of the specimen gauge length (blue line), and the other test has 3°C temperature variation with the top temperature at 550 °C and bottom temperature at 547°C (red line). More scatter can be seen as a result of the temperature variation (red line), which was affected by thermal currents inside the furnace. Thus, reducing the temperature variation between the top and bottom gauge length has a significant improvement in the DIC measurement.

4.1.3.2 Fan Test and Averaged Image

A small fan was added outside the furnace window cover in order to reduce the hot air in front of the camera lens. A simple displacement measurement was conducted in order to find out the effect of the fan. A specimen was placed inside furnace with no load at a constant temperature of 550°C. Then the images were acquired every 10 seconds. Fourteen images were saved and the pixel displacements were computed between two images. One test is with a fan on and the other with a fan off. The result is shown in Figure 4.14. The blue line is the measured pixel displacement without a fan, which has error in the order of ±0.2 pixels. The displacement error with the fan is plotted in pink with an error in the order of ±0.1 pixels, which shows that there is much less scatter when a fan is

used. The red line shows the effect of averaging images. Three different images were averaged by using the commercial photo editing software (Photomatix Pro 4.0.2) [12] and the displacements were calculated by DIC in the same way as before. The displacement error is within ±0.05 pixels, which shows a considerably reduced effect from the thermal currents in the air.

4.2 Specimen Design

While measuring the creep properties of materials such as elastic-plastic-creep deformation and rupture strength, it is very important that the size and shape of the specimens do not affect the measurement results [13],[14]. In general, creep test specimens are designed with reference to international standards (for example ASTM E139 [15]). Although in creep tests, cylindrical specimens are typically used, measurement of surface deformations using DIC is best achieved with flat-surface specimens as this allows accurate images to be acquired from a single camera.

4.2.1 Initial Specimen Design

An initial design of test specimen for measurement of creep deformation using DIC was based on the ASTM E8/E8M Standard Test Method for Tensile Testing of Metallic Materials [16], as there is little published work on DIC measurement at high temperature [2],[4],[17],[3]. The initial creep test specimen geometry had a 10mm diameter shoulder, 40mm gauge length and M12 screw

end. The gauge area was machined flat to 6mm width and 3mm thickness along a 32mm long gauge length for DIC measurement as shown in Figure 4.15.

The initial specimen design was used in four pilot creep tests undertaken at 650°C. In each case it was found that the specimen ruptured at the stress concentration region around the neck position, as shown in Figure 4.16. Therefore, a 2D finite element model was developed to characterize the stress concentration near the neck and to assist in finding more suitable specimen configuration for the DIC creep tests.

4.2.2 Proposed New Specimen Design

Ideally, the creep deformation should be contained and lead to rupture in the central region of the gauge length. In order to reduce the stress concentration at the fillet, the gauge length transition radius was increased from 3.5mm to 30mm. Also the overall length of the specimen was extended to 120mm to increase the gauge length while keeping the threaded region and shoulder the same size, as illustrated in Figure 4.17. Two small holes (Diameter =2mm) were drilled at top and bottom positions, outer of gauge length which thermocouple tips were inserted to ensure good thermal contact.

4.2.3 Finite Element Analysis

Finite element analysis using the ABAQUS [18] code was undertaken to predict the location and magnitude of peak stress in the initial specimen design and to assess the reduction in stress in the new specimen design. Considering the

symmetry of the model and loading conditions, it is required to model only one quarter area of the whole specimen geometry, and as the specimen thickness is 3mm, it can be considered thin enough to be idealised by a 2D plane stress mode in the region of the gauge length. The mesh module within ABAQUS was used to create the modes using quadratic plane stress elements. The model included approximately 2000 elements. A fine mesh was applied to the corner area of specimen expected to show a stress concentration.

A temperature elastic and elastic-plastic analysis were applied to evaluate two different specimen designs. Linear elastic mechanical properties were defined for the mechanical analysis including Young's modulus and a Poisson's ratio of 159 GPa and 0.305 respectively. The plastic properties at a temperature 550°C are shown in Table 4.2. [19]. Figure 4.18 shows the mesh for the initial specimen used in this finite element model and the boundary condition. In order to simulate the applied tensile loading, symmetry boundary conditions were applied to the left and bottom edge of the geometry and a tensile load applied to the right edge. The loads were applied until the material yielded that is stress of 113MPa to the right edge for the initial and proposed designs respectively.

4.2.4 Results

Figure 4.19 and Figure 4.20 show the elastic analysis results of contour plots of predicted stresses in the tensile direction of the initial design and the new proposed design respectively. Figure 4.21 also shows the comparison along the specimen surfaces between the initial design and the new proposed design. The

results indicate the stress concentration appears near the fillet of the specimen as expected. The new proposed design reduced stress concentration considerably compared to the initial design. Figure 4.22 and Figure 4.23 show the elastic-plastic analysis results of contour plots of predicted stress with the same applied loads in the tensile direction, for initial design and new proposed design respectively. Applying the plastic mechanical properties, non-linear strain concentration effect can be seen using elastic-plastic simulation. Figure 4.24 and Figure 4.25 show the line plots of contour plot of equivalent plastic strain, initial design and new proposed design respectively. The equivalent plastic strain in a material (PEEQ) is a scalar variable that is used to present the material's inelastic deformation. The results indicate the plastic strain appears near the fillet of the specimen as we expected.

Although the maximum stress and strain still appear around the fillet, the total stress concentration has reduced and the largest strain value has significantly decreased compared to the initial specimen design.

4.2.5 Conclusion

The finite element analysis showed that the initial test specimen design had a high stress concentration area at the root of the fillet radius to the shoulders where rupture occurred. The corner radius was increased from 3.5mm to 30mm to reduce the stress concentration and this has been demonstrated by finite element analysis. The improved specimen design for high temperature DIC measurement indicated a lower risk of rupture at the end of gauge length.

4.3 Sensitivity of Creep Test to Temperature and Load

The purpose of this section is to determine the sensitivity of creep life of 316H stainless steel to temperature and stress in order to determine how closely to control the test. Creep deformation strain rates can be estimated using RCC-MR law (Design and Construction Rules for Mechanical Components of Fast Breeder Reactor Nuclear Islands) [20] introduced in chapter 2.1. Two different cases are considered a temperature dependent calculation and stress dependent calculation.

4.3.1 General Equation

In the fundamental creep general equation, the creep rate depends on temperature and stress.

$$\dot{\varepsilon} \propto f_1(\sigma) \cdot f_2(T)$$

where $\dot{\varepsilon}$ is the creep deformation rate, the function $f_1(\sigma)$ describes the variation of $\dot{\varepsilon}$ with stress and function $f_2(T)$ describes the dependence of $\dot{\varepsilon}$ on temperature (in K).

In the case of temperature dependence of creep rate, the load is constant and the creep rate changes with temperature.

$$\dot{\varepsilon} \propto f_2(T)$$

A straight line relationship can be established if plotted in the form of $\ln \dot{\varepsilon}$ and $(1/T)$; i.e.:

$$\ln \dot{\varepsilon} \propto -(1/T)$$

Thus, the rupture life decreases with increasing temperature.

The temperature dependence of creep rate can be described using the Arrehenius equation

$$\dot{\varepsilon} \propto \exp-(Q_c / RT)$$

where Q_c : activation energy, and R : universal gas constant (8.31 $Jmol^{-1}K^{-1}$)

In the case of stress dependence of creep rate, the equation is described by

$$\dot{\varepsilon} \propto f_1(\sigma)$$

at constant temperature. This form also has a straight line relationships if plotted as $\log\dot{\varepsilon}$ and $\log\sigma$.

$$\dot{\varepsilon} \propto \sigma^n$$

This expression provides the basis for power law relationships and the gradient of the plot gives the value of the stress exponent, n.

Combining expressions for the creep rate gives

$$\dot{\varepsilon} = A\sigma^n \exp-(Q_c / RT)$$

where A is a constant. This power law relationship is generally used to describe high temperature creep behaviour.

4.3.2 Creep Life Calculation at Various Temperatures

In order to predict the creep life variation with constant load at various temperatures, several creep curves were calculated with the RCC-MR law [20]. The details of RCC-MR law are described in chapter 2.1.

The creep strain vs time curve at various temperatures around a target test value of 650°C with 160MPa applied stress was calculated. The temperature

variations considered are 640, 645, 648, 649, 650, 651, 652, 655, 660°C. Some of the temperature constants were not given in Table of reference, so, these calculations used linear interpolation to define interim values.

Figure 4.26 shows the predicted creep strain vs time curves at nine different temperature variations from 650 °C with 160MPa applied stress. Table 4.3 shows the variation in time to reach 1% creep strain.

For an accumulated creep strain of 1%, it is predicted that a temperature variation of ±1°C causes 5 to 7 % change in life. In the case of a temperature variation of ±10°C, the life time range is 45% to 47%.

4.3.3 Sensitivity of Creep Life Calculation to Specimen Dimensions

The purpose of this study was to find out how sensitive the creep life is to the specimen dimensions used to calculate the stress level. When the specimen cross section area is reduced, the true stress increases, which causes the test specimen life to reduce. The same equations and the coefficients were applied to this calculation.

The nominal cross section dimensions of the test specimen being considered are 6mm× 3mm. The effect of knowing the dimensions to an accuracy of -0.1mm, -0.05mm and -0.01mm are assessed by predicting the variation in creep life (time to 1% strain) as a function of stress. Refer to Figure 4.27, Table.4.4 shows the reduced cross section dimensions which result in a change in applied stress at constant load. The resulting creep life variations from a specimen with nominal dimensions

(A=18mm^2), indicate that a dimension error of only -0.01mm causes a 3.87% change in life and the case of a dimension error of -0.1mm causes more than 30% change.

4.3.4 Conclusion

The creep life variation at various temperatures and loads was assessed by calculating the accumulated creep strain using a RCC-RM constitutive law. The results show how sensitive the creep life of the test specimen is to temperature and the accuracy to which the specimen dimensions are known. It is essential to control the temperature, ideally to ±1 °C, during the creep test and the test specimen dimensions must be measured to an accuracy of at least ±0.01mm tolerance to give the best creep test data.

4.4 Temperature Stability and Distribution inside Furnace

4.4.1 Furnace Temperature Survey

There are two important conditions that determine creep deformation in a long term creep test: temperature and stress. By increasing temperature, dislocations move more easily under constant stress, thereby increasing creep deformation. According to the Arrhenius equation, the number of atoms with enough energy to move will increase with temperature. A prediction of creep

strain using the Arrhenius type RCC-MR creep constitutive law [20] shows that a temperature variation of only 1°C causes a 6 to 9 % variation in the creep life prediction under a stress of 160MPa at a temperature of 650 °C (see section 4.3). Thus, a small temperature variation affects creep life significantly and strict temperature management is necessary to obtain accurate data in the long term creep test.

In the present creep test arrangement, a tensile specimen is heated using an electric furnace. Inside of the furnace, heat is transferred to the specimen by convection and radiation, and there will be convective heat flow from any higher temperature region to a lower temperature region. The furnace has heaters in three zones. The temperature of each zone is controlled separately. A lower temperature is set in the high zone and a higher temperature in the low zone to minimise internal heat convection. Furthermore, the furnace has a small window to permit light access for digital image correlation acquisition. The influence of this image acquisition window on the temperature distribution of the furnace was investigated. In early creep tests, the specimens always ruptured near the fillet position because of the presence of a temperature variation, making the test specimen hotter towards the top of the furnace. It is informative to map the furnace temperature profile to find the temperature gradient in the gauge length of the test specimen. The main aims of these experiments were (1) to assess the effect of the DIC window, (2) to map the temperature profile along the axis of the furnace to find the temperature gradients in the specimen gauge length, (3) to check the stability of the temperature field, (4) to compare two different type of

thermocouples between Type R and Type N and (5) to determine the optimum settings of the three heating zones of the furnace to attain the desired temperature profile.

4.4.2 Test Apparatus

4.4.2.1 Furnace and Test Setting

The details of the furnace will be discussed next in section 4.5. Figure 4.28 shows a sketch of furnace with test survey probe inserted. The furnace has three heating zones and the temperature is controlled manually with three different settings. A small window, 40mm×20mm, is located in the middle and a window cover is placed at the outer wall of the furnace. Heat insulation padding is put at the top and bottom of the furnace.

4.4.2.2 Temperature Survey Probe

A temperature survey probe (Figure 4.29) was designed. The gauge length was 288mm long and had a flat rectangular shape with round screw ends for grips. The probe was made from type 316 stainless steel and therefore had the same conductivity as the test specimen. However, the shank of the specimen, grips and load train are not represented.

4.4.2.3 Thermocouples

Type R (Inconel) thermocouples were used for the furnace temperature experiment. See Table.4.5 for the product information. Type R thermocouples have higher accuracy (±1°C) than type N (±2.2°C) previously used in the Open

University's creep laboratory. Eight thermocouples were attached to the probe, two of them in the middle have the same attached positions as for a standard specimen. The tips of the thermocouples were inserted tightly into drilled holes, having a diameter of approximately 1mm.

4.4.3 Temperature Profiling

4.4.3.1 DIC Window Effect

The temperature profile along the axis of the furnace was measured using the survey probe prepared with eight type-R thermocouples. Three temperature controllers were set to the same target values and the furnace heated from room temperature to 150°C and then increased in 100°C steps to 650°C. Temperature values were continuously recorded during each stage by eight thermocouples until all readings became stable. The tests were carried out in two conditions: in the first one, the porthole, where the DIC window is located, was filled with a closely fitting brick insert, for the second, the insert was removed leaving the covering window. Table 4.6 and Table 4.7 show the temperature record for the blocked and unblocked apertures respectively. Each stage required a few hours to achieve target temperatures. The temperature stability will be discussed in section 4.4.3.3. Table 4.8 and Figure 4.30 give the comparison between a blocked window and a DIC window at a stabled temperature profile target level of 550°C. The position x=0 is the centre of the furnace vertically. The highest and most uniform temperatures were found above the centre position between 15mm to 58mm. Compared to the blocked window temperature profile with the DIC window is

more uniform in the centre between –15mm to +15mm. The thermal stability inside the furnace relies on convection and radiation. Convection is dominant under 600°C and radiation is dominant over 600°C [11]. The temperature profile with a blocked window shows the higher temperatures above the centre area. However, the temperature profile with the DIC window showed a slightly different distribution. As the furnace has a long porthole with the DIC window, heat convection occurs around the entrance, thus the temperature distribution around centre attains a symmetrically uniform distribution which is even better than without the window and also this has confirmed that the DIC window does not have a detrimental influence on the temperature distribution.

4.4.3.2 Comparison of Measurements with Types N and R Thermocouples

In order to find out the accuracy of the Types N and R thermocouples along the furnace, temperature profiles were recorded in the vertical line. Tests were carried out between types N and R, with inserted brick and DIC window. Table 4.9, Table 4.10 and Figure 4.31, Figure 4.32 shows the comparison of type R and type N thermocouples at 550°C. Type N thermocouples show slightly lower temperature in the bottom half positions in both with a blocked window and a DIC window. Furthermore, the DIC window results show more pronounced temperature variation than blocked window data.

4.4.3.3 Temperature Stability

The temperature of the specimen and room were monitored with the purpose of investigating the stability of heating and long term test duration. The optimum temperature manual settings can be determined based on the results. Figure 4.33 shows the temperature stability at the position x=15 at the nominal temperature of 550°C with DIC window. The temperature over-shot within the first 30 minutes, then stabilized gradually and became constant after 3 hours. Figure 4.34 shows the variation of furnace temperature over 7 days together with a record of the room temperature. In general, most of the heat loss from the furnace at high temperature was by thermal radiation and room temperature fluctuations did not have a significant influence on the operating temperature of the specimens. However, as mentioned before, heat convection is dominant under 600°C more than thermal radiation, the result indicated the influence from room temperature at 550 C°. The result shows a direct correlation between fluctuation in room temperature and specimen temperature. A temperature change of 1.74°C, in the specimen corresponded to a change in room temperature of 3.08°C (Table 4.11). The magnitude of specimen variation is less than room temperature which fluctuation was less than 2°C,that also conforms within creep test standards. The temperature manual settings of furnace were, top: 540°C, middle: 560°C, bottom: 580°C. The optimum settings of the three heating zones of the furnace have thus been determined.

4.4.4 Conclusion

The furnace temperature investigation was carried by mapping the temperature profile to find the temperature gradient in vertical direction over the

gauge length of the test specimen. The temperature profile with the DIC window indicated uniform gradient and actually having a DIC window contributes to reduce the temperature variation more than without. Type R thermocouples indicates higher accuracy including uniform ability along the specimen gauge length. The optimum temperature settings for creep tests for this study have been determined and the stability of temperature also confirmed.

4.5 DIC Creep Test system

A high temperature optical strain monitoring system using DIC has been developed. Several difficult issues associated with measuring creep deformation at elevated temperature have been solved and confirmed with sufficient accuracy as discussed earlier in chapter 4.1. Thus all devices can now be assembled into a system and used to monitor long term creep tests at high temperature.

4.5.1 Creep Testing

High temperature structural assessment of engineering components uses models based on measured creep properties of the materials used. In particular creep deformation curves and creep rate data are an essential input for determining material life. A conventional creep test is conducted under a constant tensile load at constant temperature as detailed in the ASTM E-139 standard [15]. Usually, the specimen elongation is recorded at specified intervals by our extensometer and this creep deformation versus time diagram is plotted as a creep

curve. The slope of the curve at any point is the creep rate from which the minimum creep rate in the secondary region can be determined.

Figure 4.35 shows a schematic illustration of a simple load controlled creep test machine. A specimen is heated in a furnace until a constant temperature is achieved in the gauge length, and then weights are loaded onto a pan to achieve a constant applied load. The tensile force is applied to specimen through a level loading arm with an auto level adjustment system which maintains the lever arm horizontal. The adjustment system comprises a sensor attached to a disk (flat circular plate as shown in Figure 4.35). This is connected to the loading weight bar beneath the loading plate, and a reversible motor which adjusts the loading train to achieve the balance position of the loading lever arm. It is desirable to keep the loading arm level to avoid changes in effective arm length and thereby applied load during the test as the test specimens extend. The global strain is monitored and recorded continuously by a Linear Variable Displacement Transducer (LVDT), see Chapter 2.2 for details. The frame of the LVDT is placed perpendicular to the axis of the specimen and four screws are attached to the cylindrical section of top and bottom of the specimen.

4.5.2 Temperature Control

4.5.2.1 Furnace

A Severn Thermal Solutions Furnace is used for this creep test. The internal diameter and height of the furnace is 100mm and 360mm respectively. The top and bottom of the furnace is open to accommodate the load train, thermocouples

and extensometers. The furnace consists of three different heating zones, top, middle and bottom, where temperatures are individually controlled by a Eurotherm control system. Three Type K thermocouples are embedded in the furnace, one for temperature control for each of the three heating zones. Each heating zone temperature can be set manually to adjust the target temperature of the test specimen and thereby minimize the variation inside the furnace. The furnace has a maximum operating temperature of 1100 °C. Long term temperature stability requirements for creep testing are described in the ASTM standard test method [15]. The permitted maximum temperature gradient must be less than 2°C across the specimen gauge length and deviations between the specified temperature and the indicated temperature should be ±2°C. Ceramic fibre insulation is placed on the top of the furnace and put into the gap between the loading bar and bottom of the furnace to prevent heat loss and to keep the temperature inside the furnace stable. Sheet type insulation was chosen for this DIC creep experiment system because it produces less fluff compared with other types of insulation and helps to keep the glass window of the DIC system clear. The furnace was manufactured with a special porthole through which images can be taken. A window cover which supports the sapphire window glass is attached to the outside of the furnace over the porthole in order to prevent heat loss and reduce thermal currents and thereby improve the likelihood of stable image acquisition. The specimen is heated in the furnace at the specified temperature and the specimen, gripping and extensometer reach thermal equilibrium. It usually takes at least one hour to stabilise before applying the load. The maximum time

for which the specimen is held at the temperature before loading should not exceed 24 hours according to ASTM 139.

4.5.2.2 Thermocouples

The specimen temperature is measured by thermocouples. In order to achieve a stable target temperature, the three settings of heaters inside the furnace are manually adjusted by referring to the specimen temperature. In ASTM 139, at least two thermocouples should be used with a specimen gauge length less than or equal to 50mm and three thermocouples should be used with a gauge length greater than 50mm. Thus standard creep tests usually employ three thermocouples placed at the top, middle and bottom of the specimen and attached with twisted wires. However, in this DIC optical measurement system we need to monitor the entire gauge surface visually via the camera, thus the visible specimen surface must be kept clear. Therefore, the middle position thermocouple was discarded. The specimen gauge is 40mm length, however, the camera usually captures approximately 32-35mm, because it is limited by the window size (40mm length) and the placement of the optical fibre for illumination.

Thermocouples need to make good contact with the surface of the specimen. In this study, two small holes were drilled at the top and bottom of the test specimen (outside the gauge section) into which thermocouple tips were inserted to ensure good thermal contact. The thermocouples were attached to a data logger (Picolog) and the temperatures were monitored and recorded at specified time intervals during the creep test.

A thermocouple is a device consisting of two different conductors that produce a voltage proportional to a temperature difference between either ends of the pair of conductors. The main limitation with thermocouples is their accuracy and monitoring system error of less than 1° C can be difficult to achieve. Table 4.5 (section 4.4) shows the product information for various types of thermocouple. As you can see, a Type N thermocouple has a temperature variation of ±2.4°C at 600°C and a Type R thermocouple has a temperature variation ±1°C. There are errors from emf (electric motive force), the connector, cable and measurement devices which give us total measurement errors. As discussed before the temperature variation along the gauge length should not be greater than ±2°C, and the specimen should be within ±2°C of the target temperature. As well as choosing an accurate type of thermocouple its essential that the sensors are calibrated. The highest accuracy Type R thermocouples were chosen for all three creep tests which demonstrated in this study.

4.5.3 Load Control

The auto leveling system is important to keep the specimen position constant in the camera's field of view through the window during the creep test.

The tensile force is applied to the specimen through a level loading arm in order to maintain a balance. Figure 4.36 (left) shows a schematic illustration of the lever arm mechanism. The weights are applied to one end which applies the tensile force at the other end. The lever arm ratio is a/b, where P is the applied load, the specimen receives the tensile force P(a/b). The creep frame used has a

lever arm ratio of 1:10. Considering the calculation of strain, the specimen length increases during a creep test. Figure 4.36 (right) shows schematic illustration of a lever arm having a tensile extension after loading. At the beginning of the test, the loading lever is balanced horizontally the load is applied by the lever ratio a/b. As the specimen extends due to creep deformation, the lever ratio changes due to lever rotation. The ratio of the decrease b to b′ is equal to the extension l to l_0. Figure 4.37 is a simple example of a lever arm calculation. The arm balance is 1:10 and the actual length is 40mm: 400mm in the creep machine used in this study. For example, when a tensile stress of 160MPa is applied to the specimen, which causes the total specimen length to extend by 5mm, the lever arm would rotate by an angle of θ=7.12. So, if the auto adjustment mechanism for leveling the angle were not used, the actual stress on the specimen would reduce to 158.76 MPa. A sensor attached to the weight hanger makes a reversible motor work as the specimen is extended, which keeps the specimen position steady. Thus the camera's field of view is able to capture the whole gauge length continually through the DIC window.

4.5.4 DIC Creep Testing Machine System

Figure 4.38 shows a picture of the DIC high temperature creep deformation measurement system and detailed system diagram. The system includes a camera, a furnace, a loading frame for applying the tensile load, a light source and a PC for image acquisition control. The camera is positioned approximately 100mm in front of the furnace from the window. A Nikon D300, camera is used with a 200mm

macro lens in order to zoom in into the specimen gauge section. The resolution of the camera was 12.3 megapixels, which is sufficient to obtain local behaviour of creep test sample. A fibre optic light is set outside of the window glass for illumination. The fibre optic line is connected to a flash light which is synchronised with the camera's shutter action. The camera is focused on a length of about 32 to 35mm vertically including the gauge section of the specimen. The image is acquired through a 40mm x 20mm window and saved in PC. For a few month creep test, 2000 images are saved approximately, with images taken every hours. LVDT transducer continuously monitored the creep strain, thus when the tertiary stage began, the image acquisition was changed to 15 min intervals. A description of image analysis for DIC will be given next in section 4.6.

4.5.5 Test Environment

The camera monitoring system requires a stable environment, free from vibrations from equipment used in the lab. A vibration survey of the test system (i.e. the camera stand and the furnace) was undertaken using a laser doppler vibrometer to confirm that any device used in the lab (e.g. the air conditioning system) did not affect the measurements. The laboratory room temperature is kept to 20°± 1°C by an air conditioning system which reduces temperature variation and assists to achieve better specimen temperature test conditions. In order to take better contrast images, the room lights were switched off during tests and black window blinds were used to keep off the sun light from the lab. The access to the

laboratory was restricted to avoid disturbance of the equipment and the location was chosen in far from the entrance door which is locked during the creep test.

4.6 DIC Analysis Procedure

The flow chart of the DIC analysis procedure is shown in Figure 4.39. The procedure can be divided into three parts which are pre-processing, correlation analysis and post-processing.

The pre-processing is preparation for image analysis. Images are converted into grey scale format and the shift and intensity correction are applied in software in order to remove any temporary movement from system vibration and variation in lighting or contrast from the images.

In the correlation analysis, the region under investigation is extracted and divided into small subsets for computation. The correlation analysis is performed between two subset images, which are derived by the correlation function. Once the peak position is computed, the displacement vector is determined. A few algorithmic factors can be adapted to improve the computation such as the window overlap and the multi-pass iterations and facilitate finding the corresponding position on the images.

The two dimensional displacement fields obtained by the DIC technique were then imported into a Matlab [21] script to calculate the u and v strain fields, which were then subsequently processed to obtain the required creep properties.

4.6.1 Pre-Processing

4.6.1.1 Image Processing

Images were acquired by a digital SLR Nikon D300 camera with a 200 mm focal length macro lens. The resolution of the camera is 12.3 megapixels. Uncompressed raw format (RGB 48 bit format) were captured and then converted into 8 bit gray scale format via Corel-Draw software [7].

The speckle size is an important factor in DIC analysis as described in Chapter 2.3 [22],[23]. In order to include the whole specimen gauge area in the image a pixel size of approximately 10μm was found to be sufficient and is used througout this study. A speckle size of about 50μm was found to give sufficient accuracy for pattern matching in DIC analysis. Finally, the converted images were exported to DaVis Strain Master [8] DIC software for the image correlation computation.

4.6.1.2 Rigid Body Motion

The DIC software has a facility for the correction of rigid body motion (i.e. translation and rotation) that may occur during the testing. This function eliminates rigid body motions relative to the first image. A reference point is required for adjustment and usually the middle position of specimen gauge length is selected. All images are shifted (and rotated if required) to match the reference image using the selected point; the intensity is also corrected to the same mean value of the first image [8].

4.6.2 Correlation Analysis

The basic theory of the search algorithm of the correlation function in DIC was introduced in Chapter 2.3. As technology advances, various DIC computational algorithms have been developed [24] and fast and robust commercial software is widely used. The displacement vector is calculated using the standard FFT based algorithm in this study from DaVis Strainmaster software [8]. The equation simply compares the intensity functions to compute a correlation strength using correlation formula [25],[26],[27],[28].

4.6.2.1 Definition of Analysis Region and Subset Size

The analysis region is defined as a rectangular shape. The whole specimen gauge length is extracted from the original photograph and the unwanted area (e.g. background) is removed. The analysis region is then divided into small subset windows by the software for the correlation computation. The selection of subset size is an important parameter to decide the measurement accuracy as discussed in the previous Chapter 2.3. Although a large subset generally gives better accuracy in homogeneous material [23], in order to observe local deformation of heterogeneous material such as cross-weld sample, an appropriately small subset size is essential in this study. However, analysis accuracy can be affected at small subset sizes if there is not enough speckle pattern information within the subset. In order to achieve a reliable correlation analysis in DIC, the balance of this subset size selection needs to be considered. In this

experiment, the most suitable subset size was found to be 64×64 pixels with this magnification and speckle size.

4.6.2.2 Cross-Correlation

The correlation function operates on the intensities inside each subset window. Using cross-correlation a displacement vector is calculated between the same subset between two images, which is selected by the correlation peak position determined by above equation. There are a number of settings for the cross-correlation algorithm. Using a setting called integral correlation, displacement is measured relative to the first image 1*n by taking the sum of the differential vector fields such as 1*2, 1*2+2*3, 1*2+2*3+3*4,... This method typically selected for strain measurement and most of cases used for in this study. The differential correlation works between two successive images n*(n+1), which calculates a displacement vector of movement between those two images, or a strain rate. This method was used for the thermal current measurement in this study.

4.6.2.3 Window Overlap and Multi Pass Iteration

There are a few algorithm functions that are set by the user that affect the DIC analysis accuracy. The window overlap is one of them. The subset size and percentage of the window overlap determine the grid size of the displacement vector field. For example, 128×128 pixels subset size with 50% overlap gives a half subset size vector spacing of 64×64 pixels. Multi-pass with decreasing window size is another function that can be applied to the iteration computation for

accuracy improvement. In this method the algorithm calculates the vector field via a number of iterations, the first iteration starts with larger window size to provide a robust initial displacement estimation for subsequent iterations. In the next pass, the window size decreases to half the size of the first pass; the vector is then calculated using the result from the previous pass as an initial estimate. In the case of large deformation, starting the larger subset helps to capture the destination point after deformation, then smaller window can be used as a better much between sub-regions. This method improves to compute the displacement vectors more accurately and more reliably.

4.6.2.4 Correlation Peak Ratio

The cross-correlation is performed for each integer pixel displacement position. Then the peak position is fitted by a Gaussian peak fit employing three-point estimator in this program. The peak positions can be measured to sub-pixel accuracy to the order of 0.1 to 0.05 pixels [8] depending on the quality of recording and evaluation parameters, such as subset size and correlation function. Two independent two-dimensional Gaussian functions are fitted to the peak intensity profile in the x and y direction respectively [8]. Figure 4.40 shows the localization of the four highest correlation peaks in one dimension. The peak height (P) indicates the correlation strength of the cross correlation of two images. The correlation peak ratio is defined as the ratio of the highest correlation peak to the second highest and is used to evaluate reliability of the displacement vector. Here,

the correlation peak ratio of two images is given by $Q = \frac{P_1 - \min}{P_2 - \min} > 1$. If this ratio is high, e.g above 1.5 or 2.0, it indicates that vector field is quite likely a valid vector.

4.6.2.5 Image interpolation

The image interpolation scheme is applied for final computation. The detail of interpolation (image reconstruction) has already been described in Chapter 2.3. This scheme is one of the most important factors affecting the accuracy of displacement vector. There are two options to select in this analysis, bilinear interpolation and Whittaker reconstruction. In order to obtain high accuracy for final vector result, Whittaker algorithm is used for this image reconstruction computation.

4.6.3 Post-Processing

4.6.3.1 Strain Calculation

The displacement data calculated using the above method is exported to Matlab general purpose computing software [21], for strain field calculation. The strain calculation programme was written at the Open University [29], which determines strain values in each subset by differentiating several neighbouring points. Figure 4.41 shows the method for strain calculation using Matlab script.

Figure 4.41 (a) shows the strain calculation using the displacement data of 3 subsets next each other, $\varepsilon n = (\Delta Y\ n+1 - \Delta Y\ n-1)/(Y\ n+1 - Y\ n-1)$. Figure 4.41 (b) shows the displacement range $n-k$ to $n+k$, strain is expressed by $\varepsilon n = (\Delta Y\ n+k - \Delta Y\ n-k)/(Y\ n+k - Y\ n-k)$. As the value of k is increased, the strain calculation is

smoothed but, using large number of k gives us excessive interpolation of the data, which loses small features in the strain . The number of k is user defined, here we have a selection of k values used in this study: k=1(3 subsets), 2(5 subsets), 3(7 subsets), 4(9 subsets). Most of the strain calculations in these studies were performed by using k=3(7 subsets) which frequently find good agreement with the FE results [29].

4.6.3.2 Creep Curve and Strain Distribution

The results are exported to another Matlab script programme developed for creep strain calculation. This programme calculates the creep strain value versus time, which is used to generate creep curves at each subset point. The results provide the local creep curves across the specimen gauge length including the individual weldment sections (Parent, HAZ and Weld). The strain variation across the gauge length can be delivered at different times, thus the evolution of the local creep strain increment can be seen at individual stages of primary, secondary and tertiary creep.

4.6.3.3 Reduction of Area

The major advantage of the DIC approach is that local strain can be measured in full field across the sample surface. As DIC can measure in two dimensions, data can be obtained for not only of the tensile strain in the vertical direction but also the transverse strain in the horizontal direction. Thus, analysing the strain across the width provides the reduction of area of the specimen, assuming the strain in the thickness direction is also the same as the strain in the

width direction. The variation of the reduction in cross-sectional area across the gauge length is obtained at different times. The final reduction area, which was obtained from the final image, can be calculated at the ruptured position.

4.6.3.4 True Stress Calculation

The true stress distribution incorporates the stress concentration in a sample. Conventionally, the true stress is not calculated for creep test data because it is difficult to measure the reduction of area during the test. However, using the results of the reduction in area the true stress distribution and the stress concentration can be predicted. The creep test is conducted at constant load, thus the local true stress is determined by dividing the applied load by the modified cross sectional area at each measurement point along the specimen gauge length.

$$\sigma_t = \frac{F}{A}$$

σ_t: True stress

F : Constant load at creep test

A : Section area at each subset position

The true stress variation can be seen at different times and the final true stress distribution is obtained from the last image.

The true stress distribution is provided not only along the gauge length but also across the gauge width. According to the pixel size of 10μm and the specimen width 6 mm in this experiment, 8 subsets are obtained across the width when using a subset size of 64×64 pixels. These 8 data points provide us with the true

stress variation across the specimen width and tell us how much the true stress rises at the ruptured position when the specimen fails (Figure 4.4.2).

4.7 Validation of DIC measurements at high temperature

Preliminary tests were performed on Type 316H stainless steel plain specimens to validate the measurement accuracy of the DIC technique at high temperatures. A high temperature tensile test and a short term creep test were carried out for this purpose. The global strain in each test was measured by extensometers and the results were compared to the averaged strain, obtained by DIC, over a distance equivalent to the gauge length of the extensometer.

4.7.1 High Temperature Tensile Test

Two tensile tests were performed at 545°C. In one of the tests the extension of the gauge section was measured using an extensometer, whereas DIC technique was used in the second test to monitor the extension. The specimen design was the same as the one used for the creep tests (see Chapter 4.2). The specimen was machined from a Type 316H stainless steel round bar (diameter D=12mm) using EDM. An Instron slow strain rate tensile testing machine with a 100kN load cell and a three zone furnace was used for the tests (Figure 4.43). Two N-type thermocouples were attached to the top and the bottom of the specimen outside the gauge section, leaving at least 30mm length clear in the centre in order to

monitor the area by the DIC camera. This furnace has an approximately 30mm ×15mm opening at the centre and this was used for attaching the extensometer (clip gauge) in the first test. The 12.5mm long legs, made of quartz, of the extensometer were attached to the specimen gauge section using knife edges and the extension of the gauge section was recorded at a rate of once every two seconds during the test. For the second test, an optical window made of quartz was used to cover the opening through which imaging of the gauge section was continuously acquired during the test with a DIC camera. A small fan was used to reduce thermal currents between the window and the camera lens to eliminate image distortion, as described in Chapter 4.1. Although it would have been ideal to execute two measurements simultaneously in one test for comparison purposes, this was not possible due to having only one furnace window.

In both tests, the specimen was heated overnight to attain the target temperature of 545°C and tests were started within 24 hours. The tensile extension rate was 0.1 mm/min and in the DIC test images were taken every 10 second intervals and changed to 40 seconds intervals after 50 images, when the material was in the plastic regime. Both tests were continued until the specimens failed.

The stress-strain curves were obtained from the two individual tensile tests. In the first test the displacement was read by the clip gauge extensometer and the corresponding strain was calculated with the given gauge length. In the DIC test, 275 images were recorded and analysed in DaVis StrainMaster software[8]. The displacements were transferred to a Matlab script [21] for strain calculation along the gauge length (ε_{yy}). The total strain from the DIC measurement corresponding

to the length of the clip gauge was calculated and the results for both tests are plotted in Figure 4.44. As can be seen the agreement between stress-strain curves for both tests is excellent.

4.7.2 Creep Test

The test specimen was made from the parent material of Type 316H stainless steel. The design for creep specimen is shown in Figure 4.15. The width and thickness of the specimen were 6mm and 3mm, respectively. The specimen was attached to the creep frame using the threaded ends, whereas the gauge section was machined flat for the DIC measurements. A high temperature extensometer (LVDT) was attached to the specimen shoulders, where the straight section is 15mm and diameter is 10mm for the simultaneous measurement of the strain. This specimen was machined to the initial design given in Figure 4.15, before the final design was decided, as explained in Chapter 4.2. The same speckle preparation procedure was used as given in Chapter 4.1. The creep test was carried out at a temperature 650°C under a nominal stress of 160MPa. The camera continued taking photographs for 545 hours at 15 minutes intervals until the specimen ruptured. Three N-type thermocouples were attached to the specimen at the top and the bottom of the specimen gauge length. In this preliminary test, the temperature variation was 3°C (top: 650°C, bottom: 647°C).

A total of 260 images were recorded and analysed in DaVis StrainMaster software[8] to compute the displacement vectors. The images were selected at intervals of 75 minutes in the secondary region and 15 minutes in the tertiary

region. The displacements were transferred to a Matlab script [21] for strain calculation along the gauge length (ε_{yy}). The total strain from the DIC measurement corresponding to the length of the clip gauge was calculated and the results for both measurements are plotted in Figure 4.45. As can be seen, they have a very good agreement. Figure 4.46 shows the strain variation along the gauge length obtained by DIC measurement. The specimen ruptured near the top of the gauge length as can be seen in Figure 4.47. Here, the strain value at the top of the gauge length increased rapidly where the specimen was ruptured. The possible reason for such an increase in strain at this position is that the temperature distribution along the gauge length was not uniform. In this creep test, the temperature was about 3°C higher at the failure location compared to the bottom of the gauge section.

Figure 4.48 shows the comparison of local creep curves at the top, the middle and the bottom of the gauge length as measured by DIC (the positions are showing in Figure 4.47). These local creep curves show different creep strain increments related to temperature variation. The top position result was located approximately 10mm above the centre (middle position), where the specimen ruptured. The creep curve indicates tertiary dominated shape and creep strain accelerates after 350 hours. The creep curves at the middle and the bottom positions have smaller strain increments relative to the top position; especially the bottom position creep curve has constant strain increment and the total strain is less than 4% with no tertiary region.

The creep test results were compared to the RCC-MR constitutive calculation [20] as discussed in Chapter 4.3, as shown in Figure 4.49. The temperatures were chosen at 645°C, 648°C and 650°C for calculation. The strain variation is 3.13% at 550 hours between 645°C and 650°C however, it is important to note that the RCC-MR law does not consider the tertiary deformation which usually causes large variations in the end. The middle position of the creep curve seems closer to the RCC_MR results. However, the differences at the top and the bottom of the gauge section are large which indicates the significance of the temperature variation on the creep curves. Although the top and the bottom temperature variation was only 3 °C, the results show very large variation in creep strain.

DIC measurements were also used to demonstrate the usefulness of the full field strain determination in creep analysis. The DIC data would also allow the strain measurement across the width of the gauge section (ε_{xx}). The data can then be used to determine the reduction of area and the true stress, if strain in the thickness direction is assumed to be the same as in the width of the specimen.

As strain across the width is smaller than tensile strain, only one fifth numbers of the images were required for strain calculation, thus 52 images were used for this across the width (ε_{xx}) analysis. Consequently, images were selected at time intervals of 375 minutes in the secondary region and 75 minutes in the tertiary region. The standard cross-correlation mode and correlation function (standard FFT) were chosen for the vector calculation with a subset size of 128

×128 in the first two passes then decreased to 64 × 64 in the next passes without overlap.

Figure 4.50 shows the ε_{xx} distribution along the gauge length at various times during the creep test. Figure 4.51 shows the reduction of area using this ε_{xx} data. (The details of the reduction of area and the true stress calculations were described in section 4.6). The result indicates a large reduction of area at the ruptured position which is 6 to 7% at the top of the gauge length. Figure 4.52 shows the true stress distribution and increment at each area along the gauge length. The nominal applied stress was 160MPa. As creep deformation increases at higher temperature locations, the true stress rises up to around 190MPa at the ruptured position at 545 hours.

4.7.3 Conclusions

The preliminary tests were performed on a Type 316H stainless steel plane specimen to validate the measurement accuracy of the DIC technique. The stress-strain curves from high temperature tensile tests at 545°C and a creep curve test 650°C showed that the strain measurements using the DIC technique agree well with those obtained by extensometers measurement. The local creep curves obtained at different parts of the creep specimen indicated how critical is the uniformity of temperature distribution along the specimen gauge section for creep behaviour. It has also been demonstrated the usefulness of full field measurements by determining the true stress-strain data from DIC measurements.

4.8 Summary

1. A high temperature DIC optical system has been developed. The major problems which conventionally have prohibited strain measurement at elevated temperature, such as surface oxidation, illumination and thermal currents, are solved in this study.

2. VHT high temperature resist paint was chosen and applied to sample surface. This coating has stayed for 5 months at 600°C in the paint durability test and its surface condition is sufficient to obtain for DIC pattern matching.

3. A fibre-optic flash light is installed in order to improve the surface illumination in this system. The bright flash light creates a higher contrast image and allows us to carry on long term creep test.

4. The image distortion is caused by thermal air current at high temperature. The variation of pixel movement was measured. The thermal current can be reduced by using a fan and by minimizing the temperature variation inside furnace provides better results.

5. A new specimen design has been developed for the DIC creep test. As the flat gauge length is required for optical measurement, which is adapted to the standard creep specimen design. The finite element analysis is

demonstrated to the new specimen design. The stress concentration at shoulders has been reduced by increasing the corner radius.

6. A simple creep life calculation has been carried out using RCC-MR constitutive equation at various temperatures and loads. The results indicated how important temperature control and specimen dimensions are.

7. The temperature survey was carried out in order to map variation inside the furnace. Adapting the DIC window provides us with a good temperature gradient along the gauge length. The optimum temperature setting and stability are confirmed.

8. The validation tests were performed on a plane specimen to confirm measurement accuracy. DIC results of stress-strain curve at high temperature and creep curve at creep test have good agreement with the global strain measured by the extensometers.

4.9 References

[1] B.M.Grant, "High temperature strain field measurement using digital image correlation," *J. Strain Analysis*, vol. 44, 2009.

[2] J.S.Lyons, J.Liu, and M.A.Sutton, "High-temperature deformation measurement using digital-image correlation," *Experimental Mechanics*, pp. 64–70, 1996.

[3] Jed.Lyons, Michael.Sutton, and Anthony.Reynolds, "Experimental Characterization of Crack Tip Deformation Fields in Alloy 718 at High Temperatures," *Journal of Engineering Material and Technology*, vol. 120, January, 1998.

[4] Jin.Liu, M.Sutton, Jed.Lyons, and Xiaomin.Deng, "Experimental investigation of near crack tip creep deformation in alloy 800 at 650°C," *International Journal of Fracture*, 1998.

[5] B.Pang, "High Temperature digital image correlation method for fill-field deformation measurement at1200°C," *Measurement Science and Technology*, vol. 22, 2011.

[6] "VHT paints, A division of Dupli Color, Inc, A Sherwin-Williams Company." .

[7] "Corel PHOTO-PAINT X4, (c) 2008 Corel Corporation." .

[8] "Strain Master, LaVision GmbH, Anna-Vandenhoek-Ring 19 Gottingen Germany," 2007.

[9] Y.Q.Wang and M.A.Sutton, "Image matching error assessment in digital image correlation," *SEM annual conference Albuquerque, New Mexico, USA*, 2009.

[10] "DaVis StrainMaster Software, Manual, LaVision GmbH." 2007.

[11] F.T.Wallenberger, *Fiberglass and Glass Technology: Energy-Friendly Compositions and Applications*. 2010.

[12] "HDRsoft Photomatix Pro 4.0.2, HDRsoft Ltd." .

[13] Z. Wang, C. K. Chiang, and T. J. Chuang, "Optimum design of a ceramic tensile creep specimen using a finite element method," *Journal of Research of the National Institute of Standards and Technology*, vol. 102, no. 1, p. 15, Jan. 1997.

[14] D.L.Marriott, "Specimen design for creep characterization under multiaxial stress," *ASME Pressure Vessels and Piping Division Conference*, 2005.

[15] "ASTM E-139 Standard Test Method for Conducting Creep, Creep-Rupture, and Stress-Ruptured Test of Metallic Material(21st April 2009)."

[16] "ASTM E8/E 8M-08 Standard Test Method for Tensile Testing of Metallic Materials." 2008.

[17] J. Liu, J. Lyons, M. Sutton, and X. Deng, "Experimental investigation of near crack tip creep deformation in alloy 800 at 650°C," *International Journal of Fracture*, 1998.

[18] "ABAQUS/CAE, Dassault Systems."

[19] P.J.Holt, "Prediction of Reheat Crack Initiation by Continuum Damage Mechanics Incorporated infinite Element Creep Analysis. Nuclear Electric Ltd,Barnwood Glos. GL4 3RS"

[20] "RCC-MR, Section 1,Sub-section Z, Technical Appendix A3, AFCFN, Paris 1985." .

[21] "MATLAB The Mathwork Inc3 Apple Hill Drive Natick, Massachusetts 01760 USA." 2012.

[22] S. Yaofeng and J. H. L. Pang, "Study of optimal subset size in digital image correlation of speckle pattern images," *Optics and Lasers in Engineering*, vol. 45, no. 9, pp. 967–974, Sep. 2007.

[23] D.Lecompte, A.Smits, S.Bossuyt, J.Vantomme, D. V. Hemelrijck, and A.M.Habraken, "Quality assessment of speckle patterns for digital image correlation," *Optics and Lasers in Engineering*, vol. 44, no. 11, pp. 1132–1145, Nov. 2006.

[24] M.A.Sutton, J.J.Orteu, and H.W.Schreier, *Image Correlation for Shape, Motion and Deformation Measurements*. Springer, 2009.

[25] M. Fincham and G. R. Spedding, "Low cost, high resolution DPIV for measurement of turbulent fluid flow," *Experiments in Fluids*, vol. 23, no. 6, pp. 449–462, Dec. 1997.

[26] A. Fincham, G. Delerce, and Fourier-cnrs-inpg, "Advanced optimization of correlation imaging velocimetry algorithms," 2000.

[27] H. P. Douglas, "Super-Resolution PIV by Recursive Local-Correlation," vol. 10, pp. 1–10, 1999.

[28] Richard.D.Keane and Adrian.J.Ronald, "Theory of cross-correlation analysis of PIV images Richard D. Keane & Ronals J. Adrain," pp. 191–215, 1992.

[29] M.O.Acar., S. Gungor., S. Ganguly., P.J.Bouchard, and M. E. Fitzpatrick, "Variation of Mechanical Properties in a Multi-pass Weld Measured Using Digital Image Correlation," *Proceeding of the SEM Annual Conference*, 2009.

4.10 Tables and Figures

Position	Displacement values		Error	
	No Paint	With Paint	No Paint	With Paint
1	0.999496	0.999947	0.000504	0.000053
2	0.99933	0.99984	0.00067	0.00016
3	0.999209	0.999778	0.000791	0.000222
4	0.99933	0.999894	0.00067	0.000106
5	0.999174	0.999797	0.000826	0.000203
6	0.999043	0.999734	0.000957	0.000266
7	0.999229	0.999849	0.000771	0.000151
8	0.999077	0.999748	0.000923	0.000252
9	0.998949	0.99968	0.001051	0.00032
Average	**0.999204**	**0.999807**	**7.96E-04**	**1.93E-04**

Table 4.1 Summary of calculated displacement values and error at different pixel movement and averaged values

Plastic Properties	
Stress (MPa)	Plastic Strain(%)
198.0	0
201.2	0.114
203.5	0.199
209.1	0.374
216.4	0.526
219.0	0.683
221.4	0.922
416.5	20

Table 4.2 Plastic Properties at 550°C used in Finite Element Analysis [1]

Temperature	$t(\varepsilon_{o=1\%})$	% reduction in creep life
(°C)	(h)	(%)
640	157.3	47.5
645	115.5	28.5
648	95.8	13.8
649	89.2	7.4
650	82.6	0
651	78.2	-5.3
652	73.8	-10.7
655	60.5	-26.7
660	45.0	-45.5

Table 4.3 Predicted time to reach 1% strain time at various temperatures

Stress	$t(\varepsilon_{o=1\%})$	Cross section of area	% reduction in creep life
(MPa)	(h)	(mm^2)	(%)
160	82.6	A=6x3=18mm^2	0
160.8	79.4	A=5.99x2.99=17.9mm^2	3.8
164	68.1	A=5.95x2.95=17.6mm^2	17.6
168	56.9	A=5.9x2.9=17.1mm^2	31.1

Table 4.4 1% Predicted strain time at various loads

Type	Conductor Combination	Temperature Range	Output Tolerances	Temp. Variation @ 600C
K	NiCr / NiAl	0 – 1100C	-40 - 375C +/- 1.5C 375 -1000C +/- 0.004 (t)	+/- 2.4C (= 0.4%)
N	NiCrSi / NiSiMg	0 – 1200C	-40 – 375C +/- 1.5C 375 – 1000C +/- 0.004 (t)	+/- 2.4C (=0.4%)
R	Pt 13%Rh / Pt	0 – 1600C	0- 1100C +/- 1.0C	+/- 1.0C (=0.16%)
	Inconel	0-850C		

Table 4.5 Product information of thermocouples

Thermocouples Position (mm)	Initial temperature record at RT	Target temperature					
		150°C	250°C	350°C	450°C	550°C	650°C
144	20.8	127.4	221.8	320.5	420.1	519.7	616.9
101	20.8	142.	242.8	344.0	444.0	543.4	640.9
58	20.6	147.2	249.3	351.2	451.9	550.6	648.8
15	20.4	148.1	250.2	351.6	451.6	550.2	648.1
-15	20.5	146.9	248.3	349.3	448.8	547.0	644.9
-58	20.7	142.6	241.9	342.2	441.6	540.7	639.2
-101	20.8	127.7	218.0	313.6	411.4	511.4	612.5
-144	20.8	83.4	143.3	215.2	298.2	389.9	487.5

Table4.6 Temperature record with a brick inserted (blocked window)

Thermocouples Position (mm)	Initial temperature record at RT	Target temperature					
		150°C	250°C	350°C	450°C	550°C	650°C
144	21.0	129.2	223.0	321.3	419.4	518.7	617.5
101	20.9	143.3	243.3	344.0	445.0	544.2	642.0
58	20.7	147.1	249.	350.9	452.1	551.2	649.2
15	20.5	146.3	247.7	349.2	450.0	548.8	646.8
-15	20.5	144.1	244.8	346.6	448.1	547.4	646.0
-58	20.9	135.	233.5	337.3	443.3	544.3	644.4
-101	20.9	122.2	212.9	312.2	415.9	519.0	621.5
-144	21.0	84.5	145.0	214.4	293	377.5	466.4

Table 4.7 Temperature record with a DIC window

Thermocouple Position (mm)	Temperature 550°C	
	Brick	DIC
144	519.7	518.7
101	543.4	544.2
58	550.6	551.2
15	550.2	548.
-15	547.0	547.
-58	540.7	544.3
-101	511.4	519.0
-144	389.9	377.5

Table 4.8 Temperature record comparison between a brick and DIC window at 550°C

Thermocouples	Temperature (°C)							
Position (mm)	114	101	58	15	-15	-58	-101	-144
Type R	519.6	543.2	550.5	550.1	546.9	540.6	511.3	389.9
Type N	526.0	545.2	550.5	548.0	544.7	535.3	495.2	342.8

Table 4.9 Temperature record Type R and Type N thermocouples with a blocked window at 550°C

Thermocouples	Temperature (°C)							
Position (mm)	114	101	58	15	-15	-58	-101	-144
Type R	518.7	544.2	551.2	548.8	547.4	544.3	519.0	377.5
Type N	520.4	542.0	547.4	542.9	538.0	528.5	511.7	384.2

Table 4.10 Temperature record Type R and Type N thermocouples with a DIC window at 550°C

	Maximum temperature change during 7 days period (°C)
Specimen Temperature	1.74
Room Temperature	3.08

Table 4.11 Temperature variation during 7 days (Furnace/specimen temperature at 550°C)

(a) Specimen Surface on day 1

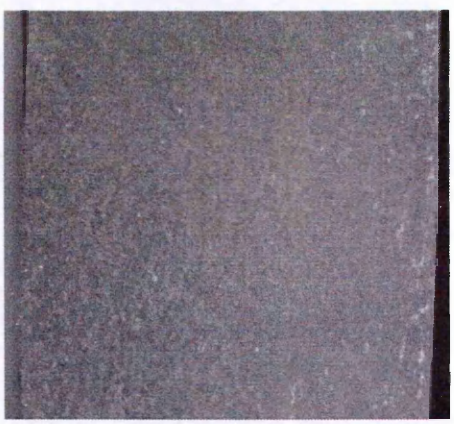

(b) Specimen Surface after 7days

Figure 4.1 Comparison of a specimen surface at 650°C

Figure 4.2 Painted specimen surface at 600 °C for 5 months

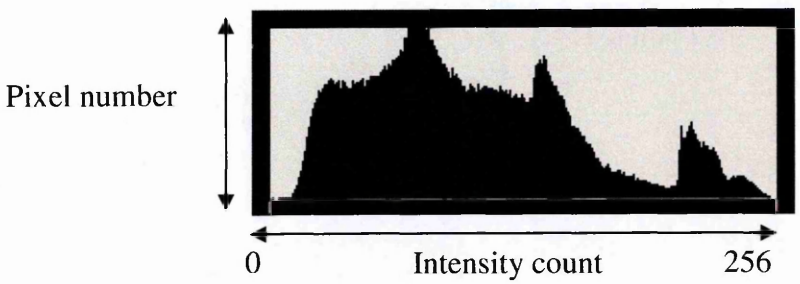

Figure 4.3 Example of image histogram

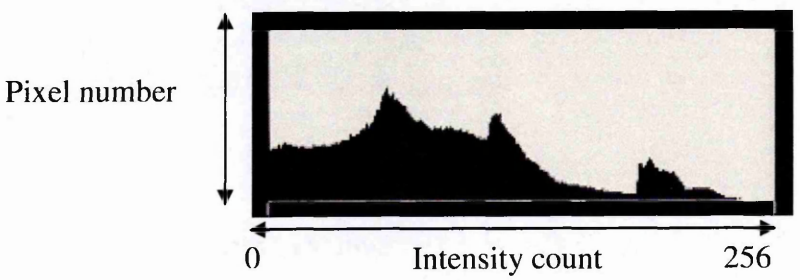

Under exposure

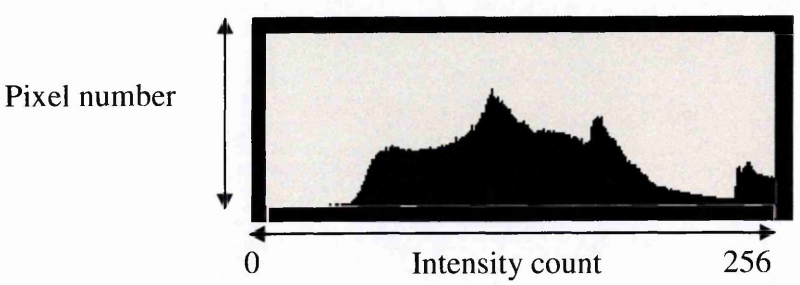

Over exposure

Figure 4.4 Example of exposure

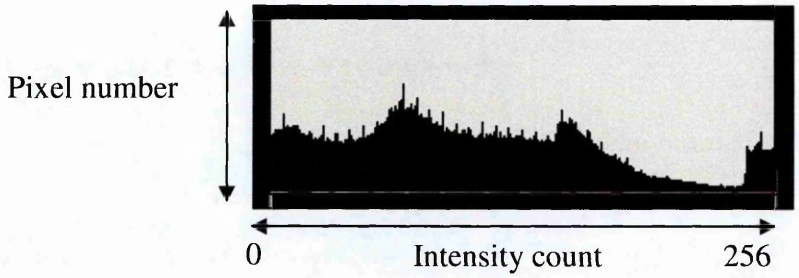

Over contrast

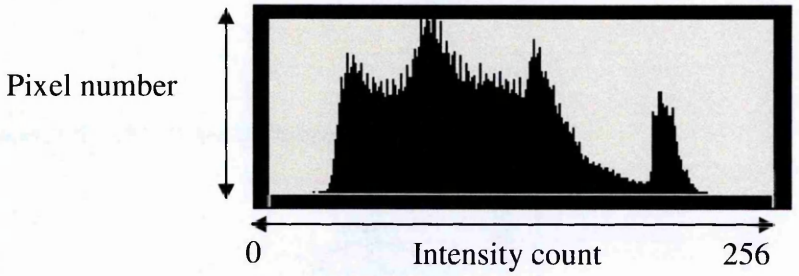

Under contrast

Figure 4.5 Example of contrast

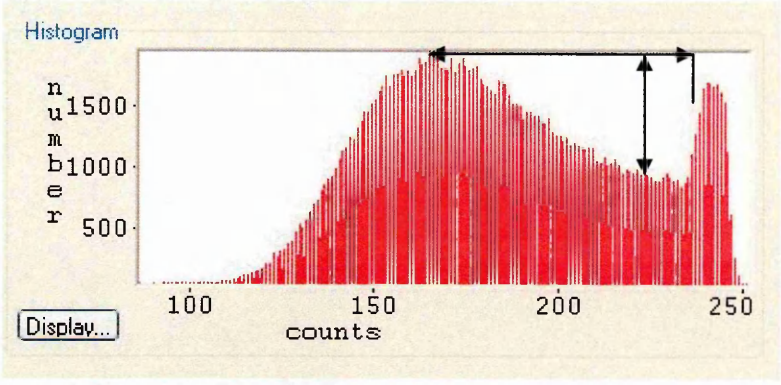

(a) The non painted image histogram

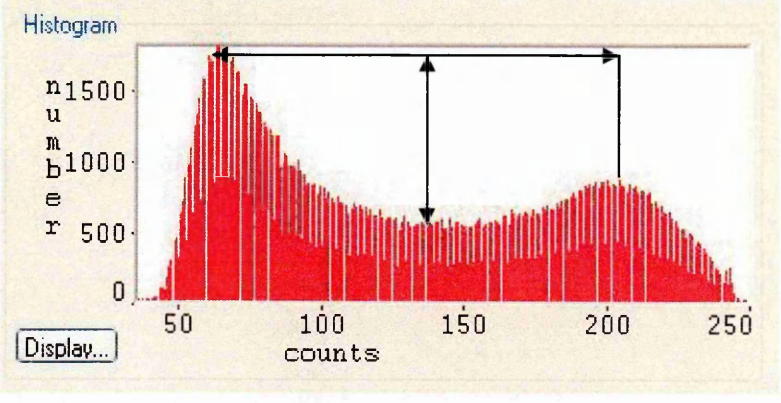

(b) The painted image histogram

Figure 4.6 Image histogram

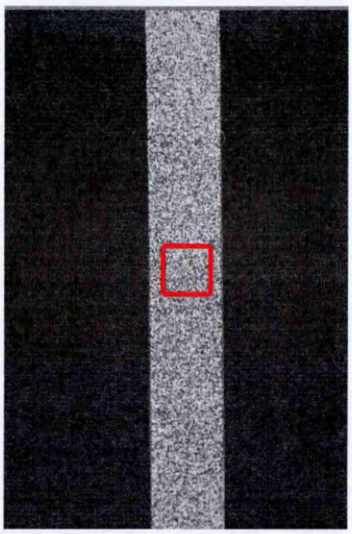

Figure 4.7 Extracted position of specimen image

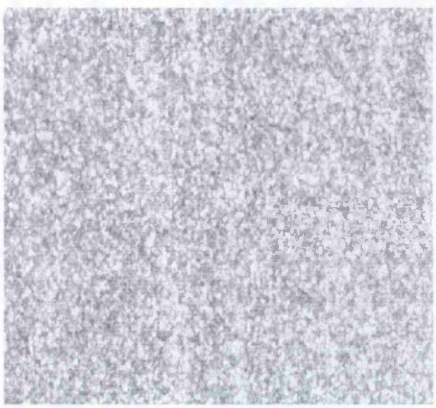

EDM surface (without paint)

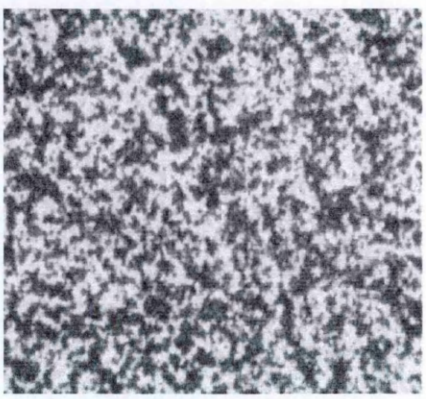

Painted surface

Figure 4.8 Extracted images

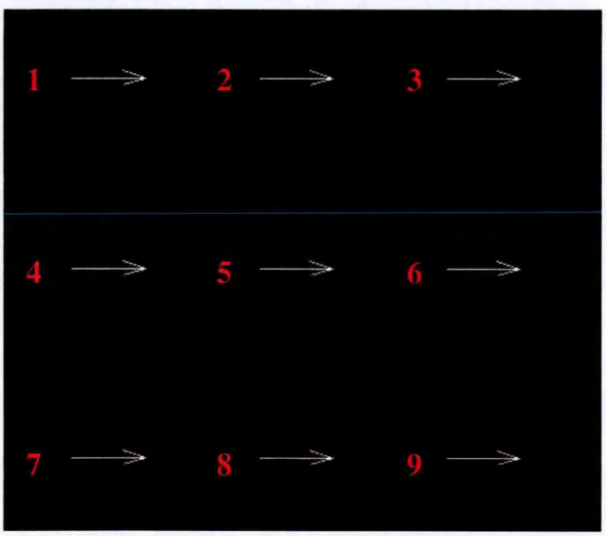

Figure 4.9 Displacement vectors at each subset

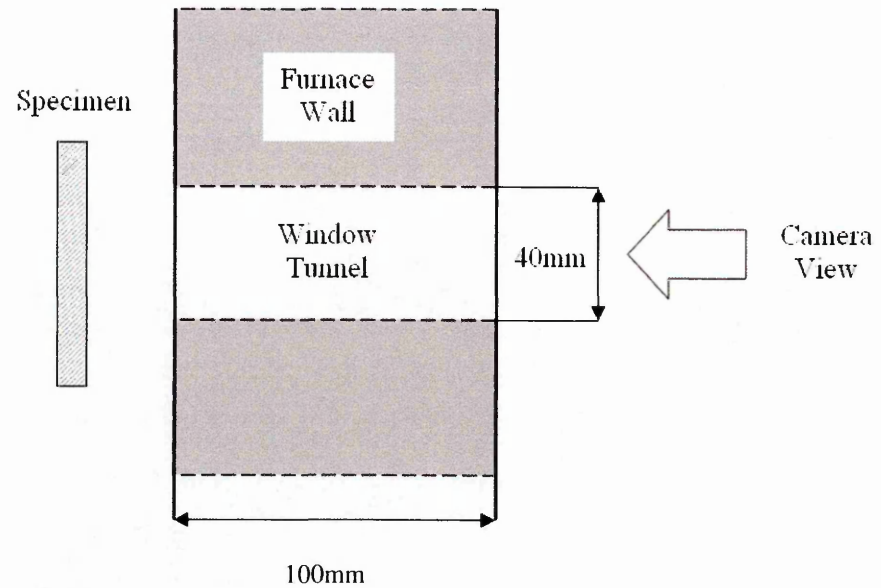

Figure 4.10 Furnace window profile with a long hole tunnel

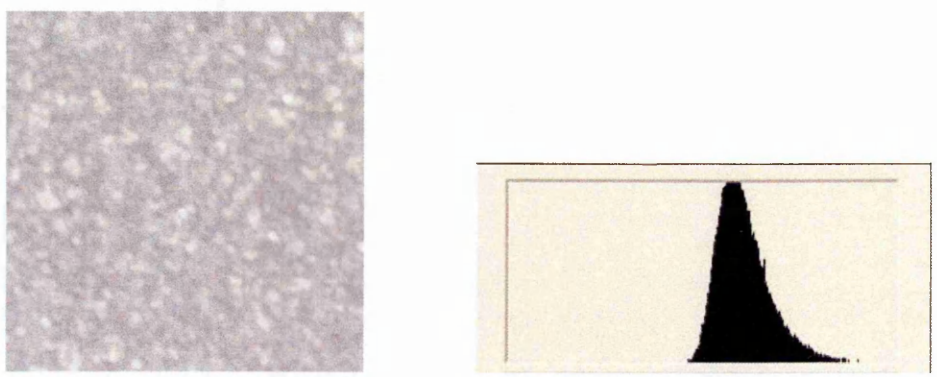

Old system with the fibre optic light source

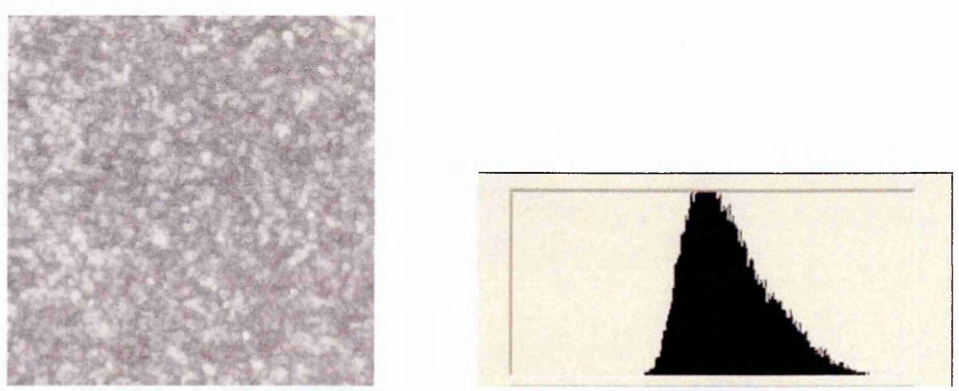

New system with the strobe flash light source

Figure 4.11 Image comparison of old and new lighting systems with histograms

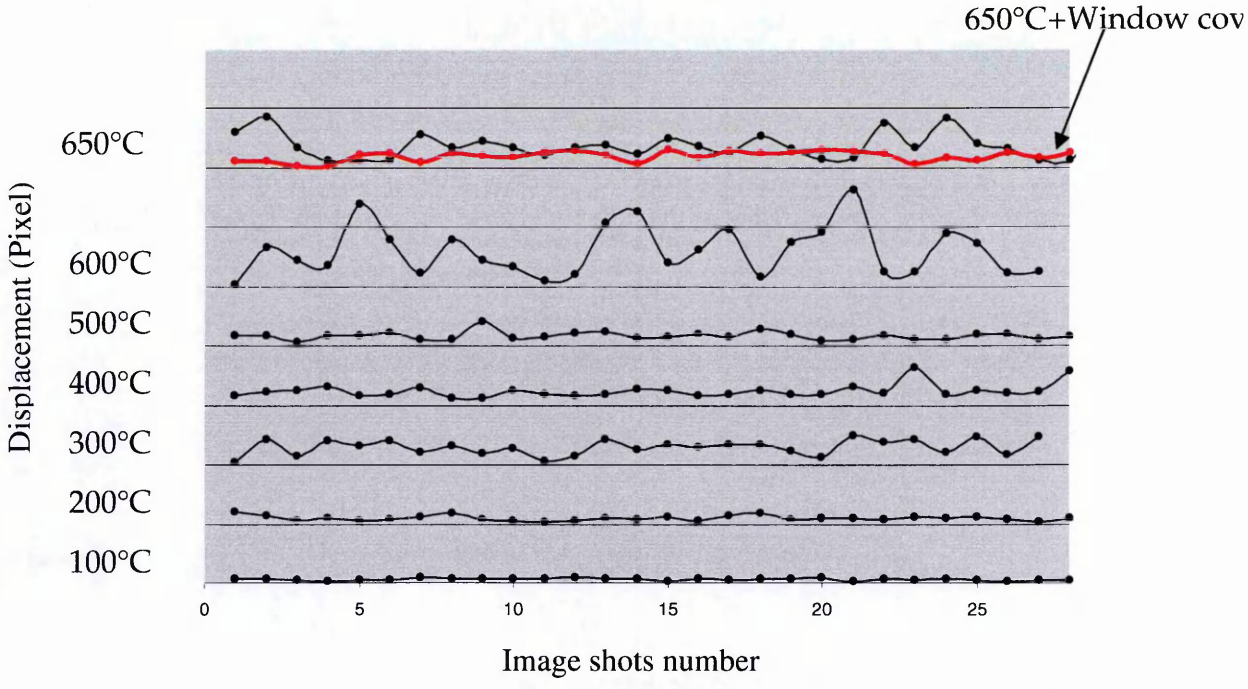

Figure 4.12 Effect of thermal currents on image distortion, measured variation at temperature between 100°C to 650°C and window cover effect (Red line)

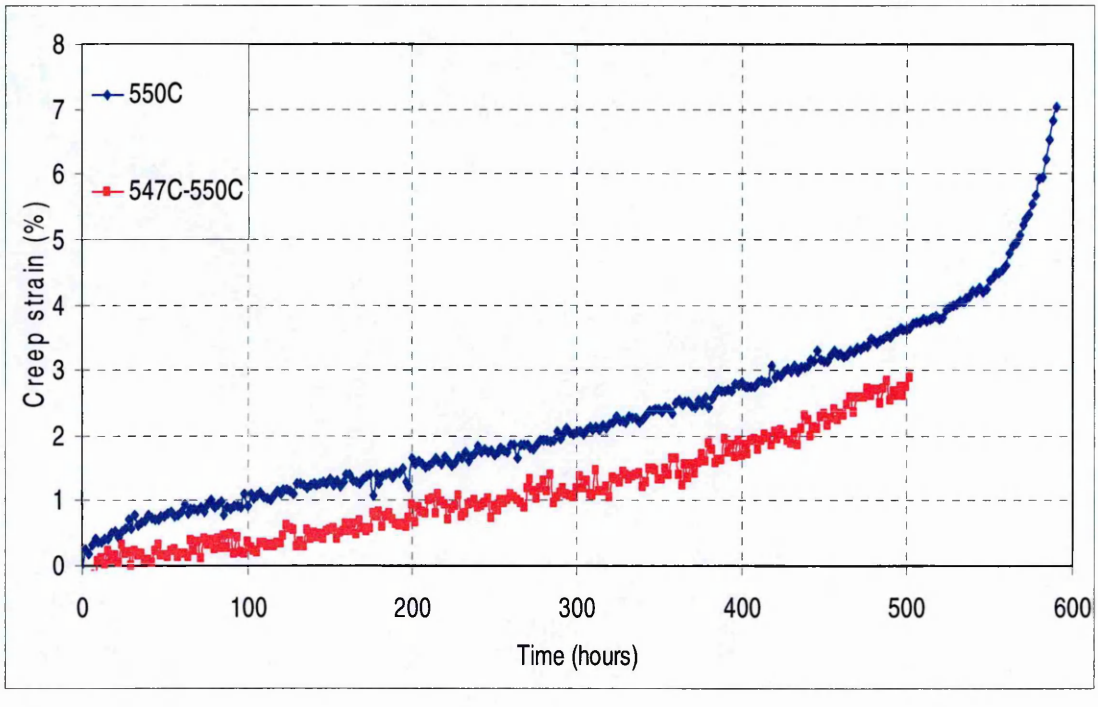

Figure 4.13 Creep curves at temperature 550°C (Blue)and temperature variation between 547°C to 550°C (Red)

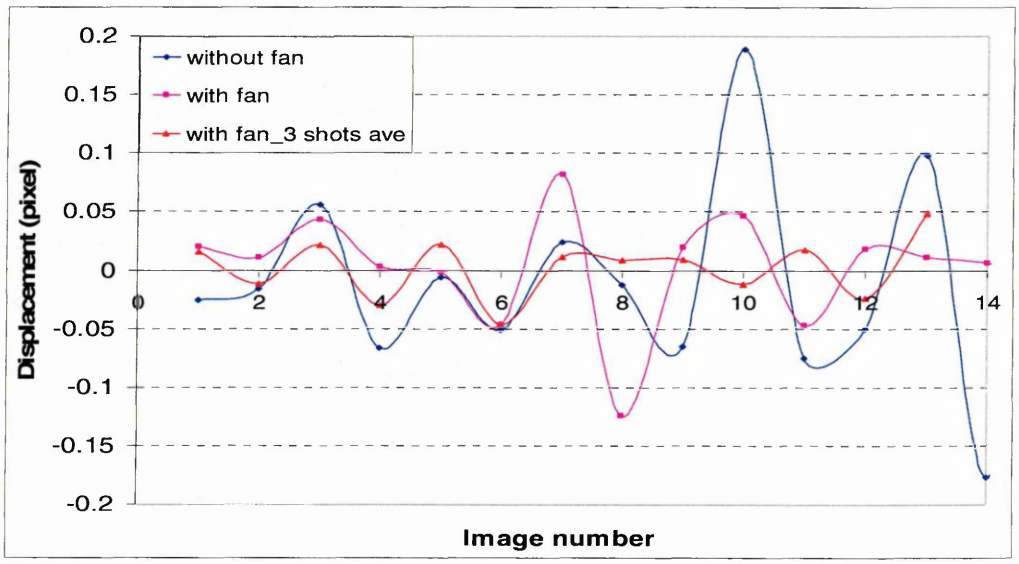

Figure 4.14 Measured displacement on a specimen with no load at 550°C, without fan (Blue), with fan (Pink) and averaged image of 3 shots with fan (Red)

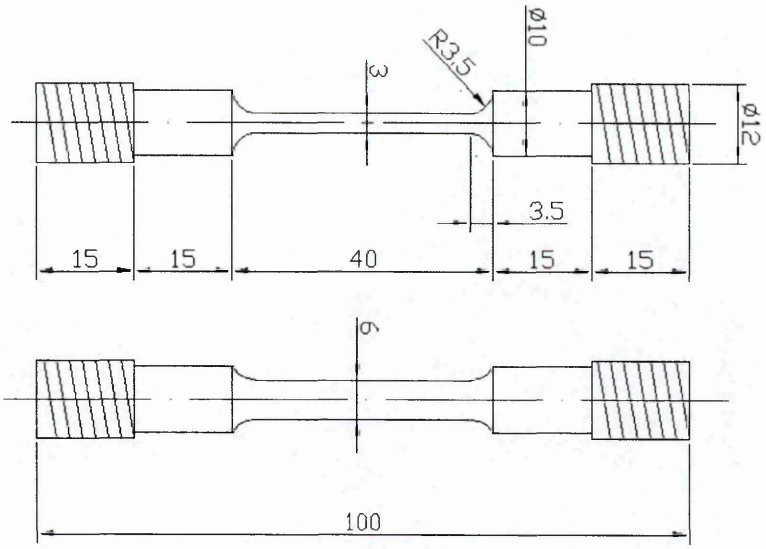

Figure 4.15 Initial specimen design

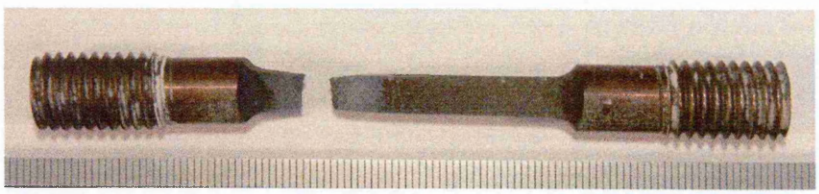

Figure 4.16 Initial design of test specimen showing creep rupture position at stress concentration

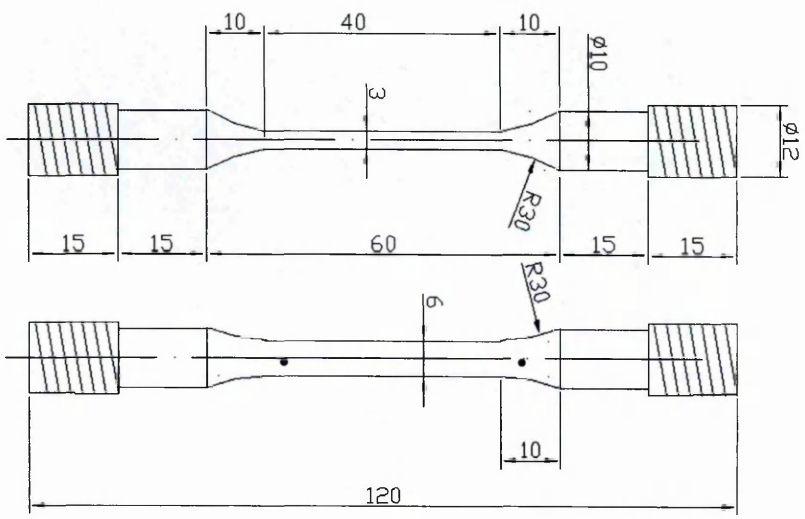

Figure 4.17 Proposed new specimen design

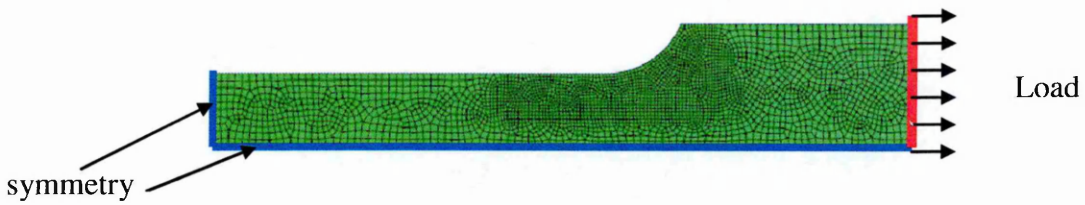

Figure 4.18 Mesh for Initial Specimen Design and Boundary Condition

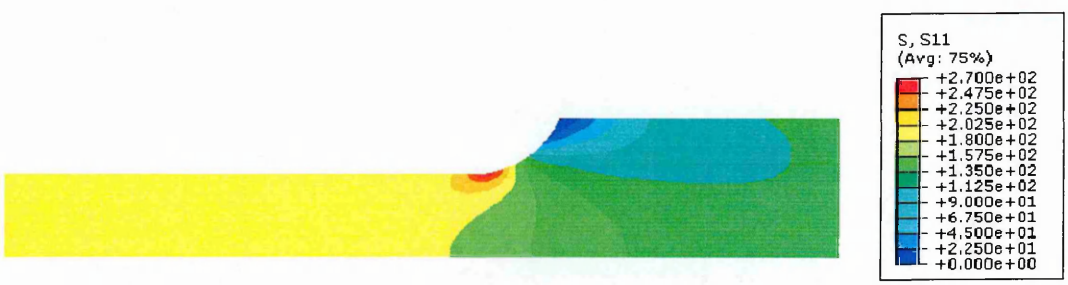

Figure 4.19 Contour plots of predicted stresses in the tensile direction of the initial design (Elastic analysis result)

Figure 4.20 Contour plots of predicted stresses in the tensile direction of the new proposed design (Elastic analysis result)

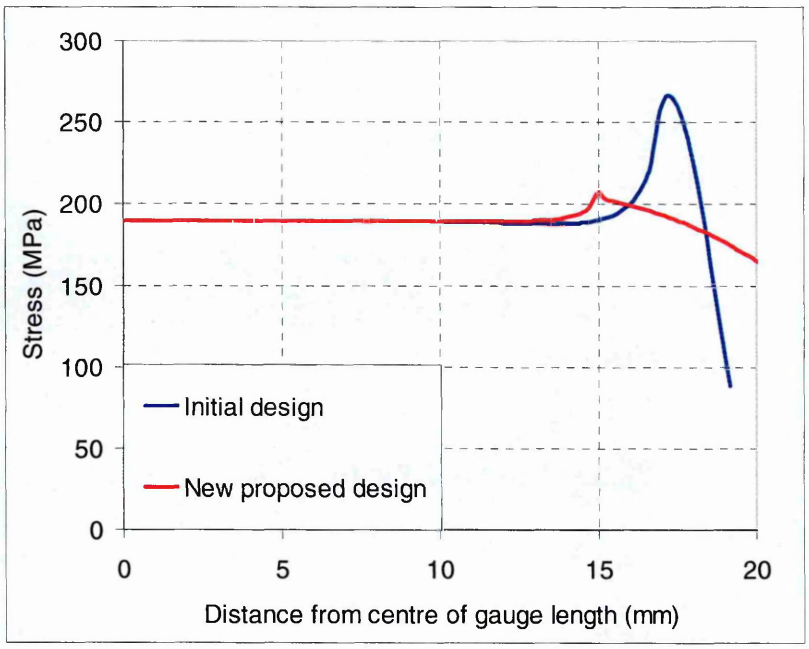

Figure 4.21 Line plots of comparison along specimen surfaces between the initial design and the new proposed design (Elastic analysis result)

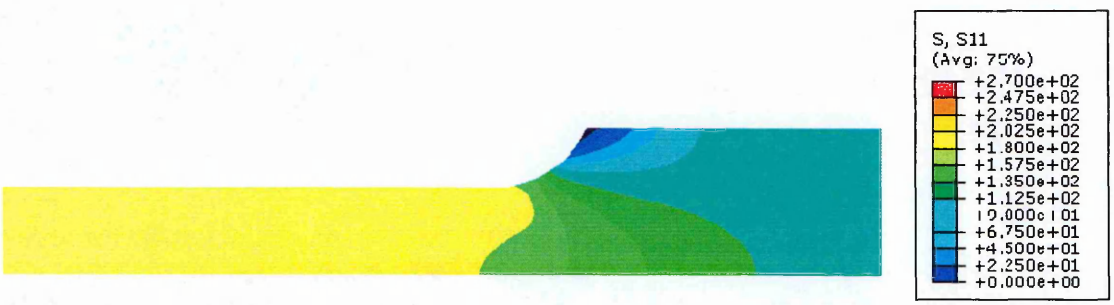

Figure 4.22 Contour plots of predicted stresses in the tensile direction of the initial design (Elastic-plastic analysis result)

Figure 4.23 Contour plots of predicted stresses in the tensile direction of the new proposed design (Elastic-plastic analysis result)

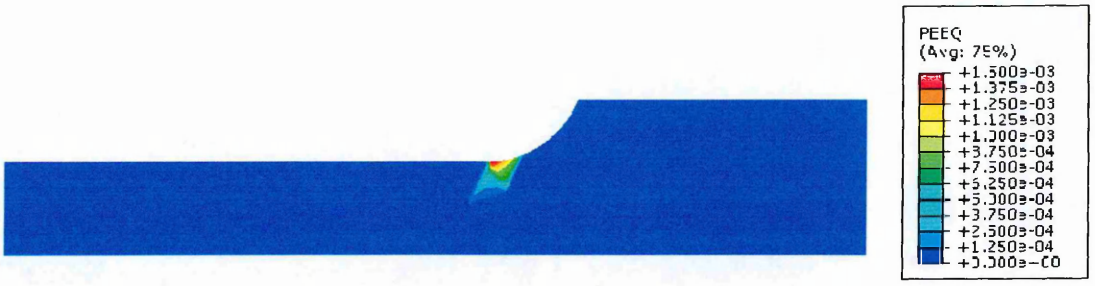

Figure 4.24 Contour plot of PEEQ in the tensile direction of the initial design

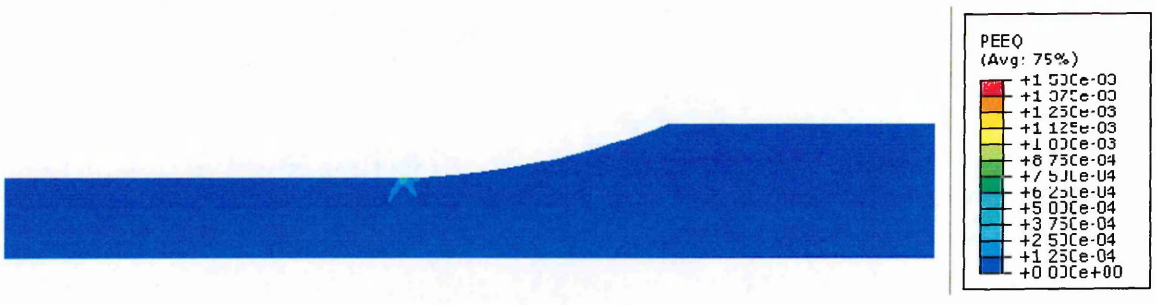

Figure 4.25 Contour plot of PEEQ in the tensile direction of the new proposed design

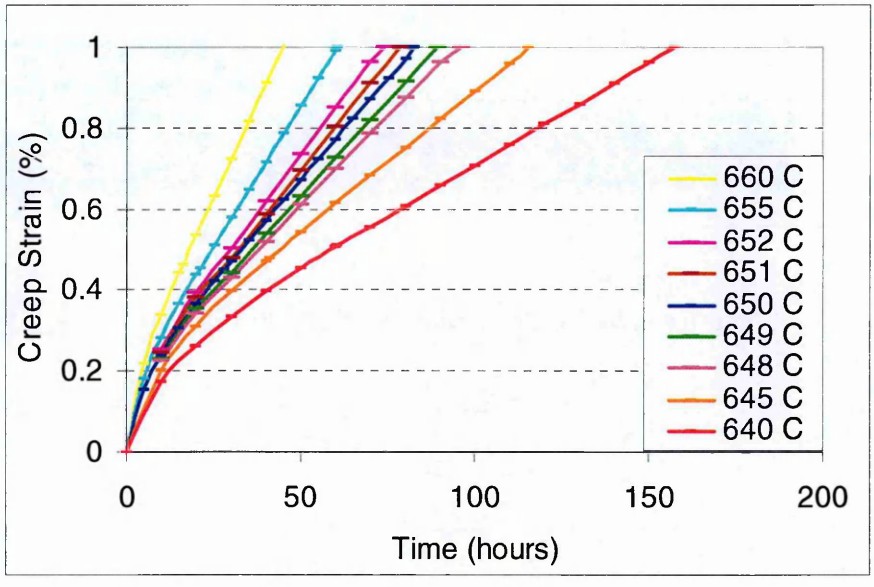

Figure 4.26 Predicted creep strain vs time curve at various temperatures

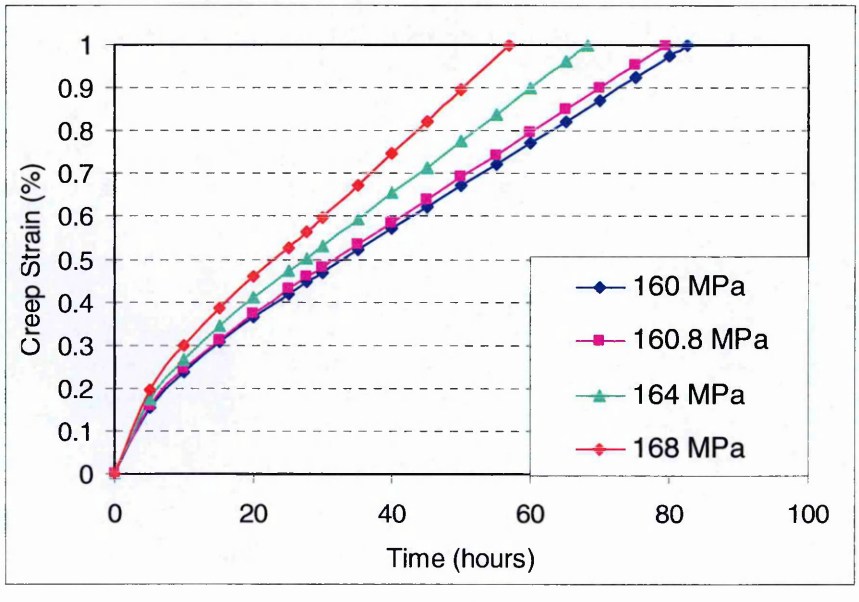

Figure 4.27 Predicted creep strain vs time curve at various loads (650 °C) –effect of specimen dimension

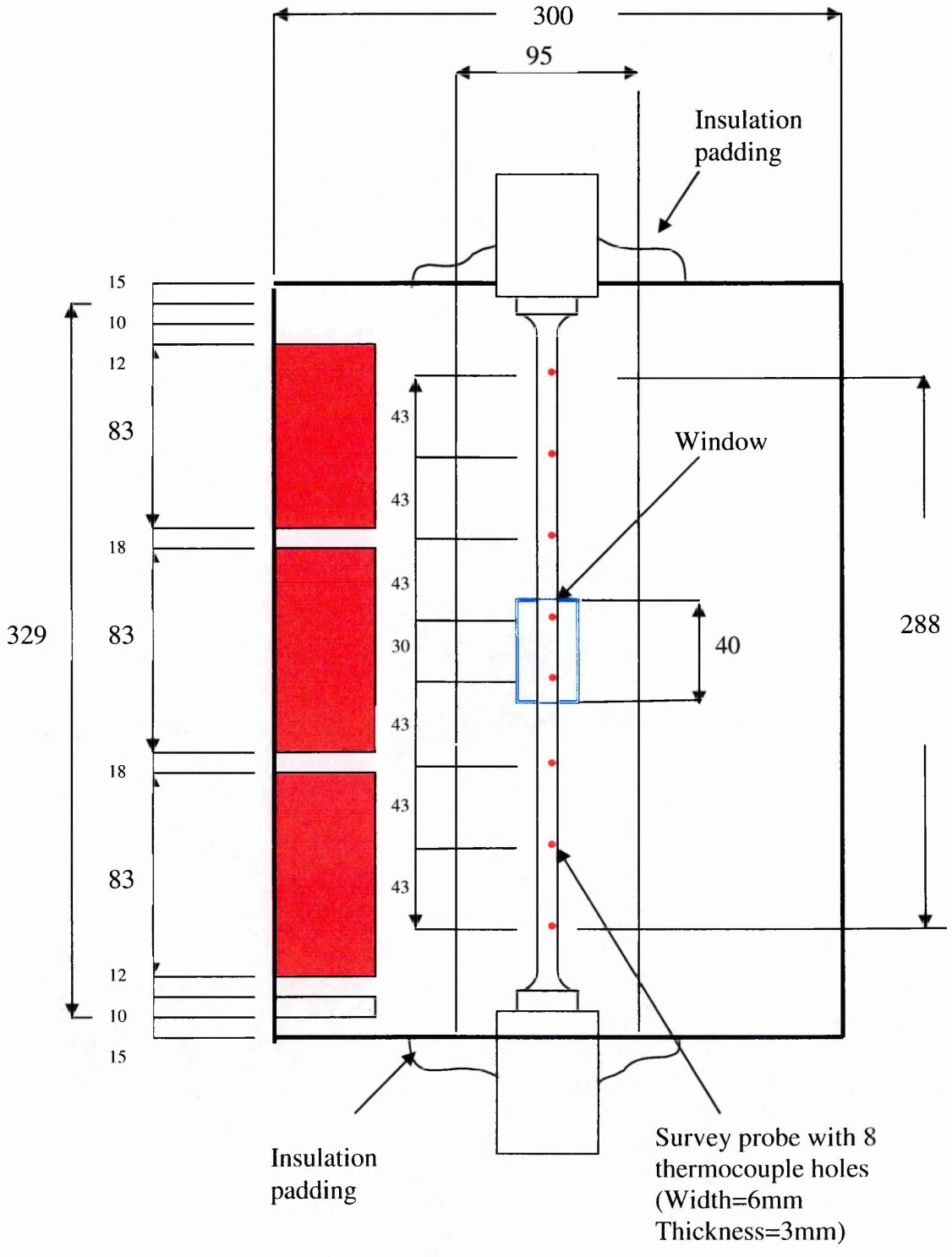

Figure 4.28 Sketch showing a cross section of the furnace with the temperature survey probe inserted (All dimensions are in mm)

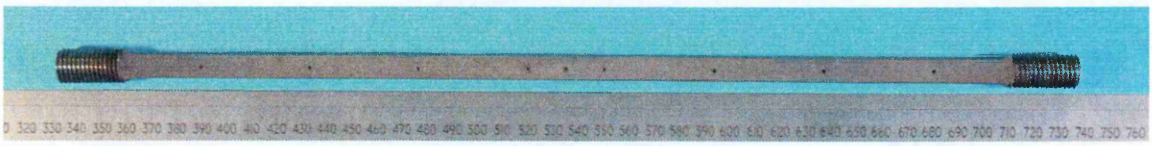

Figure 4.29 Furnace temperature survey probe

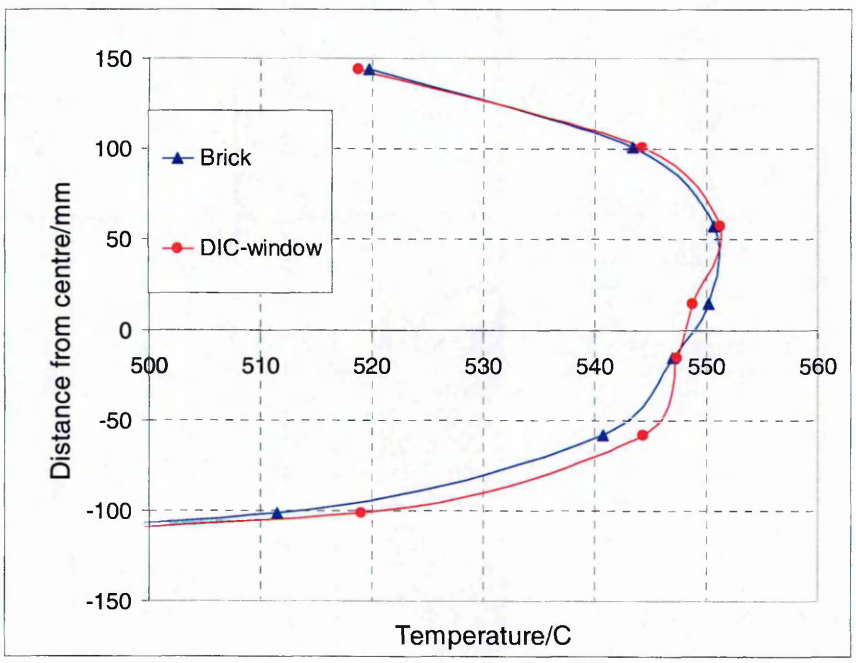

Figure 4.30 Temperature Profile with a blocked window and exposed DIC window at 550°C

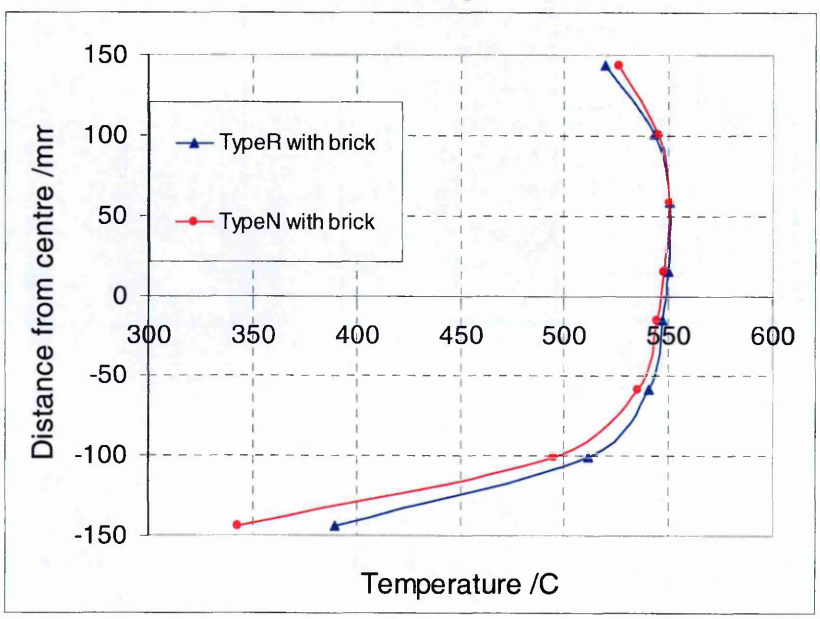

Figure 4.31 Comparison of temperature profile between Type R and Type N thermocouples with a blocked window at 550°C

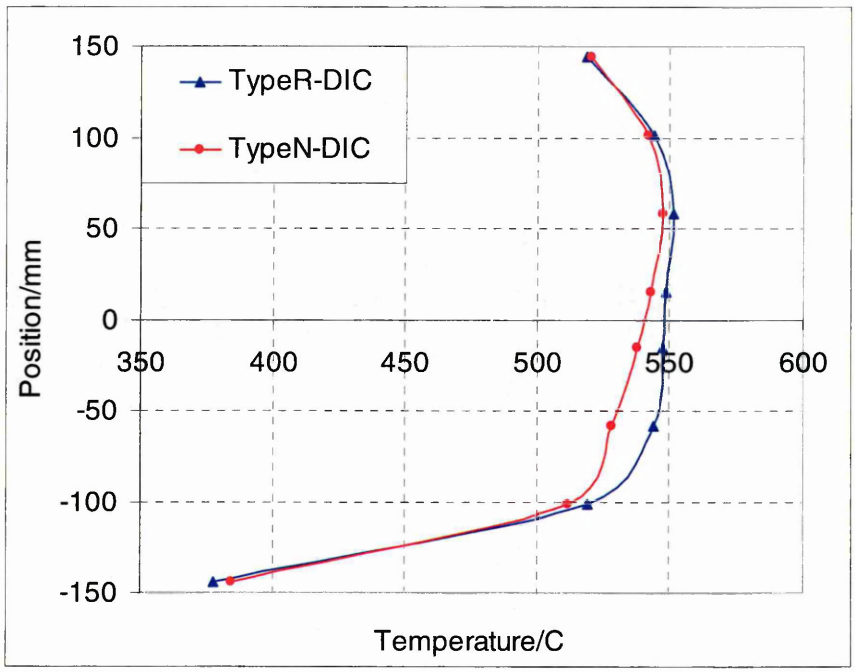

Figure 4.32 Comparison of temperature profile between Type R and Type N thermocouples with a DIC window at 550°C

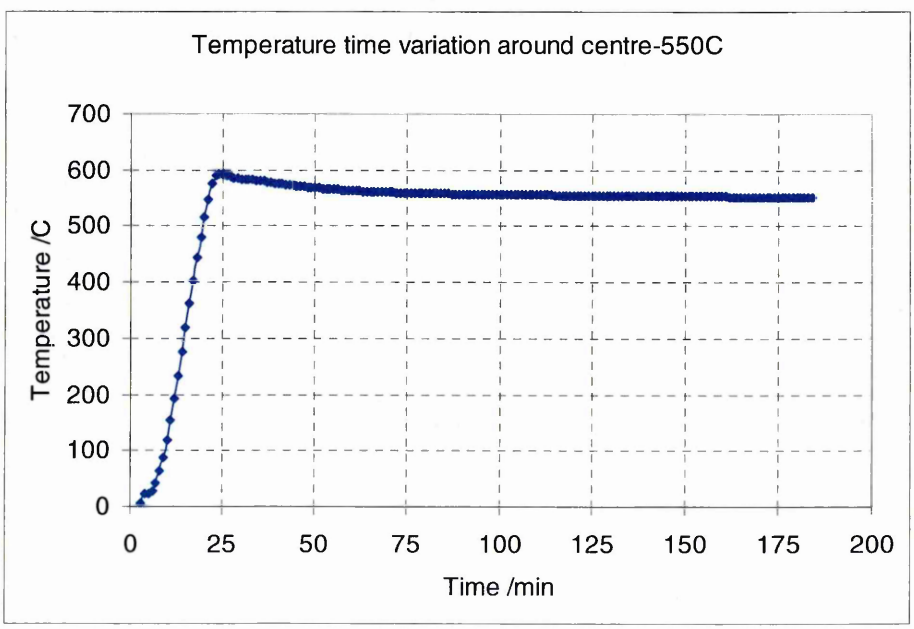

Figure 4.33 Temperature time variations around centre at 550C°

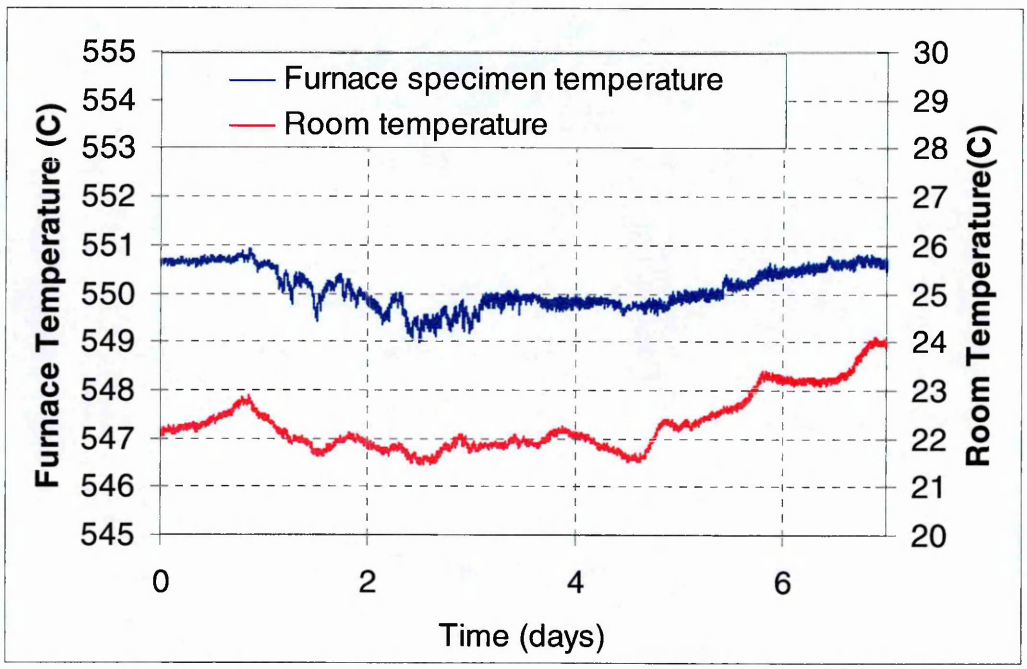

Figure 4.34 Variation of furnace and room temperature over 7 days

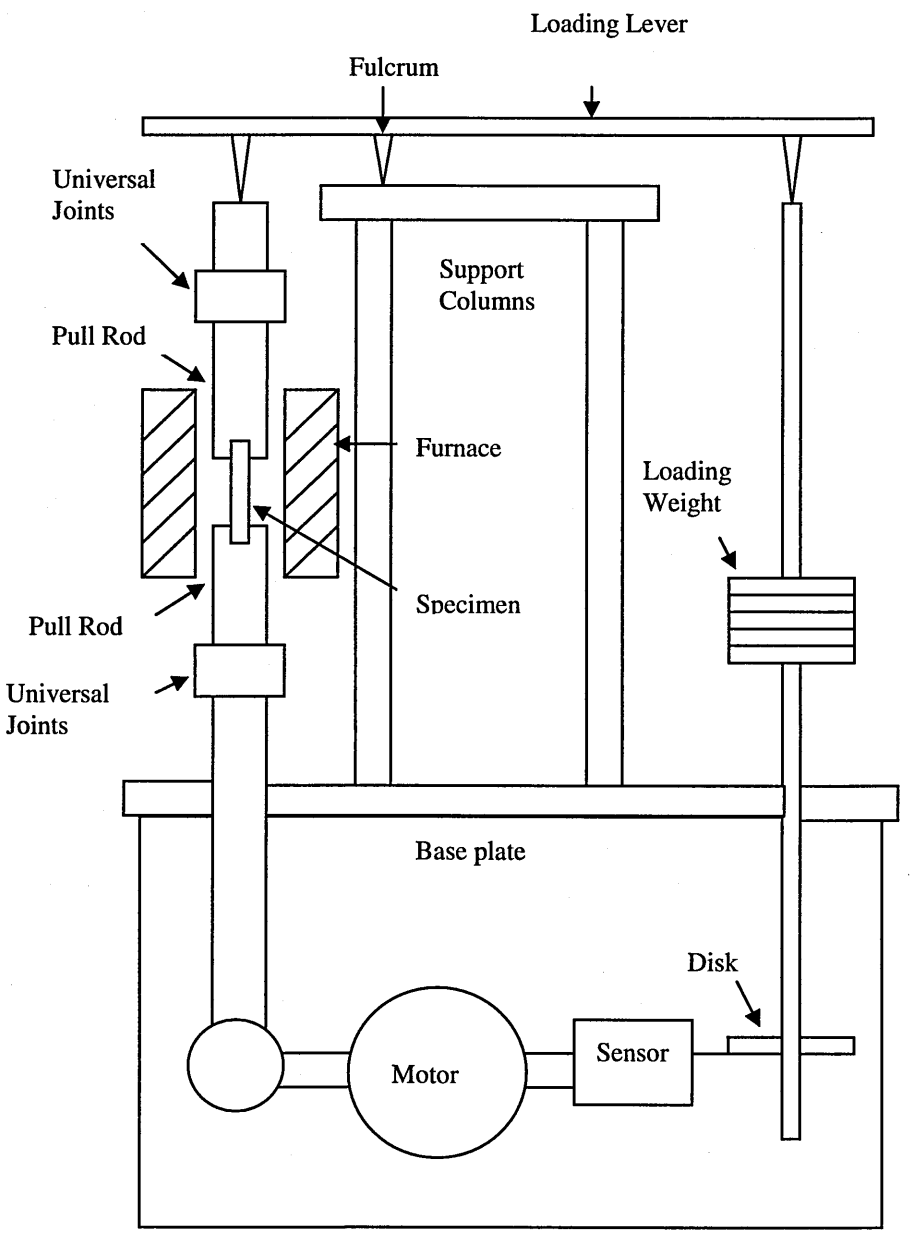

Figure 4.35 Schematic illustration of a creep test machine

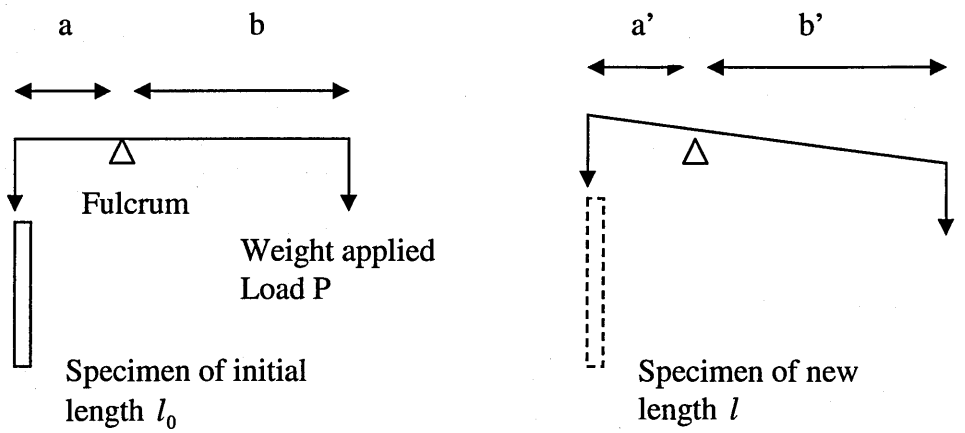

Figure 4.36 Schematic illustration of lever arm mechanism and after loading

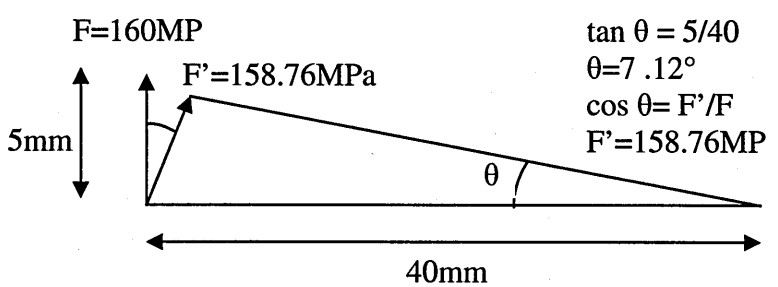

Figure 4.37 Example of simple calculation of lever arm

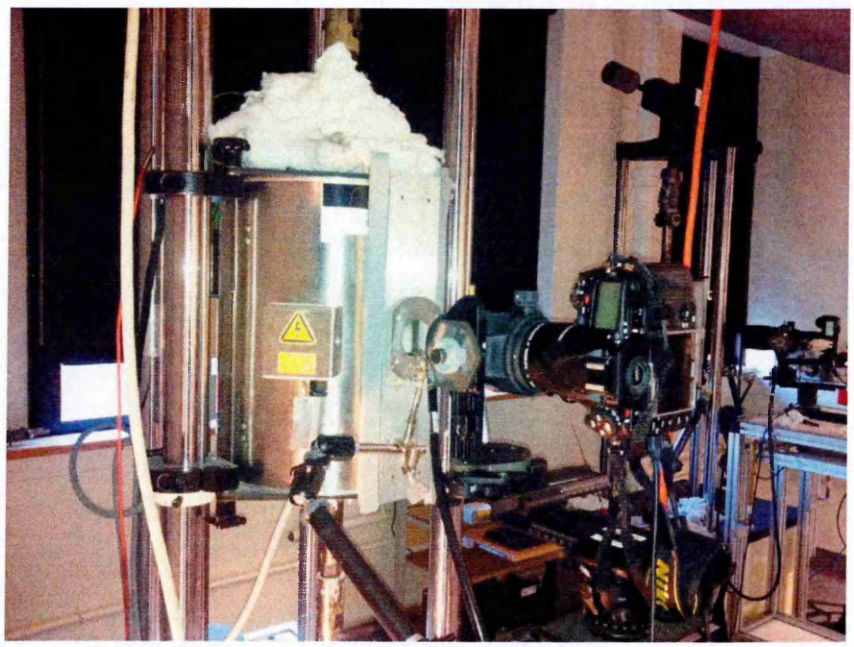

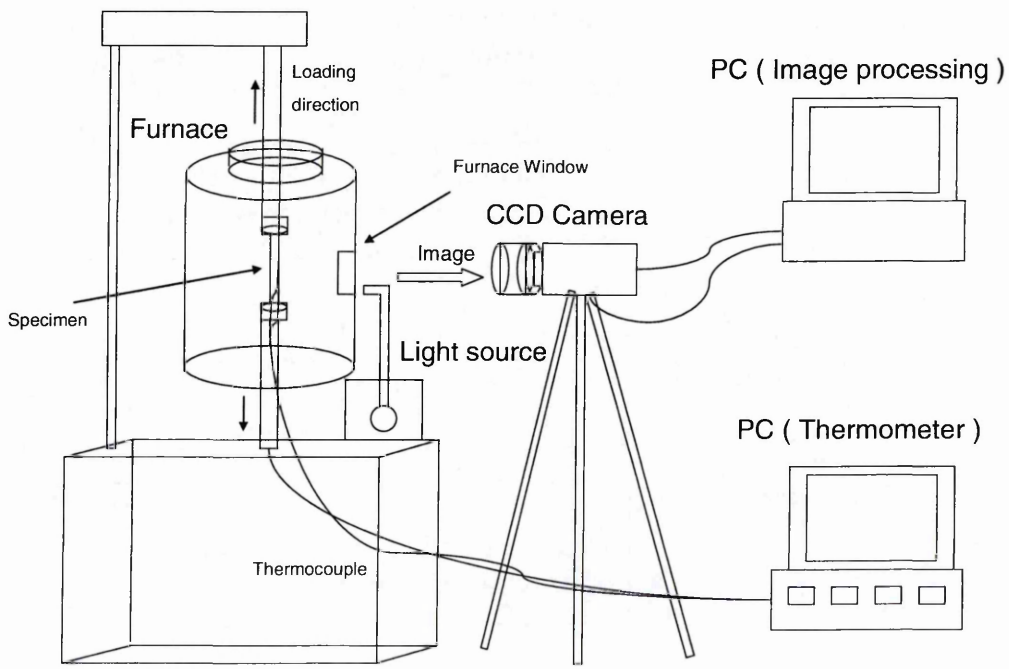

Figure 4.38 DIC high temperature creep deformation measurement system

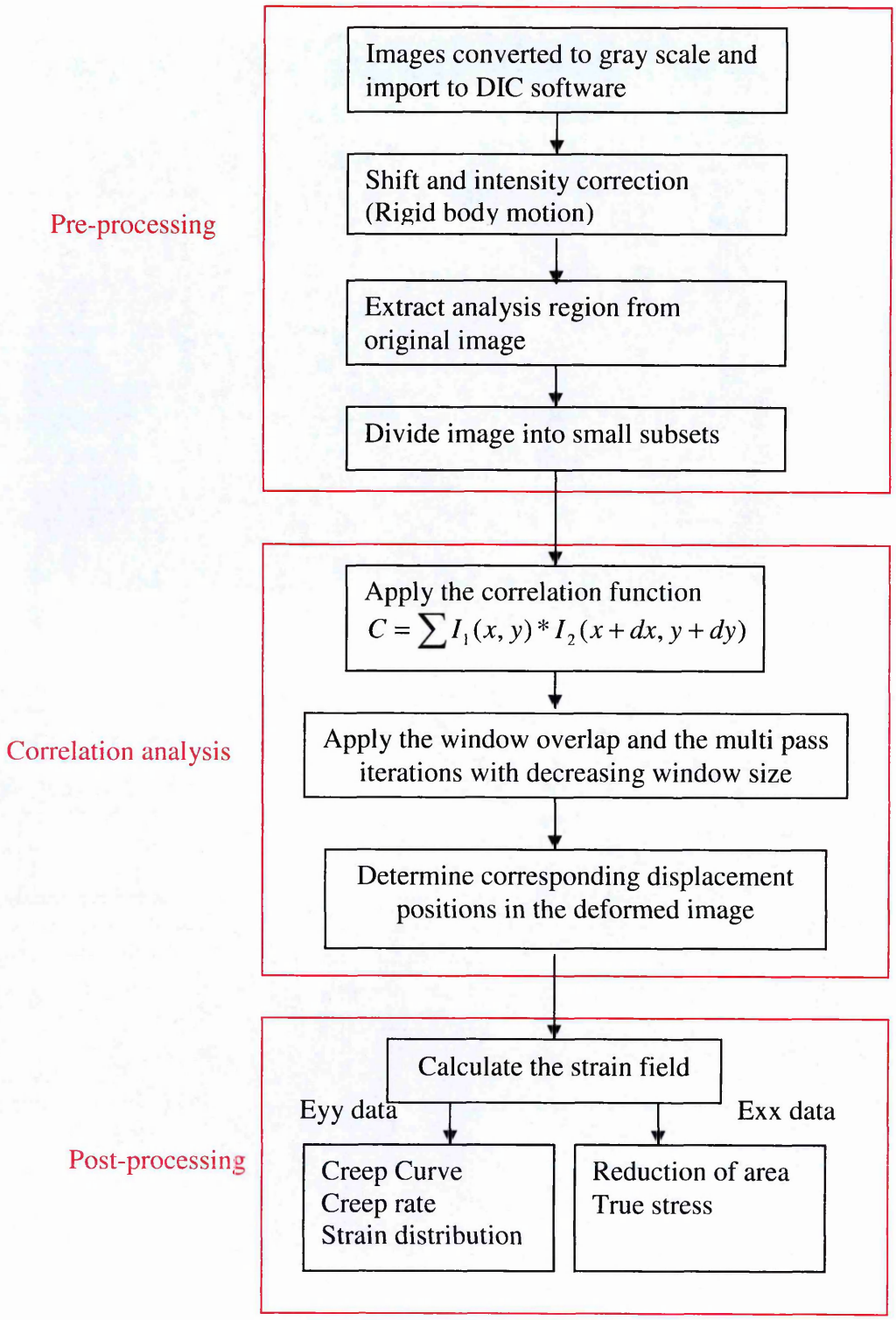

Figure 4.39 Schematic algorithm of DIC analysis procedure

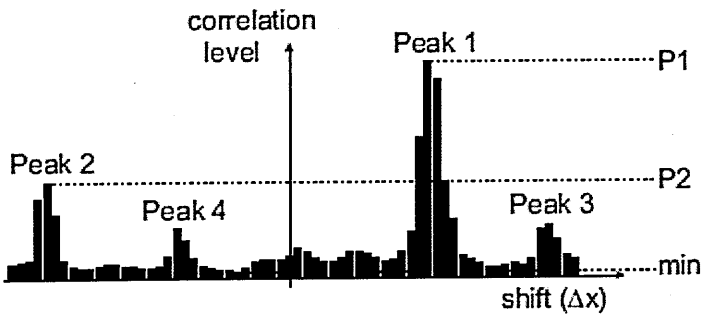

Figure 4.40 Localization of the four highest correlation peaks

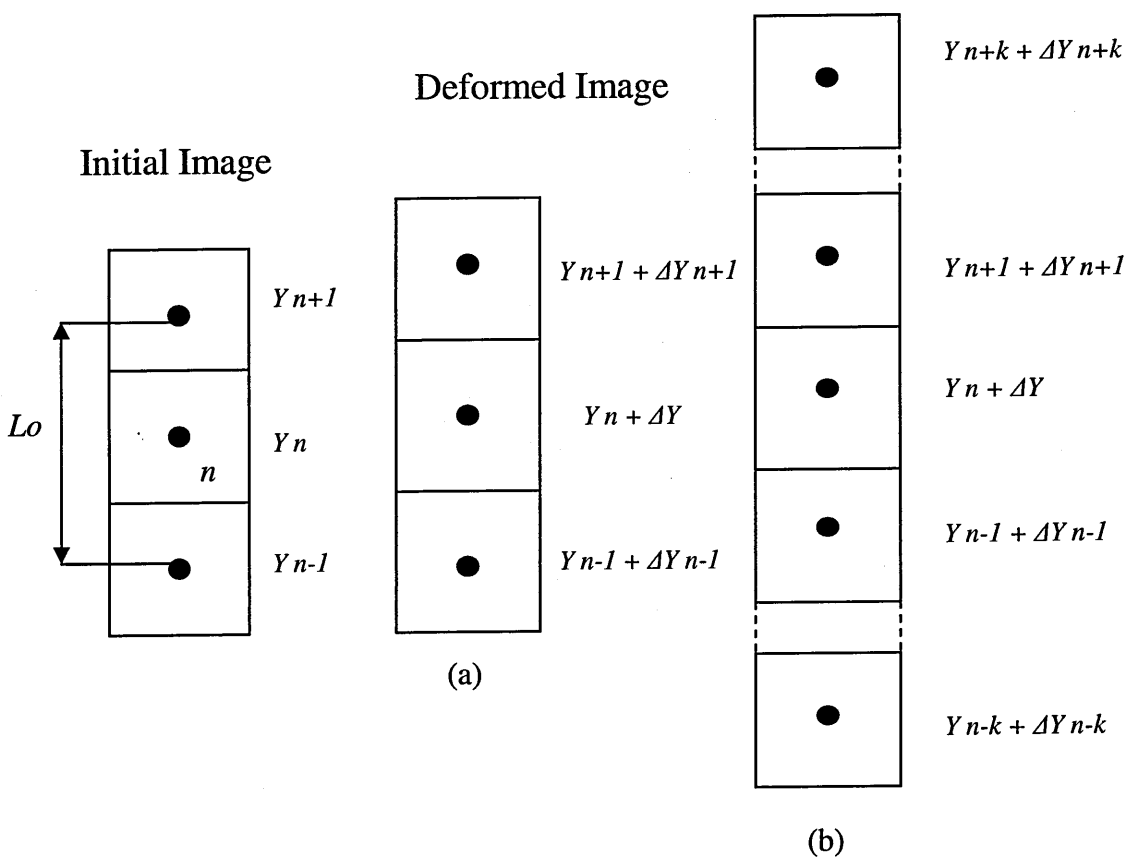

Figure 4.41 Method for strain calculation using Matlab program

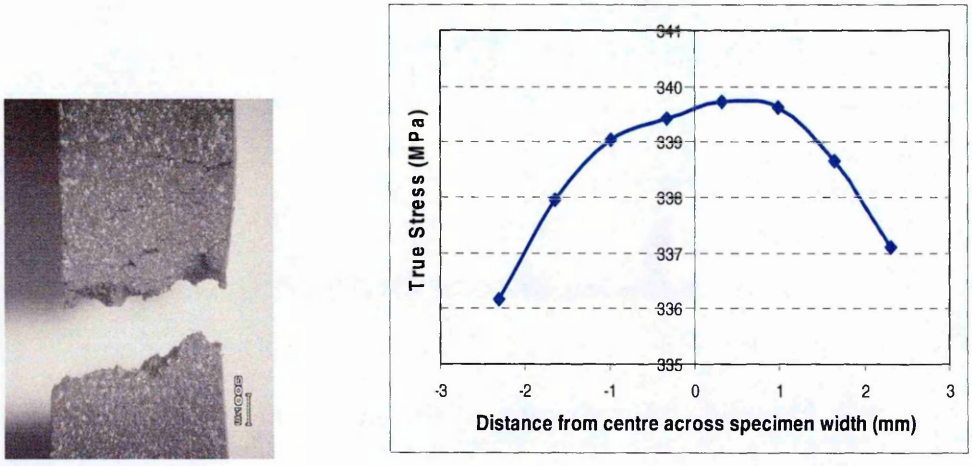

Figure 4.42 True stress distribution across the cross section

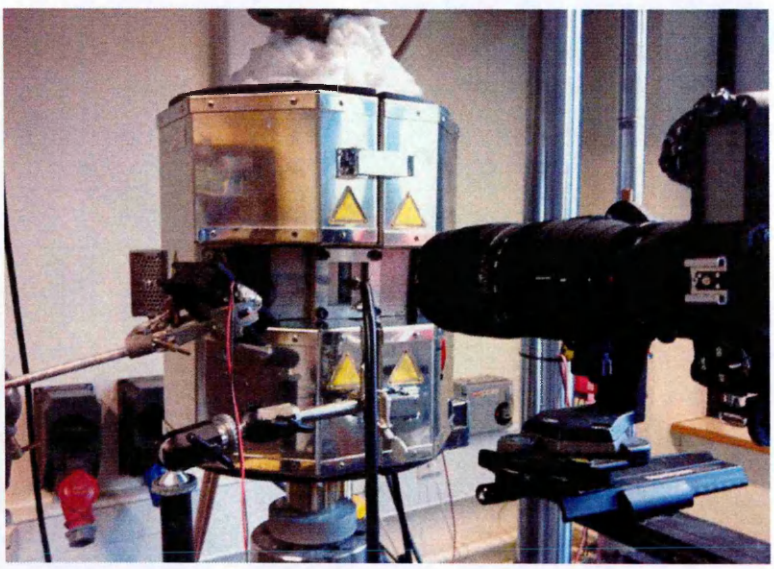

Figure 4.43 DIC high temperature tensile test measurement system

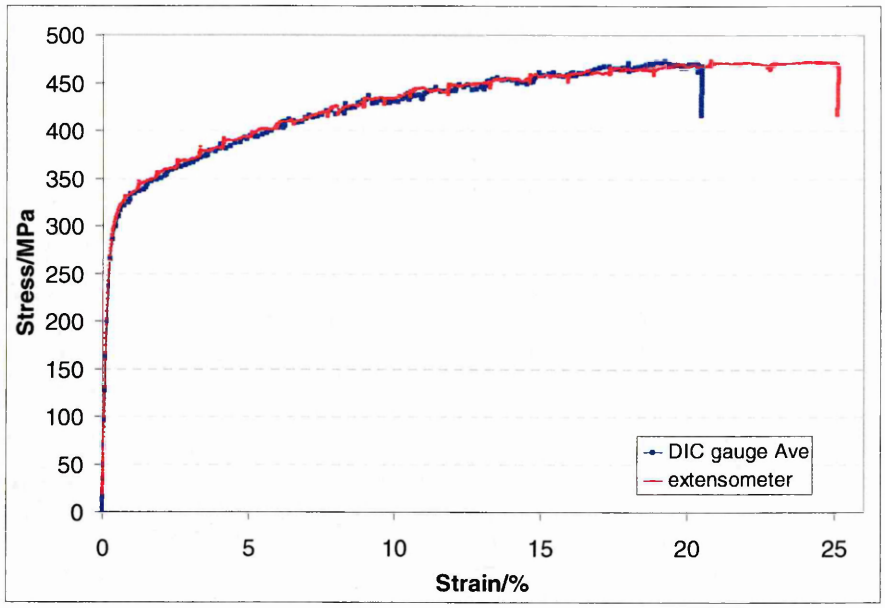

Figure 4.44 Comparison of stress-strain curve of average strain along the gauge length measured by DIC and extensometer

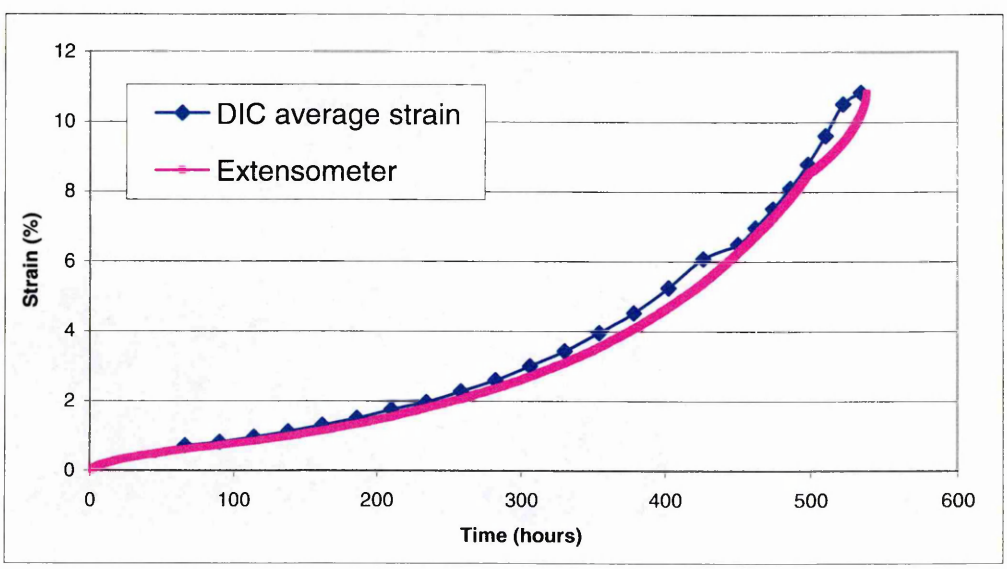

Figure 4.45 Comparison of creep curve of average strain along the gauge length measured by DIC and extensometer

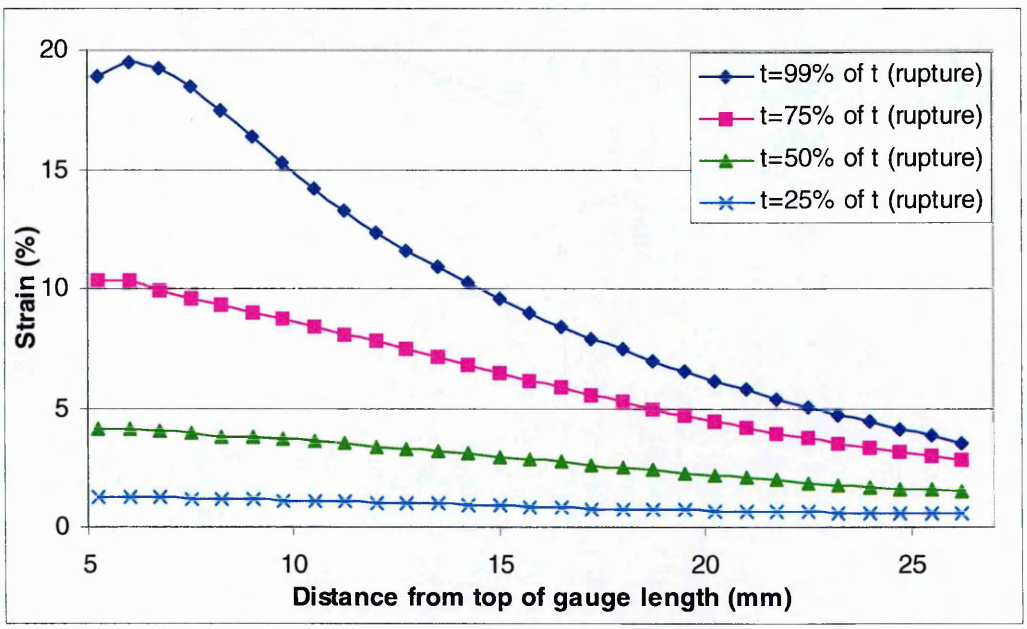

Figure 4.46 Strain distribution measured by DIC along the centre-line off the plane parent specimen

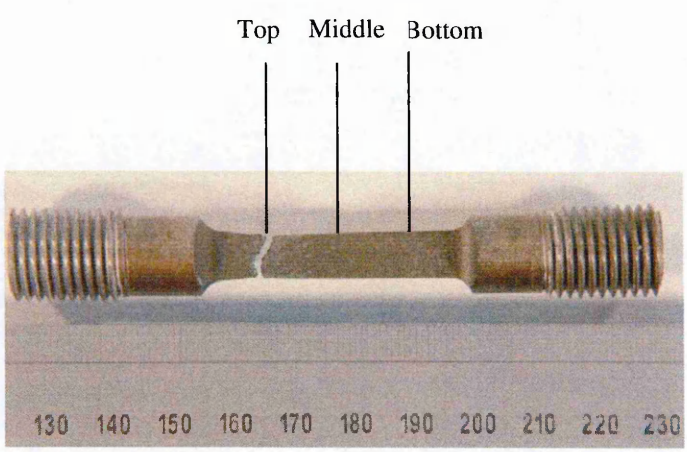

Figure 4.47 Fracture position in the plane creep specimen at 650°C under an applied stress of 160MPa.

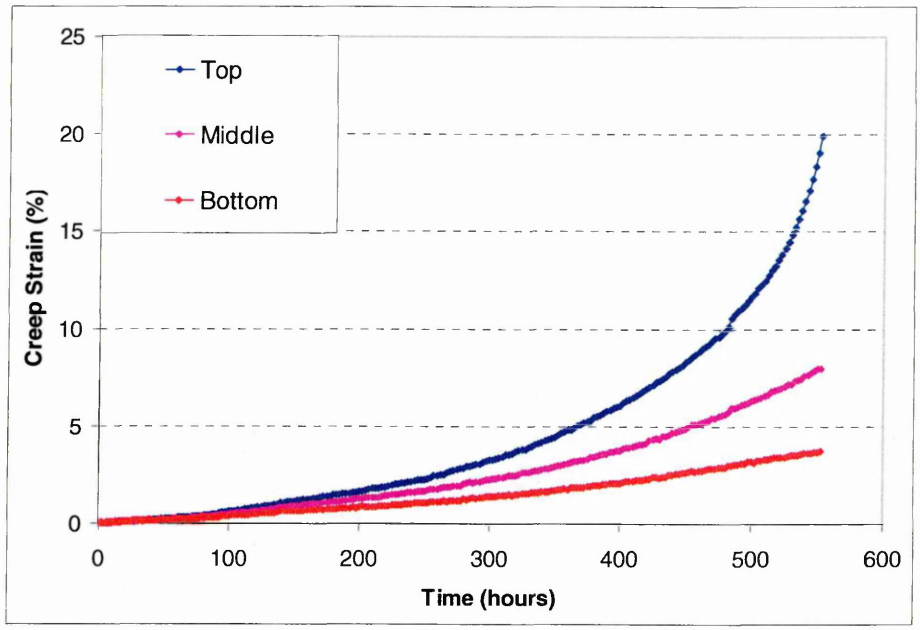

Figure 4.48 Comparison of creep curves at local positions, top, middle, bottom of the gauge length measured by DIC

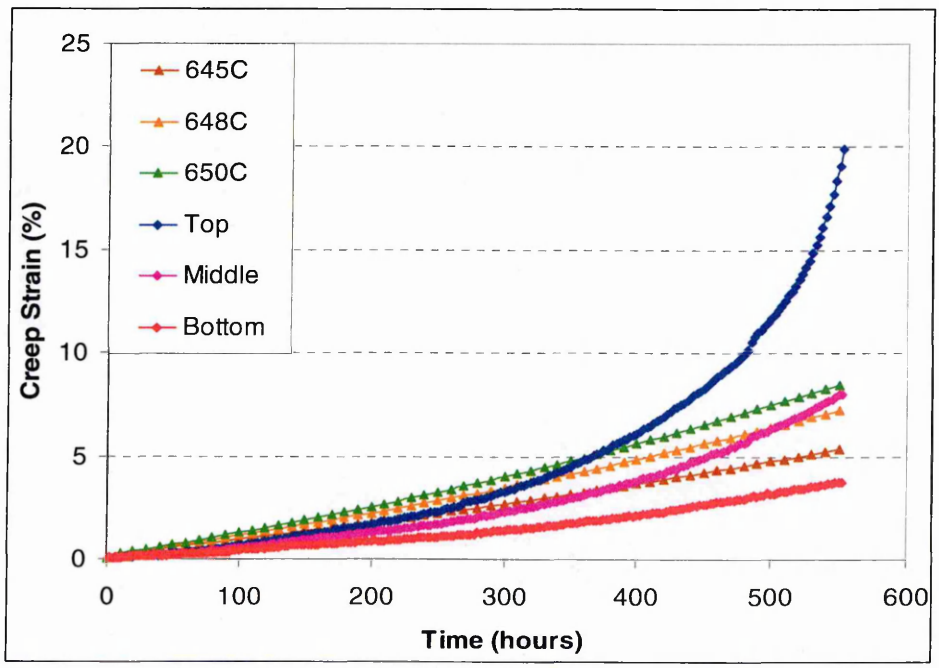

Figure 4.49 Comparison of creep curves at local positions, top, middle and bottom of the gauge length measured by DIC with RCC-MR law calculation results at temperature 645C°,648C°and 650C°

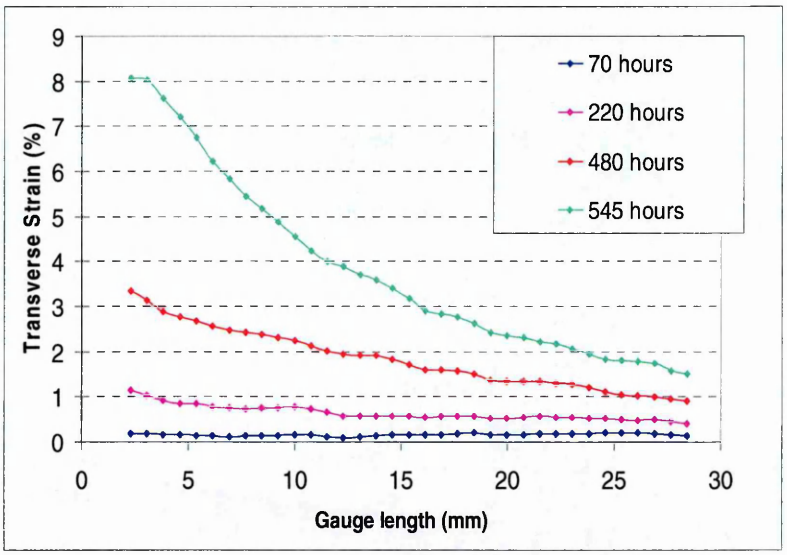

Figure 4.50 Transverse strain (ε_{xx}) distribution along the specimen length

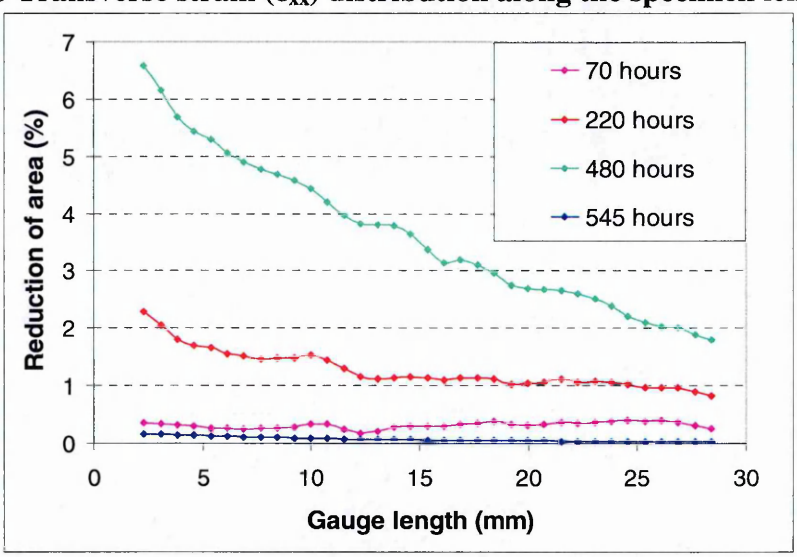

Figure 4.51 Reduction of area computed by Transverse strain horizontal direction (specimen width)

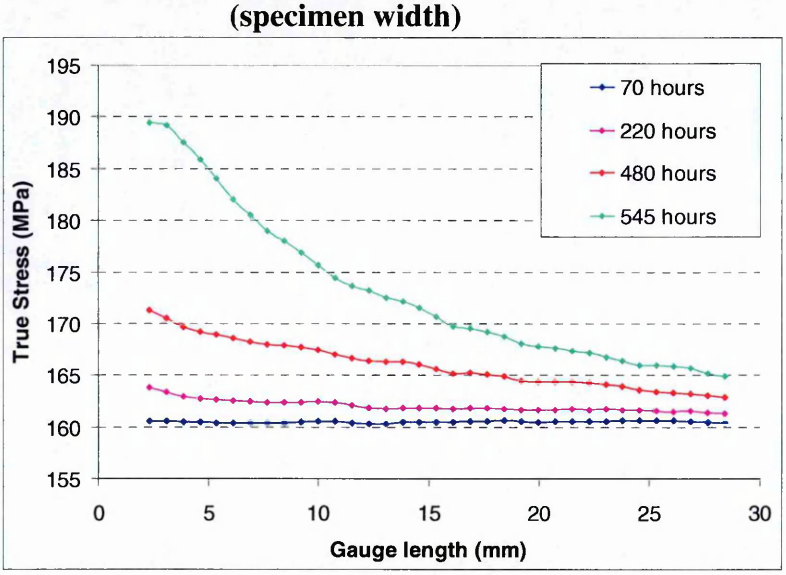

Figure 4.52 True stress distribution along the gauge length

Chapter 5

Application to a Multi-pass Welded Joint

5.1 Introduction

Welded joints are the most vulnerable regions of a structure owing to the local metallurgy which may be inferior, altered mechanical properties, residual stress and the presence of welding defects. It is desirable to quantify the mechanical deformation properties of a welded joint in order to develop more accurate methods for predicting its life and integrity [1][2]. This is especially the case when joints are exposed to high temperature operating environments where creep deformation mechanisms prevail.

A thick section multi-pass welded joint is a structure in its own right, across which tensile and creep deformation properties will vary. If better models characterizing the behaviour of such welds are to be developed, it is vital that the local deformation properties across the weld can be measured at low and elevated temperature.

The objective of this chapter is to demonstrate how the DIC based experimental technique developed in the present work can be applied to measuring the local deformation behaviour of a thick section multi-pass stainless steel weld. The behaviour has been quantified by testing cross-weld specimens from a zone near the weld cap (top position), from the central region (middle

position) and from the zone near the root (bottom position) of a 65mm thick weldment (Figure 5.1) at room temperature and at elevated temperature (545°C).

This chapter is set out as follows. First, the test weldment is described. Secondly, the methods used are briefly reviewed with details of the test specimens. Thirdly, the hardness, tensile stress-strain and creep deformation test results are presented. An extended discussion is then presented comparing the measurements and attempting to relate the observed variations in properties across the parent, HAZ and weld metal, and also through the thickness of the weldment, to the geometry of the weld and the welding history.

5.2 Test Weldment

The material for the present test work was supplied by EDF Energy. Test samples were extracted from an AISI type 316H austenitic stainless steel thick section cylindrical butt weld of outer diameter 430mm and 65 mm wall thickness as shown in Figure 5.1. The weldment has an unusual geometry with a 45° wall preparation on one side and a 0° (vertical) wall angle on the other (reference figure 5.2). It was specifically designed this way by EDF Energy so that compact tension specimens could be extracted for other test work. The weld was made using 316L austenitic stainless steel wire with 129 passes and 26 layers starting at the root (bottom surface). The weld pass sequence moves from right to left and finishes at the top left angled weld preparation surface, as shown in Figure 5.2. A GTAW (Gas Tungsten Arc Welding) process was applied for the root run (the first pass as shown in pink in Figure 4.2) using a 2.4mm diameter TIG wire and completed to

required dimension using a SMAW (Shielded Metal Arc Welding) process with a MMA (Manual Metal Arc) electrode.

Cross-weld specimens were extracted from three different locations, top, middle and bottom positions of the thick section weld (Figure 5.1), in order to compare creep properties which might be related to the multi-pass welding thermo mechanical history through the thickness of the joint. The DIC creep and high temperature tensile specimen design has been described previously in Chapter 4.2. The DIC measured surface is face up to the top surface of the welded joint. Specimens were cut from the top and middle positions with the vertical fusion boundary at the centre of each sample gauge length to ensure the camera fields of view sampled the HAZ as well as parent material and weld [3].

5.3 Experimental Methods

5.3.1 Hardness

Hardness measurements can provide an approximate indication of the material yield properties of stainless steel [4]. The hardness variation across the supplied weldment was mapped with the aid of an automated Struers Duramin-A300 hardness testing machine. The sample surface was first prepared by grinding with 120, 220, 500, 800, 1200, 2500, 4000 grades of wet and dry papers and polishing with 1-WP, 3-WP, 6-WP size of diamond particles in suspension. Then the sample surface was electronically etched in 60% nitric acid solution for 10min with an electric potential of 2V. The Vickers hardness tests were performed using a load of 5 kgf with a grid spacing of 2mm.

5.3.2 Tensile cross-weld DIC tests at room temperature

Room temperature cross-weld tensile tests were carried out in order to characterize the mechanical stress-strain properties of the multi-pass welded joint. Three flat specimens for DIC tensile testing were cut from the top, middle and bottom positions of the weldment by Electric Discharge Machining (EDM). The specimen design is given in Figure 5.3, based on the ASTM E8/E8M Standard Test Method for Tensile Testing of Metallic Materials [5]. The gauge length is 70 mm, the width at the gauge section is 6 mm and the thickness is 3 mm. The measured thickness and width of each specimen are shown in Table 5.1.

An Instron screw-driven tensile testing machine was used with a calibrated 30kN capacity load cell with universal joint grips. The extension speed of the tensile test was set to 0.1mm/min and all tests were run until the specimens ruptured. The DIC technique described in Chapter 2.3 was applied to measure the full field strain evolution in the tensile test specimens. A digital SLR camera with a full-frame CMOS sensor with 21 megapixels (Canon EOS 5D Mark2) and 150mm macro lens were used for the experiments. Images were acquired every 10 seconds in the elastic region and changed to 40 second intervals after yielding. Images were converted to 8 bit grey scale and exported to DIC software DaVis[6]. Details of the DIC analysis and post processing procedure have already been described in Chapter 4.6.

5.3.3 Tensile cross-weld DIC tests at elevated temperature

High temperature tensile tests were executed in order to measure the cross-weld mechanical deformation properties at 545 °C. The tensile specimen design employed the same dimensions as the creep test samples introduced in Section 4.2, the ends of the specimens had M12 threads for fixing into the testing machine and the gauge length was machined flat to give a cross-section 6mm wide by 3mm thick to provide a surface suitable for DIC measurement. Three specimens were extracted from the top, middle and bottom regions of the weldment (Figure 5.1) using EDM. The gauge length of the top and middle cross-weld specimens covered part of the weld and HAZ but the bottom specimen contained only one weld bead in the centre of the gauge length.

An Instron slow strain rate screw driven testing machine was used for this high temperature tensile test. The specimen was heated approximately 8 hours to 545°C and the test was executed with an extension rate of 0.1mm/min. Images were taken each 10 seconds in the elastic region and then changed to 40 second intervals after yielding. The test was loaded until the specimen failed.

Results from these tests are presented showing the mechanical properties across the weldment for a stress level of 315MPa, which is the same applied stress level used in the creep tests, see Section 5.3.4. Thus the strain distribution associated with this load should correspond to the instantaneous strain introduced during initial loading of the creep tests. In addition, the advantage of the DIC high temperature tensile test is that true stress true strain curves can be provided at any

subset region across the cross-weld, which is especially useful information for finite element simulation of weldment mechanical behaviour.

5.3.4 Creep DIC tests

All creep tests were carried out at a nominal temperature of 545°C. The design and sampling locations of the creep specimens was the same as for the high temperature tensile tests described in the previous section. Each specimen was placed in the middle of the furnace and vertically aligned to give the required view of the gauge section in the camera. The specimen was subjected to a constant load, which gave an initial stress of 315 MPa. Two thermocouples were attached to the specimen at the top and bottom, beyond the gauge length, using drilled small holes. Type R thermocouples were used for these tests. The temperature variation was kept within 1°C along the gauge length of the top and bottom position tests but this level of control was not achieved for the middle position test. Based on the ASTM E139 standard [7], the temperature variation should be maintained within 3°C for conventional creep tests.

Thermal currents caused by temperature gradients inside the furnace make it difficult to obtain stable images and this produces scatter in acquired creep data. Therefore, minimizing temperature variations along the gauge length is significantly more important for DIC creep tests. The specimen was heated approximately 8 hours in order to stabilize the furnace temperature and thereby minimise this problem.

The specimen surface was illuminated using a fibre optic light bundle, which was coupled to a strobe flash unit triggered by the digital camera. Images of the specimen surface were taken during tests at regular intervals, 1 hour for primary and secondary creep phases and 15 minutes for tertiary, using time-lapse photography software. The acquired images were analyzed for creep tests lasting up to 3 months duration.

5.4 Results

5.4.1 Hardness

Hardness results mapped across the entire multi-pass weldment are shown in Figure 5.4. The area of multi-pass weld metal is clearly indicated by hardness values greater than 220HV on the map. The variations across the top, middle and bottom locations in the horizontal direction are shown in Figure 5.5. The hardness of the parent material at the top and middle positions (x=0-28mm) reduces to a value of approximately 170HV, and the weld varies between values of approximately 220HV and 250HV. The middle line weld values are slightly higher than the top position. The variation along the bottom line is almost symmetric because it includes HAZ and parent material on both sides of the weld. Figure 5.6 shows the variation in the thickness direction along vertical lines x=-20mm, -10mm, 0mm, 10mm, 20mm. The x=0mm line corresponds to the weld fusion boundary.

5.4.2 Tensile Cross-weld DIC Tests at Room Temperature

Figure 5.7 shows a photograph of the ruptured specimens from the room temperature tensile tests, sampling material at the top, middle and bottom of the weldment. The top and middle specimen ruptured at the extreme left hand side of the multi-pass weld, and the bottom specimen ruptured in parent material well to the left of the weld (note this specimen includes only one weld pass in the centre of the gauge length). Table 5.2 summarizes the final elongation, test duration to rupture and analyzed image numbers of each specimen. The test duration of the bottom specimen was significantly longer than the top and middle specimens. The average elongation of the middle specimen was only 5.8% but both the top and bottom specimens ruptured at higher elongations of 10.4% and 11.7% respectively. Figure 5.8 shows an example of DIC test images at different stage and corresponded to their strain vectors and contour full field maps, results is from middle position test.

Figures 5.9 to 5.11 show measured strain distributions along the test specimens for the top, middle and bottom positions of the multi-pass welded joint, for applied stress levels of 300MPa and 525MPa (plastic region) and the final distribution from the last images prior to rupture, respectively. It is worth mentioning that the top position test was repeated, because in the first test the specimen ruptured at a position out of the field of view of the camera. The repeat test was executed. In addition, it was attempted to take images of the expected rupture location. Extending the field of view in this repeat test gave results from a longer span of the gauge length than for the middle and bottom location tests.

The strain evolution across the specimen gauge length varies depending on the specimen position (top, middle, bottom). The strains are essentially elastic in the weld metal region up to a stress level of 300 MPa, but at this stress, strains in the parent material are high for the middle and bottom specimens. After the weld metal has yielded, at 525MPa, the strain variation in the weld metal becomes more significant. The strain in the first weld bead deposited in a layer (x=0 to 6mm) has smaller values than elsewhere along the gauge length of all the specimens, top, middle and bottom. The strains in the weld metal of the top and middle specimens vary with location in the weld whereas in the bottom specimen, which contains only one weld bead weld at the root in the middle of the specimen, the strain becomes larger on both sides in the parent metal. Comparing the strain in the first pass of each weld layer shows that greater strain is accumulated in the bottom specimen than in the top and middle specimens (see 1st pass weld region indicated in Figures 5.9 to 5.11). In the HAZ and parent material greater strains develop in both the bottom and middle specimens.

Figures 5.12 and 5.13 show the stress-strain curves in parent material at locations x=12mm and x=18mm for each specimen. Although the parent material properties remote from the weld should be the same, it is seen that yield stress at the top position (Fig 5.12 and 5.13) is slightly higher than the middle and bottom positions. A similar variation is observed in the hardness measurements (Figure 5.5).

Figure 5.14 shows the stress-strain curves in the HAZ (x=2mm) for the top, middle and bottom specimens. Again, the top position specimen HAZ has a higher yield stress than the middle and bottom positions.

Figure 5.15 show the stress-strain curves at the first-pass weld (x=-2mm) of each weld layer from the top, middle and bottom specimens. The stress-strain properties of each weld pass are clearly different with the middle pass showing a higher yield strength than the top and bottom passes. This is broadly consistent with the hardness map shown in Figure 5.4.

Figure 5.16 shows the 1% proof stress results calculated across the weld from the three different positions in the weldment. The proof stress data were obtained from local stress-strain curves obtained from DIC measurements. A linear line was fitted to the elastic region of these stress-strain curves with a user defined range and shifted by certain values of strain, such as 0.2%, 1% etc. The stress value at the intersection between the shifted linear line and the stress-strain curve defines the proof stress. The maximum proof stresses are found at the centre of the gauge length, around the first weld pass in each layer for all specimens. Comparing the three different position results at the weld (x= 2mm), the highest values appear in order of middle, top and bottom.

5.4.3 Tensile Cross-weld DIC Tests at Elevated Temperature

The ruptured specimens from the high temperature tensile tests are shown in Figure 5.17. The photograph contains an additional position No.4 specimen which is from between middle and bottom locations. But the results are presented

comparing the standard three different positions, top, middle and bottom. The top and middle specimens ruptured in the far left weld bead (i.e.a later deposited bead) of each layer within the gauge length, and the bottom specimen ruptured between the HAZ and parent material (left side). Figure 5.18 shows an example of DIC test images at different stage and corresponded to their strain vectors and contour dull field maps, results is from bottom position test.

5.4.3.1 Top Position

Figure 5.19 shows the strain variation in the top specimen along the gauge length for the applied stress level of 315MPa (i.e. the same load as applied in the creep test). It can be seen that the strain in the HAZ is smaller relative to the weld and substantially smaller than the parent metal. A strain fluctuation within the weld metal zone associated with the weld passes can be observed.

Figure 5.20 shows stress-strain curves for parent, HAZ and weld materials from the top specimen at a temperature of 545°C. The sampling positions for the curves are x=10mm (parent), x=2.5mm (HAZ) and x=-2.5mm (weld) from the vertical weld fusion boundary, respectively. The results show that the yield stress of parent metal is considerably smaller than weld metal and HAZ material.

The 0.2% proof and hardness variations along the cross-weld specimen are shown in Figure 5.21. Both show the same trend. The yield strength of the weld metal is higher than parent material, and the HAZ has similar properties to the weld.

DIC also provides information about the transverse strain across the gauge section. The variation in the reduction of area (RA) was calculated on the

assumption that the transverse strain across the width of the gauge is the same as the transverse strain through the thickness of the gauge (described in Chapter 4.6). The variation of RA along the gauge section of the specimen at the stress of 315MPa is shown in Figure 5.22. It can be seen that the parent has a large RA due to its higher strain and that the RA gets larger moving from the right hand side weld fusion boundary towards the later deposited weld beads on the left hand side. Moreover there is a periodic fluctuation due to individual weld beads.

5.4.3.2 Middle Position

Figure 5.23 shows the strain variation along the gauge length at 545°C in the middle specimen, after loading to a stress level of 315MPa. Although the specimen ruptured at the outermost left hand weld pass (which could not be observed by the camera in this test), the strain increased in the HAZ and a large strain was observed to develop towards the parent metal on the right side. Fairly constant small magnitude strains developed in the weld passes.

Figure 5.24 shows stress-strain curves at sampling positions x=2 mm (HAZ) and x=-2 mm (weld), respectively. The weld and HAZ have similar curves and yield at approximately 300MPa (note the parent data were not obtained due to the camera's limited field of view in this test).

Figure 5.25 shows the 0.2% proof stress variation along the cross-weld specimen together with the hardness survey results. The profiles show a similar trend. The 0.2% proof stress drops rapidly outside the HAZ but does not reach a plateau within the field of view at x=8mm.

Figure 5.26 shows the variation in reduction of area at different stages of deformation, marked A, B, C and D on stress-strain curves at selected positions x=4.7mm (this is weld/HAZ), and x=-2.7mm. A relates to the applied stress σ=59MPa (elastic region), B to σ=215MPa (yielding point of S-S curve at x=4.7mm), C to σ=313MPa (yielding point of S-S curve at x=-2.7mm) and D to the final RA distribution. The RA distribution at C corresponds to the stress applied in the creep test, that is it represents the instantaneous RA on first loading. The strain was also calculated in the direction transverse to loading however this showed similar strain distribution results to the tensile direction. As you can see at a stress level of 315MPa the yield point and RA at x=-2.7 (Weld) is still small whereas at x=4.7mm considerable plastic strain has occurred with a large associated RA.

5.4.3.3 Bottom Position

Figure 5.27 illustrates the measured strain variation along the gauge length of the bottom position specimen at a temperature of 545°C, and the stress level of 315MPa. Although the specimen ruptured at the boundary between the HAZ and weld at around x=-7mm, large strains are observed on both sides in the parent materials. On the other hand, small strain is seen at the weld and in the HAZ, indicating a high yield stress compared with the parent material.

Figure 5.28 shows stress-strain curves of sampling positions at x=11.5mm (parent), x=2.5 mm (HAZ) and x=-2.3 mm (weld). The results show that the yield stress of parent metal is lower than weld metal and HAZ material. Figure 5.2 shows the 0.2% proof stress variation along the bottom cross-weld specimen together with the hardness results. It was difficult to determine the 0.2% proof stress on the left

hand side because of the lack of data points in the elastic region linear line fitting in this test. The profiles again follow a similar trend with higher values in the weld metal than in the parent. The 0.2% proof stress of the weld metal is under 300MPa. This is lower than the top and bottom positions and also smaller than the initial applied stress in the creep tests (see Figure 5.21 and Figure 5.25). Figure 5.30 shows the variation of RA at 315MPa loading along the specimen gauge length. The distribution tendency was similar to the strain distribution in the tensile direction with a large reduction on both sides in parent material.

5.4.4 Creep Cross-Weld DIC Tests

Figure 5.31 shows a photograph of the ruptured specimens from the creep tests for the top, middle and bottom positions. The top specimen ruptured in a weld bead adjacent to the right hand side weld preparation wall. The middle specimen ruptured in parent material (right side of specimen) and the bottom specimen ruptured in the HAZ/weld region (left side). The duration, applied stress and temperatures for each creep test are summarized in Table 5.3. The middle creep test, which failed in parent material, had the longest duration.

Here, the creep strain is defined as inelastic strain that increases progressively with time. The displacement recorded after initial loading was used to calculate the instantaneous strain which was then subtracted from the total measured strains. The creep strain data (from DIC or the test machine) were then plotted as a function of time and fitted using polynomials in order to remove data scatter and create each local creep curve. The creep strain rates were then

calculated by first order differentiation of creep strain curves. Creep strain rates were subsequently used to produce the creep strain rate vs time curves. But for creep strain rate distribution across the gauge length , the minimum creep strain rates were obtained by linear fit of gradients (strain/time) in the secondary creep region (e.g time between 500 hours to 1500 hours in the middle position test). The results are presented for each of the three different positions in turn. The characteristics of the three positions are then compared with each other in Section 5.4.4.4. Figure 5.32 shows an example of DIC test images at different stage and corresponded to their strain vectors and contour dull field maps, results is from bottom position test.

5.4.4.1 Top Position

The acquired images over 3 months test duration were analysed. Figure 5.33 shows the creep strain evolution along the gauge length of the specimen at different times. Parent, HAZ and weld metal zones showed clearly different creep deformation behaviours. Although the high temperature tensile test indicated that parent material accumulated the largest strain, here the weld metal zone is seen to be accumulating much more creep strain than the parent material. It is seen that the creep strain increases from the first pass of each layer on the right hand side (centre of specimen gauge length) towards later deposited beads towards the left side of each weld layer. Furthermore, it is notable that the creep strain developing in the HAZ is considerably smaller than that accumulating in the parent metal and weld metal.

Local creep deformation curves corresponding to three different positions, parent metal (x=10mm from the weld boundary), HAZ (x=2.5mm) and weld (x=–2.5mm) are shown in Figure 5.34. The HAZ is creep-strong relative to the parent and the weld materials. Although the instantaneous strain of the parent metal was large in the high temperature tensile test (Figure 5.19), the creep strain in the weld metal is observed to be higher than in the parent metal.

Figure 5.35 shows the secondary creep rate distribution along the gauge length of the cross-weld specimen and Figure 5.36 shows the creep rate as a function of increasing time at different positions (parent, HAZ and weld). The results indicate that the HAZ has the highest creep strength and that the creep rate of both the weld metal and parent material increases with increasing distance from the weld fusion line.

The variations in reduction of area and true stress along the specimen at different creep times are shown in Figure 5.37 and Figure 5.38. The data were obtained using the same approach as for the tensile tests, that is based on the assumption that the strain through the thickness is the same as the measured transverse strain across the gauge width. The RA and hence true stress in the HAZ is significantly lower than the other regions once they have started to accumulate creep strain. However, the true stress of the parent on the right hand side increases to more than 323MPa at 2000 hours and in the left hand side weld pass rises up to more than 345MPa. By knowing the true stress distribution along the cross-weld sample, we can estimate the stress change with time and potentially

take account of its effect on creep deformation during the test (which of course cannot be done with conventional creep testing).

5.4.4.2 Middle Position

The middle specimen ruptured in the parent material on the right hand side, a different position to the high temperature tensile test which failed in weld metal on the far left hand side (compare Figure 5.31 with Figure 5.17). A total of 480 images were taken over a test duration of 2300 hours (over 3 months) and analyzed to determine development of strains as a function of time and position. Figure 5.39 shows the strain evolution with time along the gauge length of the specimen. The strain accumulations in the weld and the HAZ (up to x=2mm) are low but rapidly increase several-fold in the parent material.

Figure 5.40 shows the local creep curves at different positions, parent metal (x=12mm from the weld boundary), HAZ (x=2.4mm), and 1st pass weld (x=-2.1mm). It is clearly seen that significantly greater creep strain accumulates in the parent material than in the HAZ and weld metal. Comparison of the shapes of the creep curves suggests that primary phase creep makes a strong contribution to the additional strain in the parent material. In the weld metal, the amount of creep strain increases slightly with deposition sequence (i.e. moving to the left along the gauge length).

Figure 5.41 shows the secondary creep rate distribution along the gauge length of the cross-weld specimen. The secondary creep rate was averaged in the region between 500 hours 1500 hours. Unsurprisingly the trend in secondary creep rate matches the creep strain accumulation results shown in Figure 5.39. Figure

5.42 shows the creep rate at different positions, parent (x=12mm), HAZ (x=2.4mm) and weld (x=-2.1mm) with increasing time. The creep rate in the parent material starts high in the primary region, reduces to a minimum at about 600h and then slowly increases before rapidly increasing at around 1700h in the tertiary region. Interestingly the minimum creep strain rate of all three materials is similar at about 600h. The creep rates in the HAZ and weld metal, which are much lower than the parent during the primary phase, reduce to near steady state values at around 600h. In the last ≈500h of the test, the weld and HAZ creep strain rates start to reduce as creep strain concentrates in the parent at the rupture position.

The variation in reduction of area at different creep times is shown in Figure 5.43. This plot shows a very clear variation from weld bead to weld bead, not evident in the creep deformation evolution results presented in Figure 5.39. Finally the distribution of true stress (based on change in transverse dimension) is given in Figure 5.44. The true stress of parent material at the region of failure progressively increases to 340MPa at 2227h just before specimen rupture, whereas the stresses in the weld and HAZ stay around applied stress level.

5.4.4.3 Bottom Position

This specimen ruptured at the interface of the HAZ and weld metal in this bottom position creep test. The significance of all the specimen rupture positions will be discussed later in section 5.5.1.

A total of 360 images were taken during this bottom position creep test and analyzed to determine position dependent strain accumulation. Figure 5.45 shows the strain evolution along the gauge length of the specimen at different times

during the creep test. The creep strains are concentrated at the centre of the weld and reach a maximum of 20%, whereas creep strains are small in the HAZ on both sides of the weld metal. Figure 5.46 shows the local creep curves at different positions along the gauge length, parent metal (x=12mm from the weld boundary), HAZ (x=2.8mm) and weld (x=-2.2mm).

Figure 5.47 shows the secondary creep rate distribution along the gauge length of the cross-weld specimen. The secondary creep rate at the centre of the weld is an order of magnitude greater than in the HAZ which has the highest creep strength.

Figure 5.48 shows how the creep rate varies with time at different positions. The creep rate of the weld reduces to a minimum at around 200h, then slowly increases during secondary creep and accelerates during tertiary after 1000 hours. In contrast, the creep rates of the HAZ and parent materials decrease gradually over the time of the test.

The variations in reduction of area and true stress along the specimen at different creep times are shown in Figures 5.49 and 5.50 respectively. Both sets of results present the same trend as the strain distribution (Figure 5.45) with the peak value developing at the centre of weld (x=-5mm). However, the specimen ruptured at the HAZ/weld interface, that is around x=-10mm.

5.4.4.4 Comparison of Top, Middle and Bottom Position Results

Figure 5.51 shows a comparison of strain distributions from the top, middle and bottom positions at 1000 hours (that is in the secondary creep region). The middle of the weld at the bottom position (x=-4mm) has accumulated significantly

larger creep strain (8 to 9%) than elsewhere (0.4 – 3%). The bottom test specimen also had the shortest life of 1500h (see Table 5.3). This evidence suggests that the root of the weld is the weakest position in the weldment from a creep rupture viewpoint. The lowest creep strains are found in the HAZ at all positions.

Figure 5.52 compares the local weld metal creep curves at x=-2mm from the three positions. As might be expected the bottom position creep strain increases much faster than the middle and top positions, but interestingly the middle position accumulates the least creep strain. This is particularly evident in Figure 5.53 where the secondary creep rates are compared. Finally Figure 5.54 shows how the creep rate in the weld metal varies as a function of through-wall location.

5.5 Discussion

Figure 5.31 shows the specimen rupture locations of the top, middle and bottom position cross-weld creep tests. The top specimen ruptured at the extreme left hand side of the multi-pass weld within the gauge length of the specimen, the middle specimen ruptured in parent material and the bottom specimen ruptured at the HAZ/weld material interface to the left side of the weld (a single pass at the centre of the gauge length in this case). Figure 5.55 indicates the rupture locations for all three specimen positions (top, middle and bottom) from the room temperature tensile tests, the high temperature tensile tests and the creep tests. (Note: the specimen design and gauge length were different in the room temperature tensile tests). The exact rupture locations relative to the vertical fusion boundary are summarised in Table 5.4 together with the elongation at each failure

location. The elongation obtained by total elongation of specimen length. Figure 5.56 also shows the weld pass deposition sequence with an enlarged detailed photograph indicating the position of the specimen gauge sections and rupture position of top and bottom (note: middle position specimen ruptured at parent material which location is out of photograph). There is a consistency in the pattern of rupture positions, with two out of the three types of test failing in weld metal either at the extreme left side of the gauge length of the top and middle specimens (i.e. later deposited weld beads in a layer) or in the HAZ/Weld material adjacent to the weld root in the bottom specimens.

5.5.1 Top Position

Figure 5.57 shows a photograph of the top specimen prepared for creep testing and one of the pieces of material removed by wire EDM to create the flat gauge length. The cut face of the removed piece was ground, polished and etched in order to reveal the macrostructure of the weldment in the creep specimen. It is difficult to discern the structure of this multi-pass, multi-layer weld from this view of the weldment looking down from the top of the specimen. The hardness results for the top position measured along a weld layer (Figure 5.5) show higher values in the weld metal and HAZ because of cyclic hardening associated with the welding process. Fluctuations are observed in the weld metal, with the weld beads near the fusion boundary (at around x=0mm) which were deposited earlier, having higher Vickers hardness than beads deposited later to the left of the weld.

Weld beads and fusion boundaries at the ruptured location are identified on the photograph shown in Figure 5.58 of the top specimen. The photograph also shows the specimen final widths (reduction of area, RA) at three different positions across the multi-pass layers which were measured by micrometer. As you can see the centre of the weld beads have a larger RA, on the other hand, the RA of the weld fusion boundaries are smaller. This may be because of local variations in cyclic strain hardening/softening associated with multi-pass welding or solidifaction effects near fusion boundaries. That is why RA of the fusion boundaries are smaller than centre of the weld beads which also shown in Figure 5.37. This RA distribution results (Figure 5.37) have some fluctuations in the weld region due to individual weld beads. The specimen failed at the fusion boundary of a weld bead at the far left side of the weld (within the specimen gauge length), that is one deposited later in a layer. But this was out of the camera's field of view, thus, it was difficult to identify the exact position. The location is judged to be between the 4^{th} and 5^{th} weld beads at approximately x=-20mm from the initial vertical weld fusion boundary.

5.5.2 Middle Position

Figure 5.59 shows the photograph of the piece removed from the middle specimen gauge length. Weld beads (each approximately 6mm wide) are observed in the weld metal. It is interesting to note here a strong correlation between the RA and individual weld beads.

The middle position specimen ruptured in the parent material, see Figure 5.55. This is different to the room and high temperature tensile tests which failed in the weld metal. The major issue that can affect the creep behaviour and rupture position is the influence of temperature during the creep test. In the middle position creep test, there was some temperature variation (approximately 3 to 4 °C, see Table 5.3) between the thermocouple readings from the top and bottom of the gauge length. Small temperature changes can significantly increase creep strain rates as discussed in Chapter 4.3, and this affects the creep deformation and material life appreciably. The specimen was set up with the parent material in a higher position in the furnace where it would have experienced the higher temperature history. Figure 5.60 shows the creep curves of top, middle and bottom positions of parent material (x=12mm). The middle position indicates larger strain increment. It is judged that the temperature variation had a significant effect on this middle position creep test. In addition, the creep strain of top position is small. According to the tensile test mechanical properties (Figure 5.16), the proof stress of top area is much higher than middle and bottom position.

5.5.3 Bottom Position

Figure 5.61 shows a photograph of the metallographically prepared piece removed from the bottom position test specimen gauge length. The bottom creep specimen contains HAZ and parent material on both sides of a single weld bead, note the fusion boundary. Figure 5.61 also shows an edge view of the test specimen and indicates the 45 degree angle of the fusion boundary. Although the

weld metal of this specimen must have been subjected to several sequential heat cycles from following passes, the hardness values are not as high as the middle position (see Figure 5.5).

A large creep strain was observed in the weld metal. Figure 5.62 compares the stress-strain curves from the three positions in the first pass weld metal of each layer (at x=-2mm), and Figure 5.63 compares the variation of 0.2% proof stress along each specimen from the high temperature tensile tests. The bottom position yield stress is lower than top and middle. Figure 5.64 shows a photograph of the bottom specimen at the ruptured location. Although a large creep strain developed at the middle of the weld metal, the specimen ruptured in the HAZ/Weld region at x=-9mm. The large deformation and reduction of area of the weld metal can be seen in the photograph of the tested specimen, whereas the brittle fracture occurred along the HAZ/Weld region. Table 5.4 also shows the summary of elongation of each cross-weld specimen tested at room temperature, elevated temperature and creep. In the room temperature tensile test the test specimen failed in the parent with longest elongation in this bottom position. On the other hand, in the high temperature and creep indicate small elongation. Obviously, the ductility of the material has changed at elevated temperature. Figure 5.64 also shows how the specimen fracture surface ran parallel to the 45° angled side-wall of the weld. This suggests that the fusion boundary introduced by the welding process changes the local mechanical properties and metallurgy (higher carbon and silicon content). Each weld bead has different mechanical and creep properties due to order of welding process, thus, the drastic change in

properties contains interfaces. These fusion boundaries can cause crack initiation points and impairs the fracture toughness.

5.5.4 Multi-pass Weldment Behaviour

The local ductilities of the multi-pass weldment at the failure locations (see Figure 5.55) of the room temperature tests, high temperature tests and creep tests are summarised in Table 5.4. The creep rupture strength of a welded joint is determined by the weakest part whether in the multi-pass weld or parent material [8]. The present results show that the heat affected zone of the weldment has particularly high deformation resistance compared with the parent material and weld metal, as reported elsewhere [9]. But the "creep strength" is determined by how quickly the creep strain reaches the local creep ductility. Figure 5.65 shows 3D plots of accumulated creep strain along the cross-weld specimens in the tensile loading direction. Although the bottom specimen accumulated the largest creep strain in the weld region the specimen actually ruptured between the HAZ and weld metal because the local ductility was extremely low (1.7%).

The top position creep and high temperature specimens ruptured in the last pass of a weld layer lying within the specimen gauge length. Figure 5.52 shows that creep strain accumulated faster at the top and bottom positions than at the middle. Hongo et al [10] also found that the creep rates of the weld metal were smaller at the middle position than near to the surfaces of a plate weldment. The middle region weld metal has much higher creep strength compared to the surfaces due to thermal cyclic hardening effect. They also observed microstructure

of multi pass weld. It was found larger number of voids appeared near the surface more than middle position of multi pass weld. Thus, our result of accumulation of creep strain (Figure 5.52) is similar to their findings. Furthermore, in our material, the middle position parent material has much lower proof stress than the weld metal (see Figure 5.60) which may cause failure in the parent rather than the weld metal. However, as mentioned previously in section 5.5.2, it is judged that the middle specimen failed in the parent material in the present creep test because the temperature variation along the specimen was less well controlled than the top and bottom position tests.

Figure 5.66 shows combined hardness, high temperature tensile and creep test results as a function of location across the weld from the top position of the weldment. The variation in high temperature yield (0.2% proof stress) and room temperature hardness across the weld correlate closely with each other. The cross-weld variations in final (total inelastic) strain from the individual creep and high temperature tensile tests also seem to match reasonably well. If you look at the plastic loading strain distribution line from the high temperature test (mimicking what was initially applied in the creep test), you will see that the parent material yielded plastically far more than the weld on initial loading. This of course would have caused the parent material to work harden (see Figure 5.20) and this may have influenced the creep properties and the ductility of the parent. On the other hand, the weld metal and the HAZ had a slightly higher initial 0.2% proof stress than the constant applied stress (315MPa), thus initial plastic strain was not introduced during loading process. Davies et al [11][12] have reported that the

creep rupture life of 316H stainless steel became longer due to a plastic pre-strain effect, and Willis also reported that pre-strain had a beneficial effect on creep life and creep resistance [13]. The creep rupture position of the top cross weld was observed at the last pass of a weld layers in weld metal. As mentioned previously, the parent material has a pre-strain effect after loading, which produced higher strength. In terms of the multi-pass weld layers, the outmost weld bead received less thermal history, which give a smaller amount of dislocation motion and results in less hardening. Thus, the initiation cracking occurs in the weld metal faster than the parent material and failed at the location of the last pass of a weld layers lying with in the specimen gauge length

5.6 Conclusions

1. A DIC optical system has been successfully used at elevated temperature to acquire full field strain data in stainless steel cross-weld samples as a function of time during creep tests enduring several months.

2. The DIC technique provided local elastic, plastic and creep strain data for the parent, HAZ and weld metal, from which stress-strain curves, reduction of area, true stress distribution, creep curves and secondary rates could be obtained.

3. High temperature DIC tensile tests can be used to study more closely the instantaneous loading strain introduced during the loading phase of a creep test.

4. The DIC technique was able to resolve variations across individual weld beads in weld layers showing strains to be concentrated in the centre of the bead whereas failure occurred at the fusion boundaries.

5. Significantly lower creep strain rates were observed in the HAZ at all positions tested in the weldment.

6. The weld root position failed in the shortest time (1500h). Although the root weld bead itself exhibited the maximum creep deformation rate, failure actually occured in the HAZ/Weld location adjacent to the 45° angle fusion boundary where the creep ductility was 1.7%.

7. Elsewhere in the weldment failure occurred at longer times (>2100h) in weld beads furthest from the vertical fusion boundary where the local ductility was about 5%.

8. Creep failure in parent material occurred in the specimen extracted from the middle of the weld, possibly because of a slightly higher test temperature.

9. DIC testing can provide spatial and time resolved creep deformation data that can be used to understand the creep behaviour of weldments that have inhomogeneous properties. Moreover such tests can provide creep data that can be used to develop creep deformation models and subsequently plant creep life predictions.

5.7 References

[1] "R6 Revision 4 Assessment of the Integrity of Structure containing Defects. EDF Energy Ltd, October 2011,Gloucester. UK" .

[2] "R5 Issue3 Assessment procedure for the high temperature response of structure. EDF Energy Ltd, May 2012. Gloucester. UK" .

[3] Doosan Babcock Enery, "Production of stainless steel butt weld on ex-service headers," 2009.

[4] G.E.Dieter, *Mechanical Metallurgy*. SI Metric Edition McGraw-Hill Book Company, 1988.

[5] "ASME E8/E 8M-08 Standard Test Method for Tensile Testing of Metallic Materials." 2008.

[6] "Strain Master, LaVision GmbH, Anna-Vandenhoek-Ring 19 Gottingen Germany."

[7] "ASTM E-139 Standard Test Method for Conducting Creep, Creep-Rupture, and Stress-Ruptured Test of Metallic Material (21st April 2009)." .

[8] Hiromichi.Hongo, "Creep deformation behaviour of weld metal and heat affected zone on 316 steel thick plate welded joint," *Japan Society of Material Science*, vol. 48, no. 2, pp. 116–121, 1999.

[9] Junichi.Kinugawa, Muramatsu.Yoshiki, Monma.Yoshio, Y. Masayoshi, Hongo.Hiromichi, and Watanabe.Takashi, "Computation of creep deformation of welded joint of 304 stainless steel by using finite element method," *Japan Welding Society*, vol. 7, no. 1, pp. 117–124, 1989.

[10] Hongo.Hiromichi, Yamazaki.Masayoshi, Watanabe.Takashi, Tabuch.Masaaki, Tanabe.Tatsuhiko, and Monma.Yoshio, "Evaluation for creep properties of 316FR weld metal with miniture weld metal and full-thickness welded joint specimens," *The Society of Material Science, Japan*, vol. 53, no. 5, pp. 566–571, 2004.

[11] C.M.Davis, David.W.Dean, A.N.Mehmanparast, and K.M.Nikbin, "Compressive pre-strain effects on the creep and crack growth behaviour of 316 stainless steel," *Proceeding of the ASME 2010 Pressure Vessels & Piping Division /K-PVP Conference PVP2010 Bellevue, Washington, USA.*, 2010.

[12] D.F.Li, N.P.O'Dowd, C.M.Davies, and K.M.Nikbin, "A review of the effect of prior inelastic deformation on high temperature mechanical response of engineering alloys," *International Journal of Pressure Vessels and Piping*, vol. 87, p. 531, 2010.

[13] M.Willis, A.McDonaugh-Smith, and R.Hales, "Pre strain effect on creep ductility of a 316 stainless steel light forging," *International Journal of Pressure and Piping*, vol. 76, p. 355, 1999.

5.7 Tables and Figures

Specimen ID	Specimen width (mm)	Specimen thickness (mm)	Specimen area (mm^2)
Top	5.935	3.063	18.179
Middle	5.950	3.060	18.207
Bottom	5.974	3.031	18.025

Table 5.1 Measured width and thickness of the gauge length of each tensile test specimen prior to testing

Position	Elongation (at failure)	Test duration (time to failure)	Analyzed image number
Top	10.4%	3.1 hours	151
Middle	5.8%	4.5 hours	201
Bottom	11.7%	7.9 hours	322

Table 5.2 Elongation, test duration and analyzed image number of each cross-weld specimen tested at room temperature

Position	Top		Middle		Bottom	
Test duration	2100 hours		2300 hours		1500 hours	
Applied stress	315MPa		315MPa		313MPa	
Temperature	top	bottom	top	bottom	top	bottom
	545.2°C	544.5°C	547.1°C	544.8°C	544.8°C	545.2°C

Table 5.3 Duration, applied stress and temperature of each creep test

	Top	Middle	Bottom
Room temperature	Weld x=-36mm 10.4%	Weld x=-18mm 5.8%	Parent x=-36mm* 11.7%
High temperature	Weld x=-18mm* 4.2%	Weld x=-18mm* 3.3%	HAZ/Weld x=-10mm 1.7%
Creep	Weld x=-18mm* 5.0%	Parent x=12mm 10.4%	HAZ/Weld x=-10mm 1.7%

* Estimated position (outside of camera's field of view)

Table 5.4 Rupture positions and total elongation over length of specimen of each cross-weld specimen tested at room temperature, elevated temperature and after creep

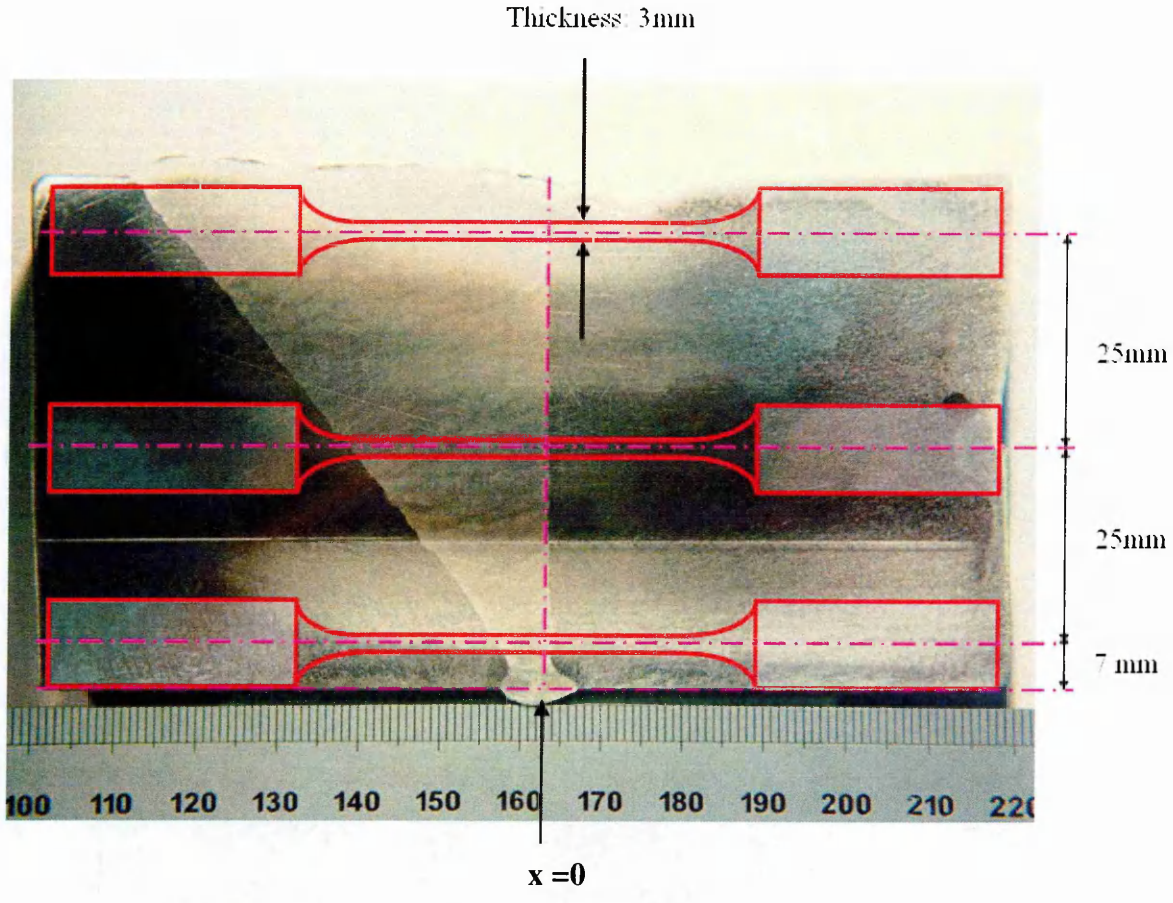

Figure 5.1 Thick section test weldment made from ex-Heysham I service material and showing test specimen extraction locations

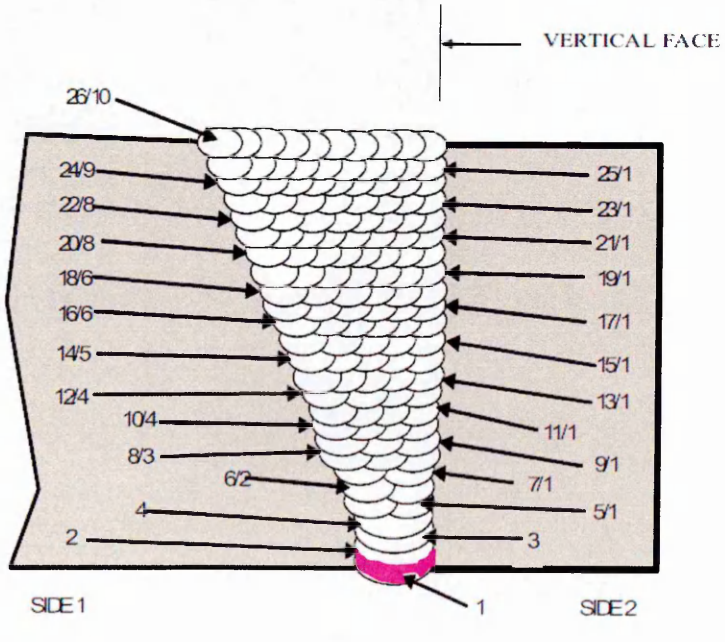

Figure 5.2 Multi-pass weld deposition sequence

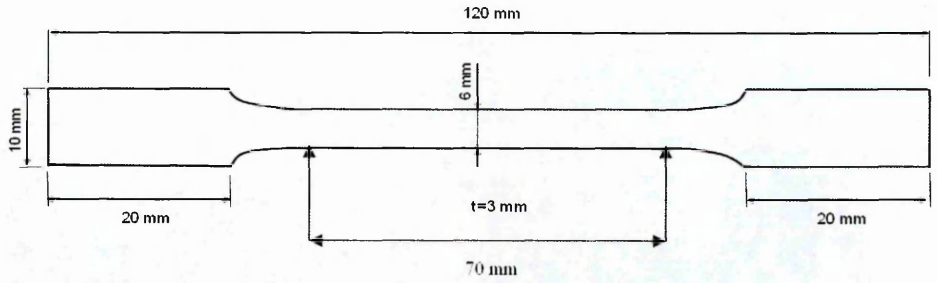

Figure 5.3 Specimen design for room temperature DIC tensile tests

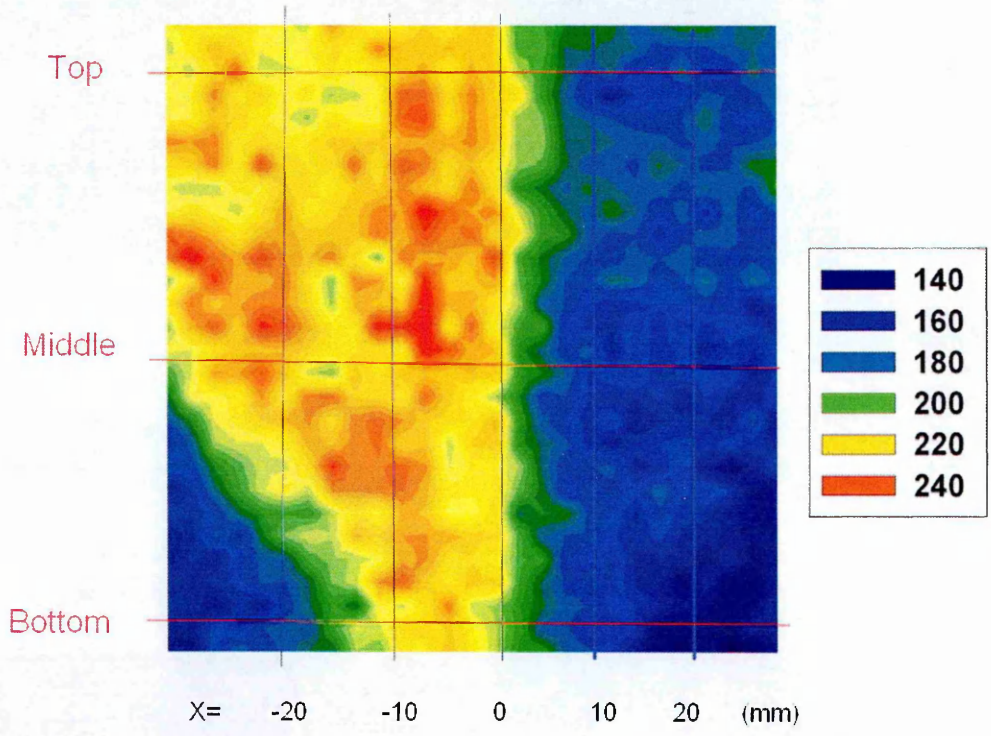

Figure 5.4 Vickers hardness survey of multi-pass weldment

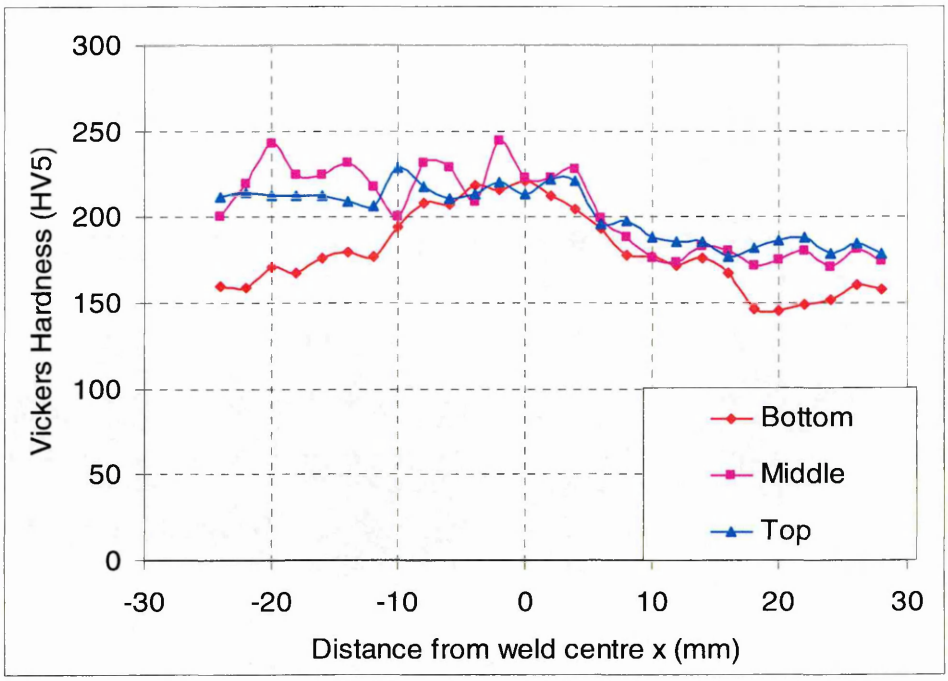

Figure 5.5 Hardness variation across the weldment at the top, middle and bottom positions (horizontal direction)

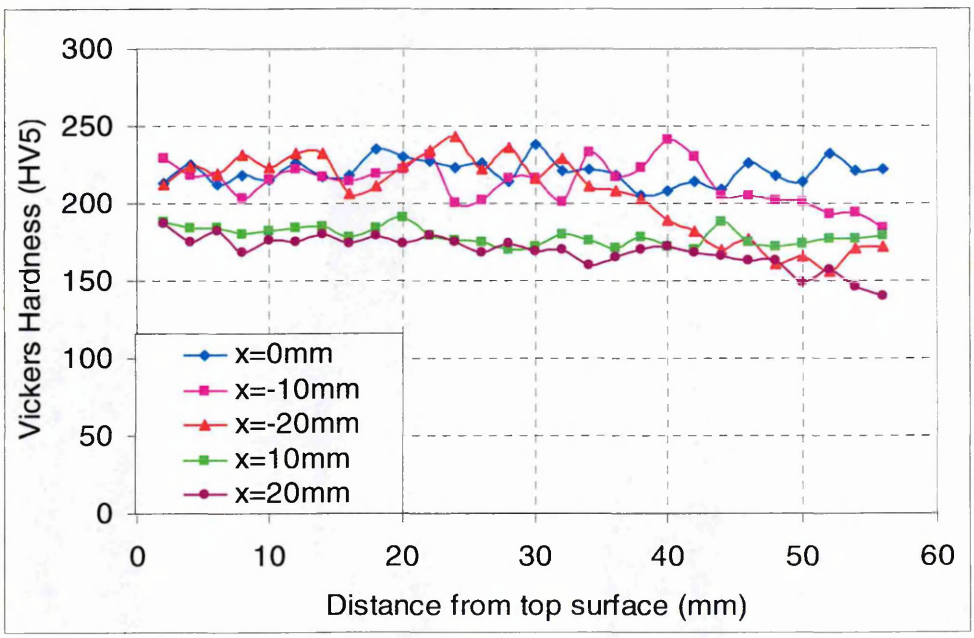

Figure 5.6 Hardness variation through the thickness of the weldment at the weld fusion boundary (x=0mm), x=10mm, x=20mm and x=-20mm (vertical direction)

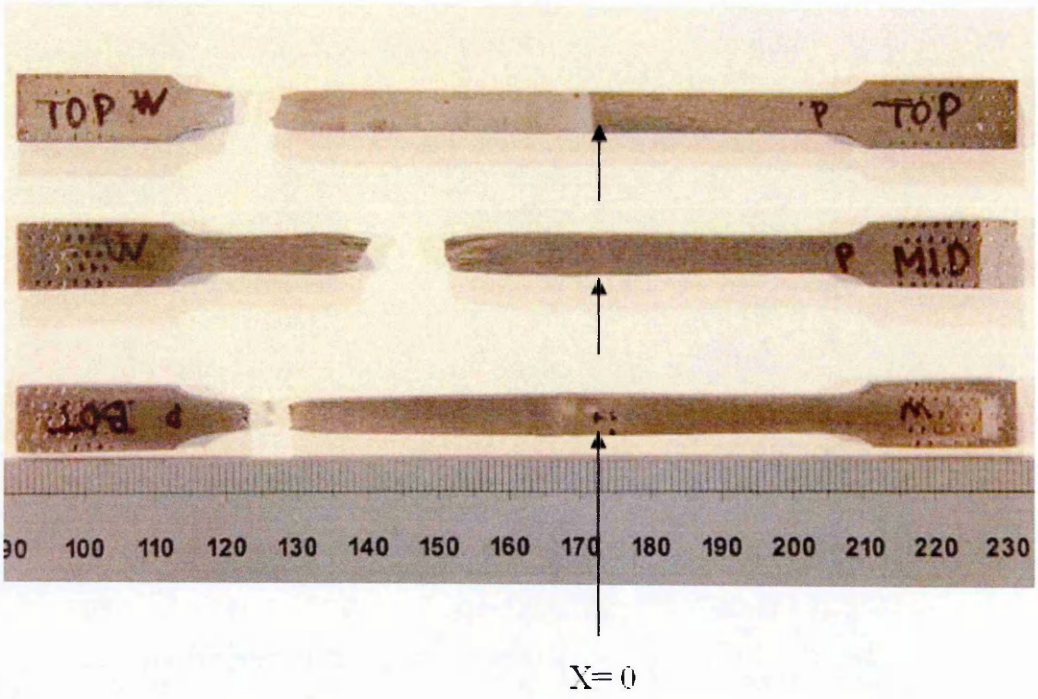

Figure 5.7 Ruptured specimens from room temperature tensile tests, sampling materials at the top, middle and bottom of the weldment.

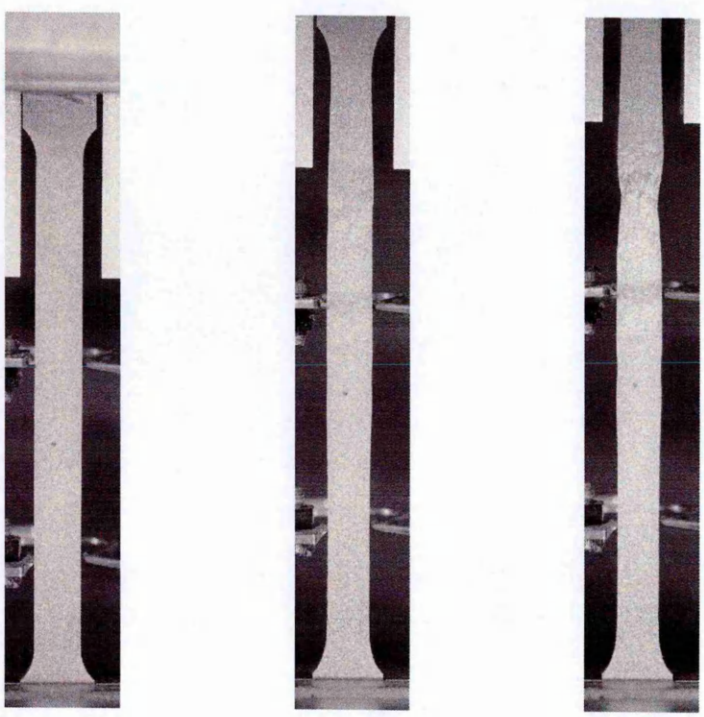

(a) Elastic region **(b) Plastic region** **(c) Last**

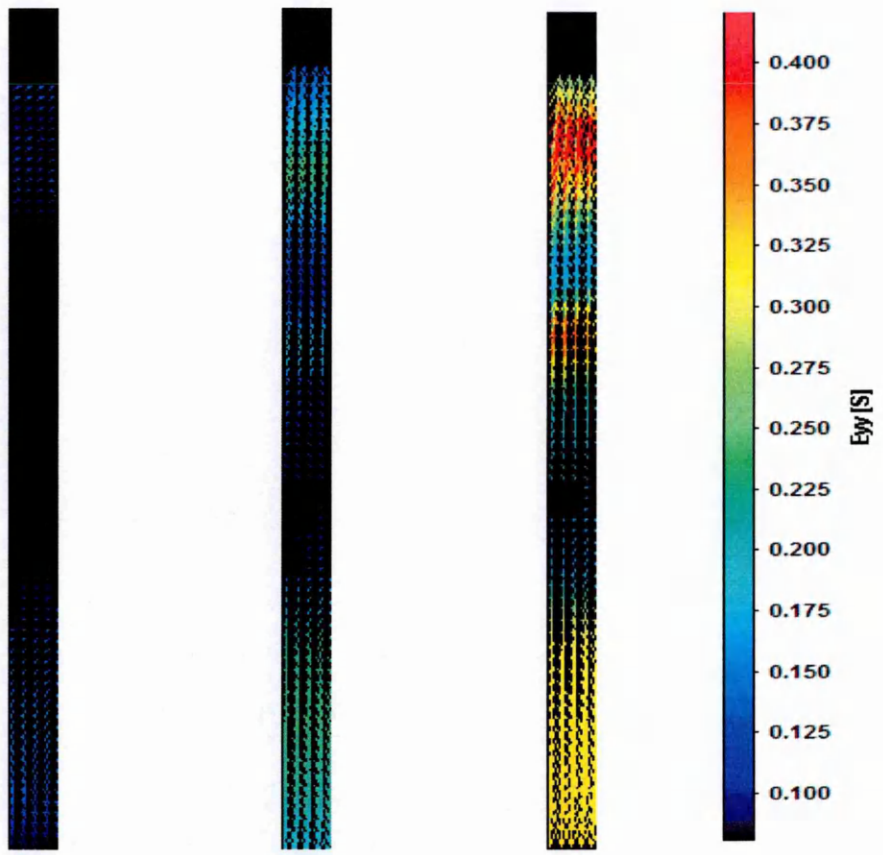

(a) Elastic region (b) Plastic region (c) Last

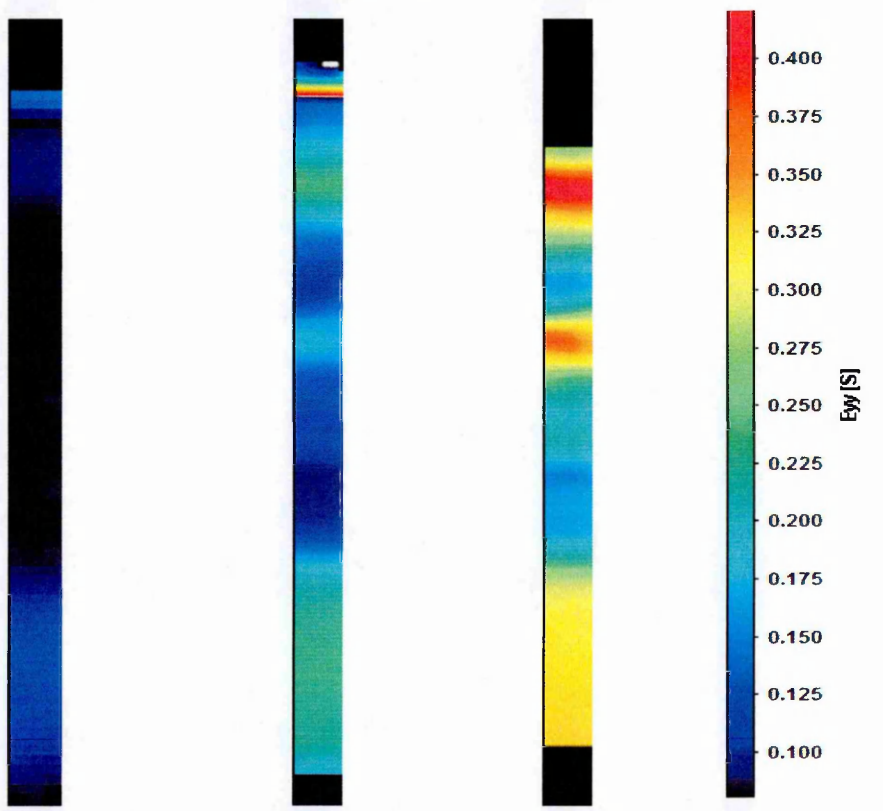

(a) Elastic region (b) Plastic region (c) Last

Figure 5.8 Example of DIC test images at different stage and corresponded to their strain vectors and contours maps from middle position test (room temperature)

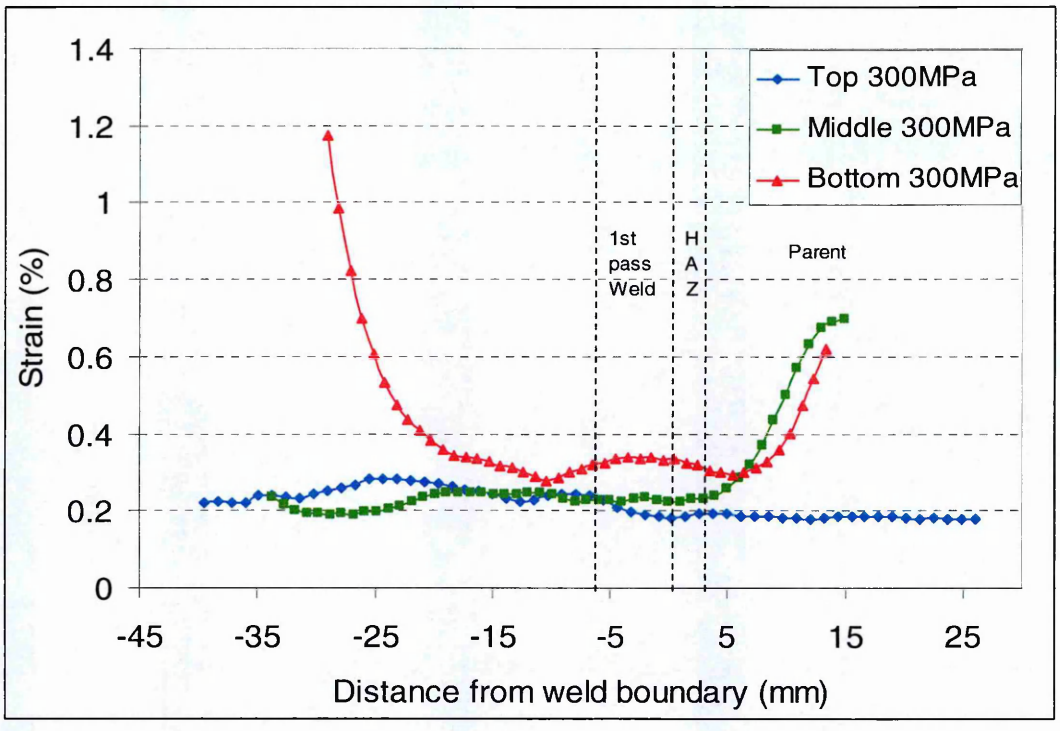

Figure 5.9 Strain distribution across the weld at a stress of 300MPa in the room temperature tensile tests

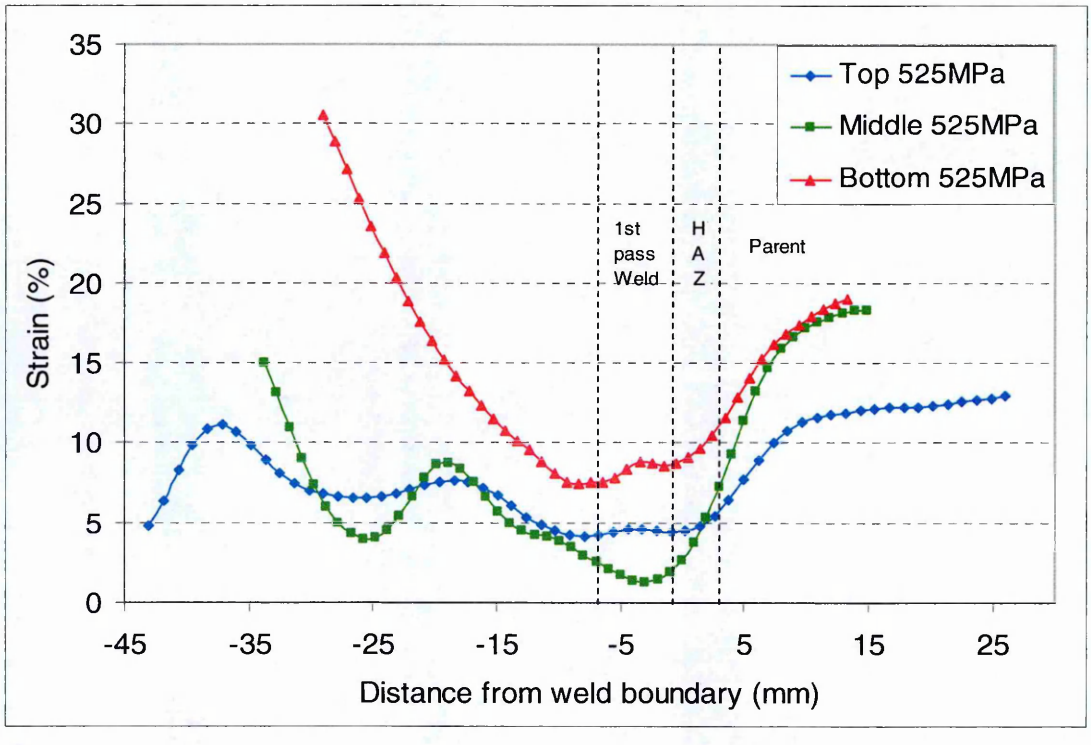

Figure 5.10 Strain distributions at a stress of 525MPa in the room temperature tensile tests

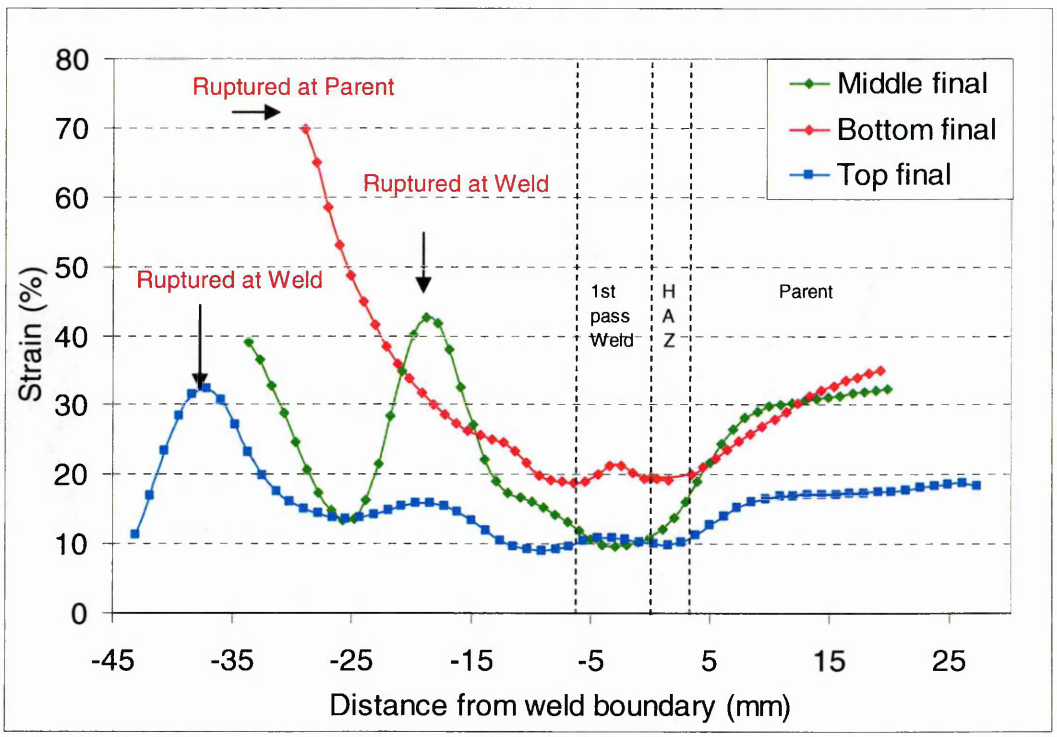

Figure 5.11 Final strain distributions prior to failure in the room temperature tensile tests

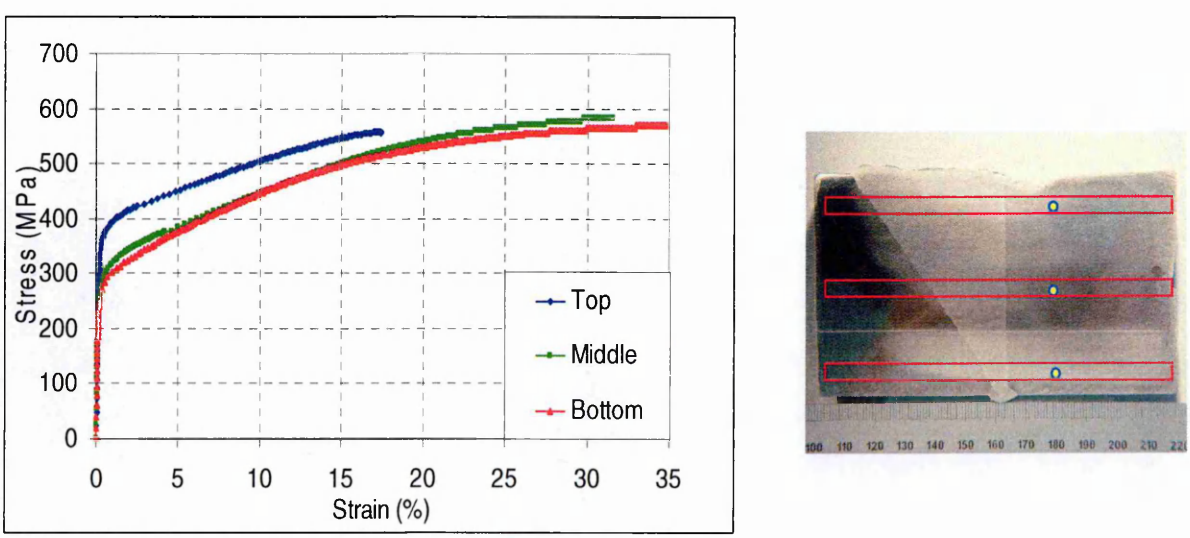

Figure 5.12 Stress-strain curves of parent material (x=12mm) from top, middle and bottom specimens at room temperature.

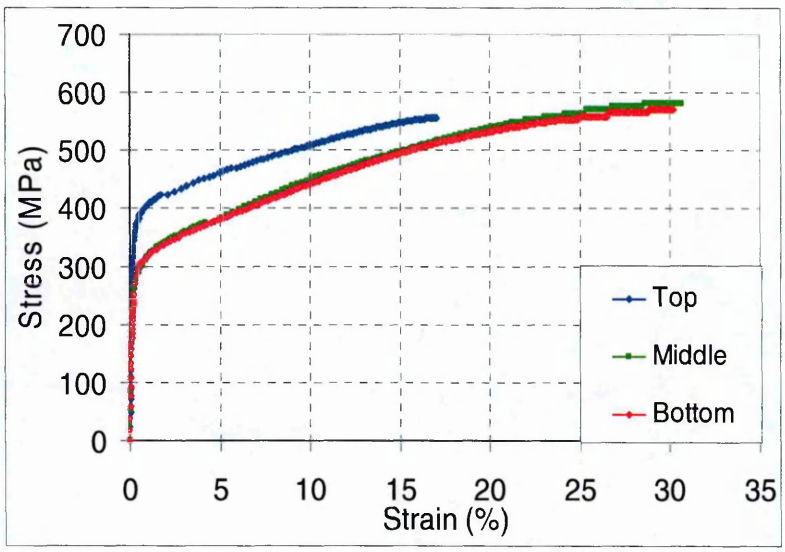

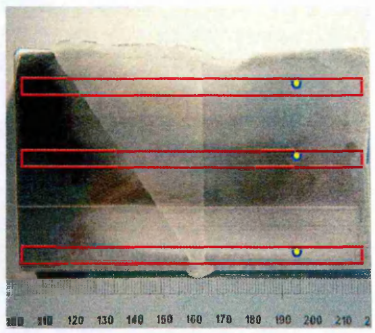

Figure 5.13 Stress-strain curves of parent material (x=18mm) from top, middle and bottom specimens at room temperature.

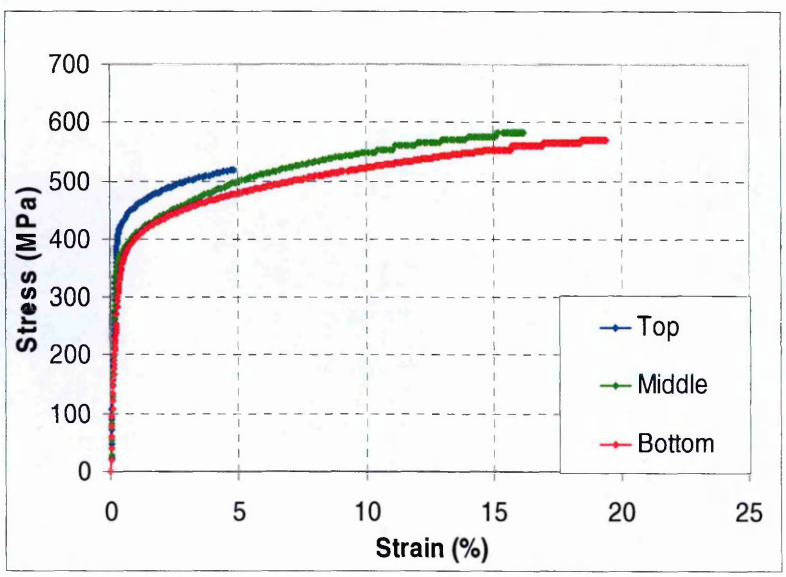

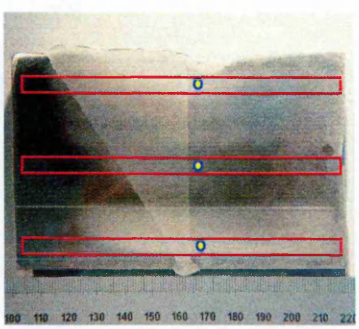

Figure 5.14 Stress-strain curves of HAZ material (x=2mm) from top, middle and bottom specimens at room temperature.

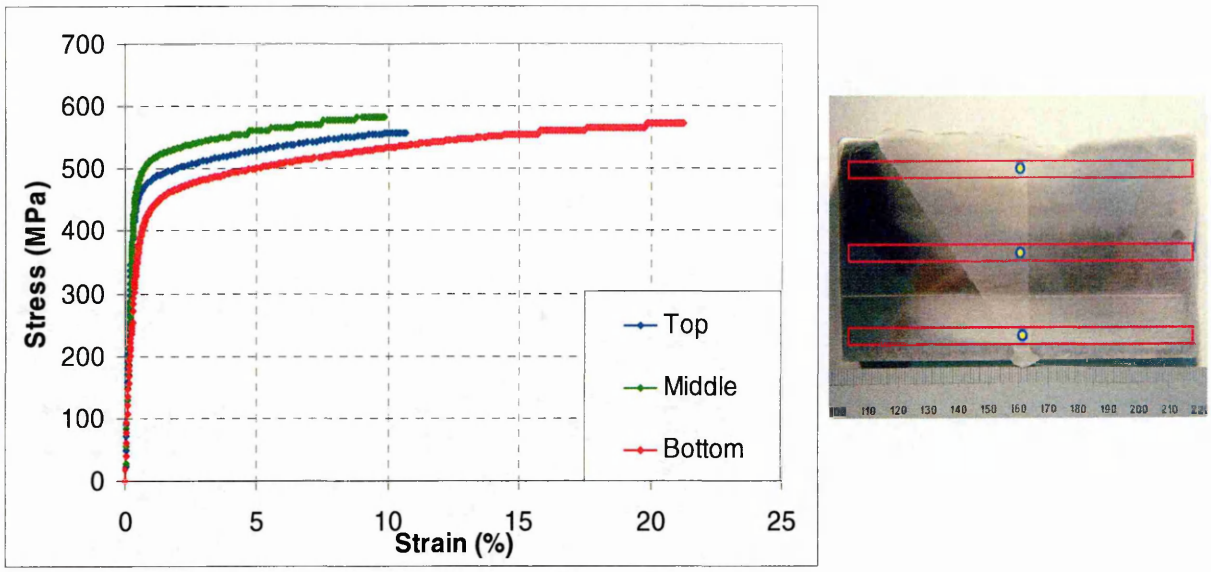

Figure 5.15 Stress-strain curves of the first-pass weld pass of each levels (x=-2mm) at top, middle and bottom specimens at room temperature.

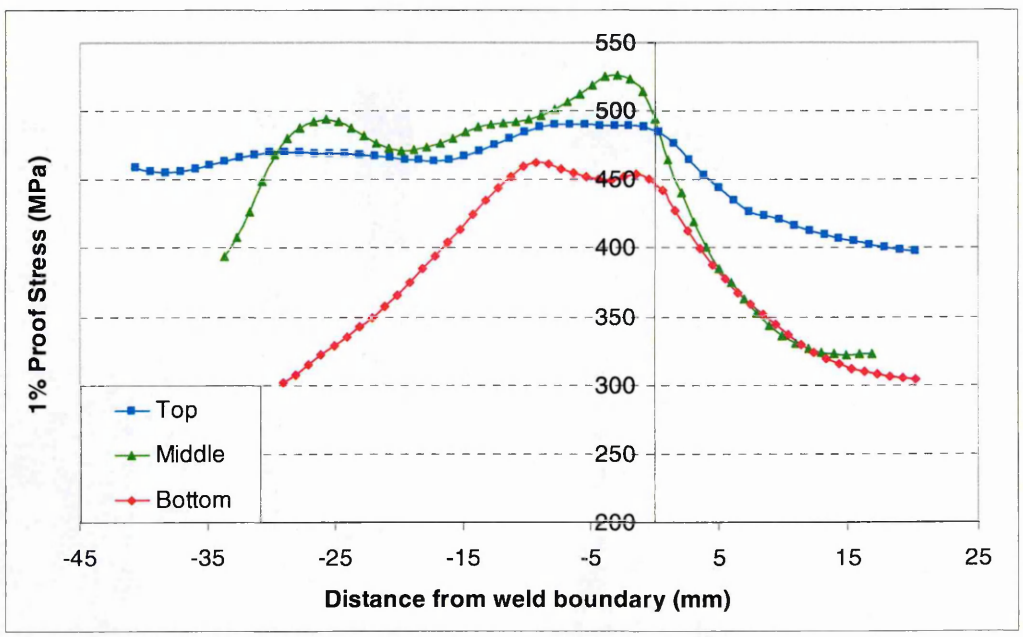

Figure 5.16 Variation of 1% proof stress across the specimens at the top, middle and bottom positions at room temperature

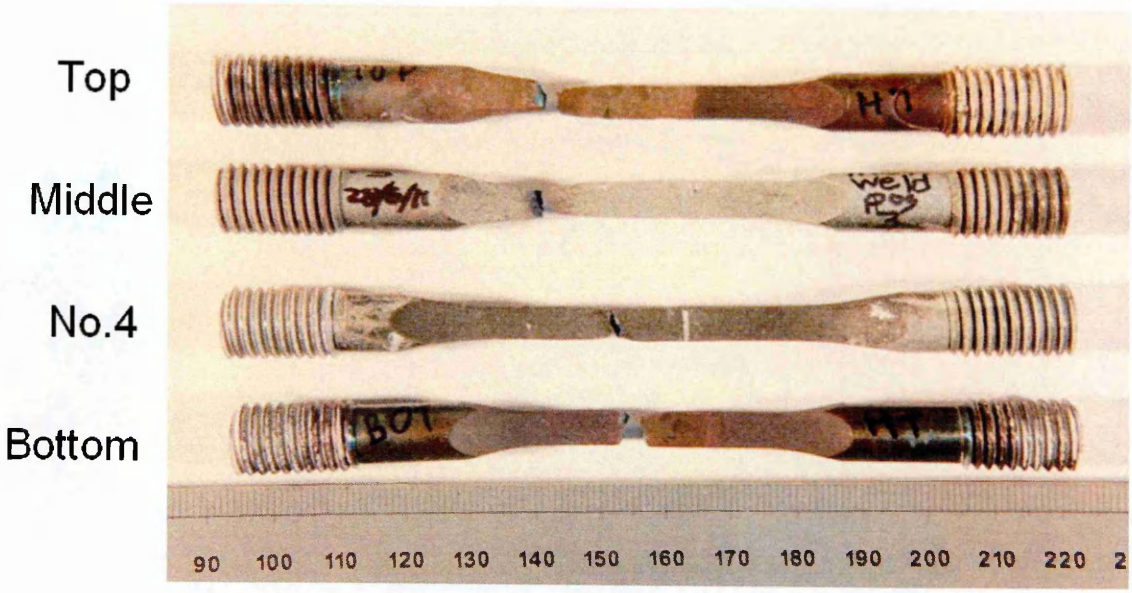

Figure 5.17 Ruptured specimens from high temperature tensile test

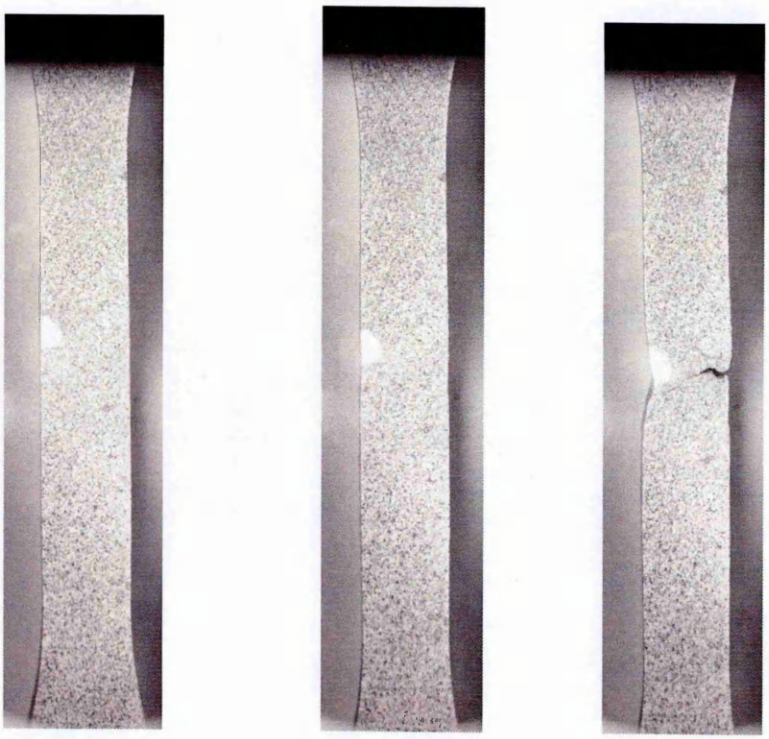

(a) Elastic region **(b) Plastic region** **(c) Last**

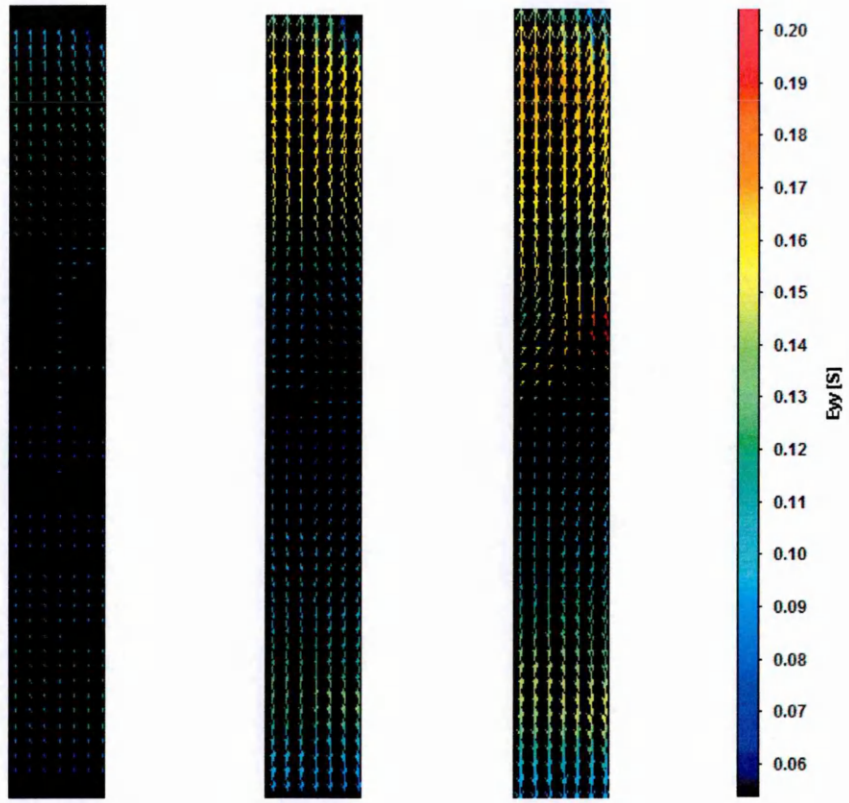

(a) Elastic region (b) Plastic region (c) Last

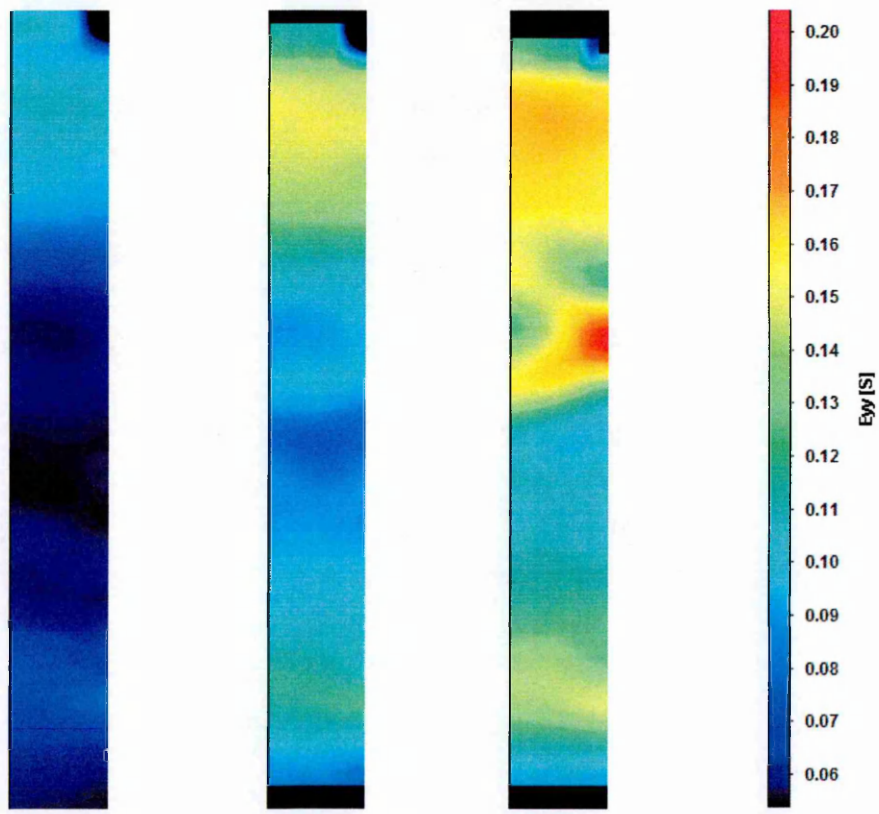

(a) Elastic region (b) Plastic region (c) Last

Figure 5.18 Example of DIC test images at different stage and corresponded to their strain vectors and contours maps from bottom position test (high temperature)

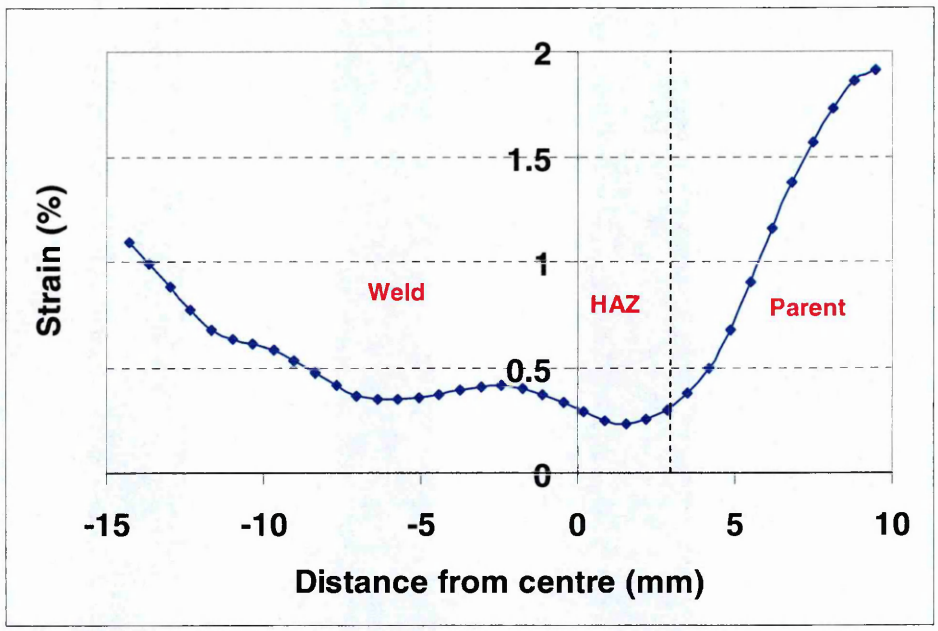

Figure 5.19 Strain variation at 545°C along the gauge length at a stress level of 315MPa from the high temperature tensile test (top position)

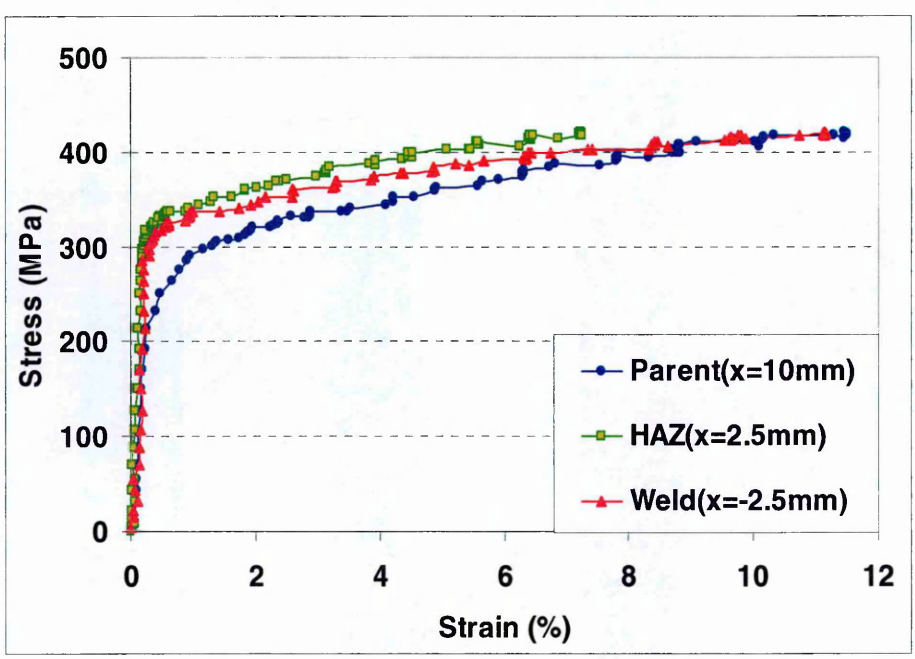

Figure 5.20 Stress-strain curves of parent, HAZ and weld at 545°C (top position)

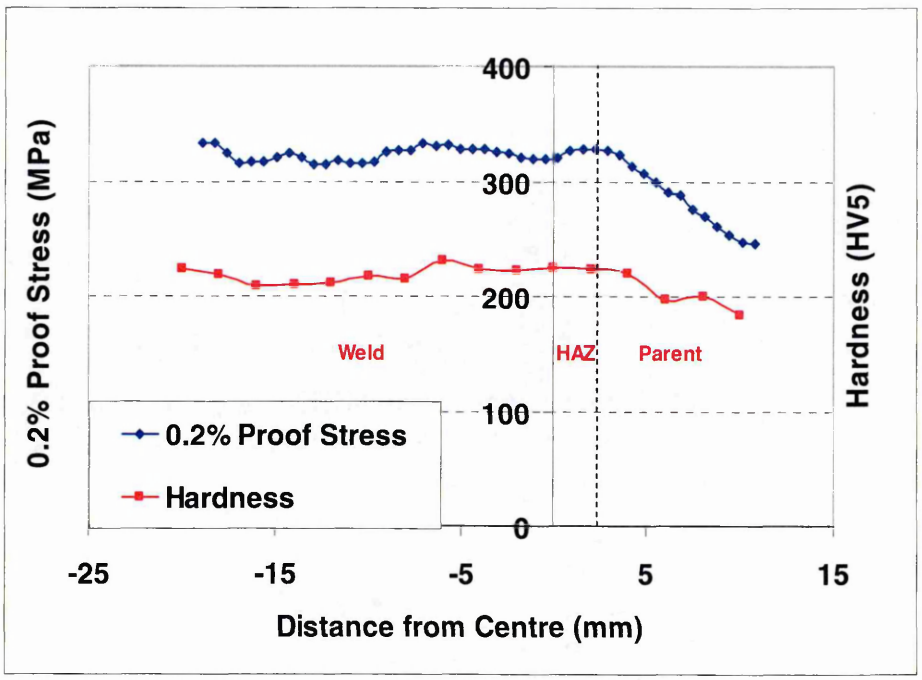

Figure 5.21 0.2% proof stress at 545°C and hardness variations along the cross-weld specimen (top position)

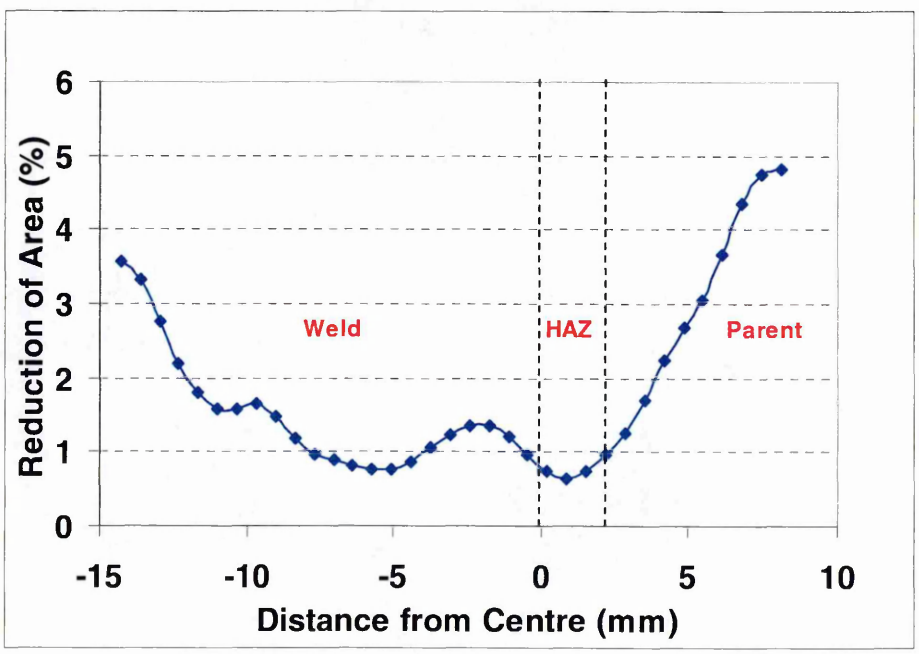

Figure 5.8 Reduction of area at 545°C along the cross-weld specimen gauge length based on measured change of width (top position)

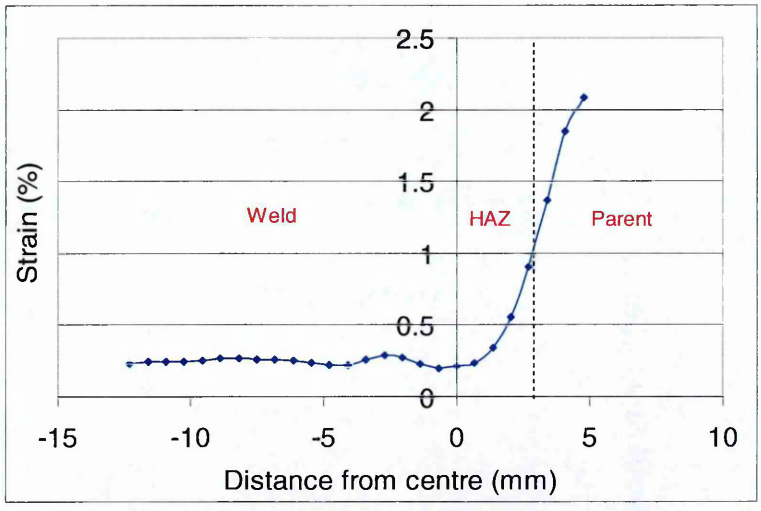

Figure 5.23 Strain variations at 545°C along the gauge length at stress level of 315MPa from high temperature tensile test (middle position)

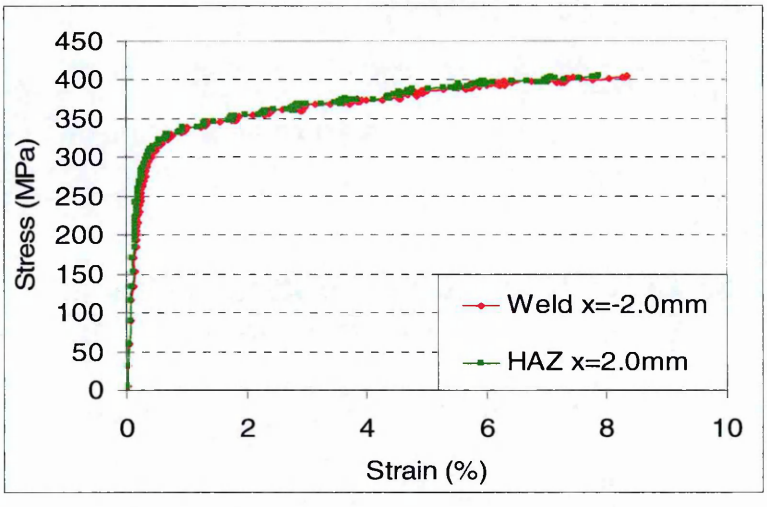

Figure 5.24 Stress-strain curves of HAZ and weld at 545°C (middle position)

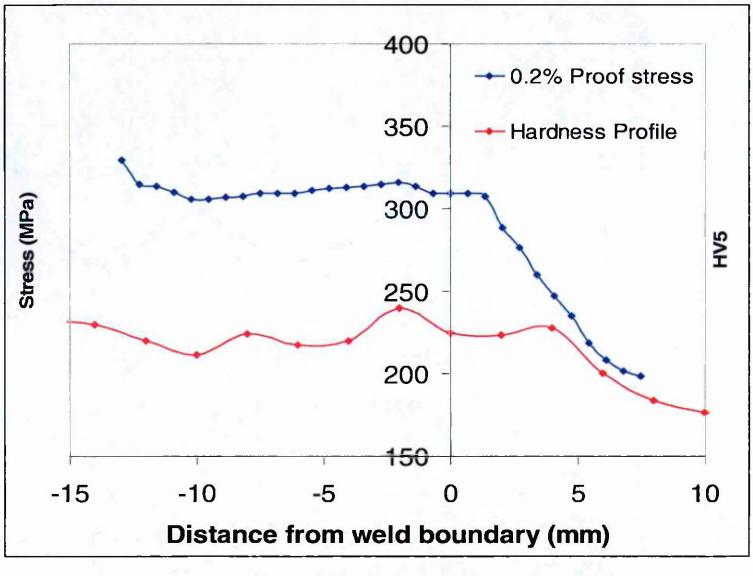

Figure 5.25 0.2% proof stress at 545°C and hardness variation along the cross-weld specimen (middle position)

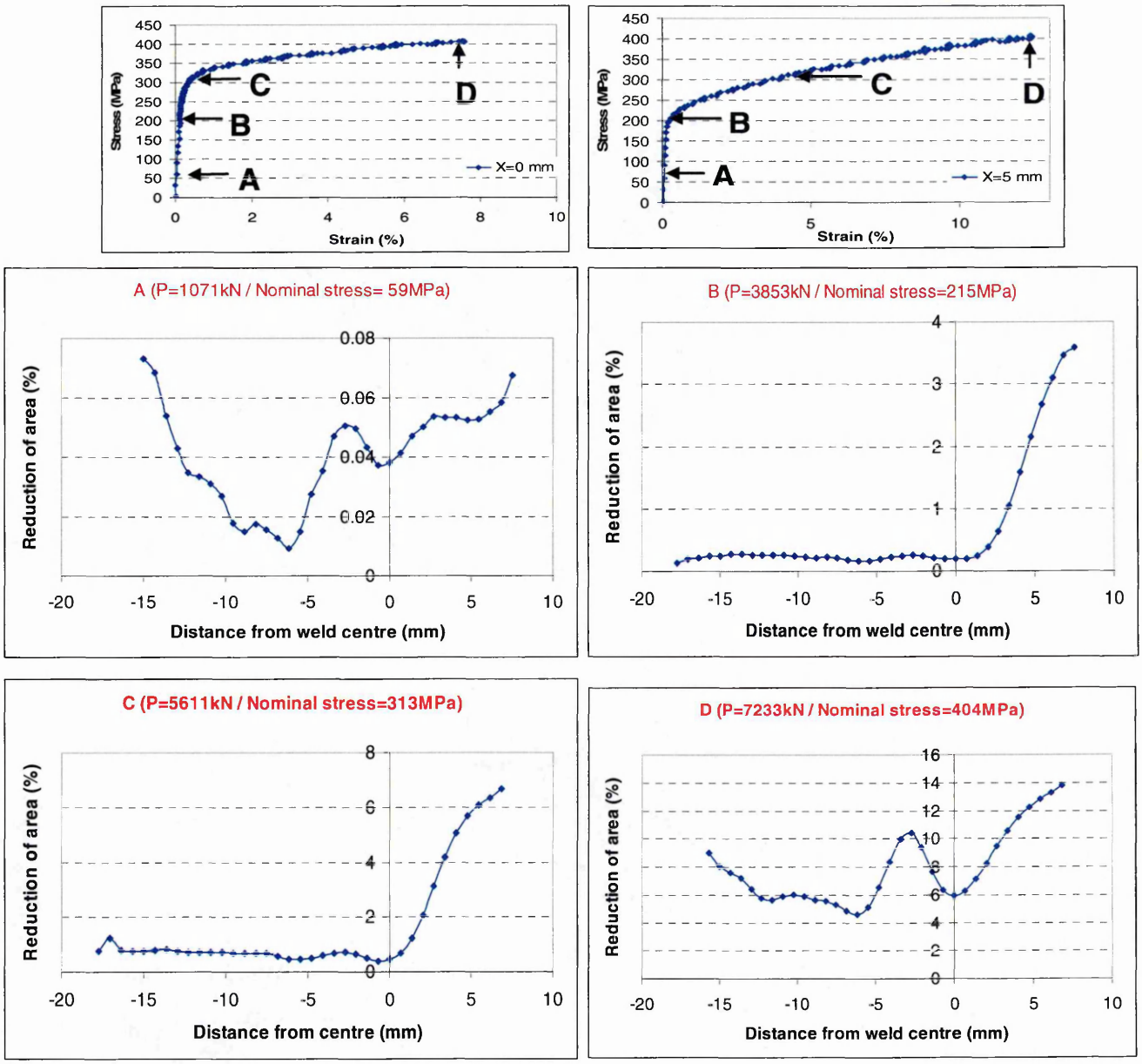

Figure 5.26 Middle position specimen reduction of area along the cross-weld specimen gauge length (based on measured change of width) at different stages of deformation indicated on the stress-strain curves (a) and (b)

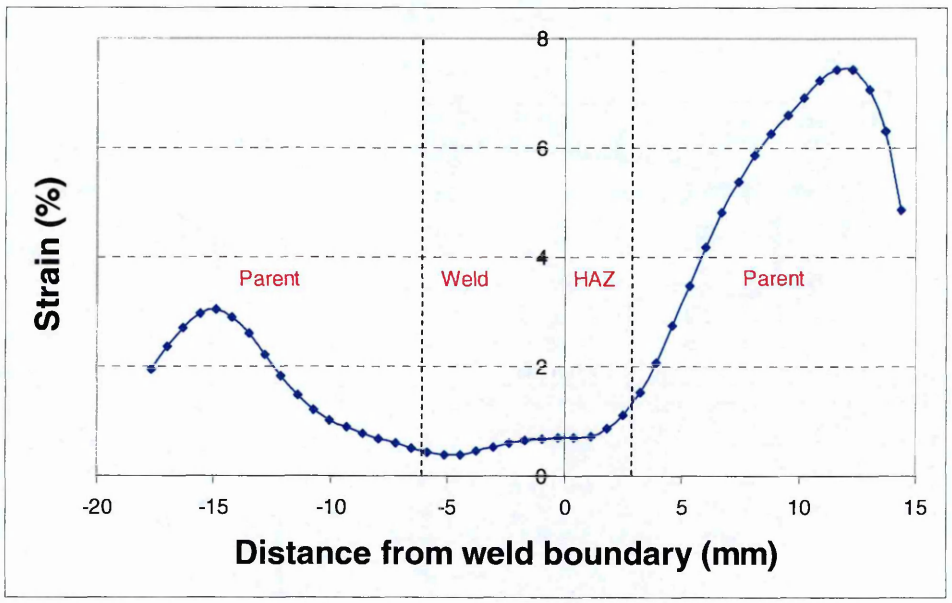

Figure 5.27 Strain variations at 545°C along the gauge length at a stress level of 315MPa from high temperature tensile test (bottom position)

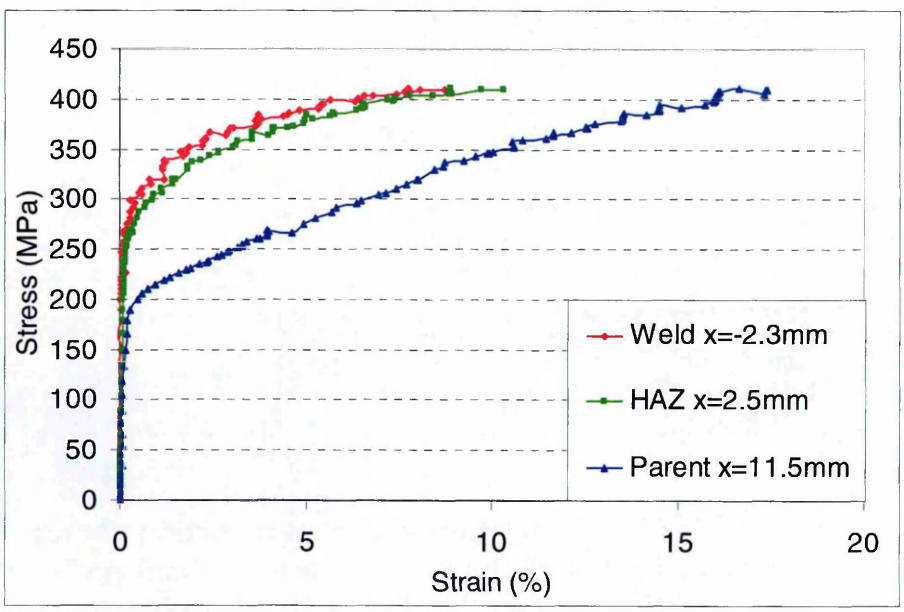

Figure 5.28 Stress-strain curves of parent, HAZ and weld at 545°C (bottom position)

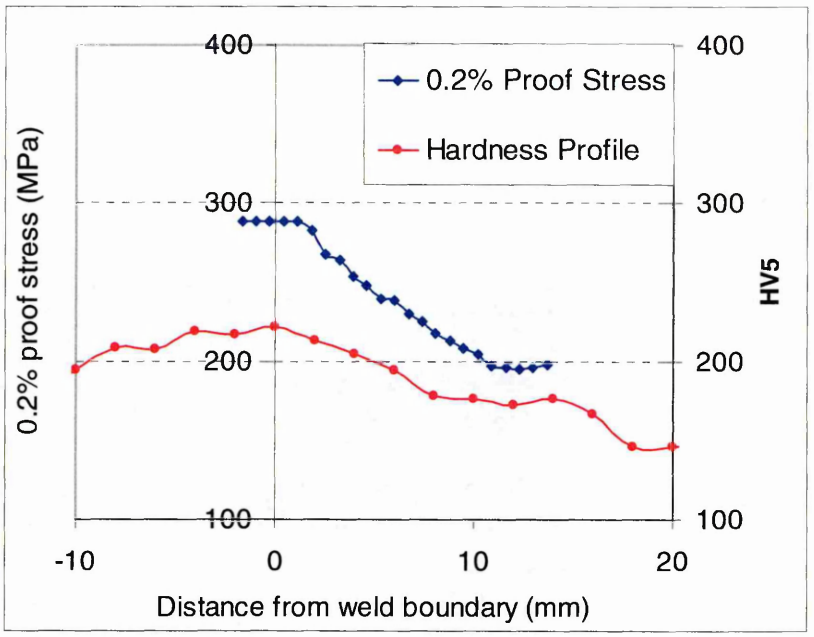

Figure 5.29 0.2% proof stress at 545^{0}C and hardness variation along the cross-weld specimen (bottom position)

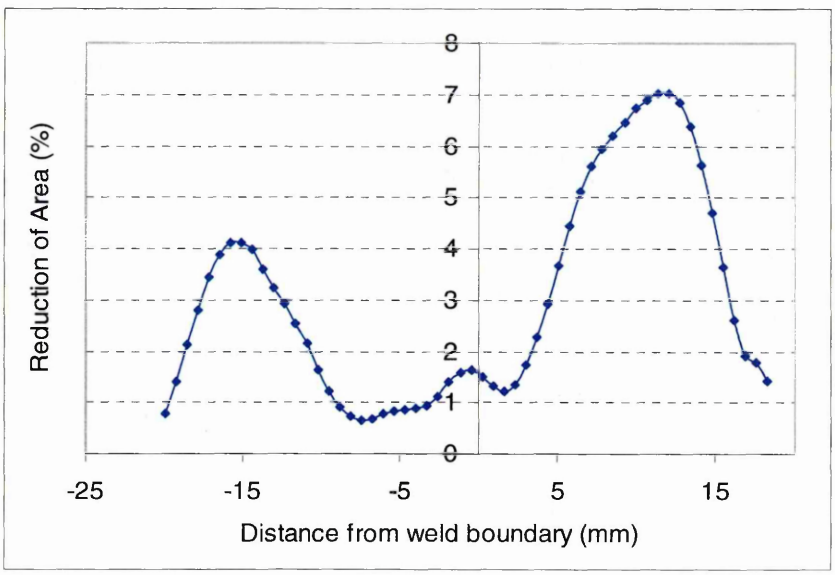

Figure 5.30 Reduction of area at 545^{o}C along the cross-weld specimen gauge length (Bottom position)

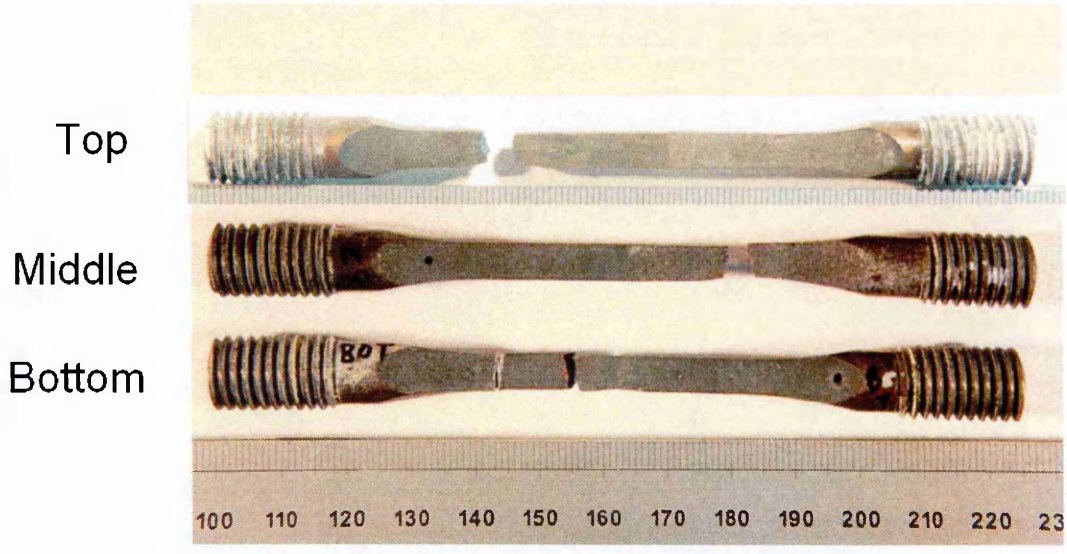

Figure 5.31 Photograph of ruptured specimens from creep tests at 545°C

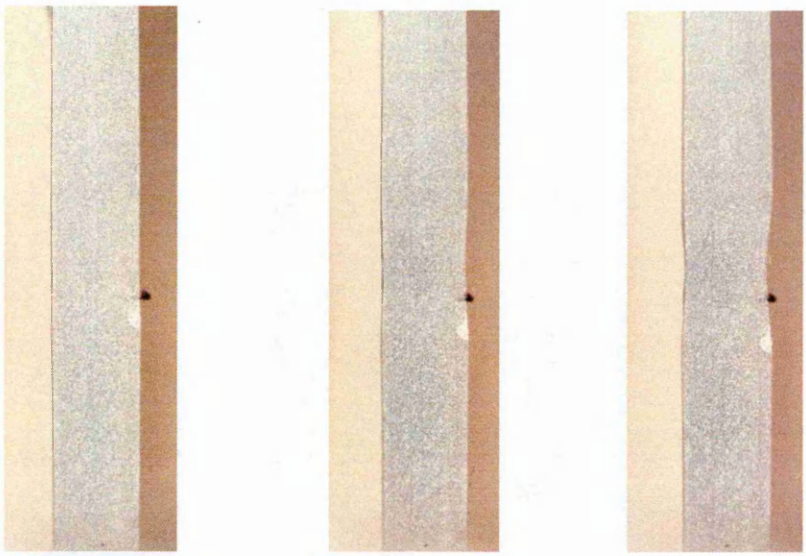

(a) Elastic region (b) Plastic region (c) Last

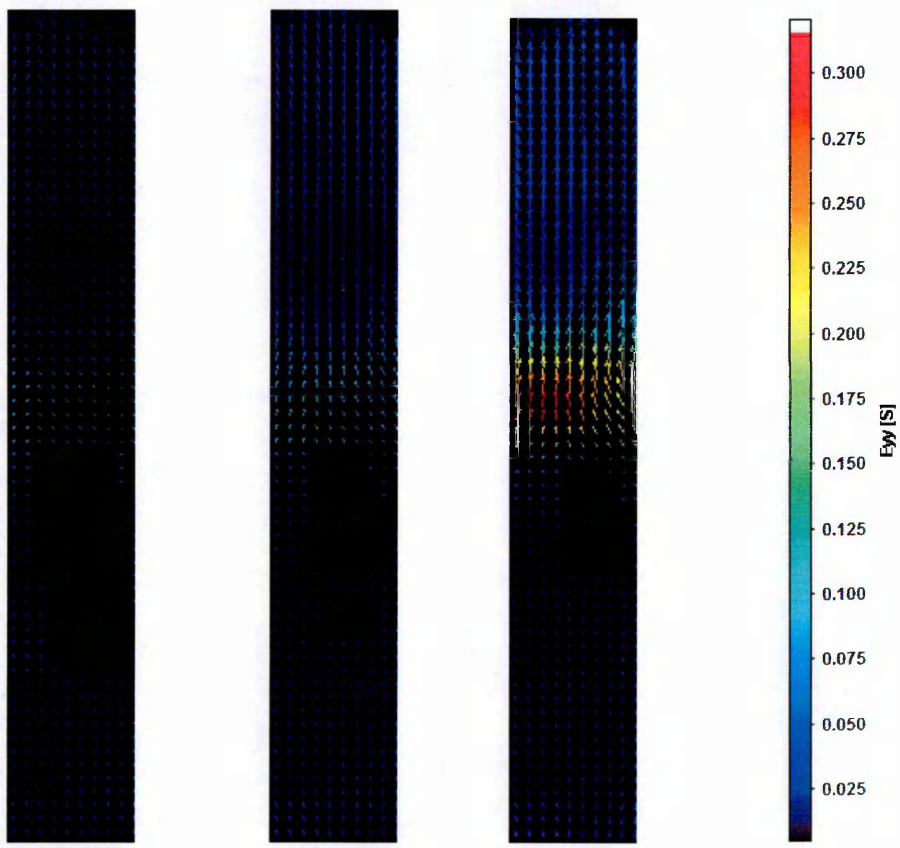

(a) Elastic region (b) Plastic region (c) Last

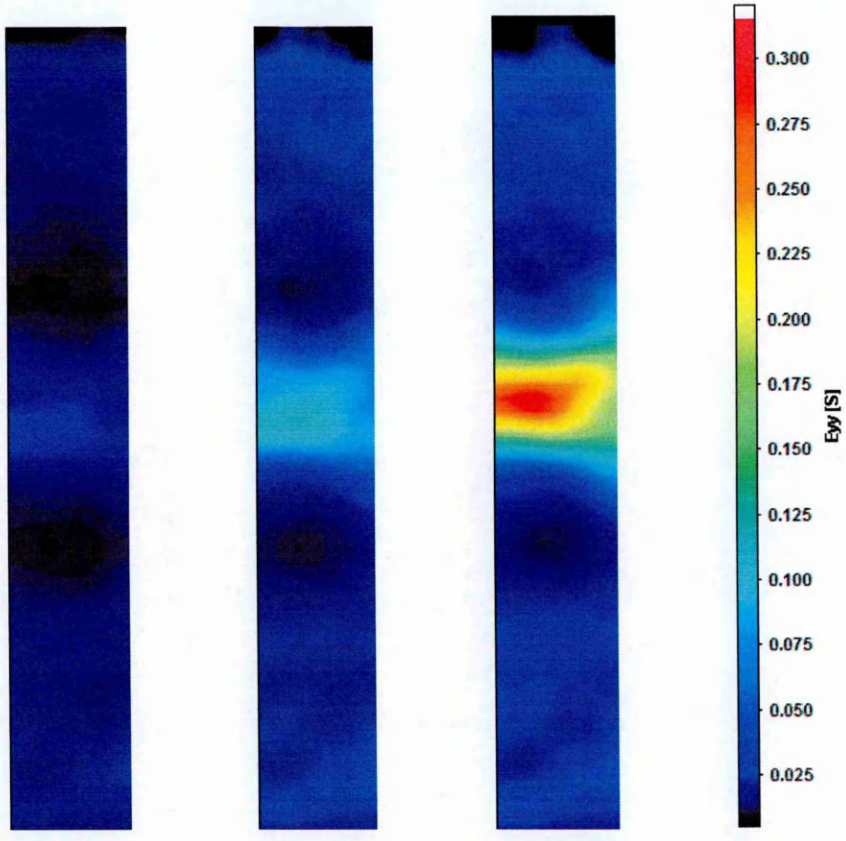

(a) Elastic region (b) Plastic region (c) Last

Figure 5.32 Example of DIC test images at different stage and corresponded to their strain vectors and contours maps from bottom position test (creep)

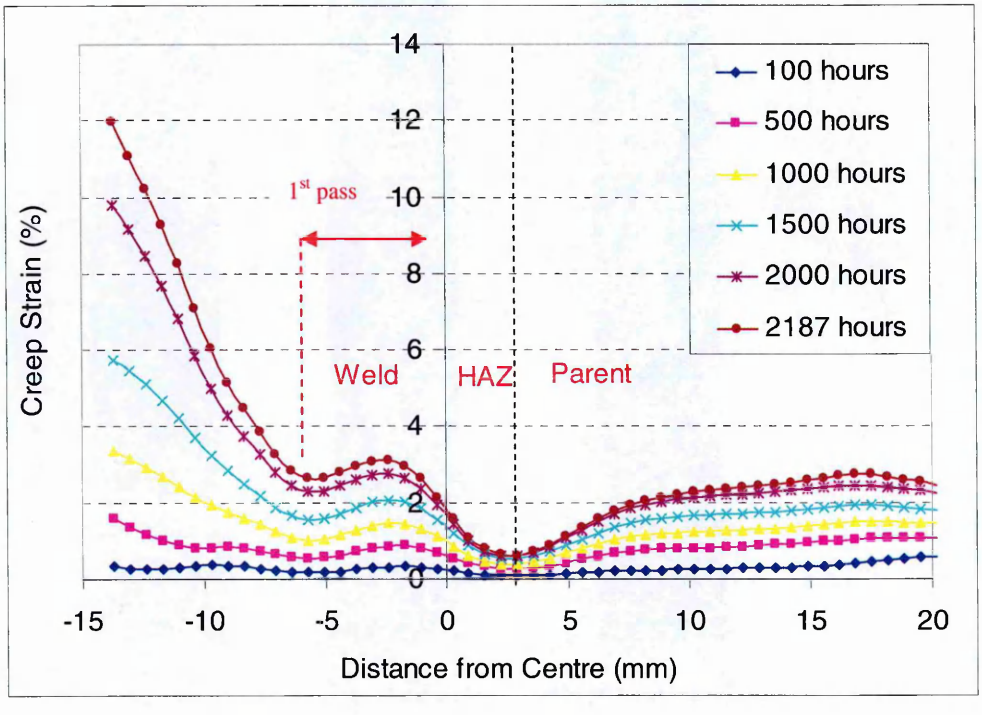

Figure 5.33 Creep strain evolutions along the gauge length of the specimen at different times (top position)

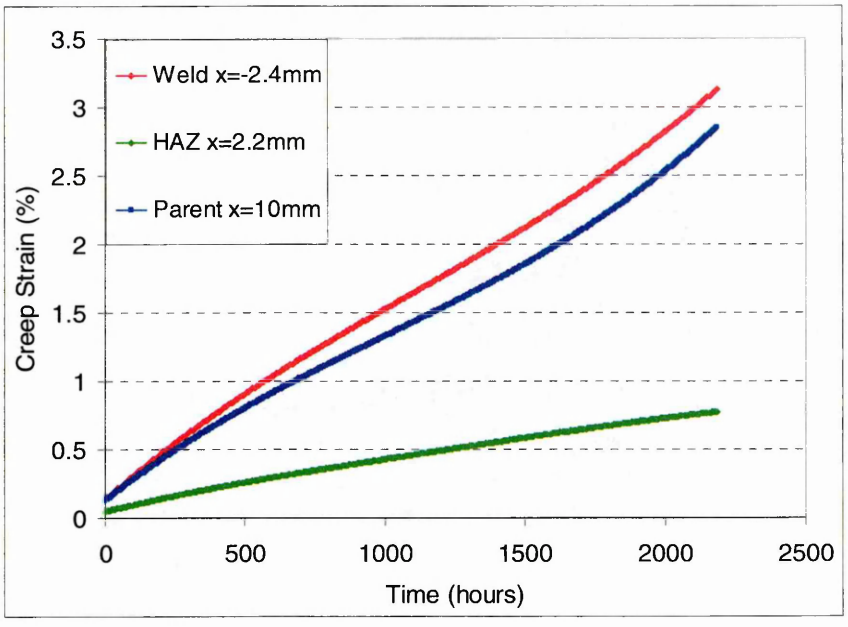

Figure 5.34 Local creep deformation curves of parent metal (x=10mm), HAZ (x=2.5mm) and weld (x=–2.5mm) (top position)

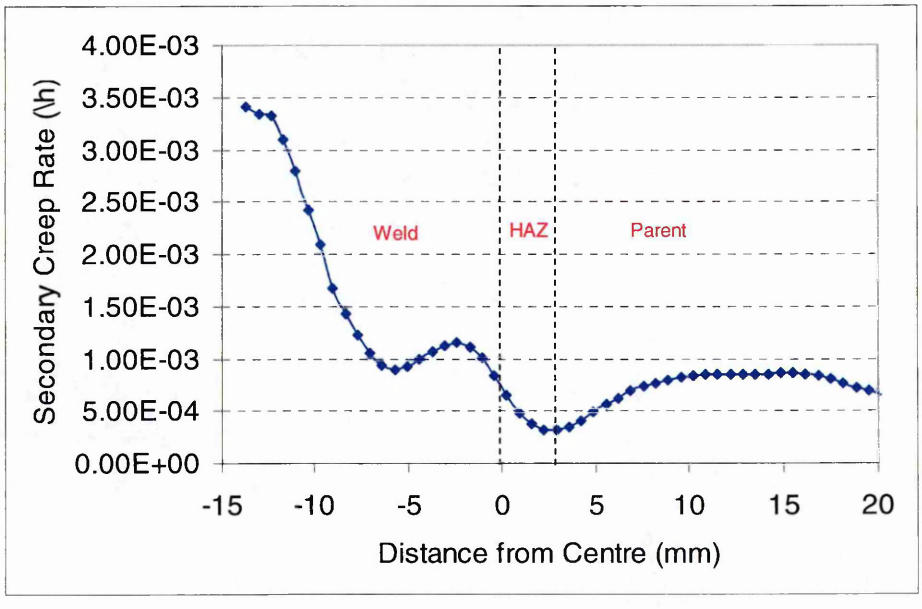

Figure 5.35 Secondary creep rate distribution along the cross-weld test specimen under applied load of 315MPa at 545°C (top position)

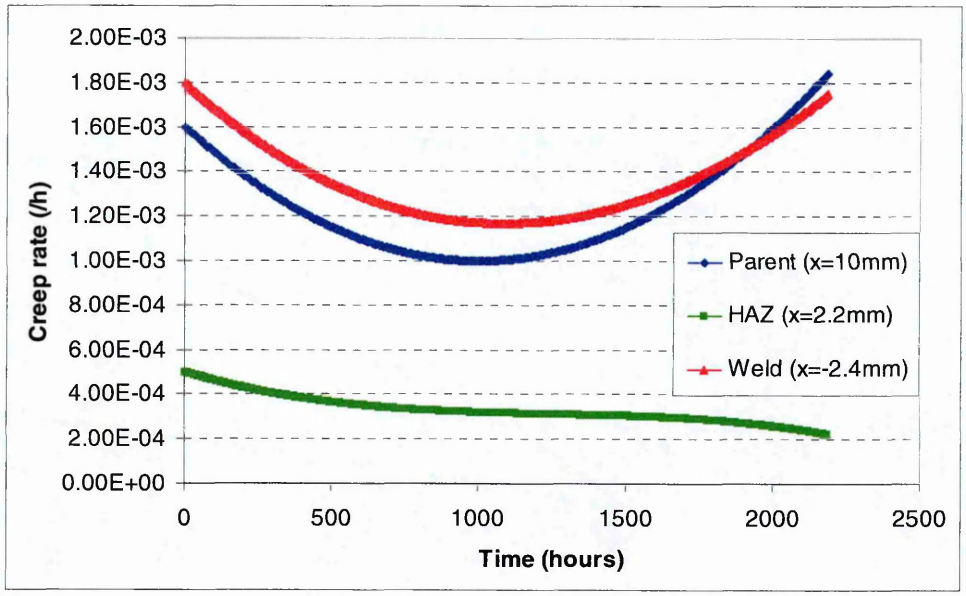

Figure 5.36 Creep rate in parent HAZ and weld with increasing time (top position)

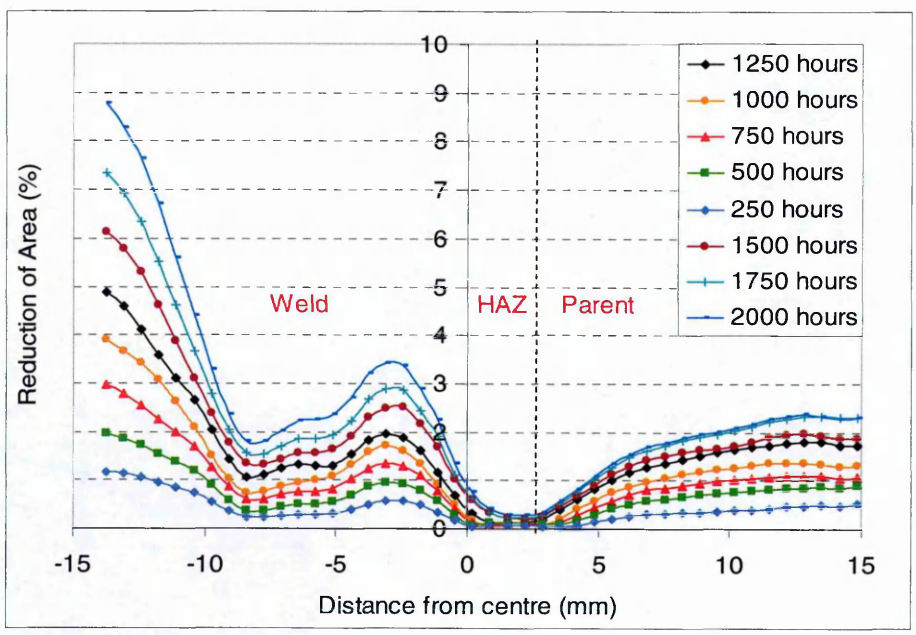

Figure 5.37 Reduction of area across the specimen based on width direction data (top position)

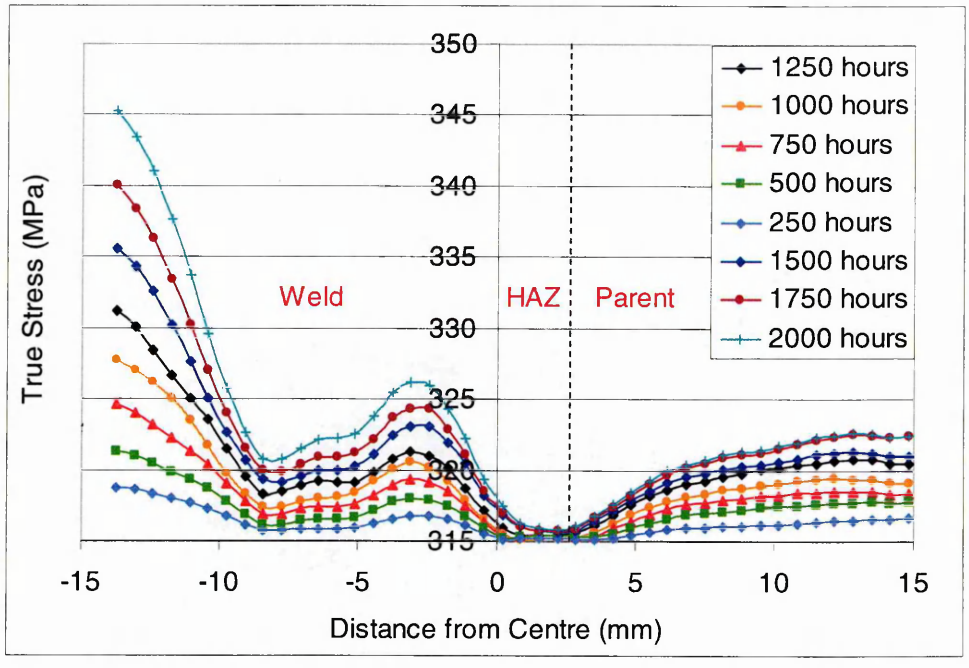

Figure 5.38 True stress distribution across the cross-weld specimen based on change in specimen width data (top position)

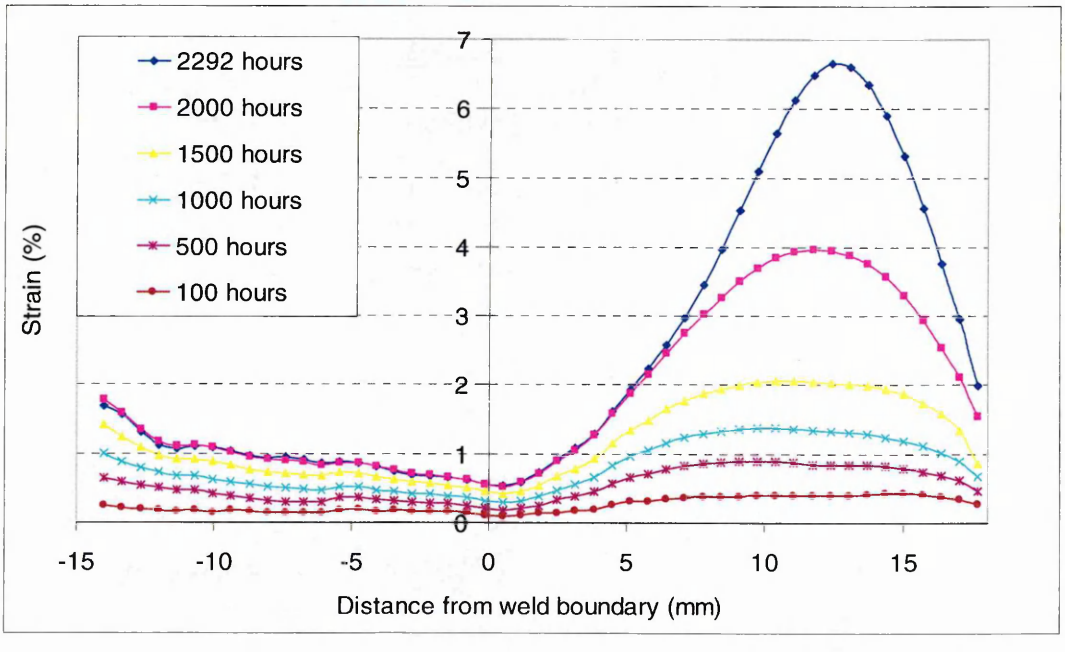

Figure 5.39 Strain evolutions along the gauge length of the specimen at different times (middle position)

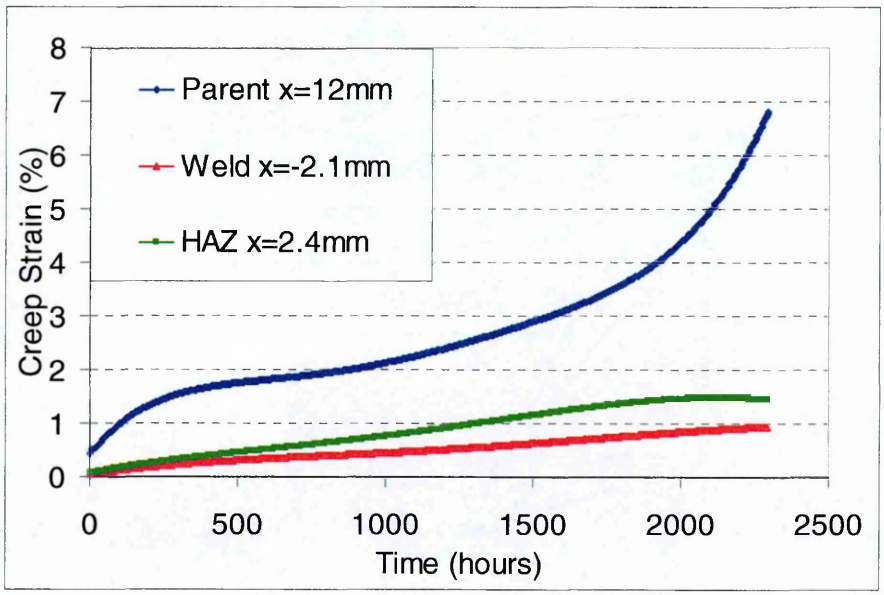

Figure 5.40 Local creep deformation curves of parent metal (x=12mm), HAZ (x=2.4mm) and weld (x=–2.1mm) (middle position)

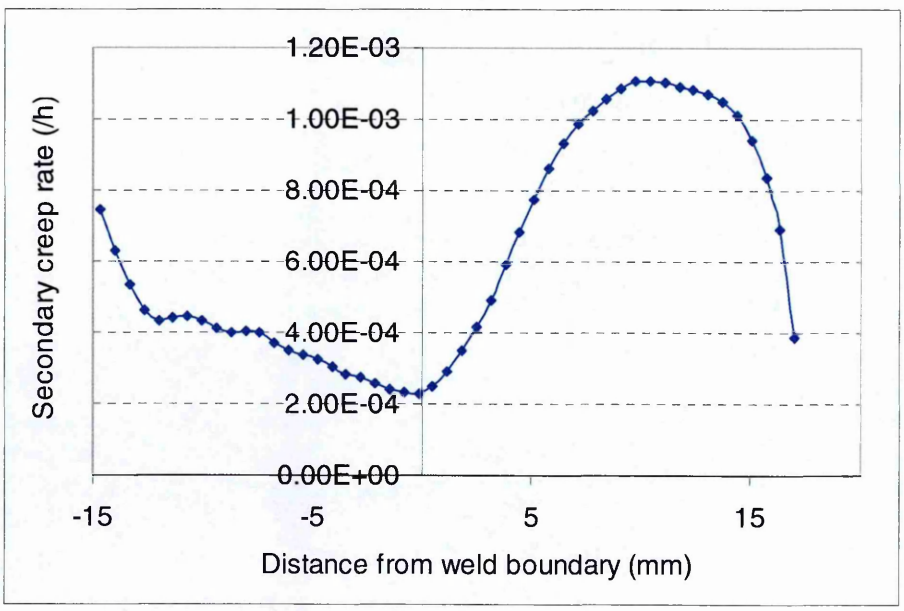

Figure 5.41 Secondary creep rate distribution along the cross-weld test specimen under applied load of 315MPa at 545°C (middle position)

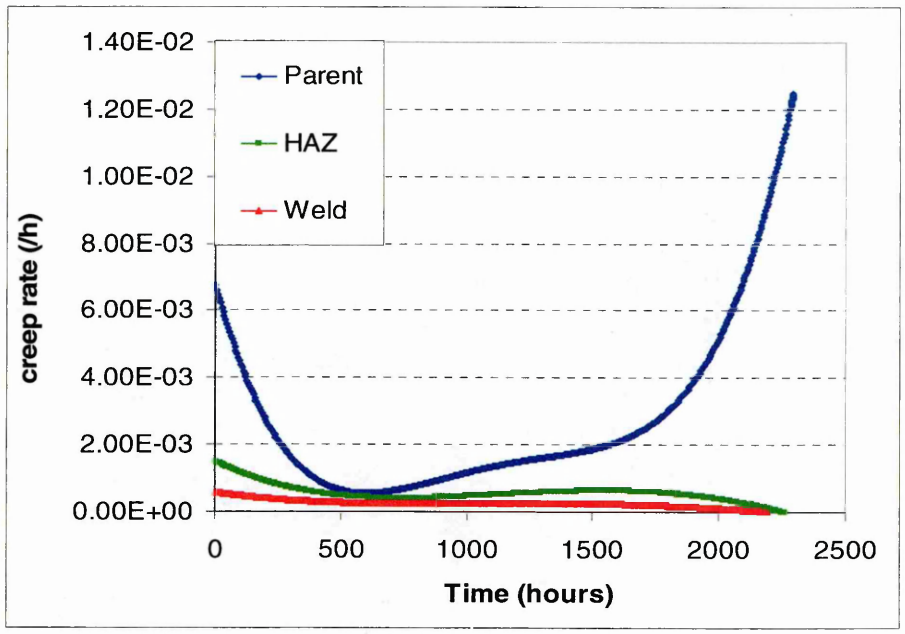

Figure 5.42 Creep rate at Parent HAZ and Weld with increasing time (middle position)

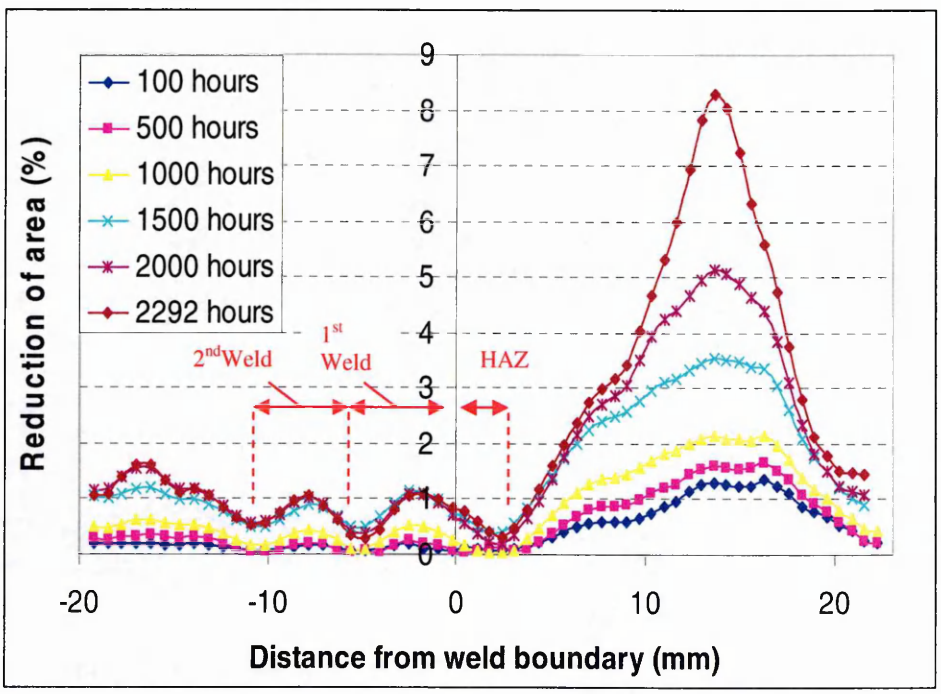

Figure 5.43 Reduction of area distribution across the cross-weld specimen based on specimen width direction data (middle position)

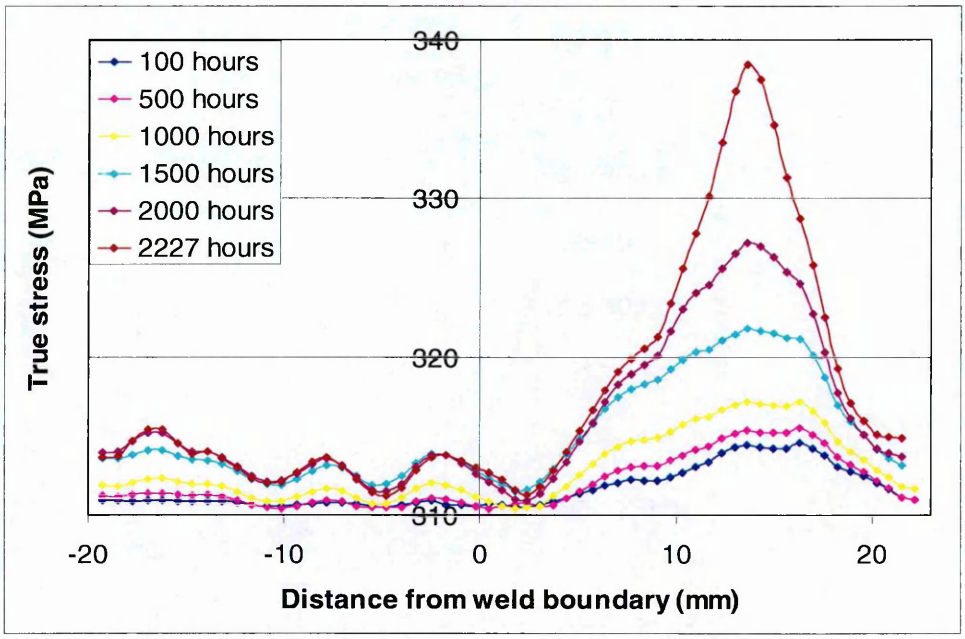

Figure 5.44 True stress distribution across the cross-weld specimen based on change in specimen width data (middle position)

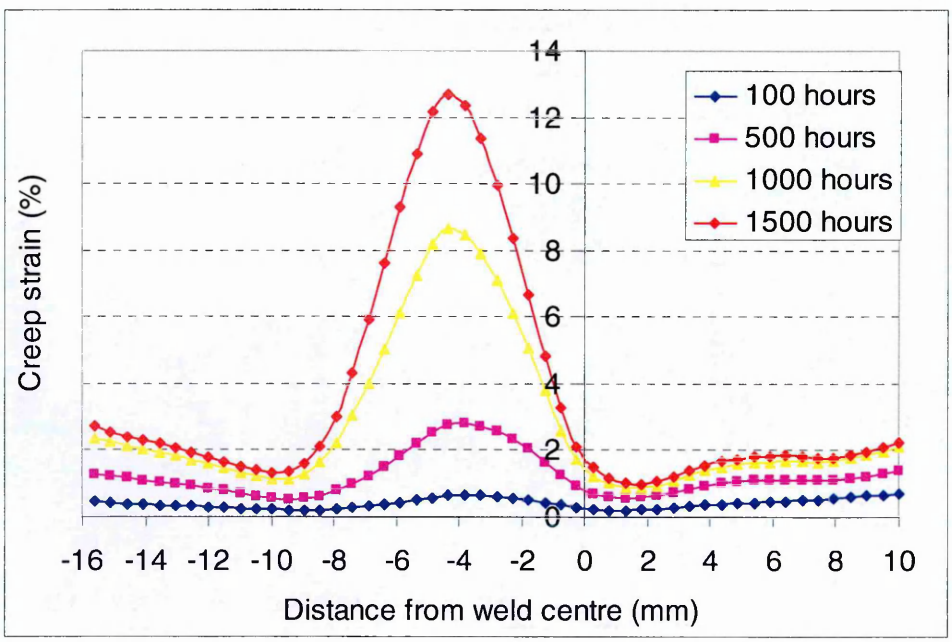

Figure 5.45 Strain evolutions along the gauge length of the specimen at different times (bottom position)

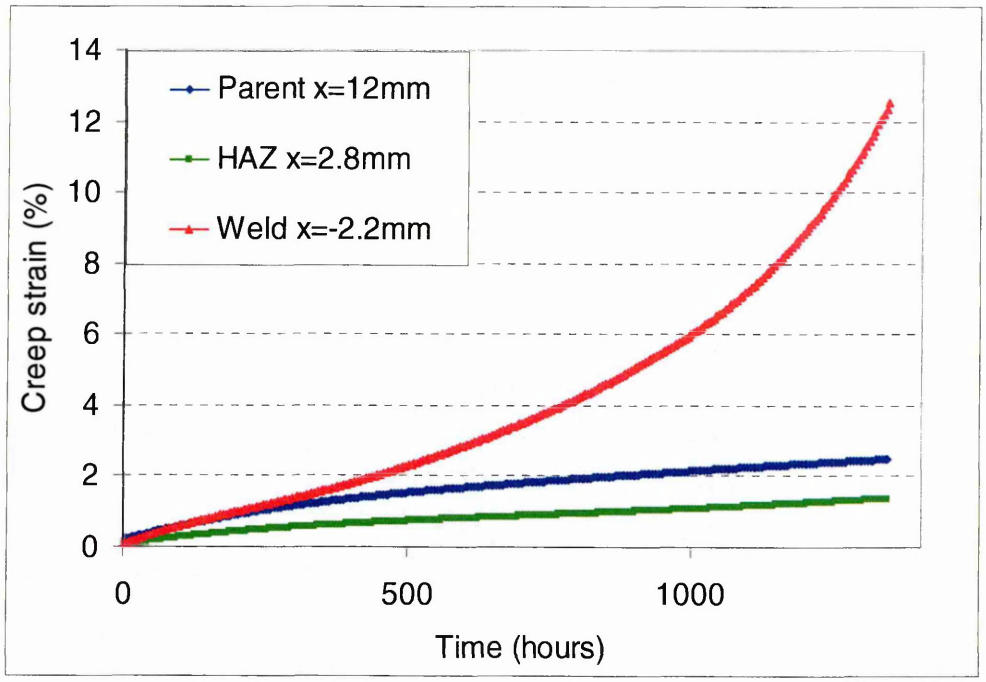

Figure 5.46 Local creep deformation curves of parent metal (x=12mm), HAZ (x=2.8mm) and weld (x=–2.2mm), (bottom position)

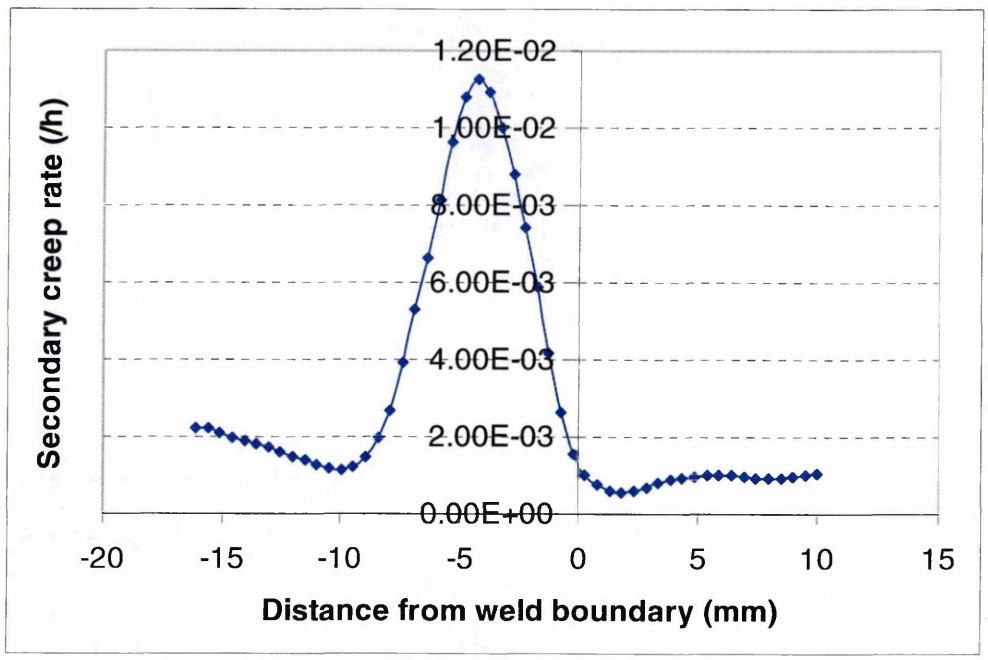

Figure 5.47 Secondary creep rate distribution along the cross-weld test specimen under applied load of 315MPa at 545°C (bottom position)

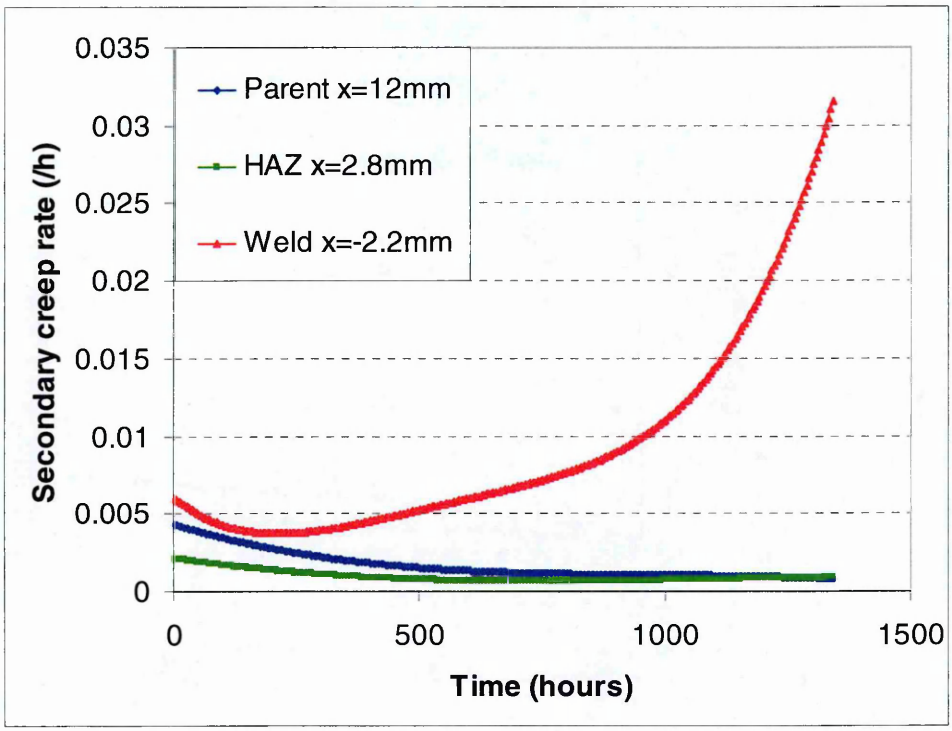

Figure 5.48 Secondary creep rate at in parent, HAZ and weld metal with increasing time (bottom position)

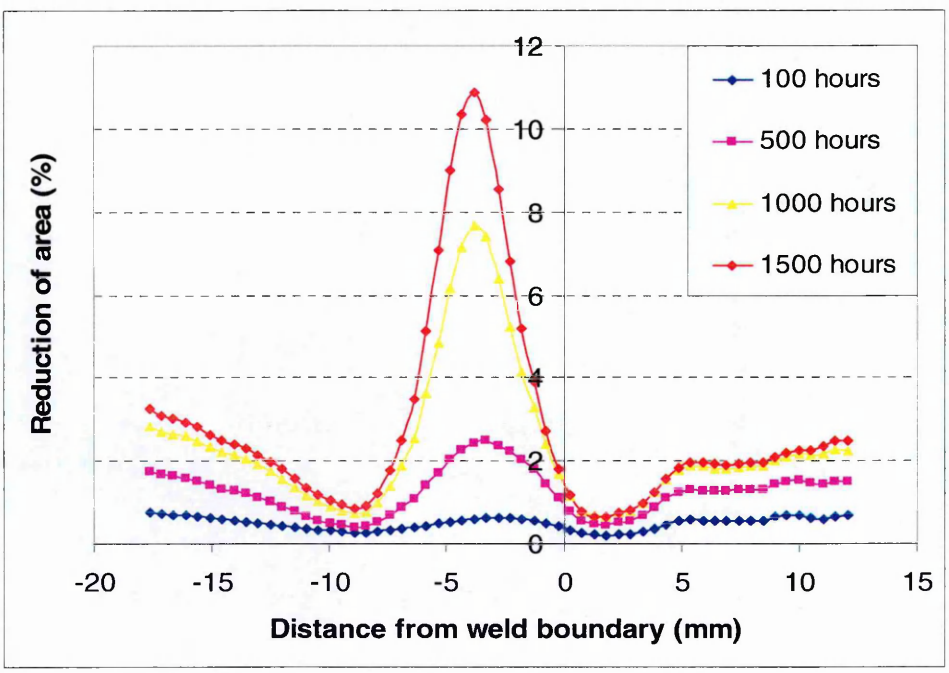

Figure 5.49 Reduction of area distribution across the cross-weld specimen based on specimen width direction data (bottom position)

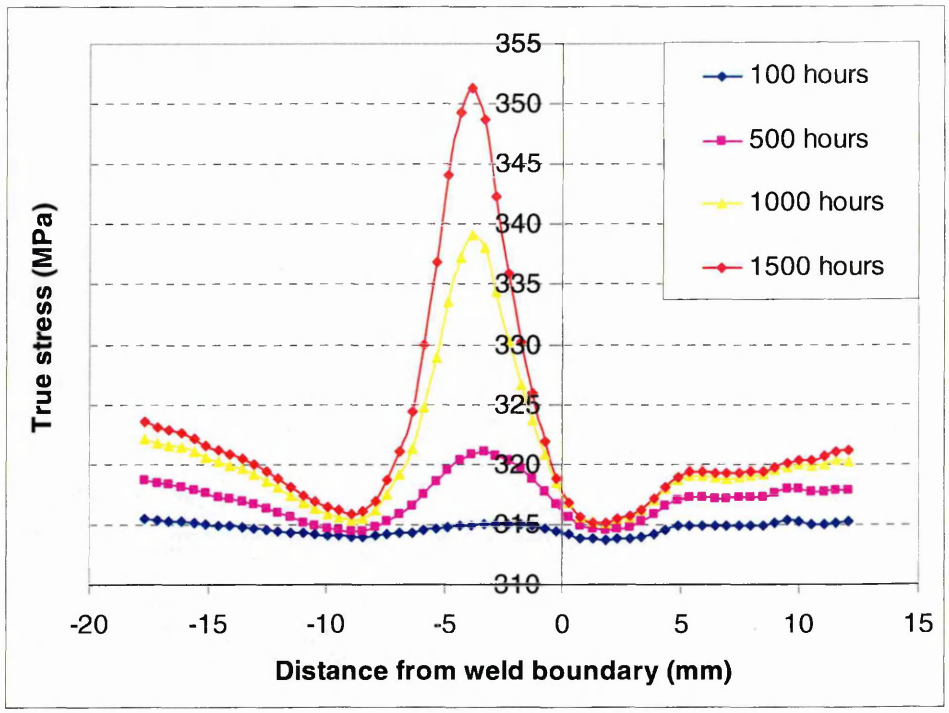

Figure 5.50 True stress distribution across the cross-weld specimen based on change in specimen width data (bottom position)

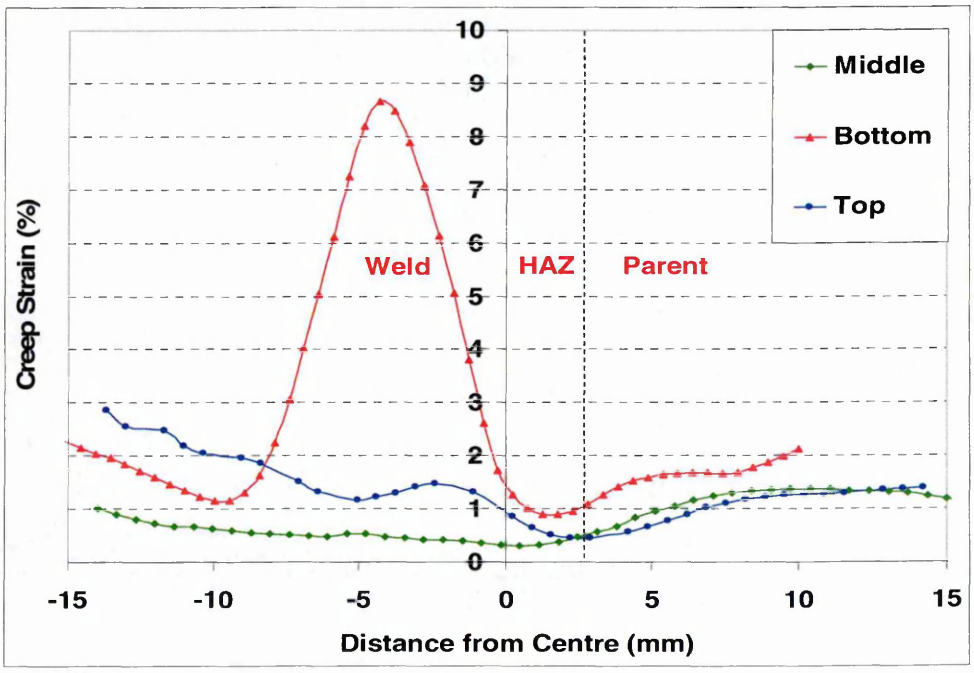

Figure 5.51 Strain distributions of top, middle and bottom positions at 1000 hours (secondary creep region)

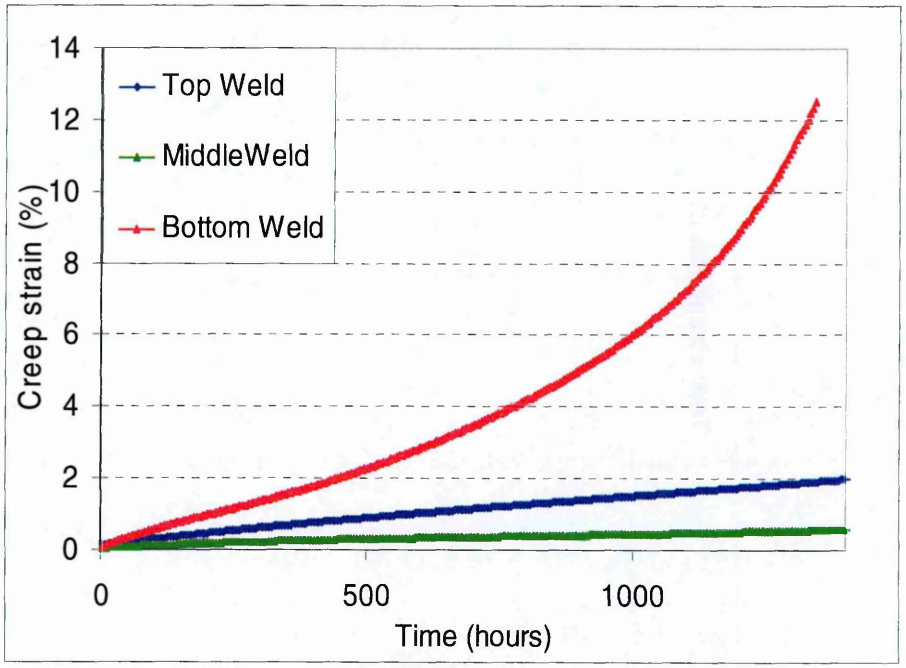

Figure 5.52 Local creep curves of top, middle and bottom positions in the weld metal (x=-2mm)

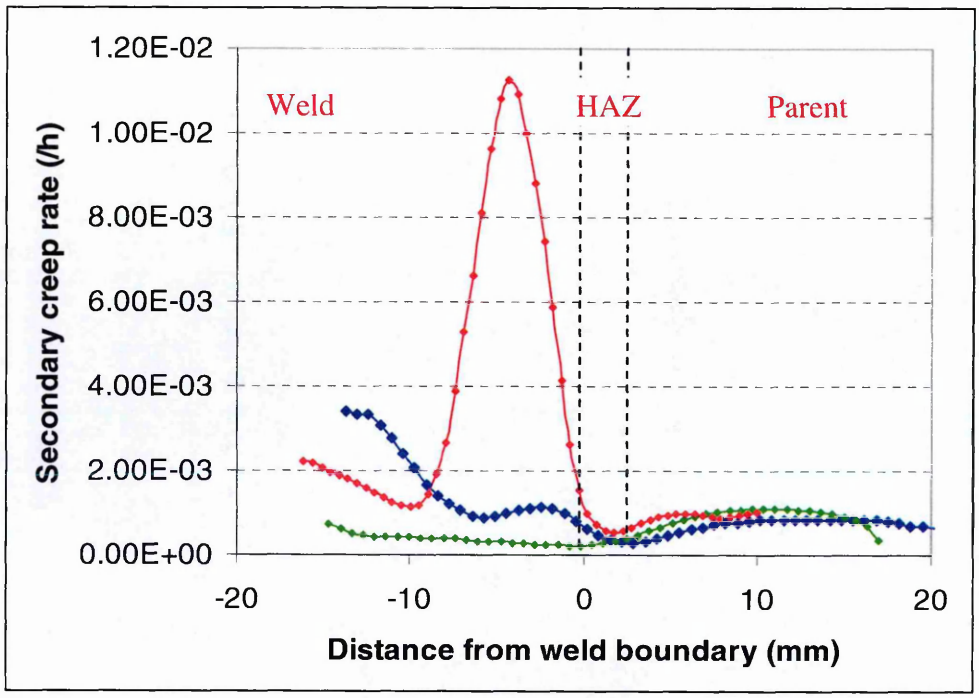

Figure 5.53 Secondary creep rate distribution across the weld at the top, middle and bottom positions

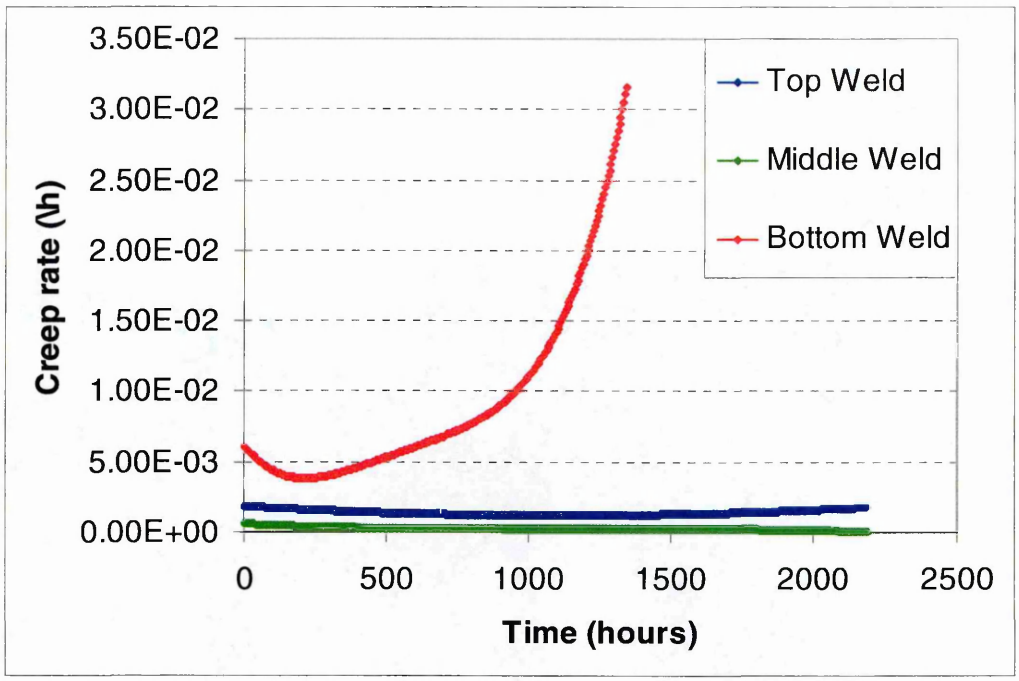

Figure 5.54 Secondary creep rate vs time of weld metal at top, middle and bottom positions

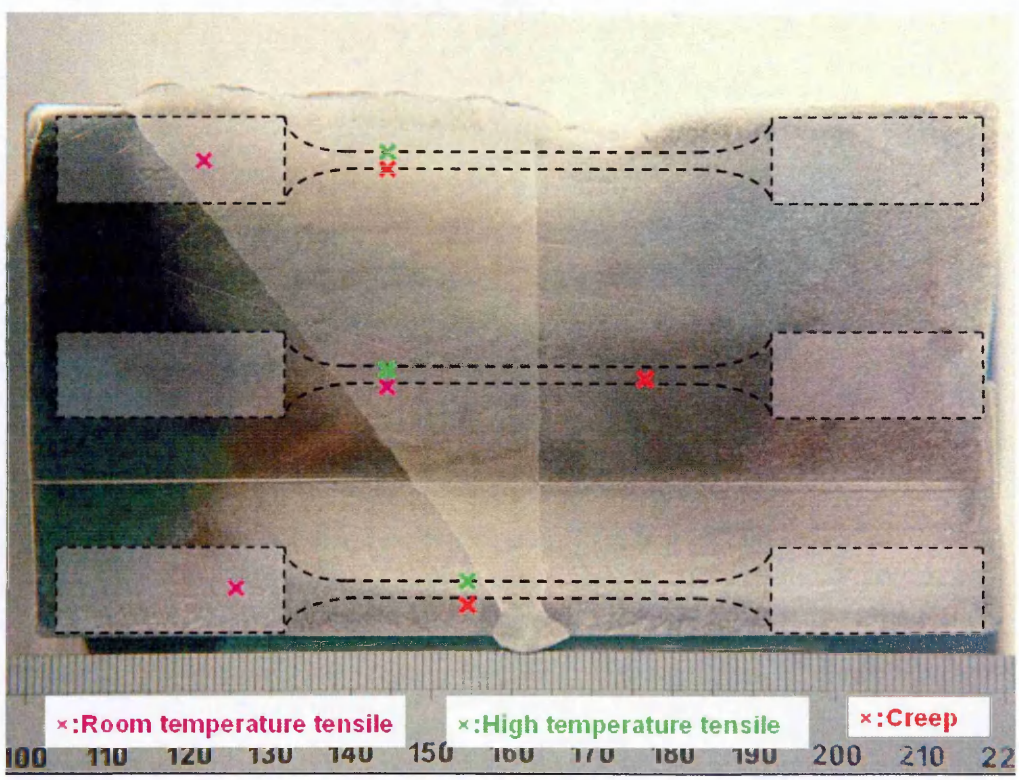

Figure 5.55 Specimen rupture positions in the room temperature tensile tests, high temperature tensile tests and creep tests. Note: Room Temperature specimens have a different design, with a longer gauge length (70mm)

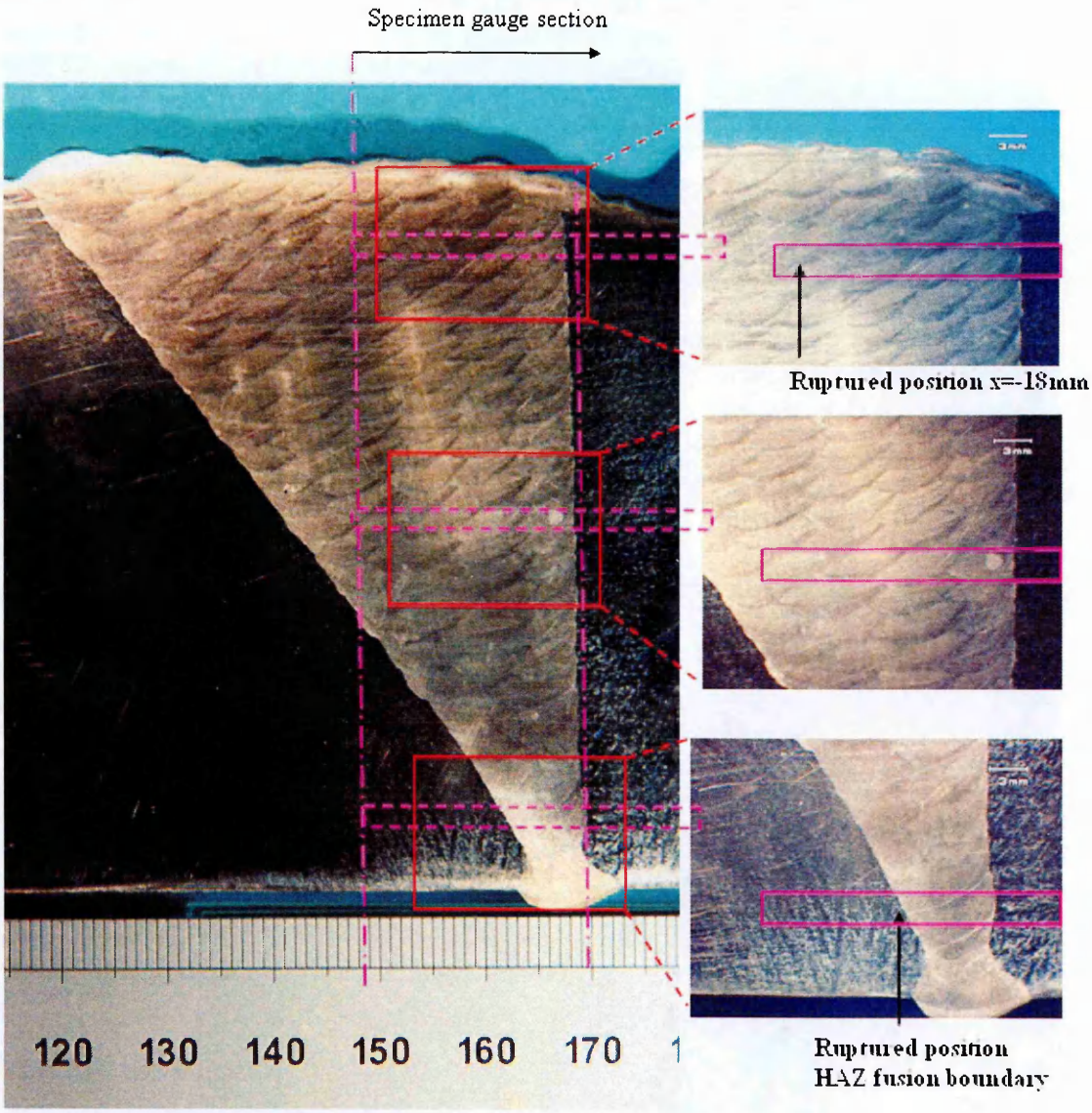

Figure 5.56 Photograph of etched section showing the stainless steel weld pass deposition sequence with enlarged details indicating positions of the specimen gauge sections and rupture (top and bottom)

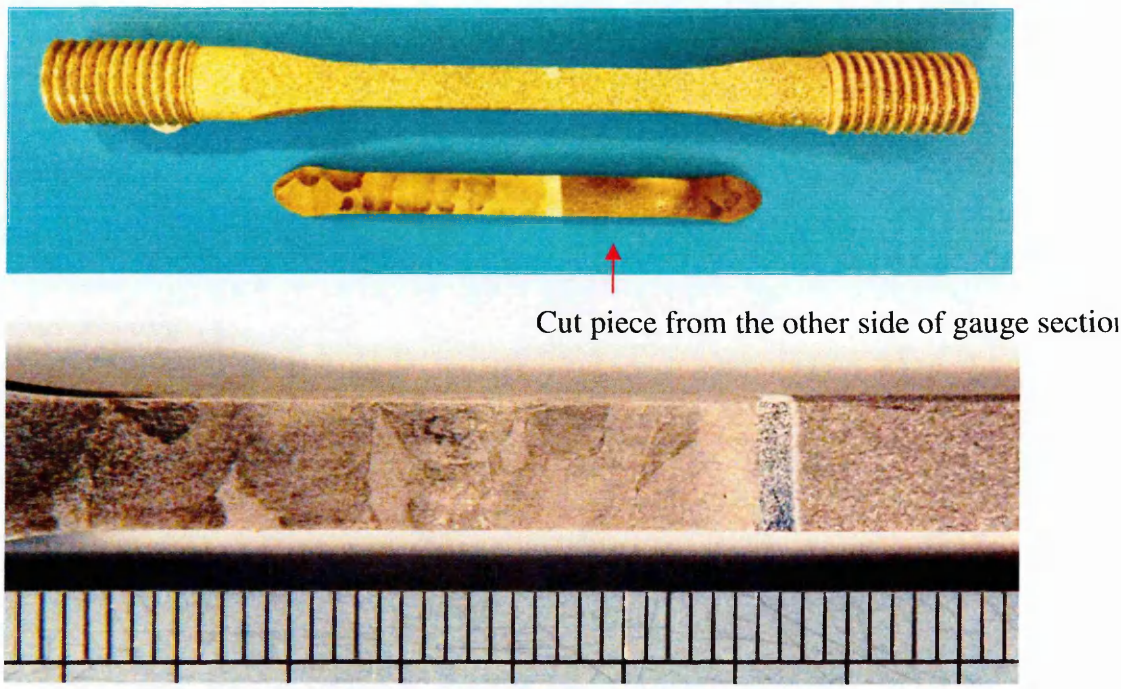

Figure 5.57 Photograph of the top creep specimen and a metallographically prepared sample cut from the side of the specimen gauge length to create flat sides. Below an enlarged photo showing details of the multi-pass weldment.

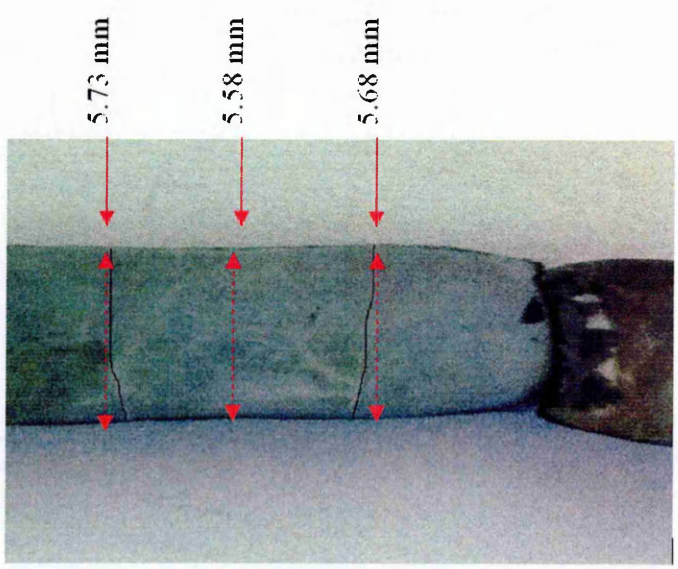

Figure 5.58 Weld beads and fusion boundaries adjacent to the ruptured location are indicated on the photograph from the top specimen

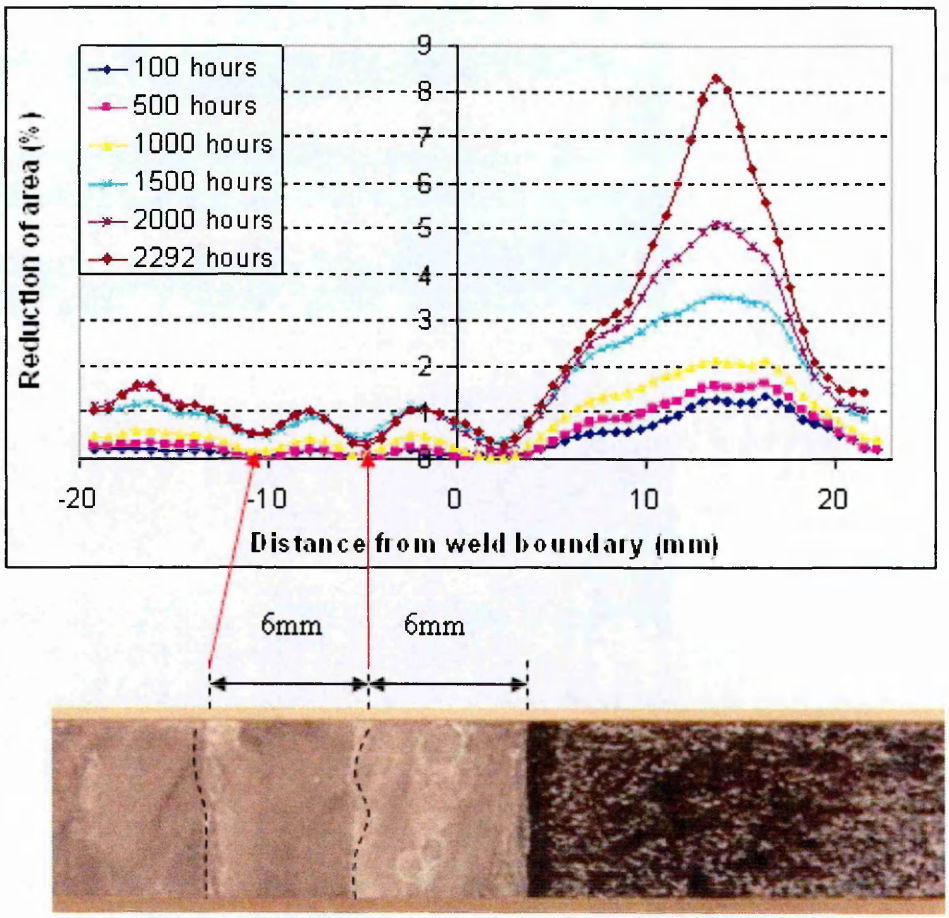

Figure 5.59 Photograph of the metallographically prepared sample cut from the side of the middle position specimen gauge length. The beads correlate with the with reduction of area variation shown above.

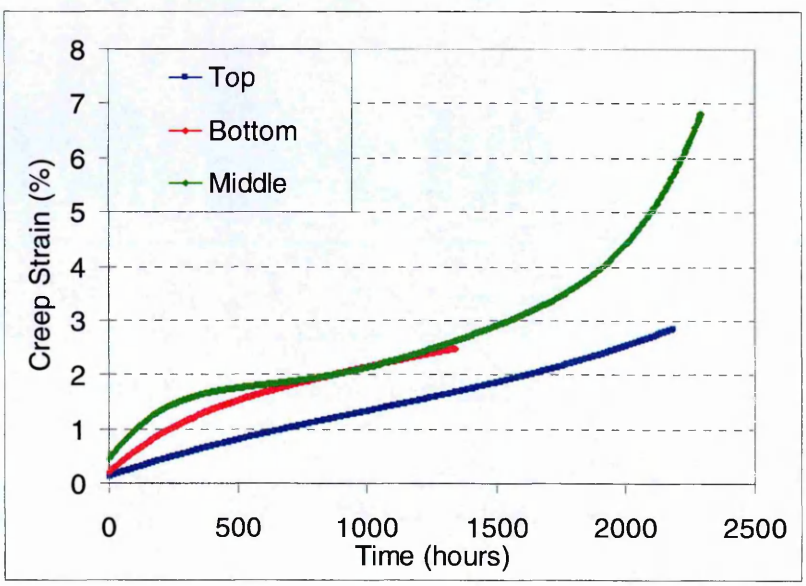

Figure 5.60 Creep curves of top, middle and bottom at parent material (x=12mm)

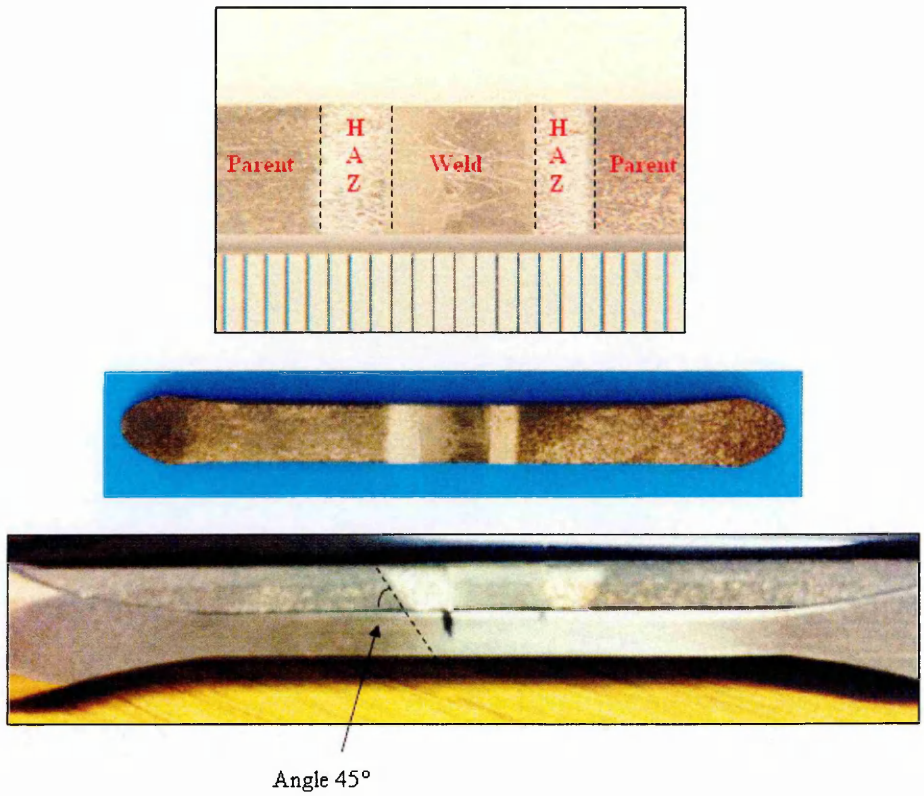

Figure 5.61 Photograph (upper) showing the metallographically prepared sample cut from the side of the bottom position specimen gauge length, and photograph (lower) showing edge view of creep specimenand removed piece.

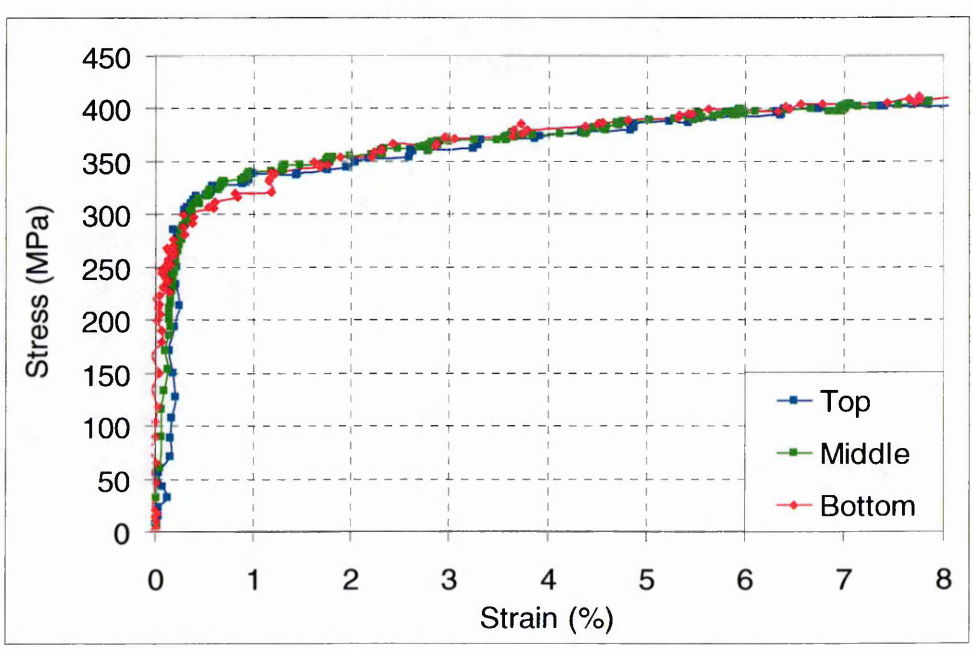

Figure 5.62 Stress-strain curves from the top, middle and bottom specimens at weld metal position x=-2 mm at 545°C

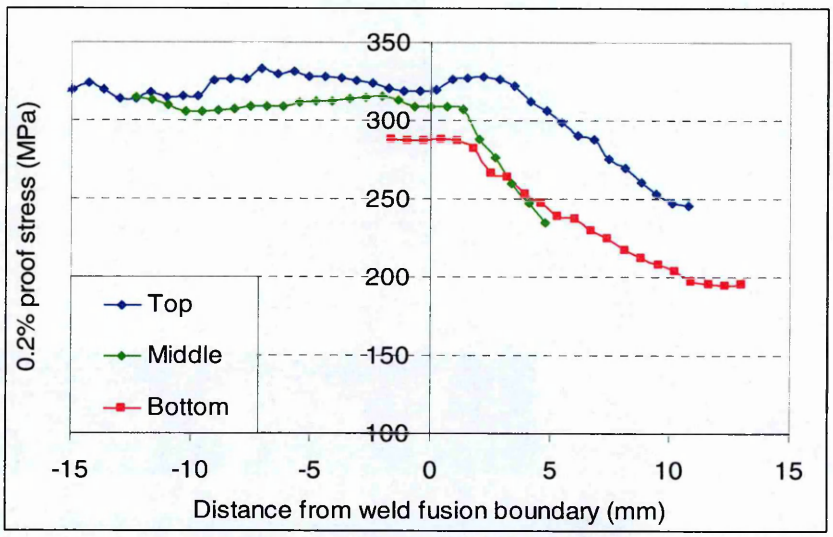

Figure 5.63 Comparison of the 0.2% proof stress variation across the weldment at the top, middle and bottom positions at 545°C

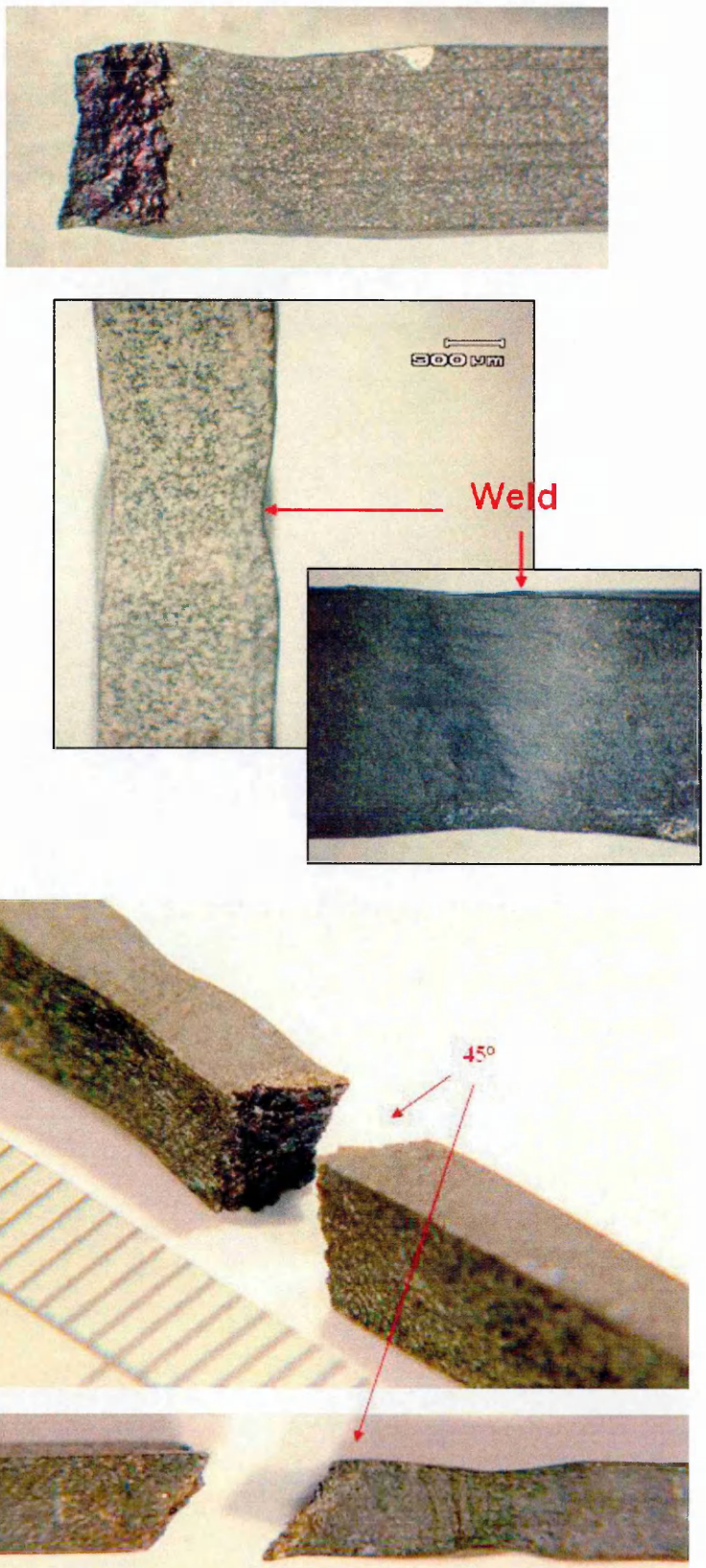

Figure 5.64 Ruptured specimen from bottom position shows large deformation, reduction of area at the middle of the weld and the inclined rupture (thickness section)

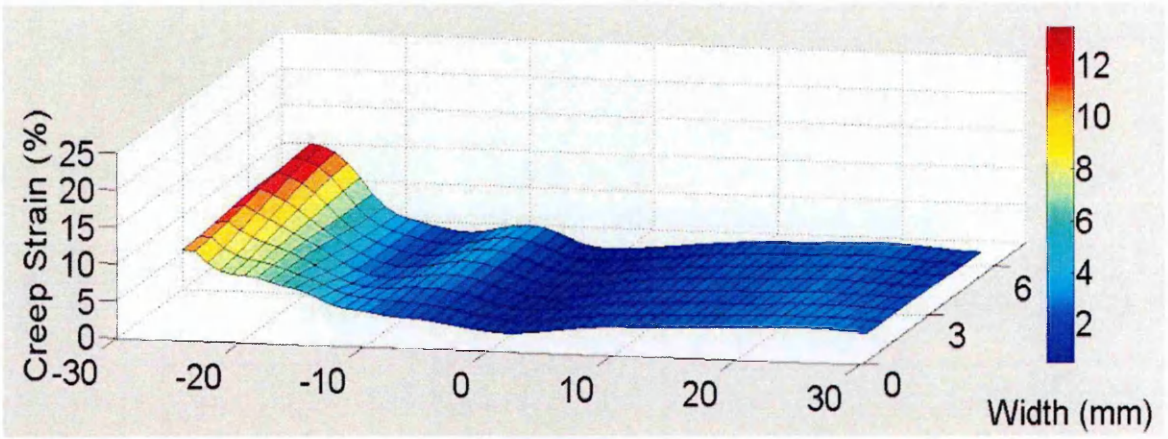

Top position

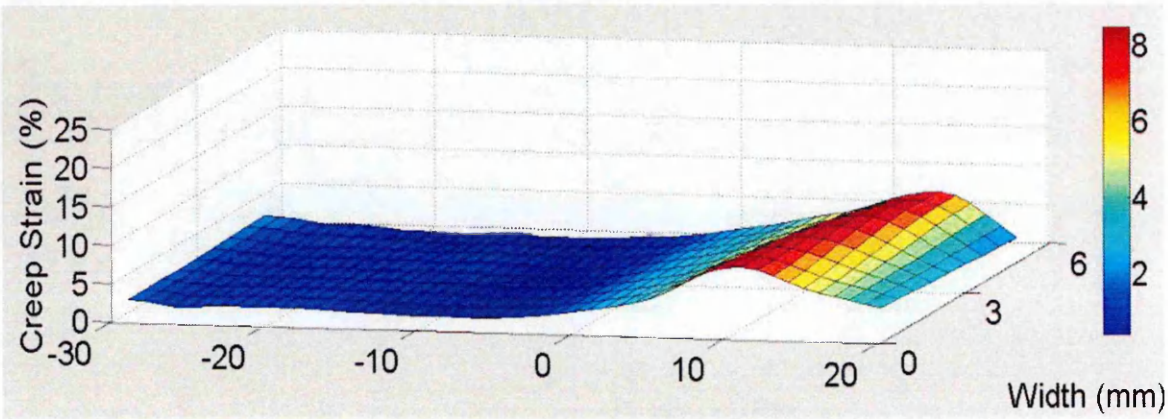

Middle position

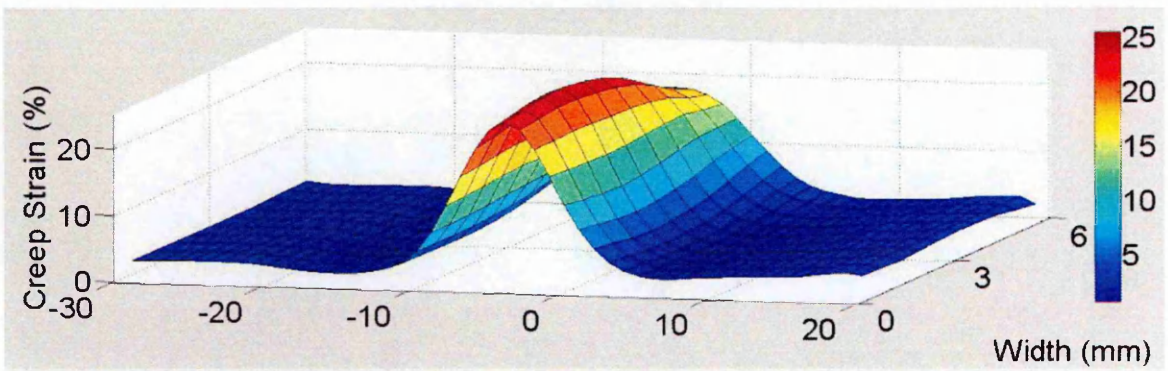

Bottom position

Figure 5.65 3D plot of creep strain along the gauge length prior to failure for the top, middle and bottom positions

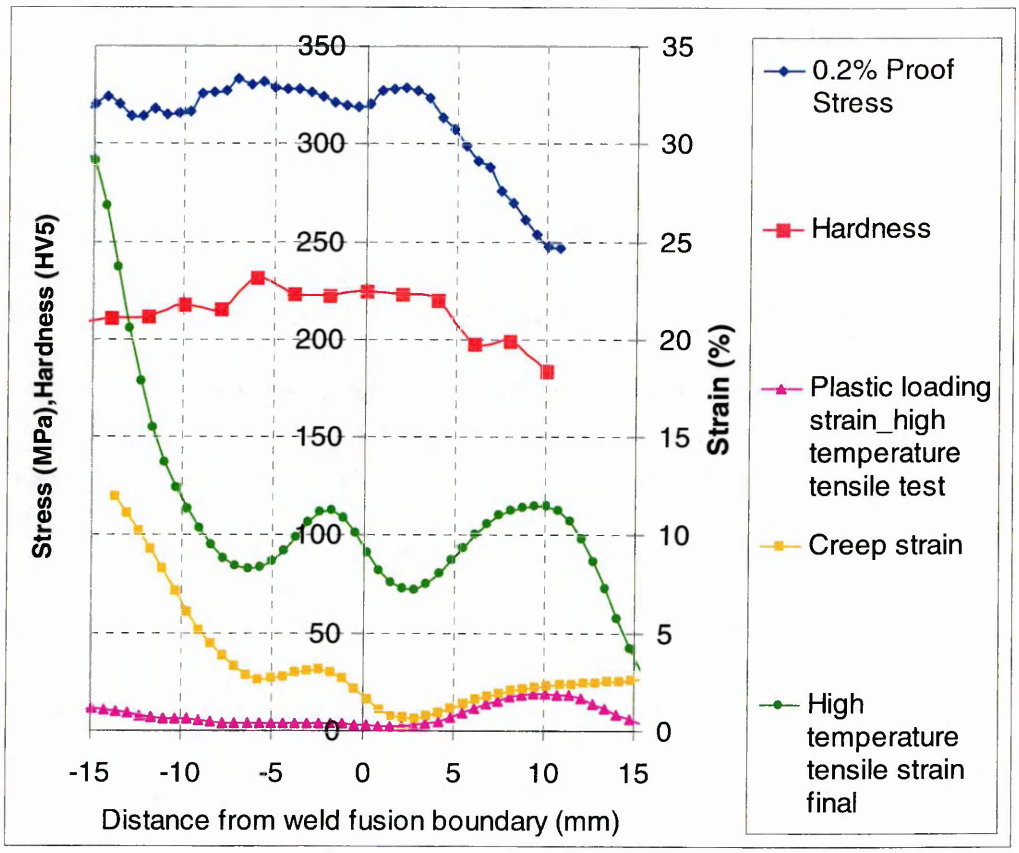

Figure 5.66 Combined hardness, DIC high temperature tensile and creep test results for the top position in the multi-pass weldment

Chapter 6 Conclusions

A high temperature strain measurement system for creep deformation has been developed in this PhD project using digital image correlation. Instead of measuring global strain with a conventional extensometer, this newly developed system provides spatially resolved deformation data for inhomogeneous material under load. Local time dependent creep deformation properties of weld, HAZ and parent material in a multi-pass weldment have been measured in long term creep tests at elevated temperature. Results from the system can be used to infer the reduction of area as strain accumulates and thereby the true stress as well as observe tertiary rupture behaviour.

6.1 High Temperature DIC System Development

This project has addressed the challenges of measuring high temperature strain in cross-weld samples under applied load using DIC. The difficulties in measurement of creep strain at elevated temperature using an optical method have been discussed in Chapter 4. A prime concern is control of the sample surface condition to avoid undue oxidation owing to long term high temperature exposure as this can lead to a deteriorated specimen surface speckle pattern. This has been solved by applying high temperature resistant paint which maintained the sample surface in good condition during thermal soak tests at 600 ^{o}C lasting 3600 hours. Furthermore, creating an adequate speckle pattern by spraying with black and white paint produced a clearer image with better contrast and

contributed to higher accuracy analysis of DIC results. Good illumination of the specimen surface in the furnace is essential for good quality photographs. A camera with a strobe flash light was installed and this produced superior white intensity illumination. The system worked by synchronising with the shutter of the camera and this improved the reliability of lighting compared with a continuous light system. Image distortion due to thermal currents is another issue that hampers high temperature deformation measurement. This problem was controlled by introducing a glass window across the furnace access aperture and attaching a small fan outside the furnace window to reduce local air variations around the test system. Finally, a new specimen design was developed for the creep test system and its suitability confirmed by simple finite element analysis and testing.

Preliminary tests of a plain (homogeneous) specimen indicated good agreement with global strain measured by extensometers during a high temperature tensile test and a creep test. This confirmed that the major problems associated with the measurement of creep strain at elevated temperature using DIC had been solved and validated satisfactorily.

6.2 Multi-pass Welded Joint

The new measurement system has been applied to examine the creep behaviour of a thick section multi-pass welded joint made from Type 316H austenitic stainless steel, which was supplied by EDF Energy. Specifically the local creep deformation properties across the weldment in the parent material,

HAZ and multi-pass weld layers have been investigated in creep tests under a nominal stress of 315 MPa at a temperature of 545°C lasting over 2000 hours. Spatially resolved stress-strain (tensile) and strain-time (creep) results have been obtained transversely across the multi-pass weldment and for three positions across the thickness direction (top, middle and bottom). Significantly lower creep strain rates were observed in the HAZ at all positions tested in the weldment. The DIC in-situ measurements also provided strain information in the transverse to loading direction from which the reduction of area of the specimen and true stress and strain distribution were calculated. Visual information presented evidence of a clear variation in creep strain across the weld metal which correlated with individual weld passes in the welded joint. Interestingly the peak of creep strain in individual passes corresponded to the centre of a weld bead. However, the final failures occurred mainly at the fusion boundaries of welds. The full-field measurement results allowed the development of creep deformation leading to ultimate rupture to be observed. The weld root position failed in the shortest time (1500h). Although the root weld bead itself exhibited the maximum creep deformation rate, failure actually occured in the HAZ/weld location adjacent to the 45° angle fusion boundary where the creep ductility was 1.7%. Elsewhere in the weldment failure occurred at longer times (>2100h) in weld beads furthest from the vertical fusion boundary where the local ductility was about 5%.

High temperature tensile tests made clear how much instantaneous plastic strain had been introduced at the applied stress level of the creep test. These results suggested the potential importance of initial plastic strain (observed in the

parent material) on the creep properties because the weld metal showed generally faster creep rates than HAZ and parent materials.

Creep testing using a DIC based deformation monitoring system provides spatial and time resolved creep deformation data that can be used to understand the creep behaviour of weldments that have inhomogeneous properties. Moreover such tests provide high quality creep data that can be used to develop better creep deformation models that will subsequently lead to improved plant creep life predictions.

6.3 Suggested Future Work

6.3.1 Use of DIC Creep Data

This work has succeeded in measuring creep deformation properties at high temperature using a DIC method. Spatially resolved creep deformation information across inhomogenous weldments in the form of local creep curves are available for creep deformation modelling. In addition, data relating to true strain and true stress, based on reduction of area, can be obtained. These measured data could be used to develop and validate improved creep constitutive equations covering both primary and secondary creep for different material states across the weld. For example the RCC-MR constitutive equation (introduced earlier in this thesis) is currently the most reliable model for the creep deformation behaviour of Type 316H stainless steel (parent material). Coefficients for this model could be derived for different zones of weldment material (parent, HAZ and weld). The

model could then be implemented in a finite element analysis for more precise simulation of the full field creep deformation behaviour of a thick section multi-pass welded joint. The performance of the prediction could then be compared with DIC results. The data might also be able to contribute to creating new creep deformation models capable of capturing the detailed variation in creep properties across a weldment.

6.3.2 Creep Crack Growth Measurement

High temperature fracture mechanics can be a next challenge for DIC application. The detection of damage, crack growth and the deformation field around a crack tip is important for material development, design and for life assessment of engineering components operating at high temperature. There are not many examples of work in this area using the DIC technique. Currently, the most common crack-growth measurement technique is called 'potential-drop', where a high electrical current is passed through the sample and the potential drop, i.e. the voltage, is measured across the crack [1]. However, the propagation path is not always straight and also estimates of the location of the crack tip affects the key parameter of evaluation, that is the stress intensity factor, K. Mathieu et al [2] proposed to use DIC to identify parameters governing crack propagation at room temperature. The most widely used standard specimen for high temperature creep crack growth testing is the compact tension (CT) specimen. Reliable measurement of load line displacement (Δ) and crack length (a) in a CT specimen test affects the calculation of evaluation parameters, K and C*, which are

used to determine steady-state creep crack growth rate properties. Although the load line displacement can be measured using a displacement gauge, DIC has the potential to provide a history of the full field crack opening displacement and crack length accurately. The optical observation also can give the 2D distribution of strain field around the tip, which may be analysed and related to K and C* as well. The technology could also be used to investigate the development of cracks in inhomogenous material associated with weldments.

6.3.3 Weld Strength Mismatch Effects at High Temperature

DIC experimental research can be suggested to clarify elastic, plastic and creep property mismatch effects across weldments at high temperature. The constraint associated with variations across material interfaces or sharp gradients in properties has an important influence upon structural deformation and localisation of damage and failure. For example the effect of the mismatch ratio of yield strength between parent and weld material can be measured during a high temperature tensile DIC test, and the effect of a nearby weld interface on a crack tip deformation field during creep crack growth could be assessed.

6.3.4 Anelastic Strain Measurement

An abrupt reduction of stress at high temperature can induce anelastic strain, which can be defined as the time-dependent recovery of plastic strain after unloading [3], [4]. For anelastic strain measurement, a LVDT transducer is commonly used during a high temperature creep test. Although LVDTs are

generally reliable, the newly developed DIC optical measurement system described in this thesis might capture the back strain more precisely. For inhomogeneous samples, such as cross welds, the DIC method could measure the full field local response. The anelasticity behaviour is expected to be different across a weldment owing to the local microstructure, variation in properties, mismatch and structural effects.

6.3.5 System Development

Although a DIC high temperature creep measurement system has been developed satisfactorily, there are more improvements for future work that I can suggest.

1. Temperature control along the gauge length was more difficult than in conventional creep testing due to the furnace window. Because DIC measures the local strain rather than strain averaged along the gauge length, temperature control is especially important to avoid introduction of another source of scatter in measured creep data. I recommend maintaining the gauge length temperature difference between top and bottom positions within one degree centigrade and calibrating thermocouples before the creep test.
2. Using a bigger size furnace window is the next challenge. This will enable creep crack growth to be measured by DIC in CT specimens. It will also allow larger specimens to be tested, for example, a whole thick section

multi-pass welded joint rather than using small specimens extracted from different position in the weldment. This would characterise the whole welded joint and give us the answer of weld preparation angle effect on failure location.

3. Local strain measurement using a high temperature strain gauge could be done and the results used to validate local creep strain measurements made using DIC.

4. The temperature variation along the specimen gauge length is especially important. Monitoring the spatial variation using a thermal camera during the test would be ideal. Knowing the local temperature at a certain position in the full field would allow material temperature effects to be assessed more precisely. Thus the activation energy could be calculated based on the local temperature when fitting constitutive models. But the temperature resolution of a thermal camera has to be better than ±0.5°C, and this may not be achievable if the device is sensitive to surface oxidation effects.

6.4 References

[1] "Structure Integrity Designing against Failure: T357, The Open University." .

[2] F.Mathieu, "Identification of a crack propagation law by digital image correlation," *International Journal of Fatigue*, vol. 36, p. 146, 2012.

[3] K.Sawada., K.Kimura, and F. Abe, "Mechanical response of 9% Cr heat-resistant martensitic steel to abrupt stress loading at high temperature," *Material Science and Engineering*, vol. A358, no. 52, 2003.

[4] A. Rao, P. J. Bouchard, S. M. Northover, and M. E. Fitzpatrick, "Anelasticity in austenitic stainless steel," *Acta Materialia*, vol. 60, no. 19, pp. 6851–6861, 2012.